Physics Area - Ph.D. course in
Theory and Numerical Simulations of Condensed Matter

CHARGE AND HEAT TRANSPORT IN IONIC CONDUCTORS

Candidate:
Paolo Pegolo

Advisors:
Prof. Stefano Baroni
Dr Federico Grasselli

Academic Year 2021-2022

ABSTRACT

Transport coefficients relate the off-equilibrium flow of locally conserved quantities, such as charge, energy, and momentum, to gradients of intensive thermodynamic variables in the linear regime. Despite their mathematical formalization dating back to the middle of the last century, when Green and Kubo developed linear response theory, some conceptual subtleties were only recently understood through the formulation of the gauge-invariance and convective-invariance principles. In a nutshell, these invariance principles suggest that transport coefficients are mostly independent of the microscopic definition of the densities and currents. In this thesis, we analyze the consequences of gauge and convective invariances on the charge and heat-transport properties of ionic conductors.

The combination of gauge invariance with Thouless' theorem on charge quantization reconciles Faraday's picture of ionic charge transport—whereby each atom carries a well-defined integer charge—with a rigorous quantum-mechanical definition of atomic oxidation states. The latter are topological invariants depending on the paths traced by the coordinates of nuclei in the atomic configuration space. When some general topological conditions are relaxed, we show that oxidation states lose their meaning, and charge can be adiabatically transported across macroscopic distances without a net ionic displacement. This allows for a classification of the different regimes of ionic transport in terms of the topological properties of the electronic structure of the conducting material.

Invariance principles also allow one to compute thermal conductivity in multicomponent materials such as ionic conductors through equilibrium molecular dynamics simulations. In particular, heat management is of paramount importance in solid-state electrolytes, solid materials relevant for the production of next-generation batteries, where ionic conduction is mediated by diffusing vacancies and defects. The aforementioned conceptual difficulties in the theory of thermal transport are the root cause of a lack of systematic exploration of such properties in solid-state electrolytes. We showcase the ability of the invariance principles to overcome these issues together with state-of-the-art data analysis techniques in the paradigmatic example of the Li-ion conductor Li_3ClO. We provide a simple rationale to explain the temperature and vacancy-concentration dependence of its thermal conductivity, which can be interpreted as the result of the interplay of a crystalline component and a contribution from the effective disorder generated by ionic diffusion.

PUBLICATIONS

This Thesis is based on the following publications:

[1] Paolo Pegolo, Federico Grasselli, and Stefano Baroni. "Oxidation States, Thouless' Pumps, and Nontrivial Ionic Transport in Nonstoichiometric Electrolytes." In: *Physical Review X* 10 (4 Nov. 2020), p. 041031. DOI: 10.1103/PhysRevX.10.041031. URL: https://link.aps.org/doi/10.1103/PhysRevX.10.041031.

[2] Paolo Pegolo, Stefano Baroni, and Federico Grasselli. "Temperature- and vacancy-concentration-dependence of heat transport in Li3ClO from multi-method numerical simulations." In: *npj Computational Materials* 8.1 (Jan. 2022), p. 24. ISSN: 2057-3960. DOI: 10.1038/s41524-021-00693-4. URL: https://doi.org/10.1038/s41524-021-00693-4.

[3] Paolo Pegolo, Stefano Baroni, and Federico Grasselli. "Topology, Oxidation States, and Charge Transport in Ionic Conductors." In: *Annalen der Physik* 534.10 (2022), p. 2200123. DOI: https://doi.org/10.1002/andp.202200123. eprint: https://onlinelibrary.wiley.com/doi/pdf/10.1002/andp.202200123. URL: https://onlinelibrary.wiley.com/doi/abs/10.1002/andp.202200123.

[4] Paolo Pegolo. "Minimum mean square error estimation of transport coefficients." (In preparation). 2022.

CONTENTS

ACRONYMS

ACS Atomic Configuration Space

AF Allen-Feldman

AIC Akaike Information Criterion

AIMD Ab Initio Molecular Dynamics

BE Bose-Einstein

BEC Born Effective Charge

BTE Boltzmann Transport Equation

BZ Brillouin Zone

CGF Cumulant Generating Function

CM Classical Mechanics

DFPT Density Functional Perturbation Theory

DFT Density Functional Theory

DP Deep Potential

EMD Equilibrium Molecular Dynamics

ET Electron Transfer

FF Force Field

GK Green-Kubo

HE Helfand-Einstein

HOMO Highest-Occupied Molecular Orbital

IFC Interatomic Force Constant

iid independent identically distributed

KS Kohn-Sham

LHS left-hand side

LO-TO Longitudinal Optical-Transverse Optical

LP Landau-Pekar

LTE Local Thermal Equilibrium

LUMO Lowest-Unoccupied Molecular Orbital

MEP Minimum Energy Path

MMSE Minimum Mean Square Error

MSDD Mean Square Displaced Dipole

MSE Mean Square Error

MUB Marcolongo-Umari-Baroni

NAC Nonanalytic Contributions

NN Neural Network

OBCs Open Boundary Conditions
OS Oxidation State
PBCs Periodic Boundary Conditions
PBE Perdew-Burke-Ernzerhof
PES Potential Energy Surface
PSD Power Spectral Density
QHA Quasi-Harmonic Approximation
QHGK Quasi-Harmonic Green-Kubo
QM Quantum Mechanics
QSA Quasi-Static Approximation
RHS right-hand side
RT Room Temperature
RTA Relaxation Time Approximation
SA Strong Adiabaticity
SG Savitzki-Golay
SM Slack Model
SSE Solid-State Electrolyte
VDOS Vibrational Density Of States
WC Wannier Center
WF Wannier Function
XC Exchange and Correlation

INTRODUCTION

Ionic conductors are materials with highly mobile ions that, moving around, transport charge while the material stays electronically insulating. Electrolytes had a fundamental role of the foremost importance since the dawn of the atomistic theory, at a time when continuum theories of mechanics and thermodynamics were deemed to be final. Even decades before atoms were accepted to exist, Michael Faraday's experiments of the 1830s made a connection between the charge flowing from one end of an electrode to the other and the amount of substance in the electrolytic cell. The proportionality constant between the transported charge and mass is indeed an integer multiple of the electronic charge, as Faraday himself somewhat pointed out by computing a *table of ions* filled with numbers strikingly resembling the atomic weights of many different chemical species. Faraday was actually measuring charge-to-mass ratios that, once properly scaled by the atomic masses, can be thought of as *ante litteram* oxidation states. Faraday's measurements lead him to hypothesize, despite being an ardent experimental physicist with little taste for theoretical speculations, that *atoms* in solution—in case they exist—are likely to be endowed with a definite charge they displace along their motion.

Significantly, the experiments that first suggested the concept of oxidation states involved measuring the charge in transit between two electrodes: at the foundation of this phenomenon is the theorem of charge quantization that David J. Thouless formulated 150 years after Faraday's work. Like experiments in electrolysis, Thouless' theorem involves the motion of charges across macroscopic distances, rather than a static view, a *snapshot*, of the microscopic system of particles. Charge quantization is rooted in topology, and in topology is rooted a formal, quantum-mechanical definition of oxidation states that fulfills all the properties that chemical intuition and tradition have attributed to oxidation states ever since their widespread usage as a bookkeeping device, first and foremost, their being integer-valued. As oxidation states are ultimately associated with dynamics, their specific value has, in turn, an impact on ionic charge transport in electronically insulating materials. In fact, under suitable topological conditions, one can remarkably make use of atomic oxidation states to understand a material's ability to conduct electricity, even in a rigorous quantum-mechanical picture where integer charges cannot be identified. This forces charges to be bound to the erratic motion of ions in a fluid and thus be transported only alongside mass. The situation is hardly as clear when the aforementioned topological conditions are relaxed: here, surprising effects such as the loss of correlation between charge and mass transport manifest themselves. Ionic transport is encoded in the value of ionic conductivity, σ, the transport coefficient relating the flux of electrical (ionic) charges to an applied electrostatic field.

Transport coefficients are quintessential examples of off-equilibrium properties in the linear regime. They relate the flow of locally conserved quantities, such as charge, energy, and momentum, to gradients of intensive thermodynamic variables. They ultimately describe entropy production and the approach to equilibrium of macroscopic systems weakly driven outside of it. The math-

ematical description of this phenomenon was formulated in the 1950s by Melville Green and Ryogo Kubo. The Green-Kubo theory provides a rigorous and elegant way to compute transport coefficients in terms of equilibrium time correlation functions of the currents they are related to. This feature makes the computation of transport coefficients accessible to equilibrium molecular dynamics simulations, and it is thus applicable to all states of matter.

Besides the flux of ionic current, another dissipative phenomenon happening in ionic conductors is of paramount importance for technological applications: thermal transport. The microscopic mechanisms of heat transport, in fact, govern heat management in any realistic device, such as next-generation batteries based on solid-state electrolytes. Despite its indisputable relevance, thermal transport in solid-state ionic conductors is rarely investigated. A reason behind this fact might be that *thermal conductivity has proven to be one of the most difficult transport coefficients to calculate*, quoting Evans and Morriss' *Statistical mechanics of nonequilibrium liquids*. Methods based on lattice dynamics, where normal modes are the heat carriers, and thermal conduction is governed by the scattering processes responsible for the normal modes' decay, are only helpful when the system can be described in terms of well-defined equilibrium positions around which the atoms vibrate, and at low temperature, where the harmonic approximation applies or anharmonic effects are small enough to be treated in a perturbative fashion. In solid-state electrolytes, ionic diffusion is mediated by vacancies and defects. This conflicts with the existence of equilibrium positions required by a lattice-dynamical approach. Regardless of the great successes of anharmonic lattice dynamics in the last few years, which preeminently include the unification and extension of the theory of heat transport in periodic solids with the harmonic theory of thermal transport in glasses, these methods are of little use in the case of ionic conductors. One needs to resort to molecular dynamics simulations, which do not require equilibrium positions and come with the further benefit of automatically accounting for full anharmonicity, possibly an issue at the relatively high operating temperatures of the devices that could be based on solid-state electrolytes.

The leitmotiv threading the results presented in this Thesis is the application to ionic conductors of some recently introduced invariance principles in the theory of transport coefficients; such principles, namely the *gauge* and *convective* invariance principles, formalize the notion that the microscopic definition of the local densities and currents of the conserved quantities being transported is unimportant. Gauge invariance, combined with the topological definition of atomic oxidation states, leads to a clear understanding of Faraday's first law of electrolysis in light of quantum mechanics. Convective invariance allows for the computation of thermal conductivity in multicomponent systems such as electrolytes. The content of this Thesis, whose aim is to investigate some peculiar charge and heat transport properties of ionic conductors using methods from topology and the Green-Kubo theory of transport coefficients, is divided into four Parts.

Part I of this Thesis is devoted to reviewing the Green-Kubo theory of linear response and the data analysis techniques helpful to compute transport coefficients from molecular dynamics simulation accurately. In Ch. 1, Green-Kubo theory is presented from a modern perspective, where the role of recently discovered invariance principles and their consequences on the computation of transport coefficients is stressed. Ch. 2 deals with data analysis; in partic-

ular, *cepstral analysis* is thoroughly reviewed and extended to cases where its standard formulation can be ineffective.

Part II involves charge transport. Ch. 3 reviews adiabatic charge transport and is devoted to elucidating the relationship between Thouless' theorem and charge transport in the context of adiabatic dynamics. Particular emphasis is put on the intimate connection between the Thouless wavefunction and the continuity equation, and thus to transport theory. Ch. 4 contains the core of the original work presented in this Thesis on charge transport: after an excursus on the topological properties of paths traced by atoms in the space of all their coordinates, the rigorous theory of oxidation states is introduced and connected to the ionic conductivity of electrolytes. The topological assumptions needed for such analysis are then relaxed, and the consequences on ionic transport are examined in detail.

Part III is about heat transport in solid-state electrolytes. Ch. 5 reviews the theory of heat transport in solids. Starting from anharmonic lattice dynamics, the quasi-harmonic Green-Kubo theory of thermal transport for ordered and amorphous materials is introduced and linked to the Boltzmann transport equation approach in crystals and the Allen-Feldman theory of thermal conduction in harmonic glasses. The case where diffusing species exist—inducing the failure of the lattice-dynamical picture—is also addressed, together with the Green-Kubo theory of heat transport from molecular dynamics simulations, both with a semi-empirical approach and *ab initio*. Ch. 6 concerns heat transport in the solid-state electrolyte material Li_3ClO. The behavior of thermal conductivity as a function of temperature and the concentration of vacancies is comprehensively investigated and rationalized with a simple model based on the coexistence of ordered and disordered sub-domains.

Part IV contains appendices to some topics presented in the rest of the Thesis.

Part I

THEORY AND NUMERICAL SIMULATIONS OF TRANSPORT PROCESSES

> Whatever lucky stars I may have had the good fortune to walk under, surely one of the most important was the one which led Ryogo Kubo and I to meet. [...] We were both intrigued by the possibilities we saw in the correlation-function methods we had pioneered, that the calculation of response functions from the fluctuations in the equilibrium state avoided all the complications of Boltzmann's equation and the formal difficulties of irreversibility.
>
> Philip Warren Anderson, Scientific and Personal Reminiscences of Ryogo Kubo, The Physical Society of Japan, 1995

1

THEORY OF TRANSPORT PROCESSES

1.1 EXTENSIVITY AND ADDITIVITY

EXTENSIVE VARIABLES appear often in condensed matter physics. They are physical quantities associated with a composite system with the property of scaling with the number of subsystems the larger system can be divided into; common examples are the energy and the entropy [1]. An extensive property can also be additive[1]. For a system with volume Ω, an extensive quantity—or *generalized charge*, $\mathcal{Q}$—is additive with respect to two subsystems, with volumes Ω_1 and Ω_2, if the charge relative to the whole system equals the sum of the charges relative to the two subsystems:

$$\mathcal{Q}[\Omega] = \mathcal{Q}[\Omega_1] + \mathcal{Q}[\Omega_2]. \tag{1.1}$$

If additivity can be applied once again to the two subsystems, and so on for smaller and smaller volumes, one ends with being able to assign a value of $\mathcal{Q}$—its *density*, $q(\mathbf{r})$—to a volume $\mathrm{d}^3 r$, which can be thought of as infinitesimal with respect to the macroscopic size of the entire system. The function $q(\mathbf{r})$ so defined is the *generalized density* associated with the extensive quantity $\mathcal{Q}$, which is thus expressed by the volume integral

$$\mathcal{Q}[\Omega] = \int_\Omega q(\mathbf{r})\, \mathrm{d}^3 r\,. \tag{1.2}$$

In thermodynamics, the principle of maximum entropy asserts that, at thermal equilibrium, the partial derivatives of the entropy function, $\mathcal{S}$, with respect to extensive, conserved variables are intensive variables uniform across the whole system:

$$\frac{\partial \mathcal{S}}{\partial \mathcal{Q}} = \alpha = \text{const.} \tag{1.3}$$

If local inhomogeneities occur, α is not constant anymore, i.e. $\nabla\alpha \neq 0$, and $\mathcal{Q}$ flows from regions with higher α to regions with lower α. The rate of change of the globally conserved charge, $\dot{\mathcal{Q}}$, is

$$\dot{\mathcal{Q}}[\Omega] = \int_\Omega \dot{q}(\mathbf{r})\, \mathrm{d}^3 r \tag{1.4}$$

which, according to Stokes' theorem, can be recast to the form

$$\begin{aligned} \dot{\mathcal{Q}}[\Omega](t) &= \int_\Omega \dot{q}(\mathbf{r}, t)\, \mathrm{d}^3 r \\ &= -\int_{\partial\Omega} \mathbf{J}_{\mathcal{Q}}(\mathbf{r}, t) \cdot \hat{\boldsymbol{\sigma}}\, \mathrm{d}^2\sigma\,, \end{aligned} \tag{1.5}$$

1 There are peculiar examples of additive quantities which are not extensive [1]. Therefore the implication "additivity $\implies$ extensivity" does not hold in general: for the purposes of the present work, these situations are irrelevant and, as such, they will not be considered.

where $\mathbf{j}_{\mathcal{Q}}(\mathbf{r},t)$ is the *conserved current* associated with $\mathcal{Q}$. Integration by parts of Eq. (1.5) yields the *continuity equation*, which relates the time-derivative of the density to the divergence of the respective current:

$$\dot{q}(\mathbf{r},t) + \nabla \cdot \mathbf{j}_{\mathcal{Q}}(\mathbf{r},t) = 0. \tag{1.6}$$

When $\mathcal{Q}$ is locally conserved, there are neither sources nor sinks: the continuity equation formalizes such a notion.

1.2 HYDRODYNAMIC VARIABLES

Fourier-transforming in space the continuity equation yields

$$\dot{\tilde{q}}(\mathbf{k},t) = -\mathrm{i}\mathbf{k} \cdot \tilde{\mathbf{j}}_{\mathcal{Q}}(\mathbf{k},t), \tag{1.7}$$

where the tilde above a quantity indicates its Fourier transform. Since the wavelength of the Fourier mode with wave-vector $\mathbf{k}$ is proportional to $1/|\mathbf{k}|$, it follows that the longer the wavelength, the slower the time evolution of the conserved density. In an atomistic framework, where the properties of the system arise from the statistical behavior of a vast number of rapidly moving elementary constituents, a long enough wavelength ensures the dynamics of conserved densities to be adiabatically decoupled from the motion of the atoms, which happen on short timescales. *Hydrodynamic variables* are defined as the long wavelength modes of conserved densities [2–4].

The adiabatic decoupling of the hydrodynamics variables with respect to the atomic motion means that, off-equilibrium, the wavelengths and timescales of the disturbances are so large that a local notion of equilibrium can still be established, i.e., local, intensive thermodynamic properties such as temperature, pressure, and chemical potentials can be defined in a small enough—yet macroscopic if compared to interatomic distances—neighborhood of any point $\mathbf{r}$. Such a construct is called Local Thermal Equilibrium (LTE). Under this hypothesis, intensive variables become functions of space, e.g. the temperature would be $T(\mathbf{r})$.

Let us suppose the system to have a number M of conserved charges $\{\mathcal{Q}_l\}_{l=1}^{M}$, such as the number of particles, energy, momentum, etc., such that LTE is established. Without loss of generality, let us set to zero the equilibrium values of such quantities, so that the associated conserved densities $\{a_l\}_{l=1}^{M}$ and currents $\{\mathbf{j}_l\}_{l=1}^{M}$ represent deviations from equilibrium. If the latter are small enough, one can suppose the time derivative of any density to be a linear combination of all the other densities. In space and time Fourier domains, this reads:

$$\mathrm{i}\omega\tilde{q}_l(\mathbf{k},\omega) = \sum_j \tilde{\Lambda}_{lj}(\mathbf{k},\omega)\tilde{q}_j(\mathbf{k},\omega), \tag{1.8}$$

where $\tilde{\Lambda}_{lj}(\mathbf{k},\omega)$ are suitably defined coefficients. By combining the last equation with Eq. (1.7), one finds the *constitutive equations*:

$$-\mathrm{i}\mathbf{k} \cdot \tilde{\mathbf{j}}_l(\mathbf{k},\omega) = \sum_j \tilde{\Lambda}_{lj}(\mathbf{k},\omega)\tilde{q}_j(\mathbf{k},\omega). \tag{1.9}$$

This implies that, for the longitudinal component of any conserved current, the following equation holds:

$$\tilde{\mathbf{j}}_l(\mathbf{k},\omega) = \mathrm{i}\frac{\mathbf{k}}{k^2}\sum_j \tilde{\Lambda}_{lj}(\mathbf{k},\omega)\tilde{q}_j(\mathbf{k},\omega). \tag{1.10}$$

In isotropic media, the $\tilde{\Lambda}$ functions are spherically symmetric in $\mathbf{k}$, and their $\mathbf{k} = \mathbf{0}$ value is zero; otherwise, the long-range modes of the currents would be coupled to the density fluctuations, which conflicts with the hypothesis of LTE. One can thus assume that the long-wavelength, small-frequency form of such quantities is

$$\tilde{\Lambda}_{lj}(\mathbf{k},\omega) \sim k^2\lambda_{lj}. \tag{1.11}$$

Therefore, the normalized volume-integral of the stationary microscopic current, i.e., the $\mathbf{k} = \mathbf{0}$, $\omega = 0$ component of the Fourier-space current reads

$$\begin{aligned}\mathbf{J}_l =& \frac{1}{\Omega}\int_\Omega \mathbf{j}_l(\mathbf{r})\,\mathrm{d}^3r \\ =& \lim_{k\to 0}\tilde{\mathbf{j}}_l(\mathbf{k},\omega=0),\end{aligned} \tag{1.12}$$

and it is related to the density gradients, $\mathbf{D}_l = \Omega^{-1}\int \nabla q_l\,\mathrm{d}^3r$:

$$\begin{aligned}\mathbf{J}_l =& \lim_{k\to 0}\mathrm{i}\frac{\mathbf{k}}{k^2}\sum_j k^2\lambda_{lj}\tilde{q}_j(\mathbf{k},\omega=0) \\ =& \lim_{k\to 0}\sum_j \lambda_{lj}\,\mathrm{i}\mathbf{k}\,\tilde{q}_j(\mathbf{k},\omega=0) \\ =& \sum_j \lambda_{lj}\lim_{k\to 0}\frac{1}{\Omega}\int_\Omega \nabla q_j(\mathbf{r},\omega=0)\mathrm{e}^{-\mathrm{i}\mathbf{k}\cdot\mathbf{r}}\,\mathrm{d}^3r \\ =& \sum_j \lambda_{lj}\mathbf{D}_j.\end{aligned} \tag{1.13}$$

The macroscopic quantity $\mathbf{J}$ associated with a current density $\mathbf{j}(\mathbf{r})$, i.e., its normalized volume-integral, is called a *conserved flux*. Integrating by parts the continuity equation (1.6), an equivalent definition of $\mathbf{J}$ is found:

$$\mathbf{J}(t) = \frac{1}{\Omega}\int \dot{q}(\mathbf{r},t)\mathbf{r}\,\mathrm{d}^3r\,. \tag{1.14}$$

The intensive thermodynamic variables, ζ_l, conjugate to the extensive variables $\mathcal{Q}_l$ are defined as the derivatives of the thermodynamic potential—in the microcanonical case, the entropy $\mathcal{S}(\{\mathcal{Q}_l\})$—with respect to its arguments:

$$\zeta_l = \frac{\partial\mathcal{S}}{\partial\mathcal{Q}_l}, \tag{1.15}$$

while the *susceptibilities* are:

$$\chi_{lj} = \frac{1}{\Omega}\frac{\partial\mathcal{Q}_l}{\partial\zeta_j}. \tag{1.16}$$

Under LTE, local values of the intensive variables ζ_l can be defined, and the integrals of their gradients are called *thermodynamic forces*:

$$\mathbf{F}_l = \frac{1}{\Omega}\int_\Omega \nabla\zeta_l(\mathbf{r})\,\mathrm{d}^3r\,. \tag{1.17}$$

From Eq. (1.17), a relationship between the density gradients and the thermodynamic forces is found, the two quantities being coupled via the susceptibilities as

$$\mathbf{D}_l = \sum_j \chi_{lj} \mathbf{F}_j. \tag{1.18}$$

Plugging Eq. (1.18) into Eq. (1.13) yields

$$\mathbf{J}_l = \sum_j \Lambda_{lj} \mathbf{F}_j, \tag{1.19}$$

where $\Lambda_{lj} = \sum_k \lambda_{lk} \chi_{kj}$. This equation states a linear relationship between conserved fluxes, $\mathbf{J}_l$, and the thermodynamic forces, $\mathbf{F}_l$. The phenomenological Onsager's coefficients, Λ_{lj}, fulfill a reciprocity relation, $\Lambda_{lj} = \Lambda_{jl}$ [5, 6].

1.3 LINEAR RESPONSE THEORY

Linear response theory allows for a systematic evaluation of Onsager's coefficients, Λ_{lj}. Let us consider a classical system of N particles described by the Hamiltonian

$$\widehat{\mathcal{H}}_0(\mathbf{\Gamma}) = \sum_{\ell=1}^{N} \frac{P_\ell^2}{2m_\ell} + \widehat{\mathcal{V}}(\mathbf{R}_1, \mathbf{R}_2, \ldots, \mathbf{R}_N), \tag{1.20}$$

where m_ℓ, $\mathbf{R}_\ell$ and $\mathbf{P}_\ell$ are the mass, position and momentum of the ℓth atom in the system, and $\widehat{\mathcal{V}}$ is the interatomic potential energy. Phase-space variables are denoted by the short-hand notation $\mathbf{\Gamma} = \{\mathbf{R}_1, \mathbf{R}_2, \ldots, \mathbf{R}_N, \mathbf{P}_1, \mathbf{P}_2, \ldots, \mathbf{P}_N\}$, and here phase-space functions are indicated by a wide caret ($\widehat{\ }$) symbol on top. The expectation value, $\mathcal{Q} = \langle \widehat{\mathcal{Q}}(\mathbf{\Gamma}) \rangle_0$, of an observable, $\widehat{\mathcal{Q}}$, at equilibrium is given by the canonical average

$$\mathcal{Q} = \int \widehat{\rho}_0(\mathbf{\Gamma}) \widehat{\mathcal{Q}}(\mathbf{\Gamma}) \, \mathrm{d}^{6N}\Gamma \,, \tag{1.21}$$

$$\widehat{\rho}_0 = \exp\left\{ -\widehat{\Phi}_0 - \beta \widehat{\mathcal{H}}_0 \right\}, \tag{1.22}$$

where $\widehat{\Phi}_0$ is $\beta = 1/(k_\mathrm{B} T)$ times the Helmoltz free energy, k_B is Boltzmann's constant, and T is the system's temperature. At thermal equilibrium, the system is characterized by the same energy density, $e(\mathbf{r})$, at every point in space, and the particle densities, $n_1(\mathbf{r}), \ldots, n_s(\mathbf{r})$ of the N_s, possibly electrically charged, chemical species in the system are also constant throughout space.

Consider now a thermal perturbation that drives the system slightly away from equilibrium by establishing nonuniform energy and particle density distributions. In addition to the thermal perturbation, a small electrostatic external potential $\varphi(\mathbf{r})$ acts on the system as a mechanical perturbation. LTE is assumed to hold, i.e., the nonuniformity is on spatial scales large enough that meaningful intensive (local) variables can be defined, such as local inverse temperature $\beta(\mathbf{r})$. A reasonable guess for the form of the probability distribution function of this system, where each of the N_s different chemical species is characterized by its local chemical potential, $\mu_k(\mathbf{r}, t)$, is [7]

$$\widehat{\rho}_{loc} = \exp\left\{ -\widehat{\Phi} - \int \mathrm{d}^3 r \, \beta(\mathbf{r}) \left[e(\mathbf{r}) - \sum_k \left(\mu_k(\mathbf{r}) + q_k \varphi(\mathbf{r}) \right) n_k(\mathbf{r}) \right] \right\}, \tag{1.23}$$

where $\widehat{\Phi}$ is a generalized free energy, also known as Massieu-Planck functional, accounting for normalization, and q_k is the electric charge of the kth species. This form of the probability distribution formalizes LTE, since it keeps the same functional form of the equilibrium distribution, while both intensive and extensive quantities (weakly) depend on the point in space. Small perturbations from equilibrium allow one to express the deviations from uniformity of local quantities to linear order in terms of (constant) gradients:

$$\beta(\mathbf{r}) = \beta + \delta\beta(\mathbf{r}) \simeq \beta - \frac{1}{k_B T^2}\delta T(\mathbf{r}) \simeq \beta - \frac{1}{k_B T^2}\nabla T \cdot \mathbf{r}, \tag{1.24}$$

$$\mu_k(\mathbf{r}) = \mu_k + \delta\mu_k(\mathbf{r}) \simeq \mu_k + \nabla\mu_k \cdot \mathbf{r}, \tag{1.25}$$

$$\varphi(\mathbf{r}) \simeq \nabla\varphi \cdot \mathbf{r}. \tag{1.26}$$

With a slight abuse of notation, the equilibrium values of $\beta(\mathbf{r})$ and $\mu_k(\mathbf{r})$ are indicated with β and μ_k, respectively, while the equilibrium electric potential is set to zero.

The local density operator can also be expanded to linear order in the gradients; expanding part of the exponent yields

$$\begin{aligned}\widehat{\rho}_{loc} \simeq \exp\Bigg\{ -\widehat{\Phi} - \int \mathrm{d}^3 r \left(\beta - \frac{1}{k_B T^2}\nabla T \cdot \mathbf{r}\right) \Bigg[e(\mathbf{r}) + \\ - \sum_k \left(\mu_k + \nabla\mu_k \cdot \mathbf{r} + q_k(\varphi + \nabla\varphi \cdot \mathbf{r})\right) \Bigg] \Bigg\}.\end{aligned} \tag{1.27}$$

Then, defining the electrochemical potential of the species k as

$$\mu'_k = \mu_k + q_k\varphi \tag{1.28}$$

leads to a cleaner expression for the approximated $\widehat{\rho}_{loc}$:

$$\begin{aligned}\widehat{\rho}_{loc} &\simeq \exp\Bigg\{ -\widehat{\Phi} - \int \mathrm{d}^3 r \left(\beta - \frac{1}{k_B T^2}\nabla T \cdot \mathbf{r}\right) \Bigg[e(\mathbf{r}) + \\ &\qquad - \sum_k \left(\mu'_k + \nabla\mu'_k \cdot \mathbf{r}\right) n_k(\mathbf{r}) \Bigg] \Bigg\} \\ &= \exp\Bigg\{ -\widehat{\Phi} - \beta\left(\widehat{\mathcal{H}}_0 - \sum_k \mu'_k n_k\right) + \frac{1}{k_B T^2}\Bigg[\int \mathrm{d}^3 r\, e(\mathbf{r})\mathbf{r} \cdot \nabla T + \\ &\qquad - \sum_k \mu'_k \int \mathrm{d}^3 r\, n_k(\mathbf{r})\mathbf{r} \cdot \nabla T \Bigg] + \beta \sum_k \int \mathrm{d}^3 r\, n_k(\mathbf{r})\mathbf{r} \cdot \nabla\mu'_k \Bigg\}\end{aligned} \tag{1.29}$$

Up to the first order in the gradients, it becomes

$$\begin{aligned}\widehat{\rho}_{loc} \simeq \mathrm{e}^{-\widehat{\Phi}_0 - \beta\left(\widehat{\mathcal{H}}_0 - \sum_k \mu'_k n_k\right)} \Bigg[1 + \frac{1}{k_B T^2}\Bigg(\int \mathrm{d}^3 r\, \delta e(\mathbf{r})\mathbf{r} \cdot \nabla T + \\ - \sum_k \mu'_k \int \mathrm{d}^3 r\, \delta n_k(\mathbf{r})\mathbf{r} \cdot \nabla T \Bigg) + \beta \sum_k \int \mathrm{d}^3 r\, \delta n_k(\mathbf{r})\mathbf{r} \cdot \nabla\mu'_k \Bigg],\end{aligned} \tag{1.30}$$

where the phase-space densities have been replaced with their deviation from the equilibrium value, e.g.

$$\delta e(\mathbf{r}) = e(\mathbf{r}) - \langle e(\mathbf{r}) \rangle_0 \,, \tag{1.31}$$

and the average value is taken with respect to the equilibrium density operator

$$\widehat{\rho}_0 = \exp\left\{ -\widehat{\Phi}_0 - \beta \left(\widehat{\mathcal{H}}_0 - \sum_k \mu'_k n_k \right) \right\}. \tag{1.32}$$

The appearance of the deviations from equilibrium is due to the linear expansion of $\widehat{\Phi}$. Without loss of generality, one could have defined the phase-space variables to have a null equilibrium value and the expansion of $\widehat{\Phi}$ up to the first order would have been only $\widehat{\Phi}_0$.

1.3.1 *Time-evolved density operator*

Let us take Eq. (1.30) as the initial condition for the time evolution of the density operator. This means

$$\widehat{\rho}(t=0) = \widehat{\rho}_{loc}. \tag{1.33}$$

The time-evolution is given by the Hamiltonian, $\widehat{\mathcal{H}}_0$, since there are no external fields; thus

$$\widehat{\rho}(t) = \mathrm{e}^{\mathrm{i}\mathscr{L}t}\widehat{\rho}(0) = \mathrm{e}^{\mathrm{i}\mathscr{L}t}\widehat{\rho}_{loc}, \tag{1.34}$$

where the Liouvillean, $\mathscr{L}$, is

$$\mathrm{i}\mathscr{L}(-) = \left\{ \widehat{\mathcal{H}}_0, - \right\}, \tag{1.35}$$

and $\{-,-\}$ are the Poisson brackets. Applying the time-evolution operator to $\widehat{\rho}_{loc}$ yields

$$\begin{aligned} \widehat{\rho}(t) \simeq \widehat{\rho}_0 \Bigg[1 + \frac{1}{k_{\mathrm{B}} T^2} \Bigg(\int \mathrm{d}^3 r \, \mathrm{e}^{\mathrm{i}\mathscr{L}t} \delta e(\mathbf{r}) \mathbf{r} \cdot \nabla T + \\ - \sum_k \mu'_k \int \mathrm{d}^3 r \, \mathrm{e}^{\mathrm{i}\mathscr{L}t} \delta n_k(\mathbf{r}) \mathbf{r} \cdot \nabla T \Bigg) + \beta \sum_k \int \mathrm{d}^3 r \, \mathrm{e}^{\mathrm{i}\mathscr{L}t} \delta n_k(\mathbf{r}) \mathbf{r} \cdot \nabla \mu'_k \Bigg] . \end{aligned} \tag{1.36}$$

The dynamical variables evolve in time with $\mathrm{e}^{-\mathrm{i}\mathscr{L}t}$, i.e., when applied to dynamical quantities the time-evolution operator in the above equation evolves them backward in time, from 0 to $-t$. For each dynamical variable one can identically write:

$$\delta e(\mathbf{r}, -t) = \int_{\infty}^{-t} \mathrm{d}t' \, \dot{\delta e}(\mathbf{r}, t'), \tag{1.37}$$

where the boundary condition

$$\lim_{t \to \infty} \delta e(\mathbf{r}, t) = 0 \tag{1.38}$$

means that, after the full relaxation of the system to equilibrium, the deviations of the dynamical variables from their equilibrium values are zero. Since

the equilibrium value is time-independent, one also gets $\dot{\delta}e(\mathbf{r},t) = \dot{e}(\mathbf{r},t)$. In conclusion, the density operator becomes

$$\begin{aligned}\widehat{\rho}(t) \simeq \widehat{\rho}_0 \Bigg[1 + \frac{1}{k_B T^2} \Bigg(\int_{\infty}^{-t} \mathrm{d}t' \int \mathrm{d}^3 r\, \dot{e}(\mathbf{r},t')\mathbf{r}\cdot\nabla T + \\ - \sum_k \mu_k' \int_{\infty}^{-t} \mathrm{d}t' \int \mathrm{d}^3 r\, \dot{n}_k(\mathbf{r},t')\mathbf{r}\cdot\nabla T \Bigg) + \\ + \beta \sum_k \int_{\infty}^{-t} \mathrm{d}t' \int \mathrm{d}^3 r\, \dot{n}_k(\mathbf{r},t')\mathbf{r}\cdot\nabla \mu_k' \Bigg].\end{aligned} \tag{1.39}$$

By recalling the definition of macroscopic flux, Eq. (1.14), and specializing it to the total energy and the particle numbers, one obtains

$$\mathbf{J}_E(t) = \frac{1}{\Omega}\int \dot{e}(\mathbf{r},t)\mathbf{r}\,\mathrm{d}^3 r\,, \tag{1.40}$$

$$\mathbf{J}_k(t) = \frac{1}{\Omega}\int \dot{n}_k(\mathbf{r},t)\mathbf{r}\,\mathrm{d}^3 r\,, \tag{1.41}$$

so that Eq. (1.39) reads

$$\begin{aligned}\widehat{\rho}(t) \simeq \widehat{\rho}_0 \Bigg[1 + \frac{\Omega}{k_B T^2} \Bigg(\int_{\infty}^{-t} \mathrm{d}t'\, \mathbf{J}_E(t')\cdot\nabla T + \\ - \sum_k \mu_k' \int_{\infty}^{-t} \mathrm{d}t'\, \mathbf{J}_k(t')\cdot\nabla T \Bigg) + \frac{\Omega}{k_B T} \sum_k \int_{\infty}^{-t} \mathrm{d}t'\, \mathbf{J}_k(t')\cdot\nabla \mu_k' \Bigg].\end{aligned} \tag{1.42}$$

Inverting the integration path factors out an overall minus sign in front of the first-order term:

$$\begin{aligned}\widehat{\rho}(t) \simeq \widehat{\rho}_0 \Bigg[1 - \frac{\Omega}{k_B T^2} \Bigg(\int_{-t}^{\infty} \mathrm{d}t'\, \mathbf{J}_E(t')\cdot\nabla T + \\ - \sum_k \mu_k' \int_{-t}^{\infty} \mathrm{d}t'\, \mathbf{J}_k(t')\cdot\nabla T \Bigg) - \frac{\Omega}{k_B T} \sum_k \int_{-t}^{\infty} \mathrm{d}t'\, \mathbf{J}_k(t')\cdot\nabla \mu_k' \Bigg].\end{aligned} \tag{1.43}$$

1.3.2 *Average values of observables*

Eq. (1.43) can be used to compute the expectation values of fluxes. Right after the relaxation process begins, one finds

$$\begin{aligned}\langle \mathbf{J}_E \rangle_{\widehat{\rho}(0^+)} = \langle \mathbf{J}_E \rangle_0 - \frac{\Omega}{k_B T^2} \Bigg[\int_0^{\infty} \mathrm{d}t\, \langle \mathbf{J}_E \otimes \mathbf{J}_E(t) \rangle_0 \\ - \sum_k \mu_k' \int_0^{\infty} \mathrm{d}t\, \langle \mathbf{J}_E \otimes \mathbf{J}_k(t) \rangle_0 \Bigg] \cdot \nabla T - \frac{\Omega}{k_B T} \sum_k \int_0^{\infty} \mathrm{d}t\, \langle \mathbf{J}_E \otimes \mathbf{J}_k(t) \rangle_0 \cdot \nabla \mu_k'\end{aligned} \tag{1.44}$$

for the energy flux, and

$$\begin{aligned}\langle \mathbf{J}_m \rangle_{\widehat{\rho}(0^+)} = \langle \mathbf{J}_m \rangle_0 - \frac{\Omega}{k_B T^2} \Bigg[\int_0^{\infty} \mathrm{d}t\, \langle \mathbf{J}_m \otimes \mathbf{J}_E(t) \rangle_0 \\ - \sum_k \mu_k' \int_0^{\infty} \mathrm{d}t\, \langle \mathbf{J}_m \otimes \mathbf{J}_k(t) \rangle_0 \Bigg] \cdot \nabla T - \frac{\Omega}{k_B T} \sum_k \int_0^{\infty} \mathrm{d}t\, \langle \mathbf{J}_m \otimes \mathbf{J}_k(t) \rangle_0 \cdot \nabla \mu_k'\end{aligned} \tag{1.45}$$

for the mth mass flux. The "$\otimes$" symbol denotes the outer product of two Cartesian vectors, meaning that, for $\boldsymbol{v} = (v_x, v_y, v_z)$ and $\boldsymbol{w} = (w_x, w_y, w_z)$, their outer product is defined as $(\boldsymbol{v} \otimes \boldsymbol{w})_{\alpha\beta} = v_\alpha w_\beta$, with $\alpha, \beta = x, y, z$. In isotropic materials, the flux is aligned to the gradient of the intensive variable and the outer product of the fluxes is proportional to the identity. Under isotropy, and by noticing that

$$\nabla\left(\frac{\mu'_k}{T}\right) = \frac{\nabla\mu'_k}{T} - \frac{\nabla T}{T^2}\mu'_k, \tag{1.46}$$

$$\nabla\left(\frac{1}{T}\right) = -\frac{\nabla T}{T^2}, \tag{1.47}$$

one can write Eqs. (1.44) and (1.45) as

$$\begin{aligned}\langle \mathbf{J}_E \rangle = &\frac{\Omega}{3k_B}\int_0^\infty \langle \mathbf{J}_E(t)\cdot\mathbf{J}_E\rangle_0 \,\mathrm{d}t\, \nabla\left(\frac{1}{T}\right) + \\ &- \frac{\Omega}{3k_B}\sum_k \int_0^\infty \langle \mathbf{J}_k(t)\cdot\mathbf{J}_E\rangle_0 \,\mathrm{d}t\, \nabla\left(\frac{\mu'_k}{T}\right)\end{aligned} \tag{1.48}$$

$$\begin{aligned}\langle \mathbf{J}_m \rangle = &\frac{\Omega}{3k_B}\int_0^\infty \langle \mathbf{J}_E(t)\cdot\mathbf{J}_m\rangle_0 \,\mathrm{d}t\, \nabla\left(\frac{1}{T}\right) + \\ &- \frac{\Omega}{3k_B}\sum_k \int_0^\infty \langle \mathbf{J}_k(t)\cdot\mathbf{J}_m\rangle_0 \,\mathrm{d}t\, \nabla\left(\frac{\mu'_k}{T}\right).\end{aligned} \tag{1.49}$$

These equations provide a mean to compute Onsager's coefficients Λ_{ij} appearing in Eq. (1.19):

$$\langle \mathbf{J}_E \rangle = \Lambda_{EE}\nabla\left(\frac{1}{T}\right) - \sum_k \Lambda_{kE}\nabla\left(\frac{\mu'_k}{T}\right), \tag{1.50}$$

$$\langle \mathbf{J}_m \rangle = \Lambda_{Ek}\nabla\left(\frac{1}{T}\right) - \sum_k \Lambda_{km}\nabla\left(\frac{\mu'_k}{T}\right), \tag{1.51}$$

The expressions for Λ_{EE} and Λ_{Ek} are examples of Green-Kubo (GK) formulæ, which bridge the phenomenological equations of hydrodynamics with linear response theory [8–11].

1.4 INVARIANCE PRINCIPLES OF TRANSPORT THEORY

GK theory provides a rigorous way to compute transport coefficients by evaluating equilibrium time-correlation functions of suitably defined fluxes. Therefore, it makes it possible to access transport properties by means of Equilibrium Molecular Dynamics (EMD) simulations. In spite of this achievement, some conceptual misconceptions in the theory of linear response prevented its use in the field of computer simulations of transport in condensed matter systems, thus limiting its scope. The most prominent of these misunderstandings is that the intrinsic indeterminacy of any local representation of an extensive quantity, such as the atomic decomposition of total energy or charge, would hinder the uniqueness of the transport coefficient computed from them. This indeterminacy affects classical and quantum systems alike, but it stands most evidently in the latter, so much that, until recently, it was deemed impossible to combine the GK theory of thermal transport with electronic structure methods [12].

These difficulties have been overcome in the past years by the introduction of the so-called *gauge invariance* of transport coefficients, whose main message is that the value of transport coefficients is largely independent of the detailed form of the local representation of the associated conserved densities and fluxes and, as such, there are many different expression of those quantities which are effectively equivalent [4, 13–16]. In fact, the quantity to be measured in an experiment is the transport coefficient itself, not the associated density or current, so there is no *a priori* reason why conserved densities must have a unique representation. In general, gauge invariance implies that the value of a transport coefficient is insensitive to a change in the flux from which it is calculated which adds to it a vector process whose Power Spectral Density (PSD) vanishes at zero frequency. Such a process is called *non-diffusive*. Another difficulty in applying GK theory in EMD arises in thermal transport in multicomponent materials, where different chemical species coexist and the associated mass fluxes interact among each other and with the energy flux, thus complicating the definition of thermal conductivity, which is the ratio of the energy flux and the temperature gradient when all the other mass fluxes vanish. In this case, a further invariance principle, dubbed *convective invariance*, can be invoked, which states that the thermal conductivity is unchanged by adding to the energy flux any linear combination of the mass fluxes in the system [16].

While the transport coefficients enjoy the aforementioned invariances, the time series of the fluxes from which they are calculated do depend on their local representation, as so do their statistical properties. Hence, methods can be devised to exploit local representations which optimize the practical computation of transport coefficients. The statistical tools to compute transport coefficients from EMD simulations will be illustrated in Ch. 2.

Before reviewing gauge and convective invariances of transport coefficients, let us consider a different expression for the GK formula that will be expedient in the following Section. The GK integral in the expression of Onsager's coefficients, such as those appearing in Eq. (1.50), can be recast to what is known as an Helfand-Einstein (HE) formula:

$$\int_0^\infty \langle \mathbf{J}(t)\cdot\mathbf{J}(0)\rangle_0 \,\mathrm{d}t = \lim_{\tau\to\infty}\frac{1}{2\tau}\left\langle \left|\int_0^\tau \mathbf{J}(t)\,\mathrm{d}t\right|^2\right\rangle_0 . \tag{1.52}$$

The equivalence is due to the identity

$$\int_0^\tau\int_0^\tau f(t-t')\,\mathrm{d}t\,\mathrm{d}t' = 2\tau\int_0^\tau\left(1-\frac{t}{\tau}\right)f(t), \tag{1.53}$$

which is true for any even function, $f(t) = f(-t)$. Given a macroscopic flux, $\mathbf{J}(t)$, this identity can be applied to $f(t-t') = \langle \mathbf{J}(t)\cdot\mathbf{J}(t')\rangle_0$ to obtain Eq. (1.52). The HE formula was first proposed by Einstein in his celebrated paper on Brownian motion [17], and later generalized to other transport coefficients by Helfand [18]. It expresses transport coefficients in terms of the ratio of the mean-square *generalized dipole*, $\mathbf{D}(\tau) = \int_0^\tau \mathbf{J}(t)\,\mathrm{d}t$, displaced by the flux in a time τ, and time itself [16].

1.4.1 *Gauge invariance*

Microscopically, any two conserved densities whose volume integrals differ by a term scaling as the volume boundary yield the same value of the associated extensive quantity and, as such, they can effectively be considered equivalent in the thermodynamic limit. Two equivalent densities, $q(\mathbf{r},t)$ and $q'(\mathbf{r},t)$, may differ by the divergence of a bounded vector field, $\mathbf{b}(\mathbf{r},t)$:

$$q'(\mathbf{r},t) = q(\mathbf{r},t) - \nabla\cdot\mathbf{b}(\mathbf{r},t). \tag{1.54}$$

Thus, they can be thought of as two different gauges of the same scalar field. Since their (equal) volume integral is by definition a conserved quantity, each of the two densities satisfies a continuity equation (Eq. (1.6)) involving a conserved current density. The two currents—and, consequently, the respective fluxes—will transform under the gauge transformation as

$$\begin{aligned}\mathbf{j}'(\mathbf{r},t) &= \mathbf{j}(\mathbf{r},t) + \dot{\mathbf{b}}(\mathbf{r},t),\\ \mathbf{J}'(t) &= \mathbf{J}(t) + \dot{\mathbf{B}}(t),\end{aligned} \tag{1.55}$$

where $\mathbf{B} = \Omega^{-1}\int \mathbf{b}(\mathbf{r},t)\,\mathrm{d}^3r$. In order to prove that the two gauges lead to the same value of the transport coefficient, let us consider a generic transport process whose macroscopic flux is represented by a stationary stochastic process, $\mathbf{J}(t)$. According to the HE formulation, the transport coefficient λ can be expressed as

$$\lambda = c\lim_{\tau\to\infty}\frac{\langle|\mathbf{D}(\tau)|^2\rangle}{2\tau}, \tag{1.56}$$

where the factor c is a constant that depends on the transport process being considered. Changing gauge results in an additional bounded term $\mathbf{B}(\tau)$ in the generalized dipole. The resulting transport coefficient, λ', is immediately found to be equal to λ:

$$\begin{aligned}\lambda' &= c\lim_{\tau\to\infty}\frac{\langle|\mathbf{D}(\tau)+\mathbf{B}(\tau)|^2\rangle}{2\tau}\\ &= c\lim_{\tau\to\infty}\frac{\overbrace{\langle|\mathbf{D}(\tau)|^2\rangle}^{\mathcal{O}(\tau)} + \overbrace{2\langle\mathbf{D}(\tau)\cdot\mathbf{B}(\tau)\rangle}^{\mathcal{O}(\tau^{1/2})} + \overbrace{\langle|\mathbf{B}(\tau)|^2\rangle}^{\mathcal{O}(1)}}{2\tau}\\ &= c\lim_{\tau\to\infty}\frac{\langle|\mathbf{D}(\tau)|^2\rangle}{2\tau} \equiv \lambda.\end{aligned} \tag{1.57}$$

1.4.2 *Convective invariance*

In multicomponent systems, apart from the energy, the relevant conserved quantities are the particle numbers of each of the atomic species. Since the total-mass flux—i.e., the total momentum—is a constant of motion, for a system with K species there will be K independent conserved fluxes, namely, the $K-1$ independent mass fluxes and the energy flux. While this holds in general, there are cases where physical constraints of the particular system under consideration reduce the number of independent fluxes, such as the case of solids, where atoms do not diffuse, or even molecular fluids such

as liquid water, where the mass fluxes of oxygen and hydrogen depend on one another due to the molecular bonds. When different species can diffuse independently, like in molten salts or solutions, the mass fluxes of the different atomic species are not constants of motion, and their time integral is in general unbounded. This has an important consequence in the computation of the thermal conductivity, since the latter relates the energy flux to the temperature gradient it is induced by *in absence of convection*, i.e. when the nonequilibrium expectation value of all the mass fluxes is zero. The simplest case is a two-component system: the two independent fluxes are the energy flux, $\mathbf{J}_E$, and any of the two mass fluxes, $\mathbf{J}_M$. The phenomenological equations involving these fluxes are

$$\langle \mathbf{J}_E \rangle = \frac{\Lambda_{EE}}{k_B} \nabla \left(\frac{1}{T} \right) + \frac{\Lambda_{EM}}{k_B} \nabla \left(\frac{\Delta\mu}{T} \right) \tag{1.58}$$

$$\langle \mathbf{J}_M \rangle = \frac{\Lambda_{ME}}{k_B} \nabla \left(\frac{1}{T} \right) + \frac{\Lambda_{MM}}{k_B} \nabla \left(\frac{\Delta\mu}{T} \right), \tag{1.59}$$

where $\Delta\mu$ is the difference between the chemical potentials of the two species. The mass flux is, e.g., the one associated with the first species, i.e. $\mathbf{J}_M = \mathbf{J}_1$, the second being defined by the conservation of linear momentum in the barycentric reference frame: $\mathbf{J}_2 = -\mathbf{J}_1$. When the nonequilibrium expectation value of the mass flux is set to zero, one gets

$$\nabla \left(\frac{\Delta\mu}{T} \right) = -\frac{\Lambda_{ME}}{\Lambda_{MM}} \nabla \left(\frac{1}{T} \right). \tag{1.60}$$

This can be used to obtain a closed form for the phenomenological equation involving the energy flux:

$$\begin{aligned} \langle \mathbf{J}_E \rangle &= -\frac{1}{k_B T^2} \left[\Lambda_{EE} - \frac{\Lambda_{ME}^2}{\Lambda_{MM}} \right] \nabla T \\ &= -\kappa \nabla T, \end{aligned} \tag{1.61}$$

where the second line defines the thermal conductivity of a two-component system, and Onsager's reciprocal relations have been employed to say that $\Lambda_{EM} = \Lambda_{ME}$. The second term in the expression of κ, which is nonzero only when there are more than one species in the system, represents the contribution of mass diffusion to the heat flow [19].

The convective-invariance principle states that adding any linear combination of the mass fluxes to the energy flux, which in the two-component case is simply

$$\mathbf{J}'_E = \mathbf{J}_E + c\mathbf{J}_M, \tag{1.62}$$

with constant c, does not change κ, even if each Onsager's coefficient in Eq. (1.61) does change. In the general case, when there is a number $K > 2$ of different atomic species, the thermal conductivity becomes the Schur complement of Onsager's matrix [4]:

$$\kappa = \frac{1}{k_B T^2} \left[\Lambda_{EE} - \sum_{l,m=1}^{K-1} \Lambda_{EM_l} (\Lambda^{-1})_{lm} \Lambda_{EM_m} \right], \tag{1.63}$$

where $(\Lambda)_{lm} = \Lambda_{M_l M_m}$ is Onsager's matrix of mass fluxes. Convective invariance in this case states that the energy flux

$$\mathbf{J}'_E = \mathbf{J}_E + \sum_{l=1}^{K-1} c_l \mathbf{J}_{M_l} \tag{1.64}$$

yields a thermal conductivity $\kappa' = \kappa$.

The are two main consequences ascribed to convective invariance:

i) from a conceptual standpoint, in *ab initio* calculations of thermal conductivity, convective invariance justifies the fact that the value of κ must not depend on whether the atomic cores contribute to the definition of atomic energies, as in the case of all-electron calculations, or not, as when pseudopotentials are used. In the latter case, the energy of isolated atoms depends on the specific form of the pseudopotential adopted, while the thermal conductivity should not. Indeed this is not the case, as a shift of the zero of the energy of each species, δE_l, results in a redefinition of the energy fluxes of the form required by convective invariance to leave κ unchanged, i.e. $\mathbf{J}'_E = \mathbf{J}_E + \sum_{l=1}^{K-1} \frac{\delta E_l}{M_l} \mathbf{J}_{M_l}$;

ii) from a more practical point of view, convective invariance can be leveraged to improve the statistical properties of the PSD of the time-series of the energy flux even in cases where, in principle, multicomponent techniques are not required [20].

2 DATA ANALYSIS

In EMD simulations one samples the relevant fluxes to compute the time-integrals of their equilibrium time correlation functions since the former are proportional to Onsager's coefficients entering the definitions of transport coefficients. The transport coefficients estimated from the time series sampled along the system's trajectory are very sensitive to how the data are analyzed. To circumvent this problem, sophisticated methods were introduced to give accurate estimates from relatively short EMD simulations.

2.1 GREEN-KUBO AND HELFAND-EINSTEIN FORMULÆ AND THEIR LIMITATIONS

As seen in Sec. 1.4, the GK formula is mathematically equivalent to the HE formula. Despite being formally the same, the two expressions have different statistical behaviors. In order to understand why, let us schematically write the two formulations as

$$\begin{aligned}\lambda &= \lim_{\tau\to\infty} \lambda_{\mathrm{GK}}(\tau) = c \lim_{\tau\to\infty} \int_0^\tau \langle \mathbf{J}(t)\cdot\mathbf{J}(0)\rangle_0 \,\mathrm{d}t \\ &= \lim_{\tau\to\infty} \lambda_{\mathrm{HE}}(\tau) = c \lim_{\tau\to\infty} \int_0^\tau \langle \mathbf{J}(t)\cdot\mathbf{J}(0)\rangle_0 \left(1-\frac{t}{\tau}\,\mathrm{d}t\right) \\ &= \frac{c}{2} S(0),\end{aligned} \tag{2.1}$$

where c is a constant that depends on the particular transport process, and $S(\omega)$ is the PSD of the stationary stochastic process representing the conserved flux, $\mathbf{J}$, i.e.

$$S(\omega) = \int_{-\infty}^{\infty} \langle \mathbf{J}(t)\cdot\mathbf{J}(0)\rangle_0 \, \mathrm{e}^{\mathrm{i}\omega t}\,\mathrm{d}t\,. \tag{2.2}$$

The three quantities, λ_{GK}, λ_{HE}, and S can be put on the same footing by writing the first two as [16]

$$\lambda_{\mathrm{GK}}(\tau) = \frac{c}{2}\int_{-\infty}^{\infty} \langle \mathbf{J}(t)\cdot\mathbf{J}(0)\rangle_0 \, \Theta^\tau_{\mathrm{GK}}(t)\,\mathrm{d}t\,, \tag{2.3}$$

and

$$\lambda_{\mathrm{HE}}(\tau) = \frac{c}{2}\int_{-\infty}^{\infty} \langle \mathbf{J}(t)\cdot\mathbf{J}(0)\rangle_0 \, \Theta^\tau_{\mathrm{HE}}(t)\,\mathrm{d}t\,, \tag{2.4}$$

where $\Theta^\tau_{\mathrm{GK}}(t)$ and $\Theta^\tau_{\mathrm{HE}}(t)$ are functions that act like filters on the flux autocorrelation function given by

$$\Theta^\tau_{\mathrm{GK}}(t) = \begin{cases} 1, & \text{for } |t|\le\tau \\ 0, & \text{otherwise}\end{cases}, \tag{2.5}$$

$$\Theta^\tau_{\mathrm{HE}}(t) = \begin{cases} 1-\frac{t}{\tau}, & \text{for } |t|\le\tau \\ 0, & \text{otherwise}\end{cases}. \tag{2.6}$$

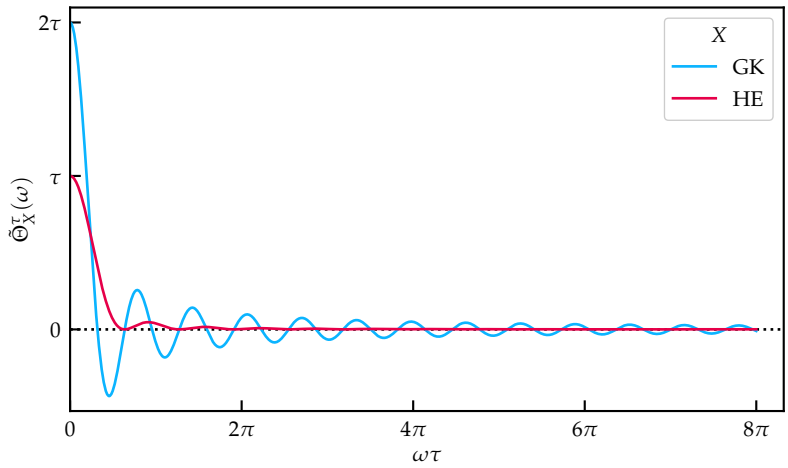

Figure 2.1: Comparison of the GK and HE filters. While both functions tend to a Dirac delta in the $\tau \to \infty$ limit, the HE function converges faster.

Using Plancherel's theorem [21], one gets

$$\lambda_X(\tau) = \frac{c}{4\pi} \int_{-\infty}^{\infty} S(\omega) \widetilde{\Theta}^{\tau}_{X}(\omega)\, \mathrm{d}\omega\,, \tag{2.7}$$

where X stands for GK or HE, and $\widetilde{\Theta}^{\tau}_{X}(\omega)$ is the Fourier transform of $\Theta^{\tau}_{X}(t)$, i.e.

$$\begin{aligned} \widetilde{\Theta}^{\tau}_{\mathrm{GK}}(\omega) &= 2\tau\, \mathrm{sinc}(\omega\tau) \\ \widetilde{\Theta}^{\tau}_{\mathrm{HE}}(\omega) &= \tau\, \mathrm{sinc}^2(\omega\tau/2). \end{aligned} \tag{2.8}$$

The sinc function is the cardinal sine, defined as $\mathrm{sinc}(x) = \sin(x)/x$. Both filters converge to a Dirac delta in the $\tau \to \infty$ limit but, for any finite τ, the HE is narrower than the GK [16], as it can be visually understood from Fig. 2.1. In fact, in practical implementations, it can be shown that the HE method provides an estimate of the transport coefficient whose variance is asymptotically one-third of the variance given with the GK formula [16].

Despite the seemingly promising features of the HE estimator, its use is severely limited from both practical and theoretical points of view. On the one hand, long EMD simulations are required to collect enough data points to have sufficient statistics. Even in that case, to estimate the error bars on the computed transport coefficient one needs to resort to standard block-averaging techniques, where the choice of the correct number of blocks is somewhat arbitrary and can lead to incompatible results [15, 22]. On the other hand, let us consider the specific case of thermal conductivity in multi-component systems, the simplest case involving two species: here, κ results from the difference (see Eq. (1.61)) of the energy-energy Onsager coefficient and the ratio of the squared mass-energy and mass-mass ones. In the HE approach, each of these coefficients is computed via a formula analogous to Eq. (2.4), i.e., by computing, up to a finite cutoff, the time-integral of a decaying function. While the true autocorrelation function is indeed a decaying function, its samples from a

numerical simulation are corrupted by numerical noise, whose effects are more evident at large times, where the actual quantity is close to zero. Performing either the GK or the HE integrals would eventually lead to the integration of noise. The integrated noise is a one-dimensional random walk, that will eventually lead to a zero-valued mass-mass coefficient, that in turn leads to a divergent thermal conductivity [15].

These problems are lifted considering the theory of transport coefficients in frequency space. A frequency-domain representation of the stochastic processes underlying transport phenomena can be obtained thanks to the Wiener-Khinchin theorem, which states that the Fourier transform of the autocorrelation function, $\langle \widehat{J}(t)\widehat{J}(0)\rangle$, of a wide-sense stationary random process, $\widehat{J}(t)$, is the PSD of that process, $S_\tau(\omega)$ [23, 24]:

$$\begin{aligned} S_\tau(\omega) &= \frac{1}{\tau}\left\langle \left| \int_0^\tau \widehat{J}(t) \mathrm{e}^{\mathrm{i}\omega t}\,\mathrm{d}t \right|^2 \right\rangle \\ &= 2\,\mathrm{Re}\int_0^\tau \left\langle \widehat{J}(t)\widehat{J}(0)\right\rangle \mathrm{e}^{\mathrm{i}\omega t}\,\mathrm{d}t + \mathcal{O}(\tau^{-1}) \end{aligned} \tag{2.9}$$

Here, wide carets ($\widehat{\ }$) indicate random processes. More generally, when there are many interacting fluxes, one can define the *cross-spectrum*, S_{lm}, of fluxes $\widehat{J}_l$, $\widehat{J}_m$ as

$$S_{lm}(\omega) = \int_{-\infty}^{\infty} \left\langle \widehat{J}_l(t)\widehat{J}_m(0)\right\rangle \mathrm{e}^{\mathrm{i}\omega t}\,\mathrm{d}t\,, \tag{2.10}$$

so that Onsager's coefficients can be expressed as

$$\Lambda_{lm} = \frac{\Omega}{2k_\mathrm{B}} S_{lm}(\omega = 0). \tag{2.11}$$

This formula, together with the invariance principles discussed in Sec. 1.4, can be exploited to obtain accurate estimates of transport coefficients leveraging the so-called *cepstral* method for the analysis of time series.

2.2 CEPSTRAL ANALYSIS

Cepstral analysis was developed in the 1960s in the context of speech recognition with the purpose of extracting useful information from noisy audio signals [25]. Its power resides in the ability to turn multiplicative noise, on which linear filters cannot be applied, into additive noise, which instead can be removed with a suitable low-pass filter.

In the case of the estimation of transport coefficients, cepstral analysis can be applied to the frequency-domain representation of the stochastic process, $\widehat{J}(t)$, that underlies the time evolution of the flux. In fact, let us take the simple case of a single flux. In an EMD simulation, what one is measuring is the time series of the flux, $\mathcal{J}_n$, $n = 1, \ldots, N-1$; the calligraphic font denotes discrete realizations of stochastic processes. The time series is sampled with time period ϵ, which is a multiple of the simulation time-step so that the length of the simulation is $\mathcal{T} = N\epsilon$. From $\mathcal{J}_n$ one can estimate the PSD of the stochastic process via the *periodogram*, $\mathcal{S}_k$:

$$\mathcal{S}_k = \frac{\epsilon}{N}\left|\widetilde{\mathcal{J}}_k\right|^2, \tag{2.12}$$

where $\widetilde{\mathcal{J}}_k$ is the discrete Fourier transform of the flux time series, i.e.

$$\widetilde{\mathcal{J}}_k = \sum_{n=0}^{N-1} \mathrm{e}^{2\pi \mathrm{i} \frac{kn}{N}} \mathcal{J}_n. \tag{2.13}$$

The sample frequency, ω_k, is

$$\omega_k = \begin{cases} 2\pi \frac{k}{N\epsilon}, & \text{for } k \leq N/2, \\ -\omega_{k-N/2}, & \text{for } k > N/2. \end{cases} \tag{2.14}$$

The periodogram is an asymptotically unbiased estimator of the true PSD, i.e., for large enough N, $\langle \mathcal{S}_k \rangle = S(\omega_k)$; as such, the periodogram will be referred to as *sample spectrum* as well. An estimator of the PSD serves us as a way to compute Onsager's coefficients—and, therefore, transport coefficients—from the frequency-domain formula of Eq. (2.11). To be able to produce a meaningful estimate, one needs to know the statistical properties of the estimator.

2.2.1 *Statistical properties of the periodogram*

The statistical properties of the periodogram descend from those of the underlying time series. In condensed matter systems, the space autocorrelation functions of conserved currents are usually short-ranged [4]. This implies that, in the thermodynamic limit, the macroscopic fluxes $\widehat{J}(t) = \Omega^{-1} \int_\Omega \widehat{\jmath}(\mathbf{r}, t) \, \mathrm{d}^3 r$ are sums of almost independent identically distributed (iid) random variables. By the central limit theorem, their probability distribution is Gaussian. The stochastic process associated with the equilibrium dynamics of conserved fluxes is therefore a Gaussian process, and any discrete realization of such process is a multi-variate Gaussian random variable: $\mathcal{J}_n \sim \mathcal{N}(0, \sigma^2_{\mathcal{J}})$. From this fact, and from Eq. (2.12), it follows that $\widetilde{\mathcal{J}}_k \sim \mathcal{N}(0, \frac{N}{\epsilon} S(\omega_k))$ for $k = 0$ or $k = N/2$; while, for $k \notin \{0, N/2\}$, $\operatorname{Re} \widetilde{\mathcal{J}}_k$ and $\operatorname{Im} \widetilde{\mathcal{J}}_k$ are independent random variables, both distributed as $\mathcal{N}(0, \frac{N}{2\epsilon} S(\omega_k))$.

Therefore, in the large-N limit (i.e., long simulation time limit) the periodogram can be written as

$$\mathcal{S}_k = S(\omega_k) \xi_k, \tag{2.15}$$

where $\xi_k \sim \frac{1}{2}\chi^2_2$, for different k are iid chi-square random variables with two degrees of freedom divided by two. Thus, $\langle \xi_k \rangle = 1$, and $\operatorname{Var}(\xi_k) = 1$.

In EMD simulations of isotropic materials, one usually samples three independent realizations, $\mathcal{J}^x_n$, $\mathcal{J}^y_n$, $\mathcal{J}^z_n$, of each stochastic process associated with the fluxes of interest, i.e., the three Cartesian directions. In such a case, the Onsager coefficient would be given by, e.g.

$$\begin{aligned} L &= \frac{\Omega}{k_\mathrm{B}} \int_0^\infty \frac{1}{3} \left\langle J^x(t) J^x(0) + J^y(t) J^y(0) + J^z(t) J^z(0) \right\rangle_0 \mathrm{d}t \\ &= \frac{\Omega}{2k_\mathrm{B}} \frac{1}{3} [S^x(\omega = 0) + S^y(\omega = 0) + S^z(\omega = 0)] \end{aligned} \tag{2.16}$$

Isotropy implies that the three PSDs in Eq. (2.16) are the same, thus making the corresponding periodograms three independent estimates of the same quantity. It is convenient to define an average periodogram as the mean of the three

periodograms associated with the Cartesian directions. In general, one might have a number of realizations of the flux different from three. With ℓ such a number, the average of ℓ periodograms is given by

$$\begin{aligned} {}^{\ell}\mathcal{S}_k &= \frac{1}{\ell}\sum_{\alpha=1}^{\ell}\mathcal{S}_k^i \\ &= S(\omega_k)\frac{1}{\ell}\sum_{\alpha=1}^{\ell}\xi_k^\alpha \equiv S(\omega_k)\,{}^{\ell}\xi_k, \end{aligned} \tag{2.17}$$

where the random variable ${}^{\ell}\xi_k \sim \frac{1}{2\ell}\chi^2_{2\ell}$ is distributed as a chi-square variate with 2ℓ degrees of freedom, divided by 2ℓ.

2.2.2 *Cepstrum and related quantities*

As said at the beginning of the Section, the idea behind the cepstral method for estimating transport coefficients is that it allows turning multiplicative noise, difficult to separate from the true signal, into additive noise, which is more treatable [26]. A way to solve this problem is to apply a logarithm to the periodogram, which defines the *log-periodogram* as

$$\begin{aligned} \mathcal{L}_k \doteq \log(\mathcal{S}_k) &= \log(S(\omega_k)) + \log\left({}^{\ell}\xi_k\right) \\ &= L(\omega_k) + \log({}^{\ell}\xi_k). \end{aligned} \tag{2.18}$$

The probability distribution of $\log({}^{\ell}\xi_k)$ does not have a closed form, but its moments can be computed exactly (see Appendix A), the mean and variance being

$$\langle \log({}^{\ell}\xi_k)\rangle = \psi(\ell) - \log(\ell), \tag{2.19}$$

$$\mathrm{Var}(\log({}^{\ell}\xi_k)) = \psi'(\ell), \tag{2.20}$$

where ψ is the digamma function, i.e. the logarithmic derivative of the Euler gamma function [27]. The goal now is to reduce the noise from the log-periodogram by discarding its high-frequency components, which are related to the noise.[1] The natural way to do so is by defining the *cepstrum*, $\mathcal{C}_n$, of the process as the inverse discrete Fourier transform of the log-periodogram:

$$\begin{aligned} \mathcal{C}_n &\doteq \frac{1}{N}\sum_{k=0}^{N-1}\mathcal{L}_k \mathrm{e}^{-2\pi\mathrm{i}\frac{kn}{N}} \\ &= \frac{1}{N}\sum_{k=0}^{N-1}\Lambda_k \mathrm{e}^{-2\pi\mathrm{i}\frac{kn}{N}} + \frac{1}{N}\sum_{k=0}^{N-1}\log({}^{\ell}\xi_k)\mathrm{e}^{-2\pi\mathrm{i}\frac{kn}{N}} \\ &= C_n + {}^{\ell}\Xi_n, \end{aligned} \tag{2.21}$$

where the last line defines the true cepstrum, C_n, and the random part of the sample cepstrum, ${}^{\ell}\Xi_n$. The mean and variance of the latter are (see Appendix A)

$$\langle {}^{\ell}\Xi_n\rangle = \delta_{n0}[\psi(\ell) - \log(\ell)], \tag{2.22}$$

$$\mathrm{Var}({}^{\ell}\Xi_n) = \frac{\psi'(\ell)}{N}. \tag{2.23}$$

1 In the cepstral jargon, the Fourier variables dual to k are called *quefrencies*, a word derived by reversing the order of the first two syllables of the word "frequencies", in a way similar to how the term "cepstrum" is obtained from "spectrum".

Let us indicate by $P^\star$ the smallest integer number such that $C_n \approx 0$ for $P^\star \leq n \leq N - P^\star$. An efficient way to estimate the zero-frequency value of the log-spectrum is limiting the Fourier transform of the sample cepstrum, Eq. (2.21), to $P^\star$ coefficients:

$$\mathcal{L}_0^\star \doteq C_0 - \psi(\ell) + \log(\ell) + 2\sum_{n=1}^{P^\star-1} C_n = C_0 + 2\sum_{n=1}^{P^\star-1} C_n + {}^\ell m^\star, \tag{2.24}$$

$${}^\ell m^\star \doteq {}^\ell \Xi_0 - \psi(\ell) + \log(\ell) + 2\sum_{n=1}^{P^\star-1} {}^\ell \Xi_n. \tag{2.25}$$

The random part of $\mathcal{L}_0^\star$, is such that, up to $\mathcal{O}(1/N)$, its mean and variance are (see Appendix A)

$$\langle {}^\ell m^\star \rangle = 0, \tag{2.26}$$

$$\mathrm{Var}({}^\ell m^\star) = \frac{4P^\star - 2}{N}\psi'(\ell). \tag{2.27}$$

Through Eqs. (2.24), (2.26), and (2.27) one can estimate the logarithm of the Onsager coefficient, and the resulting estimator is (approximately) a Gaussian random variable whose variance depends only on $P^\star$, that is a measure of the smoothness of the PSD of the flux stochastic process the time series is a particular realization of. An Onsager coefficient, Λ, together with its error, $\Delta\Lambda$, is thus estimated via

$$\Lambda = \frac{\Omega}{2k_\mathrm{B}} \exp(\mathcal{L}_0^\star) \tag{2.28}$$

$$\Delta\Lambda = \frac{\Omega}{2k_\mathrm{B}} \exp(\mathcal{L}_0^\star) \sqrt{\frac{4P^\star - 2}{N}\psi'(\ell)} \tag{2.29}$$

2.2.3 *Thermal conductivity: multicomponent cepstral analysis*

Among the many transport coefficients, thermal conductivity in multicomponent systems requires particular care, as its convoluted expression in terms of different Onsagers' coefficients, Eq. (1.63), is prone to numerical errors. Let us recall the form of the $M \times M$ Onsager matrix in frequency domain, $\Lambda(\omega)$, for a system with M different chemical species:

$$\Lambda(\omega) = \begin{bmatrix} \Lambda_{EE}(\omega) & \Lambda_{E2}(\omega) & \cdots & \Lambda_{EM}(\omega) \\ \Lambda_{2E}(\omega) & \Lambda_{22}(\omega) & \cdots & \Lambda_{2M}(\omega) \\ \vdots & \vdots & \ddots & \vdots \\ \Lambda_{ME}(\omega) & \Lambda_{M2}(\omega) & \cdots & \Lambda_{MM}(\omega) \end{bmatrix}, \tag{2.30}$$

where

$$\Lambda_{ij}(\omega) = \frac{1}{2k_\mathrm{B}} S_{ij}(\omega) = \frac{1}{2k_\mathrm{B}} \int_{-\infty}^{\infty} \langle J_i(t) J_j(0) \rangle_0 \, \mathrm{e}^{\mathrm{i}\omega t} \, \mathrm{d}t \tag{2.31}$$

and $S_{ij}(\omega)$ is a cross-spectrum. The $(M-1) \times (M-1)$ matrix obtained by removing the first line and the first column from Λ is called the *convective*

block of Λ, and κ is proportional to the zero-frequency value of its Schur's complement, $\bar{\Lambda}^E(\omega)$:

$$\kappa = \frac{1}{T^2}\bar{\Lambda}^E(\omega = 0) = \frac{1}{T^2}\left.\frac{1}{(\Lambda^{-1}(\omega))_{EE}}\right|_{\omega=0}. \tag{2.32}$$

Therefore, κ can be computed if a good estimator of $\bar{\Lambda}^E(\omega)$ is available.

The content of Sec. 2.2.1 can be now generalized to obtain the statistical properties of the cross-spectrum matrix. The latter is (proportional to) the Fourier transform of the matrix of the correlation functions between the random vectors of the multivariate Gaussian sample given by the time series of the fluxes, $\mathcal{J}_E, \mathcal{J}_2, \ldots, \mathcal{J}_M$. Thus, if there are ℓ samples for each kind of flux, the cross-periodogram matrix which estimates the matrix of the cross spectra is a complex Wishart random variable, $\mathcal{S}_k \sim \mathcal{CW}_M(\mathsf{S}(\omega_k), \ell)$. The cross spectrum matrix, $\mathsf{S}(\omega_k)$, is called the *scale matrix* of the Wishart distribution, while ℓ is its number of degrees of freedom, and M is its rank [15, 28]. A nice property of the Wishart distribution is that the Schur complement of each of the diagonal blocks of a Wishart variable is also a Wishart variable [15, 29]. In other words, if $\mathcal{S} \sim \mathcal{CW}_M(\mathsf{S}, \ell)$ is a complex Wishart matrix of rank M, and $\bar{\mathcal{S}}$ is the Schur complement of rank L of an $(M-L)$-dimensional diagonal block, one has that

$$\bar{\mathcal{S}} \sim \mathcal{CW}_L(\bar{\mathsf{S}}, \ell - M + L). \tag{2.33}$$

This allows us to know the distribution of the estimator of $\bar{\Lambda}^E(\omega) = \frac{1}{2k_B}\bar{\mathsf{S}}^E(\omega)$: in fact, the latter is the rank-1 Schur complement of the convective block, and it is thus estimated by a rank-1 complex Wishart random variable with scale matrix $\bar{\Lambda}^E$ and $\ell - M + 1$ degrees of freedom. A rank-1 matrix is just a scalar, and the complex Wishart distribution reduces to a chi-square distribution. In conclusion, for each discrete frequency, ω_k, the following expressions hold:

$$\bar{\mathcal{S}}^E_k = \bar{\mathsf{S}}^E(\omega_k)\xi_k, \tag{2.34}$$

$$\xi_k \sim \frac{1}{\nu}\chi^2_\nu, \quad \nu = 2(\ell - M + 1). \tag{2.35}$$

Remarkably, this formula has the same form of Eq. (2.17), the only difference being the number of degrees of freedom of the chi-square distribution. In particular, this means that cepstral analysis, reviewed in Sec. 2.2.2, can be used to compute κ for multicomponent as well single-component systems. The only adjustment one needs to make is to replace ℓ with $\nu/2$ wherever it appears. In particular, the mean and variance of the random part of the estimator of the zero-frequency value of the log-spectrum, i.e., Eqs. (2.26) and (2.27), change to

$$\langle \mathcal{M}^\star \rangle = 0, \tag{2.36}$$

$$\mathrm{Var}(\mathcal{M}^\star) = \frac{4P^\star - 2}{N}\psi'(\nu/2). \tag{2.37}$$

Notice that the reference to ℓ, that was indicated as a superscript in front of the symbol "$\mathcal{M}$", is suppressed here and in the following, in order to simplify the notation. The thermal conductivity and its error become

$$\kappa = \frac{\Omega}{2k_B T^2}\exp(\mathcal{L}_0^\star), \tag{2.38}$$

$$\Delta\kappa = \frac{\Omega}{2k_B}\exp(\mathcal{L}_0^\star)\sqrt{\frac{4P^\star - 2}{N}\psi'(\nu/2)}. \tag{2.39}$$

2.3 CEPSTRAL ANALYSIS IN PRACTICE

The efficacy of the cepstral method in estimating transport coefficients depends on how well one is able to find $P^\star$, the number of cepstral coefficients to retain: it must be large enough to keep the bias due to the truncation low, yet small enough to maintain the magnitude of the statistical error below an acceptable threshold. In Ref. 26, the original paper where the method is discussed, it is proposed to use the Akaike Information Criterion (AIC) [30] to choose $P^\star$. Given a model depending on P parameters, $\theta = \{\theta_1, \theta_2, \ldots, \theta_P\}$, the AIC is a sample statistic defined as

$$\mathrm{AIC}(P) = -2 \max_{\theta} \log \mathcal{L}(\theta, P) + 2P. \tag{2.40}$$

where $\mathcal{L}$ is the likelihood of the parameters. The value of $P^\star$ is the one that minimizes the AIC:

$$P^\star = \arg\min_{P} \mathrm{AIC}(P). \tag{2.41}$$

In practice, the AIC tries to balance the accuracy of the model, given by the first term in Eq. (2.40), with a term that penalizes models that are too complex—i.e., models with too many parameters. This simple method works well in those cases where the periodogram to analyze is sufficiently flat in the low-frequency region [4, 15, 20, 26, 31–35]. This is typical of, e.g., the thermal and electrical conductivities of liquid systems at high enough temperature [26, 33]. In other cases, such as thermal conductivity of solids [26, 36], and viscosity in liquids [37], this is no longer true and the AIC alone is not capable of choosing $P^\star$ in a consistent way. Before addressing this issue, let us introduce some concepts and techniques that will be useful in the following.

2.3.1 *Analytic cepstrum*

It is instructive to consider the analytic expression of the cepstrum and to see what it is possible to say about it. The cepstrum, $C(q)$, is the inverse Fourier transform of the logarithm of the PSD, i.e.

$$C(q) = \int_{-\infty}^{\infty} \log(S(\omega))\, \mathrm{e}^{\mathrm{i}\omega q} \frac{\mathrm{d}\omega}{2\pi}. \tag{2.42}$$

The Fourier-conjugate variable to ω is the quefrency q, which has the units of time. The computation of the integral in Eq. (2.42) requires some care since the logarithm of an integrable function diverges at $\pm\infty$. Let us impose a cutoff on the integral as

$$C(q) = \frac{1}{2\pi} \int_{-\omega^\star}^{\omega^\star} \log(S(\omega))\, \mathrm{e}^{\mathrm{i}\omega q}\, \mathrm{d}\omega\,. \tag{2.43}$$

Integrating by parts, Eq. (2.43) becomes

$$C(q) = \frac{1}{2\pi \mathrm{i} q} \left[\log(S(\omega))\, \mathrm{e}^{\mathrm{i}\omega q}\right]_{-\omega^\star}^{\omega^\star} - \frac{1}{2\pi \mathrm{i} q} \int_{-\omega^\star}^{\omega^\star} \frac{S'(\omega)}{S(\omega)}\, \mathrm{e}^{\mathrm{i}\omega q}\, \mathrm{d}\omega\,. \tag{2.44}$$

The integrand in Eq. (2.44) is now regular over the real numbers: the integral can be conveniently written as

$$\begin{aligned}\int_{-\omega^\star}^{\omega^\star} \frac{S'(\omega)}{S(\omega)}\, \mathrm{e}^{\mathrm{i}\omega q}\, \mathrm{d}\omega = \int_{-\infty}^{\infty} \frac{S'(\omega)}{S(\omega)}\, \mathrm{e}^{\mathrm{i}\omega q}\, \mathrm{d}\omega + \\ - 2\mathrm{i} \int_{\omega^\star}^{\infty} \frac{S'(\omega)}{S(\omega)}\, \sin(\omega q)\, \mathrm{d}\omega\,.\end{aligned} \tag{2.45}$$

Being the PSD an even function of ω, the boundary contribution—i.e., the first term in Eq. (2.44)—can be simplified as

$$\begin{aligned}\frac{1}{2\pi \mathrm{i} q} \left[\log(S(\omega))\, \mathrm{e}^{\mathrm{i}\omega q}\right]_{-\omega^\star}^{\omega^\star} &= \frac{1}{2\pi \mathrm{i} q} \log(S(\omega^\star))\, 2\mathrm{i} \sin(\omega^\star q) \\ &= \frac{\omega^\star}{\pi}\, \mathrm{sinc}(\omega^\star q) \log(S(\omega^\star)).\end{aligned} \tag{2.46}$$

Finally, the analytic cepstrum reads

$$\begin{aligned}C(q) = \frac{\omega^\star}{\pi}\, \mathrm{sinc}(\omega^\star q) \log(S(\omega^\star)) - \frac{1}{2\pi \mathrm{i} q} \int_{-\infty}^{\infty} \frac{S'(\omega)}{S(\omega)}\, \mathrm{e}^{\mathrm{i}\omega q}\, \mathrm{d}\omega + \\ + \frac{1}{\pi q} \int_{\omega^\star}^{\infty} \frac{S'(\omega)}{S(\omega)}\, \sin(\omega q)\, \mathrm{d}\omega\end{aligned} \tag{2.47}$$

The case where the PSD is a simple Lorentzian function can be dealt with analytically. It is the paradigmatic case where the current autocorrelation function, $\gamma(t)$, is a cosine modulated by a decaying exponential:

$$\gamma(t) = R_0 \cos(\omega_0 t) \mathrm{e}^{-|t|/\tau}, \tag{2.48}$$

$$S(\omega) = \frac{R_0 \tau}{1 + (\omega - \omega_0)^2 \tau^2} + \frac{R_0 \tau}{1 + (\omega + \omega_0)^2 \tau^2}. \tag{2.49}$$

The cepstrum is computed according to Eq. (2.47). The integral over the real line evaluates to

$$-\frac{1}{\mathrm{i} q} \int_{-\infty}^{\infty} \frac{S'(\omega)}{S(\omega)}\, \mathrm{e}^{\mathrm{i}\omega q} \frac{\mathrm{d}\omega}{2\pi} = \frac{2\cos(\omega_0 q)\mathrm{e}^{-q/\tau} - \mathrm{e}^{-\frac{q}{\tau}\sqrt{1+\tau^2\omega_0^2}}}{q}. \tag{2.50}$$

The tail contribution can be recast into a rather complex form involving sine- and cosine-integral functions. An asymptotic expansion of the integrand allows one to write

$$\begin{aligned}\frac{2}{q} \int_{\omega^\star}^{\infty} \frac{S'(\omega)}{S(\omega)}\, \sin(\omega q) \frac{\mathrm{d}\omega}{2\pi} \overbrace{\sim}^{\omega^\star \to \infty} - \frac{2}{\pi} \int_{\omega^\star}^{\infty} \mathrm{sinc}(\omega q)\, \mathrm{d}\omega \\ = \frac{2\,\mathrm{Si}(q\omega^\star) - \pi}{\pi q},\end{aligned} \tag{2.51}$$

where $\mathrm{Si}(z)$ is the sine-integral function:

$$\mathrm{Si}(z) = \int_0^z \mathrm{sinc}(t)\, \mathrm{d}t\,. \tag{2.52}$$

Let us now take into account that, in practice, one deals with discretized versions of the integrals written throughout this Section. In particular, q is sampled as $q = n\epsilon$, with $n \in \mathbb{Z}^+$, and a meaningful choice for the cutoff is the

Nyquist (angular) frequency of the time series, i.e., $\omega^\star = \pi/\epsilon$. Thus, Eq. (2.51) becomes

$$\frac{2}{q}\int_{\omega^\star}^{\infty}\frac{S'(\omega)}{S(\omega)}\,\sin(\omega\tau)\frac{\mathrm{d}\omega}{2\pi} \sim \frac{1}{\epsilon}\frac{2\,\mathrm{Si}(\pi n)-\pi}{\pi n}, \tag{2.53}$$

that is a function that decays to zero as n^{-2}, for large n. The boundary term is

$$\begin{aligned}\frac{\omega^\star}{\pi}\,\mathrm{sinc}(\omega^\star\tau)\log(S(\omega^\star)) &= \frac{1}{\epsilon}\,\mathrm{sinc}(\pi n)\log(S(\pi/\epsilon)) \\ &= \frac{1}{\epsilon}\delta_{n0}\log(S(\pi/\epsilon));\end{aligned} \tag{2.54}$$

this means that only the $n = 0$ cepstral coefficient is affected by the logarithmic divergence in the limit of small ϵ (i.e., the limit of large Nyquist frequency). The complete expression of $C(q = n\epsilon)$ in the case of a Lorentzian spectrum is

$$\begin{aligned}C(q=n\epsilon) = \frac{1}{\epsilon}\Bigg[&\frac{2\cos(\omega_0 n\epsilon)\mathrm{e}^{-n\epsilon/\tau}-\mathrm{e}^{-\frac{n\epsilon}{\tau}\sqrt{1+\tau^2\omega_0^2}}}{n}+ \\ &+\frac{2\,\mathrm{Si}(\pi n)-\pi}{\pi n}+\delta_{n0}\log(S(\pi/\epsilon))\Bigg].\end{aligned} \tag{2.55}$$

The usual definition of cepstral coefficient, C_n, is given in Eq. (2.21), and it is

$$C_n = \frac{1}{N}\sum_{k=0}^{N-1}\log(S(\omega_k))\,\mathrm{e}^{2\pi\mathrm{i}kn/N}. \tag{2.56}$$

This is the discrete Fourier transform of the logarithm of the spectrum. In discretizing the continuous Fourier transform, a factor $1/\epsilon$ that would come from the differential of the frequency is missing, in fact:

$$\begin{aligned}\int f(\omega)\frac{\mathrm{d}\omega}{2\pi} &\simeq \sum_k f(\omega_k)\frac{\Delta\omega}{2\pi} \\ &= \sum_k f(\omega_k)\frac{2\omega^\star}{2\pi N} \\ &= \frac{1}{N\epsilon}\sum_k f(\omega_k),\end{aligned} \tag{2.57}$$

so that

$$C_n = \epsilon\, C(q = n\epsilon). \tag{2.58}$$

One finally obtains

$$\begin{aligned}C_n = &\frac{2\cos(\omega_0 n\epsilon)\mathrm{e}^{-n\epsilon/\tau}-\mathrm{e}^{-\frac{n\epsilon}{\tau}\sqrt{1+\tau^2\omega_0^2}}}{n}+ \\ &+\frac{2\,\mathrm{Si}(\pi n)-\pi}{\pi n}+\delta_{n0}\log(S(\pi/\epsilon)).\end{aligned} \tag{2.59}$$

For any finite value of ϵ, the $n = 0$ cepstral coefficient is not well defined, since the numerators are finite and the denominator is zero. Thus, one can forget about the boundary term and simply write, for $n > 0$:

$$C_n = \frac{2\cos(\omega_0 n\epsilon)\mathrm{e}^{-n\epsilon/\tau}-\mathrm{e}^{-\frac{n\epsilon}{\tau}\sqrt{1+\tau^2\omega_0^2}}}{n}+\frac{2\,\mathrm{Si}(\pi n)-\pi}{\pi n}. \tag{2.60}$$

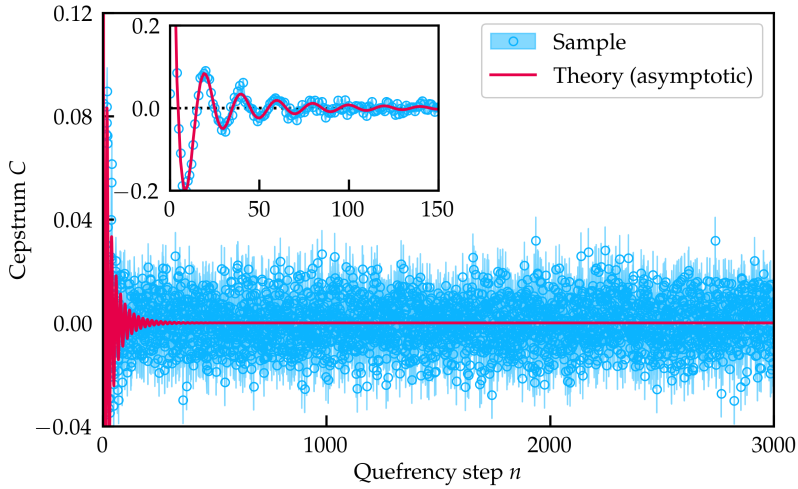

Figure 2.2: Comparison between the theoretical expression of the cepstrum of a Lorentzian PSD, Eq. (2.60), and the numerical cepstrum obtained from a 20000 steps long time series generated with parameters $\omega_0 = 10\pi$ THz, $\tau = 1$ ps.

This formula is compared to a numerical simulation in Fig. 2.2. Numerical data are obtained by generating correlated multivariate Gaussian variables with covariance matrices of the form:

$$\Sigma_{nm} = R_0 \cos(\omega_0 \epsilon (n-m)) \exp(-\epsilon |n-m|/\tau), \tag{2.61}$$

corresponding to stochastic processes with Lorentzian PSD.

2.3.2 *Resampling and resampling-invariance*

Resampling reduces the Nyquist frequency of the periodogram—i.e., its maximum frequency due to the finite sampling of the time series—to a lower frequency, $f^\star$. The procedure consists of the application of a low-pass filter, e.g., a moving average, to the flux time series, followed by a down-sampling of the filtered time series with time period $\epsilon^\star = \frac{1}{2f^\star}$, in order to avoid aliasing. Resampling with small $f^\star$ (e.g., of the order of 1 THz) turns out to be useful to have a better estimate of thermal conductivity with the AIC in cases where the PSD features a sharp peak at low frequency [26]. This is likely due to the shortening in the length of the periodogram, where all the features at frequencies larger than $f^\star$ are excluded from the cepstral filter. Let us see how the choice of $f^\star$ affects quantities such as the periodogram, the cepstrum, and the value of the transport coefficient as a function of the number of retained cepstral coefficients, P. In particular, it will be clear that, for different $f^\star$—and, consequently, $\epsilon^\star$—the transport coefficient as a function of *cesptral cutoff*, $\lambda(P \cdot \epsilon^\star)$, stays the same, despite the fact that both the periodogram and the cepstrum are modified.

In the continuous limit, resampling is basically a convolution with a window function. If $\mathcal{J}(t)$ is the continuous limit of the flux time series, the resampled

flux, $\underline{\mathcal{J}}(t)$, is the convolution of the original flux with a window function, $\Delta(t, w)$, where w characterizes the width of the window:

$$\underline{\mathcal{J}}(t) = \mathcal{J}(t) * \Delta(t, w) = \int_{-\infty}^{\infty} \mathcal{J}(t')\Delta(t - t', w)\,\mathrm{d}t\,. \tag{2.62}$$

The PSD of $\underline{\mathcal{J}}(t)$ is, by the Plancherel's identity [21]:

$$\underline{\mathcal{S}}(\omega) = \mathcal{S}(\omega)\left|\tilde{\Delta}(\omega)\right|^2, \tag{2.63}$$

where $\tilde{\Delta}(\omega)$ is the Fourier transform of Δ. The cepstrum thus reads

$$\underline{\mathcal{C}}(q) = \mathfrak{F}^{-1}[\log \underline{\mathcal{S}}](q), \tag{2.64}$$

where $\mathfrak{F}$ is the Fourier-transform operator. By plugging the expression of $\underline{\mathcal{S}}$ into Eq. (2.64), one obtains

$$\underline{\mathcal{C}}(q) = \mathcal{C}(q) + \mathfrak{F}^{-1}[\log|\tilde{\Delta}|^2](q). \tag{2.65}$$

From Eqs. (2.65) and (2.58), it can be seen that the cepstral coefficients $\mathcal{C}_n$ and $\underline{\mathcal{C}}_m$ can be directly compared for $q = n\epsilon = m\epsilon^\star$, i.e. when $m = n\epsilon/\epsilon^\star$. The cepstral estimator of the logarithm of the transport coefficient, $\mathcal{L}_0^\star$, in the continuous limit reads

$$\begin{aligned}
\underline{\mathcal{L}}_0^\star &= \underline{\mathcal{C}}_0 + 2\sum_{n=1}^{P^\star-1} \underline{\mathcal{C}}_n \\
&\approx \epsilon^\star \underline{\mathcal{C}}(0) + 2\epsilon^\star \sum_{n=1}^{P^\star-1} \underline{\mathcal{C}}(q = n\epsilon^\star) \\
&\approx 2\int_0^{p^\star} \underline{\mathcal{C}}(q)\,\mathrm{d}q\,,
\end{aligned} \tag{2.66}$$

where $p^\star = P\epsilon^\star$ and the factor $\epsilon^\star$ is used as the integration step to pass from the sum to the integral. After plugging Eq. (2.64) into Eq. (2.66), the latter becomes

$$\begin{aligned}
\underline{\mathcal{L}}_0^\star &\approx 2\int_0^{p^\star} \underline{\mathcal{C}}(q)\,\mathrm{d}q \\
&= 2\int_0^{p^\star} \left(\mathcal{C}(q) + \mathfrak{F}^{-1}[\log|\tilde{\Delta}|^2](q)\right)\mathrm{d}q \\
&= \mathcal{L}_0^\star + 2\int_0^{p^\star} \mathfrak{F}^{-1}[\log|\tilde{\Delta}|^2](q)\,\mathrm{d}q\,.
\end{aligned} \tag{2.67}$$

The difference of $\underline{\mathcal{L}}_0^\star$ and $\mathcal{L}_0^\star$ can be estimated as

$$\begin{aligned}
\underline{\mathcal{L}}_0^\star(p^\star) - \mathcal{L}_0^\star(p^\star) &= 2\int_0^{p^\star} \mathfrak{F}^{-1}[\log|\tilde{\Delta}|^2](q)\,\mathrm{d}q \\
&= \int_{-\infty}^{\infty} \left(\Theta(p^\star - q) + \Theta(p^\star + q)\right)\mathfrak{F}^{-1}[\log|\tilde{\Delta}|^2](q)\,\mathrm{d}q \\
&= \frac{1}{2\pi}\int_{-\infty}^{\infty} \tilde{\Theta}(\omega)\log|\tilde{\Delta}(\omega)|^2\,\mathrm{d}\omega
\end{aligned} \tag{2.68}$$

where Θ is the Heaviside step-function, $\tilde{\Theta} = 2\sin(\omega p^\star)/\omega$, and Plancherel's identity is used to go from the second to the third line of the above Equation. Since the above integral can be shown to evaluate to zero, the equality of $\underline{\mathcal{L}}_0^\star(p^\star)$ and $\mathcal{L}_0^\star(p^\star)$ follows, and so does the invariance of $\lambda(p^\star)$ with respect to the resampling frequency.

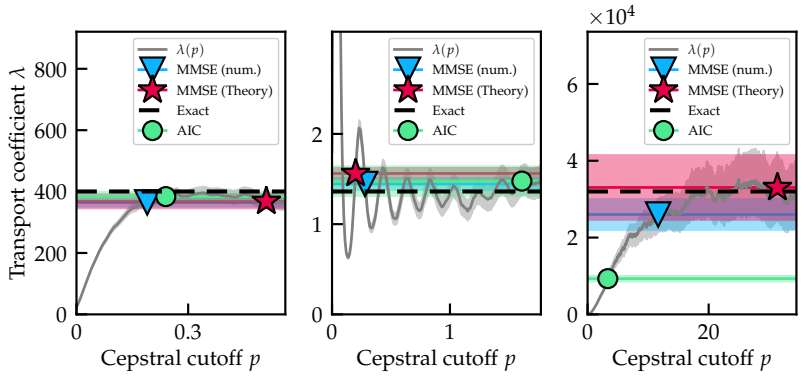

Figure 2.3: Comparison of the MMSE and AIC estimators in reproducing the exact value of transport coefficients. The left panel has parameters $R_0 = 4$, $f_0 = 0$, $\tau = 0.1$ and $\ell = 3$. The middle panel has parameters $R_0 = 4$, $f_0 = 5$, $\tau = 3$ and $\ell = 3$. The right panel has parameters $R_0 = 4$, $f_0 = 0$, $\tau = 8$ and $\ell = 10$.

2.3.3 *Minimum mean square error estimation of transport coefficients*

Being able to generate time series with PSDs of known form, and whose cepstrum is known analytically, is useful to understand how the truncation of the sum in the expression of $\mathcal{L}_0^\star$ in Eq. (2.24) to $P^\star$ cepstral coefficients introduces a bias that propagates to the estimated value of the transport coefficient. Formally, the bias of an estimator is the difference between the expectation value of the estimator and its true value. The bias of $\mathcal{L}_0^\star$ is

$$\begin{aligned}\text{bias}(\mathcal{L}_0^\star) &= \langle \mathcal{L}_0^\star \rangle - \log S(0) \\ &= \left\langle \mathcal{C}_0 - \psi(\nu/2) + \log(\nu/2) + 2\sum_{n=1}^{P^\star-1} \mathcal{C}_n \right\rangle + \\ &\qquad - \left(C_0 + 2\sum_{n=1}^{\frac{N}{2}-1} C_n + C_{\frac{N}{2}} \right) \\ &= -2\sum_{n=P^\star}^{\frac{N}{2}-1} C_n - C_{\frac{N}{2}},\end{aligned} \tag{2.69}$$

and it has the property of going to zero as $P^\star$ increases. Eq. (2.69) contains the true values of the cepstral coefficients, C_n, rather than the available cepstral samples, $\mathcal{C}_n$. Of course, the true cepstral coefficients are unknown since only finite samples of the stochastic processes underlying the relevant fluxes are available. Nonetheless, since only cepstral coefficients with $P^\star < n < N - P^\star$ appear and, under this condition, $C_n \approx 0$, only a rough estimate of the behavior of C_n as a function of n is needed to estimate the bias.

For now, let us assume that the true cepstrum is well approximated by computing the inverse discrete Fourier transform of any (reasonably) smoothed version of the log-periodogram, $L(\omega)$—this statement will be verified later. Any low-pass filter would do, in principle; to avoid any contribution to the noise arising from discontinuities in the smoothed log-periodogram sample,

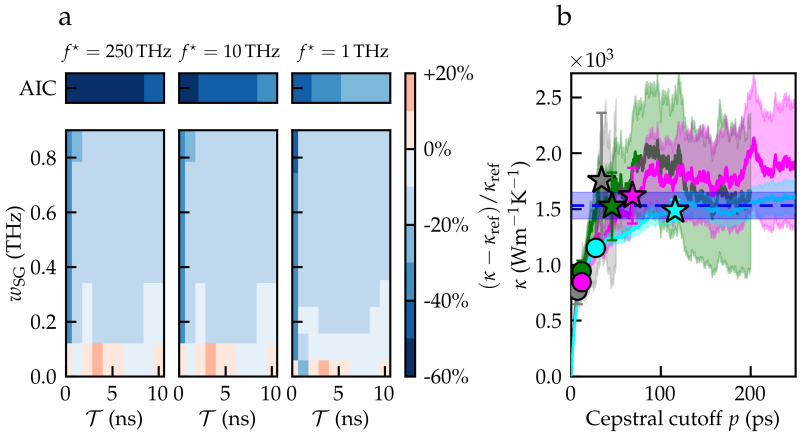

Figure 2.4: Cepstral analysis of graphene at $T = 500\,\mathrm{K}$. (a) Colormaps of the relative deviation of the thermal conductivity obtained via cepstral analysis with respect to the reference HE value for different resampling frequencies. The x-axis indicates the length of the time series of the energy flux. For the MMSE results, the y-axis indicates the width of the window of the SG filter used to smoothen the sample log-PSD. The AIC results are reported in the insets above. (b) Value of κ as a function of the cepstral cutoff $p = P \cdot \epsilon$ with its standard deviation given by the shaded areas. Note that, despite possible visual similarities, this is not the plot of a HE integral as a function of the integration time, but rather the plot of Eq. (2.38) as a function of the number of retained cepstral coefficients multiplied by ϵ. Gray, green, magenta, and cyan curves are associated with simulations of 0.1, 0.4, 1, and 10 ns, respectively. Same-color circles are the AIC results obtained with simulations of the same length and $f^\star = 1\,\mathrm{THz}$. Stars are the MMSE results with $f^\star = 250\,\mathrm{THz}$ and $w_{\mathrm{SG}} = 0.05\,\mathrm{THz}$. The blue, horizontal, dashed line is the HE result obtained from standard block averaging from 100 ns of trajectories (ten independent simulations of 10 ns each).

the smoothing of $\log \mathcal{S}_k$ is performed via the Savitzki-Golay (SG) filter [38], which consists in a least-squares polynomial fit of the signal in a window of given width around each sample point. Since this filter outputs a differentiable function, it is preferred with respect to a simple moving average, which could produce a larger number of spurious contributions to the cepstrum. The idea to partially solve the bias underestimation of the AIC is to minimize the Mean Square Error (MSE), which is the sum of the bias squared and the variance, in order to exploit the so-called bias-variance tradeoff, aiming thus at balancing bias and variance not to weight too much either of the two. The representative cepstral coefficients, $\overline{C}_n$, obtained from the inverse discrete Fourier transform of the filtered log-periodogram, are used to compute the MSE as a function of the number of retained cepstral coefficients, P:

$$\mathrm{MSE}(P) = \left(2 \sum_{n=P}^{\frac{N}{2}-1} \overline{C}_n + \overline{C}_{\frac{N}{2}} \right)^2 + \\ + \frac{4P-2}{N} \psi'\left(\tfrac{\nu}{2}\right). \tag{2.70}$$

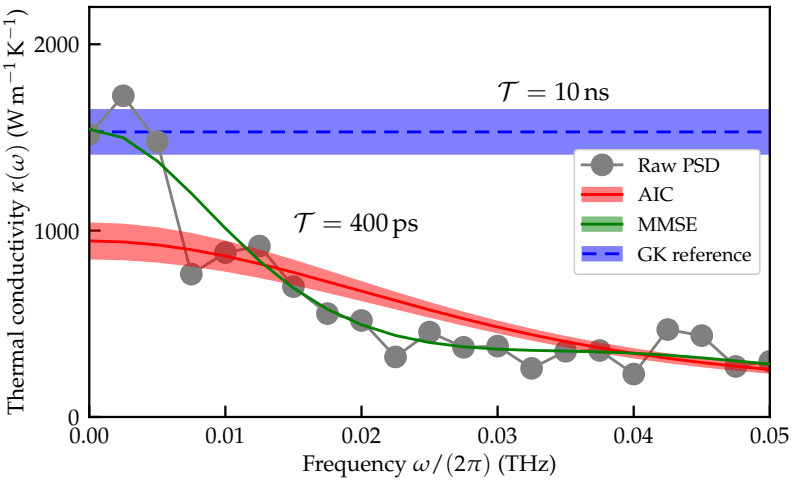

Figure 2.5: Low-frequency portion of the PSD of graphene at 500 K. The MMSE method (green curve) provides a converged estimate of κ with a simulation of 400 THz, while the AIC (red curve) is unable to capture the sharp peak at zero frequency. The raw PSD is represented by the gray circles joined by lines, that are a guide for the eye. The dashed, blue line is the reference value of the thermal conductivity computed as a HE integral over 10 ns-long EMD simulations.

The estimate of the transport coefficient and its statistical uncertainty are given by Eq. (2.38), with $P^\star$ given by

$$P^\star = \arg\min_P \mathrm{MSE}(P). \tag{2.71}$$

This method to estimate transport coefficients, called Minimum Mean Square Error (MMSE) method, is tested for time series whose PSD is Lorentzian like in Eq. (2.48). In Fig. 2.3 the transport coefficients, λ, associated with such time series are shown as a function of the cepstral cutoff p for different values of the parameters of the Lorentzian function in Eq. (2.48). The exact value of λ, given by the zero-frequency value of the exact PSD, is compared to the AIC and MMSE estimates; for the latter, both the theoretical (i.e., the one obtained minimizing the exact bias) and the numerical (which depends on the choice of the SG window) estimates are provided. For sharply peaked PSDs, the MMSE estimate outperforms the AIC method, as it is clear from the right panel of Fig. 2.3; instead, when the main peak in the PSD is at $\omega = 0$ but its width, $1/\tau$, is large enough, both methods yield results compatible with the exact value of λ. When the peak is away from the origin, such as in the case of the middle panel of Fig. 2.3, both methods work well.

The MMSE method has been tested for realistic materials in Ref. 39. The method is particularly effective in 2D materials, where the reduced dimensionality allows phonons to be in the hydrodynamic regime [40], and thermal conductivity assumes large values. In particular, in graphene, the simulation time required to have converged results is reduced by a factor of more than 20 with respect to HE integration. Fig. 2.4 and Fig. 2.5 compare the MMSE and AIC methods for graphene at $T = 500$ K, where the MMSE method provides a converged value of κ with simulations 25 times shorter than HE integration, while

the AIC fails to do so. With equal simulation lengths, the AIC method yields results that are converged only at higher temperatures, while at temperatures as low as 200 K the AIC value of κ is $\approx 60\%$ of the reference value[2], the MMSE being still able to capture the correct κ [39].

2 At 200 K the value of the thermal conductivity obtained from classical EMD might be inaccurate since quantum effects increase with decreasing temperature. Nonetheless, the point here is the ability of the estimator to recover the reference value of κ, regardless of the intrinsic accuracy of the underlying theory.

Part II

TOPOLOGICAL CHARGE TRANSPORT

Die ganzen Zahlen hat der liebe Gott gemacht, alles andere ist Menschenwerk.
God made the integers, all else is the work of men.

Leopold Kronecker,
Lecture at the Berlin Natural Scientists Meeting, 1886

3 ADIABATIC CHARGE TRANSPORT

In this Chapter I will review some concepts in the theory of adiabatic charge transport. After an excursus on how the adiabatic approximation can be obtained through different routes, each putting things under slightly different perspectives, I show how the Thouless' approximation and the continuity equation for the charge density are intertwined, making explicit the bond between the Thouless' wavefunction and transport theory. Then, the computation of the adiabatic electric flux in condensed matter systems is addressed and, finally, the computation of ionic conductivity is discussed.

3.1 THE ADIABATIC EQUATION

Let us consider a quantum system whose Hamiltonian, $\hat{\mathcal{H}}$, depends on time through a parameter, λ, which possibly represents vector quantities such as the positions of nuclei. The caret ($\hat{}$) represents quantum operators. The Schrödinger equation reads

$$\frac{\mathrm{d}}{\mathrm{d}t}\left|\Phi\right\rangle = \frac{1}{\mathrm{i}\hbar}\hat{\mathcal{H}}_\lambda\left|\Phi\right\rangle . \tag{3.1}$$

For each value of λ, there exists a complete set of eigenstates of the Hamiltonian:

$$\hat{\mathcal{H}}_\lambda\left|\Psi_n(\lambda)\right\rangle = E_n(\lambda)\left|\Psi_n(\lambda)\right\rangle \tag{3.2}$$

A full solution to the Schrödinger equation is of course impossible to find for a Hamiltonian with a general λ-dependence. Nonetheless, approximated solutions can be obtained in different ways. In particular, let us focus on the Thouless' approximation to the wavefunction [41], which will be obtained in three different ways by adding *ad hoc* requirements to standard approximation techniques. Later, it will be shown how Thouless' approximation emerges naturally as the lowest-order approximation able to describe adiabatic transport.

3.1.1 *First-order approximation with the variation of constants*

Thouless' wavefunction can be obtained from perturbation theory in the adiabatic basis. The system's state, $\left|\Phi\right\rangle$, can be expanded in the λ-dependent instantaneous basis as

$$\left|\Phi(t)\right\rangle = \sum_n a_n(t)\left|\Psi_n(\lambda(t))\right\rangle . \tag{3.3}$$

The Schrödinger equation, Eq. (3.1), can be written in the adiabatic basis as

$$\begin{aligned}\mathrm{i}\hbar\sum_m\left[\dot{a}_m(t)\left|\Psi_m(t)\right\rangle + a_m(t)\left|\dot{\Psi}_m(t)\right\rangle\right] &= \sum_m a_m(t)\hat{\mathcal{H}}_\lambda(t)\left|\Psi_m(t)\right\rangle \\ &= \sum_m a_m(t)E_m(t)\left|\Psi_m(t)\right\rangle ,\end{aligned} \tag{3.4}$$

where $|\Psi_m(t)\rangle$ is a shorthand notation for $|\Psi_m(\lambda(t))\rangle$ that, whenever the context makes it clear, will be indicated simply by $|\Psi_m\rangle$. The explicit time-dependence of a_n and E_n will be also omitted. Acting on left with $\langle\Psi_n(\lambda(t))|$, one obtains

$$\mathrm{i}\hbar\,\dot{a}_n(t) + \sum_m a_m(t)\mathrm{i}\hbar\,\langle\Psi_n(t)|\dot{\Psi}_m(t)\rangle = a_n(t)E_n(t). \tag{3.5}$$

We are left with a differential equation for the coefficients:

$$\begin{aligned}\dot{a}_n &= \frac{1}{\mathrm{i}\hbar}a_nE_n - \frac{1}{\mathrm{i}\hbar}\sum_m a_m\mathrm{i}\hbar\dot{\lambda}\,\langle\Psi_n|\partial_\lambda\Psi_m\rangle \\ &= \frac{1}{\mathrm{i}\hbar}a_n(E_n - \mathrm{i}\hbar\dot{\lambda}\,\langle\Psi_n|\partial_\lambda\Psi_n\rangle) - \frac{1}{\mathrm{i}\hbar}\sum_{m(\neq n)} a_m\mathrm{i}\hbar\dot{\lambda}\,\langle\Psi_n|\partial_\lambda\Psi_m\rangle\,.\end{aligned} \tag{3.6}$$

If the Hamiltonian is not periodic in time, one can choose the parallel transport gauge [42] and remove the $\langle\Psi_n|\partial_\lambda\Psi_n\rangle$ contribution. Thus, Eq. (3.6) becomes

$$\dot{a}_n = \frac{1}{\mathrm{i}\hbar}a_nE_n - \frac{1}{\mathrm{i}\hbar}\sum_{m(\neq n)} a_m\mathrm{i}\hbar\dot{\lambda}\,\langle\Psi_n|\partial_\lambda\Psi_m\rangle\,. \tag{3.7}$$

The a_nE_n contribution disappears after having defined $a_n(t) = c_n(t)\mathrm{e}^{\mathrm{i}\alpha_n(t)}$, with the exponent $\alpha_n = -\frac{1}{\hbar}\int_0^t E_n(t')\,\mathrm{d}t'$. What is left is

$$\mathrm{e}^{-\mathrm{i}\alpha_n}\left(\dot{a}_n - \frac{1}{\mathrm{i}\hbar}a_nE_n\right) = \frac{\mathrm{d}}{\mathrm{d}t}\left(a_n(t)\mathrm{e}^{-\mathrm{i}\alpha_n}\right), \tag{3.8}$$

so that Eq. (3.7) is reduced to

$$\dot{c}_n(t) = -\frac{1}{\mathrm{i}\hbar}\sum_{m(\neq n)} \mathrm{e}^{\mathrm{i}(\alpha_m-\alpha_n)}c_m\mathrm{i}\hbar\dot{\lambda}\,\langle\Psi_n|\Psi_m\rangle\,. \tag{3.9}$$

An approximate solution can be obtained through time-dependent perturbation theory in terms of the *adiabatic potential* $\mathrm{i}\hbar\dot{\lambda}\,\langle\Psi_n|\partial_\lambda\Psi_m\rangle$. At order zero, one simply has

$$\dot{c}_n^{(0)}(t) = 0, \tag{3.10}$$

which means that $c_n^{(0)}$ is constant. If one chooses the initial state to be close to an instantaneous eigenstate of $\hat{\mathcal{H}}$, say $|\Psi_k\rangle$, the zeroth order term reads

$$c_n^{(0)}(t) = \delta_{nk}. \tag{3.11}$$

The first order equation is obtained by replacing c_m with $c_m^{(0)}$ in Eq. (3.9):

$$\dot{c}_n^{(1)}(t) = -\frac{1}{\mathrm{i}\hbar}(1-\delta_{nk})\mathrm{e}^{\mathrm{i}(\alpha_k-\alpha_n)}\mathrm{i}\hbar\dot{\lambda}\,\langle\Psi_n|\partial_\lambda\Psi_k\rangle\,. \tag{3.12}$$

Once integrated, this yields

$$\begin{aligned}c_n^{(1)}(t) - c_n^{(1)}(0) = -\frac{1}{\mathrm{i}\hbar}(1-\delta_{nk})\times \\ \int_0^t \mathrm{e}^{\mathrm{i}[\alpha_k(t')-\alpha_n(t')]}\mathrm{i}\hbar\dot{\lambda}(t')\,\langle\Psi_n(t')|\partial_\lambda\Psi_k(t')\rangle\,\mathrm{d}t'\,.\end{aligned} \tag{3.13}$$

The above integral cannot be solved analytically. Up to higher order terms (h.o.t.) in $\dot{\lambda}$, it can be evaluated as

$$c_n^{(1)}(t) - c_n^{(1)}(0) = \mathrm{i}\hbar\dot{\lambda}(t)(1-\delta_{nk})\left(\frac{\langle\Psi_n(t)|\partial_\lambda\Psi_k(t)\rangle}{E_n(t)-E_k(t)}\mathrm{e}^{\mathrm{i}[\alpha_k(t)-\alpha_n(t)]}+\right.$$
$$\left.-\frac{\langle\Psi_n(0)|\partial_\lambda\Psi_k(0)\rangle}{E_n(0)-E_k(0)}\mathrm{e}^{\mathrm{i}[\alpha_k(0)-\alpha_n(0)]}\right)+\text{h.o.t.} \tag{3.14}$$

The value of $c_n^{(1)}(t)$ is easily recognized to be

$$c_n^{(1)}(t) = \mathrm{i}\hbar\dot{\lambda}(t)(1-\delta_{nk})\frac{\langle\Psi_n(t)|\partial_\lambda\Psi_k(t)\rangle}{E_n(t)-E_m(t)}\mathrm{e}^{\mathrm{i}[\alpha_k(t)-\alpha_n(t)]}. \tag{3.15}$$

Up to this order, the solution to the Schrödinger equation is thus

$$\begin{aligned}|\Phi(t)\rangle &= \sum_n \mathrm{e}^{\mathrm{i}\alpha_n(t)}\left(c_n^{(0)}(t)+c_n^{(1)}(t)\right)|\Psi_n(t)\rangle \\ &= \mathrm{e}^{\mathrm{i}\alpha_k(t)}\left(|\Psi_k(t)\rangle+\mathrm{i}\hbar\dot{\lambda}(t)\sum_{n(\neq k)}\frac{\langle\Psi_n(t)|\partial_\lambda\Psi_k(t)\rangle}{E_n(t)-E_k(t)}|\Psi_n(t)\rangle\right).\end{aligned} \tag{3.16}$$

This is the Thouless' adiabatic state obtained in 1983 [41].

3.1.2 *First-order approximation in the rate of change of the parameters*

The same wavefunction can be obtained as the lowest-order approximation in the derivative of the adiabatic parameters. Let us consider the *strictly adiabatic* approximation, where the only contribution to the time-evolved state is given by a phase factor. This is equivalent to saying that the rate of change of λ, i.e. $\dot{\lambda}$, is so small that a system prepared in the nth eigenstate at $t = 0$ always remains in that same eigenstate. If such assumption is relaxed, at $t > 0$ the nth eigenstate will acquire a contribution of the form

$$|\Psi_n(t)\rangle \mapsto |\Psi_n(t)\rangle + f(\dot{\lambda})\,|\delta\Psi_n(t)\rangle \tag{3.17}$$

The function f must go to zero linearly in $\dot{\lambda}$, to restore the strictly adiabatic approximation. For simplicity, let us redefine $|\delta\Psi_n(t)\rangle$ to include a linear term in $\dot{\lambda}$.

Now let us take Eq. (3.4) and rewrite it to make its dependence on $\dot{\lambda}$ explicit:

$$\mathrm{i}\hbar\sum_m\left(\dot{a}_m(t)\,|\Psi_m(\lambda(t))\rangle + a_m(t)\dot{\lambda}\,|\partial_\lambda\Psi_m(\lambda(t))\rangle\right) = \sum_m a_m(t)\hat{\mathcal{H}}_\lambda(t)\,|\Psi_m(\lambda(t))\rangle\,. \tag{3.18}$$

Using the substitution in Eq. (3.17) one obtains

$$\mathrm{i}\hbar\sum_m\left[\dot{a}_m(t)\left(|\Psi_m(\lambda)\rangle+|\delta\Psi_m(\dot{\lambda})\rangle\right)+a_m(t)\dot{\lambda}\cdot|\partial_\lambda\Psi_m(\lambda)\rangle\right] = \sum_m a_m(t)\hat{\mathcal{H}}_\lambda(t)\left(|\Psi_m(\lambda)\rangle+|\delta\Psi_m(\dot{\lambda})\rangle\right) \tag{3.19}$$

and, acting from the left with $\langle\Psi_n|$, one gets:

$$\begin{aligned} \mathrm{i}\hbar\dot{a}_n(t) + \mathrm{i}\hbar\sum_m \left(\dot{a}_m(t)\,\langle\Psi_n|\delta\Psi_m\rangle + a_m(t)\dot{\lambda}\cdot\langle\Psi_n|\partial_\lambda\Psi_m\rangle\right) = \\ E_n(t)a_n(t) + E_n\sum_m a_m\,\langle\Psi_n|\delta\Psi_m\rangle\,. \end{aligned} \tag{3.20}$$

Since the contribution of order $\dot{\lambda}$ is completely included in $|\delta\Psi_m\rangle$, the coefficients a_n must be strictly adiabatic in order to keep the equation at $\mathcal{O}(\dot{\lambda})$, i.e.

$$a_n(t) = a_n(0)\mathrm{e}^{\mathrm{i}\alpha_n(t)}. \tag{3.21}$$

Thus, the term $\mathrm{i}\hbar\dot{a}_n$ in the left-hand side (LHS) cancels out with $E_n a_n$ in the right-hand side (RHS), yielding

$$\begin{aligned} \sum_m \left(E_m(t)a_m(t)\,\langle\Psi_n|\delta\Psi_m\rangle + a_m(t)\mathrm{i}\hbar\dot{\lambda}\,\langle\Psi_n|\partial_\lambda\Psi_m\rangle\right) = \\ E_n\sum_m a_m\,\langle\Psi_n|\delta\Psi_m\rangle\,, \end{aligned} \tag{3.22}$$

that can be solved to obtain

$$\langle\Psi_n|\delta\Psi_m\rangle = \mathrm{i}\hbar\dot{\lambda}\frac{\langle\Psi_n|\partial_\lambda\Psi_m\rangle}{E_n(t)-E_m(t)}, \tag{3.23}$$

$$|\delta\Psi_n\rangle = \mathrm{i}\hbar\dot{\lambda}\sum_{m(\neq n)}\frac{\langle m|\partial_\lambda\Psi_n\rangle}{E_m(t)-E_n(t)}\,|\Psi_m\rangle\,. \tag{3.24}$$

Again, the state a time t takes the form

$$|\Phi(t)\rangle = \sum_n \mathrm{e}^{\mathrm{i}\alpha_n(t)}\left[|\Psi_n(t)\rangle + \mathrm{i}\hbar\dot{\lambda}\sum_{m(\neq n)}\frac{\langle\Psi_m(t)|\partial_\lambda\Psi_n(t)\rangle}{E_m(t)-E_n(t)}\,|\Psi_m(t)\rangle\right], \tag{3.25}$$

which is the same as Eq. (3.16). It is important to notice that, while this derivation makes it somewhat obscure, the initial condition for this solution is

$$\begin{aligned} |\Phi(0)\rangle = \sum_n \mathrm{e}^{\mathrm{i}\alpha_n(0)}\Bigg[|\Psi_n(0)\rangle + \\ +\mathrm{i}\hbar\dot{\lambda}(0)\sum_{m(\neq n)}\frac{\langle\Psi_m(0)|\partial_\lambda\Psi_n(0)\rangle}{E_m(0)-E_n(0)}\,|\Psi_m(0)\rangle\Bigg], \end{aligned} \tag{3.26}$$

which is consistent with Eq. (3.14); i.e., the initial state is *not* an instantaneous eigenstate of the Hamiltonian, but it already includes a first-order adiabatic contribution.

3.1.3 *First-order approximation of the evolution operator*

Yet another derivation involves the time-evolution operator, $\hat{\mathcal{U}}(t)$, that formally solves the Schrödinger equation, i.e. the time-ordered exponential [43]

$$\hat{\mathcal{U}}(t) = \mathcal{T}\mathrm{e}^{-\frac{\mathrm{i}}{\hbar}\int_0^t \hat{\mathcal{H}}(t')\mathrm{d}t'}, \tag{3.27}$$

$\mathcal{T}$ being the time-ordering operator. This can be factored into two terms: the first is the purely adiabatic part [44],

$$\hat{\mathcal{U}}_0(t) = \sum_n \mathrm{e}^{\mathrm{i}\alpha_n(t)} \left|\Psi_n(t)\right\rangle\!\left\langle\Psi_n(0)\right|, \tag{3.28}$$

which brings an instantaneous eigenstate at time $t = 0$, $|\Psi_n(0)\rangle$, to the eigenstate labeled by the same quantum number[1] at a later time, $t > 0$, multiplied by the phase accumulated during the time-evolution, i.e., $\mathrm{e}^{\mathrm{i}\alpha_n(t)}|\Psi_n(t)\rangle$; the second term, $\hat{\mathcal{V}}(t)$, accounts for all the nonadiabatic contributions. The full time-evolution operator reads

$$\hat{\mathcal{U}}(t) = \hat{\mathcal{U}}_0(t)\hat{\mathcal{V}}(t). \tag{3.29}$$

The nonadiabatic part can also be expressed as a time-ordered exponential [44] in terms of some operator $\hat{A}$ such that

$$\hat{\mathcal{V}}(t) = \mathcal{T}\mathrm{e}^{-\frac{\mathrm{i}}{\hbar}\int_0^t \hat{A}(t')\mathrm{d}t'}. \tag{3.30}$$

Thus, $\dot{\hat{\mathcal{V}}}(t) = -\frac{\mathrm{i}}{\hbar}\hat{A}(t)\hat{\mathcal{V}}(t)$. From Eq. (3.29), one can write $\hat{\mathcal{V}}(t) = \hat{\mathcal{U}}_0^\dagger(t)\hat{\mathcal{U}}(t)$, its derivative being

$$\dot{\hat{\mathcal{V}}}(t) = \dot{\hat{\mathcal{U}}}_0^\dagger(t)\hat{\mathcal{U}}(t) + \hat{\mathcal{U}}_0^\dagger(t)\dot{\hat{\mathcal{U}}}(t). \tag{3.31}$$

By inserting the identity as $\hat{\mathcal{U}}_0^\dagger\hat{\mathcal{U}}_0$, and using the fact that $\dot{\hat{\mathcal{U}}} = -\mathrm{i}\hat{\mathcal{H}}\hat{\mathcal{U}}/\hbar$, one obtains

$$\begin{aligned}\dot{\hat{\mathcal{V}}} &= \dot{\hat{\mathcal{U}}}_0^\dagger\hat{\mathcal{U}}_0\hat{\mathcal{U}}_0^\dagger\hat{\mathcal{U}} - \frac{\mathrm{i}}{\hbar}\hat{\mathcal{U}}_0^\dagger\hat{\mathcal{H}}\hat{\mathcal{U}}_0\hat{\mathcal{U}}_0^\dagger\hat{\mathcal{U}} \\ &= -\frac{\mathrm{i}}{\hbar}\left(\mathrm{i}\hbar\dot{\hat{\mathcal{U}}}_0^\dagger\hat{\mathcal{U}}_0 + \hat{\mathcal{U}}_0^\dagger\hat{\mathcal{H}}\hat{\mathcal{U}}_0\right)\hat{\mathcal{V}}.\end{aligned} \tag{3.32}$$

The operator $\hat{A}$ turns out to be the Hamiltonian transformed[2] in the adiabatic frame of reference via the time-dependent unitary transformation $\hat{\mathcal{S}}(t) = \hat{\mathcal{U}}_0^\dagger(t)$. Let us rename $\hat{A}$ as

$$\hat{\mathcal{H}}_{\mathrm{ad}} \equiv \hat{A} = \hat{\mathcal{U}}_0^\dagger\hat{\mathcal{H}}\hat{\mathcal{U}}_0 + \mathrm{i}\hbar\dot{\hat{\mathcal{U}}}_0^\dagger\hat{\mathcal{U}}_0. \tag{3.34}$$

With this definition, the full time-evolution operator reads

$$\hat{\mathcal{U}}(t) = \hat{\mathcal{U}}_0(t)\mathcal{T}\mathrm{e}^{-\frac{\mathrm{i}}{\hbar}\int_0^t \hat{\mathcal{H}}_{\mathrm{ad}}(t')\mathrm{d}t'}. \tag{3.35}$$

It is then natural to consider a series expansion of the time-ordered exponential at the first order in the adiabatic exponential

$$\begin{aligned}\hat{\mathcal{U}}(t) &\simeq \hat{\mathcal{U}}_0(t)\left(1 - \frac{\mathrm{i}}{\hbar}\int_0^t \hat{\mathcal{H}}_{\mathrm{ad}}(t')\,\mathrm{d}t'\right) \\ &= \hat{\mathcal{U}}_0(t)\left[1 - \frac{\mathrm{i}}{\hbar}\int_0^t \left(\hat{\mathcal{U}}_0^\dagger(t')\hat{\mathcal{H}}(t')\hat{\mathcal{U}}_0(t') + \mathrm{i}\hbar\dot{\hat{\mathcal{U}}}_0^\dagger(t')\hat{\mathcal{U}}_0(t')\right)\mathrm{d}t'\right].\end{aligned} \tag{3.36}$$

1 This is valid under the assumption that the levels do not cross during the dynamics.

2 To leave the Schrödinger equation invariant under a generic time-dependent transformation, $\hat{\mathcal{S}}(t)$, of the state vectors, the Hamiltonian, $\hat{\mathcal{H}}(t)$, needs to transform as

$$\hat{\mathcal{H}}'(t) = \hat{\mathcal{S}}(t)\hat{\mathcal{H}}(t)\hat{\mathcal{S}}^{-1}(t) - \mathrm{i}\hbar\dot{\hat{\mathcal{S}}}(t)\dot{\hat{\mathcal{S}}}^{-1}(t). \tag{3.33}$$

The first term in the integral is

$$\begin{aligned}\hat{\mathcal{H}}_0 &= \hat{\mathcal{U}}_0^\dagger \hat{\mathcal{H}} \hat{\mathcal{U}}_0 \\ &= \sum_{n,m} \langle \Psi_n(t)|\hat{\mathcal{H}}(t)|\Psi_m(t)\rangle \, |\Psi_n(0)\rangle\langle\Psi_m(0)| \\ &= \sum_n E_n(t) \, |\Psi_n(0)\rangle\langle\Psi_n(0)| \,,\end{aligned} \tag{3.37}$$

while the second term is

$$i\hbar\dot{\hat{\mathcal{U}}}_0^\dagger \hat{\mathcal{U}}_0 = -\hat{\mathcal{H}}_0(t) + i\hbar\dot{\lambda} \sum_{n,m} e^{i(\alpha_m - \alpha_n)} \, \langle \partial_\lambda \Psi_n(t)|\Psi_m(t)\rangle \, |\Psi_n(0)\rangle\langle\Psi_m(0)| \,. \tag{3.38}$$

The first term cancels out the $-\hat{\mathcal{H}}_0$ contribution in the second one; thus, Eq. (3.36) becomes

$$\begin{aligned}\hat{\mathcal{U}}(t) \simeq \hat{\mathcal{U}}_0(t) \Bigg[1 + |\Psi_n(0)\rangle\langle\Psi_m(0)| \times \\ \sum_{n,m} \int_0^t e^{i(\alpha_m(t') - \alpha_n(t'))} \, \langle \Psi_n(t')|\dot{\Psi}_m(t')\rangle \, dt' \Bigg] \\ = \sum_n e^{i\alpha_n} \Bigg[|\Psi_n(t)\rangle\langle\Psi_n(0)| + \\ + \sum_{m(\neq n)} \int_0^t e^{i(\alpha_m(t') - \alpha_n(t'))} \, \langle \Psi_n(t')|\dot{\Psi}_m(t')\rangle \, dt' \; |\Psi_n(t)\rangle\langle\Psi_m(0)| \Bigg] \,.\end{aligned} \tag{3.39}$$

This result is correct up to the first order in $\hat{\mathcal{H}}_{\text{ad}}$. Performing the integral in the same approximated way as in Eq. (3.14), one obtains

$$\begin{aligned}\hat{\mathcal{U}}(t) \simeq \sum_n e^{i\alpha_n} \Bigg[|\Psi_n(t)\rangle\langle\Psi_n(0)| + \\ + i\hbar\dot{\lambda} \sum_{m(\neq n)} \Bigg(e^{i(\alpha_m(t) - \alpha_n(t))} \frac{\langle \Psi_n(t)|\partial_\lambda \Psi_m(t)\rangle}{E_n(t) - E_m(t)} + \\ - e^{i(\alpha_m(0) - \alpha_n(0))} \frac{\langle \Psi_n(0)|\partial_\lambda \Psi_m(0)\rangle}{E_n(0) - E_m(0)} \Bigg) |\Psi_n(t)\rangle\langle\Psi_m(0)| \Bigg] \,,\end{aligned} \tag{3.40}$$

which is consistent with the result of the preceding Sections. Here, the explicit presence of the first-order contribution to the initial condition clearly expresses the fact that the approximated time evolution of a pure eigenstate of $\hat{\mathcal{H}}(0)$ *cannot* lead to the Thouless' state.

The three different methods outlined in Secs. 3.1.1, 3.1.2, and 3.1.3 introduce the adiabatic approximation with different levels of artificiality. In the following Section, the same approximation will be derived in a more natural way, where the relationship between the Thouless' wavefunction and the theory of adiabatic transport are evident.

3.2 THOULESS' APPROXIMATION FROM THE CONTINUITY EQUATION

In Quantum Mechanics (QM), the continuity equation is usually introduced in terms of the conservation of probability, and it is usually derived from the Schrödinger equation of a quantum wavefunction, Ψ, in an external potential, $\mathcal{V}$, multiplied by Ψ^*. For a single particle, one can write:

$$\mathrm{i}\hbar\Psi^*\frac{\partial\Psi}{\partial t} = -\frac{\hbar^2}{2m}\Psi^*\nabla^2\Psi(\mathbf{r},t) + \mathcal{V}(\mathbf{r},t)\Psi^*\Psi(\mathbf{r},t). \tag{3.41}$$

After rearranging the terms in the above equation, one arrives at

$$\frac{\partial}{\partial t}(\Psi^*\Psi) = -\frac{\hbar}{2m\mathrm{i}}\nabla\cdot(\Psi^*\nabla\Psi - \Psi\nabla\Psi^*), \tag{3.42}$$

which has the form of a continuity equation for the current density

$$\mathbf{j}(\mathbf{r},t) = \frac{\hbar}{2m\mathrm{i}}[\Psi^*(\mathbf{r},t)\nabla\Psi(\mathbf{r},t) - \Psi(\mathbf{r},t)\nabla\Psi^*(\mathbf{r},t)]. \tag{3.43}$$

It is instructive to derive the continuity equation in operatorial form and to show how it is related to Heisenberg's time-evolution and to transport theory. Since the continuity equation relates local densities and currents, it is expedient to express operators on the basis of position eigenstates, i.e. those states, $|\mathbf{r}\rangle$, such that

$$\hat{\mathbf{r}}\,|\mathbf{r}'\rangle = \mathbf{r}'\,|\mathbf{r}'\rangle\,, \qquad \langle\mathbf{r}'|\mathbf{r}''\rangle = \delta(\mathbf{r}'-\mathbf{r}''). \tag{3.44}$$

The matrix elements of the position and momentum operators between a position eigenstate and an arbitrary quantum state, $|\Psi\rangle$, are

$$\langle\mathbf{r}|\hat{\mathbf{r}}|\Psi(t)\rangle = \mathbf{r}\,\langle\mathbf{r}|\Psi(t)\rangle = \mathbf{r}\Psi(\mathbf{r},t), \tag{3.45}$$

$$\langle\mathbf{r}|\hat{\mathbf{p}}|\Psi(t)\rangle = -\mathrm{i}\hbar\nabla\,\langle\mathbf{r}|\Psi(t)\rangle = -\mathrm{i}\hbar\nabla\Psi(\mathbf{r},t), \tag{3.46}$$

where ∇ is the gradient with respect to the eigenvalue $\mathbf{r}$. A local particle density operator, $\hat{n}_{\mathbf{r}}$ can be defined in terms of its matrix elements over generic quantum states:

$$\langle\Phi(t)|\hat{n}_{\mathbf{r}}|\Psi(t)\rangle = \Phi^*(\mathbf{r},t)\Psi(\mathbf{r},t) \tag{3.47}$$

which, by inserting twice the resolution of the identity, $\mathbb{1} = \int \mathrm{d}^3r\,|\mathbf{r}\rangle\langle\mathbf{r}|$, becomes

$$\langle\Phi(t)|\hat{n}_{\mathbf{r}}|\Psi(t)\rangle = \int \mathrm{d}^3r' \int \mathrm{d}^3r''\,\langle\Phi(t)|\mathbf{r}'\rangle\,\langle\mathbf{r}'|\hat{n}_{\mathbf{r}}|\mathbf{r}''\rangle\,\langle\mathbf{r}''|\Psi(t)\rangle\,. \tag{3.48}$$

It is clear that the local density operator $\hat{n}_{\mathbf{r}}$ satisfies

$$\langle\mathbf{r}'|\hat{n}_{\mathbf{r}}|\mathbf{r}''\rangle = \delta(\mathbf{r}-\mathbf{r}')\delta(\mathbf{r}-\mathbf{r}''). \tag{3.49}$$

A working definition is thus $\hat{n}_{\mathbf{r}} = \delta(\mathbf{r}-\hat{\mathbf{r}})$. Let us now try to find a local current operator, $\hat{\mathbf{j}}_{\mathbf{r}}$: in analogy with Classical Mechanics (CM), let us define it as the (symmetrized) quantum version of the classical current $\mathbf{j} = n\mathbf{v}$, i.e. the density times the velocity. The current operator therefore reads

$$\hat{\mathbf{j}}_{\mathbf{r}} = \frac{1}{2}(\hat{n}_{\mathbf{r}}\hat{\mathbf{v}} + \hat{\mathbf{v}}\hat{n}_{\mathbf{r}}), \tag{3.50}$$

where the velocity operator is defined in order to satisfy the Ehrenfest theorem [43], and give $\langle \hat{\mathbf{v}} \rangle = \frac{\mathrm{d}\langle \hat{\mathbf{r}} \rangle}{\mathrm{d}t}$, and it is thus dependent on the form of the Hamiltonian. The divergence, $\nabla\cdot$, acts on $\hat{\mathbf{j}}_{\mathbf{r}}$ by differentiating $\hat{n}_{\mathbf{r}}$ with respect to the parameter $\mathbf{r}$:

$$\nabla \cdot \hat{\mathbf{j}}_{\mathbf{r}} = \frac{1}{2}(\nabla \hat{n}_{\mathbf{r}} \cdot \hat{\mathbf{v}} + \hat{\mathbf{v}} \cdot \nabla \hat{n}_{\mathbf{r}}). \tag{3.51}$$

In the simple case of a free particle (the generalization to arbitrary external and vector potentials is straightforward [45]), where

$$\hat{\mathcal{H}} = \frac{\hat{\mathbf{p}}^2}{2m}, \qquad \hat{\mathbf{v}} = \frac{\hat{\mathbf{p}}}{m}, \tag{3.52}$$

it immediately follows that

$$\begin{aligned} \nabla \cdot \hat{\mathbf{j}}_{\mathbf{r}} &= \frac{\mathrm{i}}{2m\hbar}[\hat{n}_{\mathbf{r}}\hat{\mathbf{p}}^2 - \hat{\mathbf{p}} \cdot (\hat{n}_{\mathbf{r}}\hat{\mathbf{p}}) + \hat{\mathbf{p}} \cdot (\hat{n}_{\mathbf{r}}\hat{\mathbf{p}}) - \hat{\mathbf{p}}^2\hat{n}_{\mathbf{r}}] \\ &= -\frac{1}{\mathrm{i}\hbar}\left[\hat{n}_{\mathbf{r}}, \hat{\mathcal{H}}\right]. \end{aligned} \tag{3.53}$$

Notice that, in the Heisenberg representation, $1/(\mathrm{i}\hbar)\left[\hat{n}_{\mathbf{r}}, \hat{\mathcal{H}}\right]$ is exactly the time-derivative of the local density operator. Thus, $\hat{n}_{\mathbf{r}}$ and $\hat{\mathbf{j}}_{\mathbf{r}}$ are related by a continuity equation, and the expression for $\nabla \cdot \hat{\mathbf{j}}_{\mathbf{r}}$ results from Heisenberg's equations of motion [43], i.e.

$$\begin{aligned} \frac{\mathrm{d}\hat{n}_{\mathbf{r}}^{(\mathrm{H})}}{\mathrm{d}t} &= \frac{1}{\mathrm{i}\hbar}\left[\hat{n}_{\mathbf{r}}^{(\mathrm{H})}, \hat{\mathcal{H}}^{(\mathrm{H})}\right] \\ &= -\nabla \cdot \hat{\mathbf{j}}_{\mathbf{r}}^{(\mathrm{H})}, \end{aligned} \tag{3.54}$$

where $\hat{A}^{(\mathrm{H})}$ denotes an operator in the Heisenberg picture. For N-electron systems, the local density can be generalized to

$$\hat{n}_{\mathbf{r}} = \sum_{i=1}^{N} \delta(\mathbf{r} - \hat{\mathbf{r}}_i), \tag{3.55}$$

so that the local current reads

$$\hat{\mathbf{j}}_{\mathbf{r}} = \frac{1}{2}\sum_{i=1}^{N}\left[\delta(\mathbf{r} - \hat{\mathbf{r}}_i)\hat{\mathbf{v}} + \hat{\mathbf{v}}\delta(\mathbf{r} - \hat{\mathbf{r}}_i)\right], \tag{3.56}$$

and $\hat{\mathbf{v}} = \sum_i \hat{\mathbf{v}}_i$ is now the many-body velocity operator. In the spirit of the relationship between the local density operator, the continuity equation, and Heisenberg's equations of motion (Eq. (3.54)), let us try to find the simplest quantum state able to fulfill a continuity equation for the *adiabatic* local density.

If $\hat{\rho}$ is the local density operator for a generic quantum system, the Heisenberg's equation of motion for $\hat{\rho}$ in the Heisenberg picture is

$$\frac{\mathrm{d}\hat{\rho}^{(\mathrm{H})}}{\mathrm{d}t} = \frac{1}{\mathrm{i}\hbar}\left[\hat{\rho}^{(\mathrm{H})}, \hat{\mathcal{H}}^{(\mathrm{H})}\right] + \left(\frac{\partial\hat{\rho}}{\partial t}\right)^{(\mathrm{H})} \tag{3.57}$$

In the case where $\hat{\rho}$ has no explicit time-dependence, Eq. (3.57) can be written in terms of the time-evolution operator as

$$\frac{\mathrm{d}}{\mathrm{d}t}\left(\hat{\mathcal{U}}^{\dagger}(t)\hat{\rho}\hat{\mathcal{U}}(t)\right) = \frac{1}{\mathrm{i}\hbar}\hat{\mathcal{U}}^{\dagger}(t)\left[\hat{\rho}, \hat{\mathcal{H}}\right]\hat{\mathcal{U}}(t). \tag{3.58}$$

In the purely adiabatic approximation, $\hat{\mathcal{U}}(t) = \hat{\mathcal{U}}_0(t)$, there are no contributions to the ground-state expectation value of the RHS of Eq. (3.58). The operator

$$\begin{aligned}\hat{\mathcal{U}}^\dagger(t)\left[\hat{\rho},\hat{\mathcal{H}}\right]\hat{\mathcal{U}}(t) &\simeq \hat{\mathcal{U}}_0^\dagger(t)\left[\hat{\rho},\hat{\mathcal{H}}\right]\hat{\mathcal{U}}_0(t)\\ &= \sum_{n,m} \mathrm{e}^{\mathrm{i}(\alpha_n(t)-\alpha_m(t))}\times\\ &\quad (E_n(t)-E_m(t))\left\langle\Psi_m(t)|\hat{\rho}|\Psi_n(t)\right\rangle|\Psi_m(0)\rangle\langle\Psi_n(0)|\end{aligned} \tag{3.59}$$

can be nonzero only off-diagonal; therefore, its ground-state expectation value is zero. Let us look for the simplest approximation for the evolution operator, $\hat{\mathcal{U}}_{\mathrm{Th}}$, able to fulfill a Heisenberg-like equation (and, after Eq. (3.54), a continuity equation) of the form

$$\frac{\mathrm{d}}{\mathrm{d}t}\left(\hat{\mathcal{U}}_0^\dagger(t)\hat{\rho}\,\hat{\mathcal{U}}_0(t)\right) = \frac{1}{\mathrm{i}\hbar}\hat{\mathcal{U}}_{\mathrm{Th}}^\dagger(t)\left[\hat{\rho},\hat{\mathcal{H}}\right]\hat{\mathcal{U}}_{\mathrm{Th}}(t). \tag{3.60}$$

Accordingly, the state $|\Psi_{\mathrm{Th}}\rangle = \hat{\mathcal{U}}_{\mathrm{Th}}|\Psi_0\rangle$, where $|\Psi_0\rangle$ is the ground state, will be the lowest order approximation of a state over which the expectation value of the current associated to $\hat{\rho}$ is nonzero.

Let us begin by computing the LHS of Eq. (3.60):

$$\frac{\mathrm{d}}{\mathrm{d}t}\left(\hat{\mathcal{U}}_0^\dagger(t)\hat{\rho}\,\hat{\mathcal{U}}_0(t)\right) = \dot{\hat{\mathcal{U}}}_0^\dagger\hat{\rho}\,\hat{\mathcal{U}}_0 + \hat{\mathcal{U}}_0^\dagger\hat{\rho}\,\dot{\hat{\mathcal{U}}}_0. \tag{3.61}$$

With $\hat{\rho}_0 = \hat{\mathcal{U}}_0^\dagger\hat{\rho}\,\hat{\mathcal{U}}_0$, one has

$$\frac{\mathrm{d}}{\mathrm{d}t}\left(\hat{\mathcal{U}}_0^\dagger(t)\hat{\rho}\,\hat{\mathcal{U}}_0(t)\right) = \dot{\hat{\mathcal{U}}}_0^\dagger\hat{\mathcal{U}}_0\hat{\rho}_0 + \hat{\rho}_0\,\hat{\mathcal{U}}_0^\dagger\dot{\hat{\mathcal{U}}}_0. \tag{3.62}$$

The expression for $\hat{\rho}_0$ is

$$\begin{aligned}\hat{\rho}_0 &= \sum_{n,m}\left\langle\Psi_n|\hat{\rho}|\Psi_m\right\rangle|\Psi_n(0)\rangle\left\langle\Psi_m(0)\right|\\ &= \sum_{n,m}\rho_{nm}|\Psi_n(0)\rangle\left\langle\Psi_m(0)\right|.\end{aligned} \tag{3.63}$$

According to Eq. (3.28), the derivative of $\hat{\mathcal{U}}_0$ reads

$$\begin{aligned}\dot{\hat{\mathcal{U}}}_0 &= \sum_n \mathrm{e}^{\mathrm{i}\alpha_n}\left(\mathrm{i}\dot{\alpha}_n|\Psi_n\rangle\left\langle\Psi_n(0)\right| + \left|\dot{\Psi}_n\right\rangle\left\langle\Psi_n(0)\right|\right)\\ &= \sum_n \mathrm{e}^{\mathrm{i}\alpha_n}\left(\frac{1}{\mathrm{i}\hbar}E_n|\Psi_n\rangle\left\langle\Psi_n(0)\right| + \left|\dot{\Psi}_n\right\rangle\left\langle\Psi_n(0)\right|\right)\end{aligned} \tag{3.64}$$

so that

$$\begin{aligned}\hat{\mathcal{U}}_0^\dagger\dot{\hat{\mathcal{U}}}_0 &= \sum_{n,m}\mathrm{e}^{\mathrm{i}(\alpha_n-\alpha_m)}\left[\frac{1}{\mathrm{i}\hbar}E_n\delta_{nm}|\Psi_m(0)\rangle\left\langle\Psi_n(0)\right| + \right.\\ &\qquad\left. + \left\langle\Psi_m\middle|\dot{\Psi}_n\right\rangle|\Psi_m(0)\rangle\left\langle\Psi_n(0)\right|\right]\\ &= \frac{1}{\mathrm{i}\hbar}\sum_n E_n(t)|\Psi_n(0)\rangle\left\langle\Psi_n(0)\right| +\\ &+ \sum_{n,m}\mathrm{e}^{\mathrm{i}(\alpha_n-\alpha_m)}\left\langle\Psi_m\middle|\dot{\Psi}_n\right\rangle|\Psi_m(0)\rangle\left\langle\Psi_n(0)\right|\\ &= \frac{1}{\mathrm{i}\hbar}\hat{\mathcal{U}}_0^\dagger\hat{\mathcal{H}}\hat{\mathcal{U}}_0 + \frac{1}{\mathrm{i}\hbar}\sum_{n,m}\mathrm{e}^{\mathrm{i}(\alpha_n-\alpha_m)}\mathrm{i}\hbar\left\langle\Psi_m\middle|\dot{\Psi}_n\right\rangle|\Psi_m(0)\rangle\left\langle\Psi_n(0)\right|\\ &= \frac{1}{\mathrm{i}\hbar}\hat{\mathcal{H}}_0 + \frac{1}{\mathrm{i}\hbar}\hat{\mathcal{Q}},\end{aligned} \tag{3.65}$$

where $\hat{\mathcal{Q}}$ remains defined in the last line. It is easy to show that $\hat{\mathcal{Q}}$ is Hermitian. The LHS of Eq. (3.60) becomes

$$\begin{aligned}\frac{\mathrm{d}}{\mathrm{d}t}\left(\hat{\mathcal{U}}_0^\dagger(t)\hat{\rho}\hat{\mathcal{U}}_0(t)\right) &= -\frac{1}{\mathrm{i}\hbar}\left(\hat{\mathcal{H}}_0+\hat{\mathcal{Q}}\right)\hat{\rho}_0+\frac{1}{\mathrm{i}\hbar}\hat{\rho}_0\left(\hat{\mathcal{H}}_0+\hat{\mathcal{Q}}\right)\\ &= \frac{1}{\mathrm{i}\hbar}[\hat{\rho}_0,\hat{\mathcal{H}}_0]+\frac{1}{\mathrm{i}\hbar}[\hat{\rho}_0,\hat{\mathcal{Q}}].\end{aligned} \tag{3.66}$$

Let us now consider the RHS of Eq. (3.60), i.e.

$$\frac{1}{\mathrm{i}\hbar}\hat{\mathcal{U}}_{\mathrm{Th}}^\dagger(t)[\hat{\rho},\hat{\mathcal{H}}]\hat{\mathcal{U}}_{\mathrm{Th}}(t).$$

One can assume that $\hat{\mathcal{U}}_{\mathrm{Th}}$ has the form

$$\hat{\mathcal{U}}_{\mathrm{Th}} = \hat{\mathcal{U}}_0+\hat{\mathcal{U}}_1, \tag{3.67}$$

To keep results up to $\mathcal{O}(\hat{\mathcal{U}}_1)$, anything of higher order shall be neglected. $\hat{\mathcal{U}}_{\mathrm{Th}}$ is required to be unitary up to $\mathcal{O}(\hat{\mathcal{U}}_1)$:

$$\begin{aligned}\hat{\mathcal{U}}_{\mathrm{Th}}^\dagger\hat{\mathcal{U}}_{\mathrm{Th}} &= \left(\hat{\mathcal{U}}_0^\dagger+\hat{\mathcal{U}}_1^\dagger\right)\left(\hat{\mathcal{U}}_0+\hat{\mathcal{U}}_1\right)\\ &= \hat{\mathcal{U}}_0^\dagger\hat{\mathcal{U}}_0+\hat{\mathcal{U}}_1^\dagger\hat{\mathcal{U}}_0+\hat{\mathcal{U}}_0^\dagger\hat{\mathcal{U}}_1+\mathcal{O}(\hat{\mathcal{U}}_1^2)\\ &= 1+\hat{\mathcal{U}}_1^\dagger\hat{\mathcal{U}}_0+\hat{\mathcal{U}}_0^\dagger\hat{\mathcal{U}}_1+\mathcal{O}(\hat{\mathcal{U}}_1^2).\end{aligned} \tag{3.68}$$

Then, $\hat{\mathcal{U}}_1^\dagger\hat{\mathcal{U}}_0 = -\hat{\mathcal{U}}_0^\dagger\hat{\mathcal{U}}_1$. Let us define the anti-Hermitian operator $\hat{\Xi} = \hat{\mathcal{U}}_0^\dagger\hat{\mathcal{U}}_1$. The RHS of Eq. (3.60) thus reads

$$\begin{aligned}\frac{1}{\mathrm{i}\hbar}\hat{\mathcal{U}}_{\mathrm{Th}}^\dagger(t)[\hat{\rho},\hat{\mathcal{H}}]\hat{\mathcal{U}}_{\mathrm{Th}}(t) &= \frac{1}{\mathrm{i}\hbar}\left(\hat{\mathcal{U}}_0^\dagger+\hat{\mathcal{U}}_1^\dagger\right)[\hat{\rho},\hat{\mathcal{H}}]\left(\hat{\mathcal{U}}_0+\hat{\mathcal{U}}_1\right)\\ &\simeq \frac{1}{\mathrm{i}\hbar}[\hat{\rho}_0,\hat{\mathcal{H}}_0]+\frac{1}{\mathrm{i}\hbar}\hat{\mathcal{U}}_1^\dagger[\hat{\rho},\hat{\mathcal{H}}]\hat{\mathcal{U}}_0+\frac{1}{\mathrm{i}\hbar}\hat{\mathcal{U}}_0^\dagger[\hat{\rho},\hat{\mathcal{H}}]\hat{\mathcal{U}}_1\\ &= \frac{1}{\mathrm{i}\hbar}[\hat{\rho}_0,\hat{\mathcal{H}}_0]+\frac{1}{\mathrm{i}\hbar}\hat{\Xi}^\dagger[\hat{\rho}_0,\hat{\mathcal{H}}_0]+\frac{1}{\mathrm{i}\hbar}[\hat{\rho}_0,\hat{\mathcal{H}}_0]\hat{\Xi}\\ &= \frac{1}{\mathrm{i}\hbar}[\hat{\rho}_0,\hat{\mathcal{H}}_0]-\frac{1}{\mathrm{i}\hbar}\hat{\Xi}[\hat{\rho}_0,\hat{\mathcal{H}}_0]+\frac{1}{\mathrm{i}\hbar}[\hat{\rho}_0,\hat{\mathcal{H}}_0]\hat{\Xi}\\ &= \frac{1}{\mathrm{i}\hbar}[\hat{\rho}_0,\hat{\mathcal{H}}_0]+\frac{1}{\mathrm{i}\hbar}[[\hat{\rho}_0,\hat{\mathcal{H}}_0],\hat{\Xi}]\end{aligned} \tag{3.69}$$

Equating Eqs. (3.66) and (3.69) yields an equation for the unknown operator $\hat{\Xi}$:

$$[\hat{\rho}_0,\hat{\mathcal{Q}}] = [[\hat{\rho}_0,\hat{\mathcal{H}}_0],\hat{\Xi}]. \tag{3.70}$$

Let us find the value of $\hat{\Xi}$ that solves this equation by plugging in the known expressions for $\hat{\rho}_0$, $\hat{\mathcal{Q}}$ and $\hat{\mathcal{H}}_0$. With $\alpha_{nm} = \alpha_n - \alpha_m$, the LHS of Eq. (3.70) is

$$\begin{aligned}[\hat{\rho}_0,\hat{\mathcal{Q}}] &= \sum_{n,m}\sum_{l,k}\rho_{nm}\mathrm{e}^{\mathrm{i}\alpha_{mn}}\mathrm{i}\hbar\mathrm{e}^{\mathrm{i}\alpha_{kl}}\langle\Psi_l|\dot{\Psi}_k\rangle\left[|\Psi_n(0)\rangle\langle\Psi_m(0)|,|\Psi_l(0)\rangle\langle\Psi_k(0)|\right]\\ &= \mathrm{i}\hbar\sum_{n,m,l}\mathrm{e}^{\mathrm{i}\alpha_{ln}}\left(\rho_{nm}\langle\Psi_m|\dot{\Psi}_l\rangle-\rho_{ml}\langle\Psi_n|\partial_\lambda\Psi_m\rangle\right)|\Psi_n(0)\rangle\langle\Psi_l(0)|\end{aligned} \tag{3.71}$$

where, in going from the first to the second line, dummy labels have been swapped to factor out $|\Psi_n(0)\rangle\langle\Psi_l(0)|$. The RHS of Eq. (3.70) is $\left[\left[\hat{\rho}_0, \hat{\mathcal{H}}_0\right], \hat{\Xi}\right]$. The first commutator is computed as

$$\begin{aligned}\left[\hat{\rho}_0, \hat{\mathcal{H}}_0\right] &= \sum_{n,m,l} \rho_{nm} e^{i\alpha_{mn}} E_l \left[|\Psi_n(0)\rangle\langle\Psi_m(0)|, |\Psi_l(0)\rangle\langle\Psi_l(0)|\right] \\ &= \sum_{n,m,l} \rho_{nm} e^{i\alpha_{mn}} E_l \left(\delta_{ml} |\Psi_n(0)\rangle\langle\Psi_l(0)| - \delta_{nl} |\Psi_l(0)\rangle\langle\Psi_m(0)|\right) \\ &= \sum_{n,m} \rho_{nm} e^{i\alpha_{mn}} \left(E_m - E_n\right) |\Psi_n(0)\rangle\langle\Psi_m(0)| \\ &= \sum_{n,m} \rho_{nm} e^{i\alpha_{mn}} \Delta_{mn} |\Psi_n(0)\rangle\langle\Psi_m(0)|,\end{aligned} \tag{3.72}$$

where the last line defines $\Delta_{mn} = E_m - E_n$. Thus, the RHS of Eq. (3.70) becomes

$$\left[\left[\hat{\rho}_0, \hat{\mathcal{H}}_0\right], \hat{\Xi}\right] = \sum_{n,m} \rho_{nm} e^{i\alpha_{mn}} \Delta_{mn} \left[|\Psi_n(0)\rangle\langle\Psi_m(0)|, \hat{\Xi}\right]. \tag{3.73}$$

The matrix elements of $\hat{\Xi}$ in the adiabatic basis at initial time, $\{|\Psi_n(0)\rangle\}$, are denoted by $\langle\Psi_n(0)|\hat{\Xi}|\Psi_m(0)\rangle = \Xi^0_{nm}$. Factoring out $|\Psi_n(0)\rangle\langle\Psi_l(0)|$, one obtains

$$\left[\left[\hat{\rho}_0, \hat{\mathcal{H}}_0\right], \hat{\Xi}\right] = \sum_{n,m,l} \left(\rho_{nm} e^{i\alpha_{mn}} \Delta_{mn} \Xi^0_{ml} - \rho_{ml} e^{i\alpha_{lm}} \Delta_{lm} \Xi^0_{nm}\right) |\Psi_n(0)\rangle\langle\Psi_l(0)| \tag{3.74}$$

Both Eqs. (3.71) and (3.74) have been cast in the form

$$\hat{A} = \sum_{n,l} A_{nl} |\Psi_n(0)\rangle\langle\Psi_l(0)|. \tag{3.75}$$

The two sides of the equation can be equal only if the matrix elements are the same on each side, i.e. if, for all n, l:

$$\begin{aligned}&i\hbar \sum_m e^{i\alpha_{ln}} \left(\rho_{nm} \langle\Psi_m|\Psi_l\rangle - \rho_{ml} \langle\Psi_n|\Psi_m\rangle\right) = \\ &\quad = \sum_m \left(\rho_{nm} e^{i\alpha_{mn}} \Delta_{mn} \Xi^0_{ml} - \rho_{ml} e^{i\alpha_{lm}} \Delta_{lm} \Xi^0_{nm}\right).\end{aligned} \tag{3.76}$$

In particular, when $n = l$:

$$\begin{aligned}&i\hbar \sum_m \left(\rho_{nm} \langle\Psi_m|\dot{\Psi}_n\rangle - \rho_{mn} \langle\Psi_n|\dot{\Psi}_m\rangle\right) = \\ &\quad = \sum_m \left(\rho_{nm} e^{i\alpha_{mn}} \Delta_{mn} \Xi^0_{mn} - \rho_{mn} e^{i\alpha_{nm}} \Delta_{nm} \Xi^0_{nm}\right).\end{aligned} \tag{3.77}$$

Since this must be true for any Hermitian operator $\hat{\rho}$, one can write

$$i\hbar \langle\Psi_m|\dot{\Psi}_n\rangle = e^{i\alpha_{mn}} \Delta_{mn} \Xi^0_{mn}, \tag{3.78}$$

that is

$$\langle\Psi_m(0)|\hat{\Xi}|\Psi_n(0)\rangle = i\hbar e^{i(\alpha_n - \alpha_m)} \frac{\langle\Psi_m|\dot{\Psi}_n\rangle}{E_m - E_n}. \tag{3.79}$$

Now, let us go back to $\hat{\mathcal{U}}_{\text{Th}} = \hat{\mathcal{U}}_0 + \hat{\mathcal{U}}_1$, with $\hat{\mathcal{U}}_1 = \hat{\mathcal{U}}_0 \hat{\Xi}$. One obtains that $\hat{\mathcal{U}}_1$ fulfills

$$\begin{aligned}\langle \Psi_m | \hat{\mathcal{U}}_1 | \Psi_n(0) \rangle &= e^{i\alpha_m} \langle \Psi_m(0) | \hat{\mathcal{U}}_0^\dagger \hat{\mathcal{U}}_1 | \Psi_n(0) \rangle \\ &= e^{i\alpha_m} \langle \Psi_m(0) | \hat{\Xi} | \Psi_n(0) \rangle \\ &= i\hbar\dot{\lambda} e^{i\alpha_n} \frac{\langle \Psi_m | \partial_\lambda \Psi_n \rangle}{E_m - E_n}.\end{aligned} \tag{3.80}$$

Finally, this means that $\hat{\mathcal{U}}_1$ takes the form

$$\hat{\mathcal{U}}_1 = i\hbar\dot{\lambda} \sum_{n,m} e^{i\alpha_n} \frac{\langle \Psi_m | \partial_\lambda \Psi_n \rangle}{E_m - E_n} |\Psi_m\rangle\langle\Psi_n(0)|, \tag{3.81}$$

so that

$$\begin{aligned}\hat{\mathcal{U}}_{\text{Th}}(t) = \sum_n e^{i\alpha_n} \Bigg[&|\Psi_n(t)\rangle\langle\Psi_n(0)| + \\ &i\hbar\dot{\lambda} \sum_{m(\neq n)} \frac{\langle \Psi_m | \partial_\lambda \Psi_n \rangle}{E_m - E_n} |\Psi_m(t)\rangle\langle\Psi_n(0)| \Bigg].\end{aligned} \tag{3.82}$$

If one takes a single particle prepared in the ground state at the initial time, $|\Psi_n(0)\rangle$, one obtains that the state evolved according to $\hat{\mathcal{U}}_{\text{Th}}$ is

$$|\Psi_{\text{Th}}\rangle = \hat{\mathcal{U}}_{\text{Th}}(t) |\Psi_0(0)\rangle \tag{3.83}$$

$$= e^{i\alpha_0} \left[|\Psi_0\rangle + i\hbar\dot{\lambda} \sum_{m(\neq 0)} \frac{\langle \Psi_m | \partial_\lambda \Psi_0 \rangle}{E_m - E_0} |\Psi_m\rangle \right], \tag{3.84}$$

which is exactly the Thouless' result already obtained in Eq. (3.16).

This proves the intimate relationship between the Thouless' solution and transport theory: the simplest adiabatic wavefunction able to sustain a current is given by Eq. (3.16); otherwise, it is not possible to satisfy a continuity equation, which is required to formalize transport phenomena.

3.3 ADIABATIC FLUX IN CONDENSED MATTER

So far, the system has been implicitly considered to be in Open Boundary Conditions (OBCs). As it is customary in condensed matter physics, unbounded bulk systems are treated in Periodic Boundary Conditions (PBCs), where a cubic supercell of volume L^3 containing N electrons is periodically repeated with period L along each Cartesian direction. The thermodynamic limit, $N \to \infty$, $L \to \infty$, with $N/L^3 = \langle n \rangle$, is understood. The many-body wavefunction fulfills Born-von Kármán PBCs. The macroscopic flux, $\mathbf{J}_Q(t)$, is the volume integral of the local current. For an electronically insulating system, it is the sum of nuclear and electronic contributions. In an *ab initio* framework, where nuclei are classical particles, while the quantum nature of electrons is taken into account, the nuclear contribution is simply a sum of ionic core charges times their velocities, i.e.

$$\mathbf{J}_Q^{(\text{nucl})}(t) = \frac{1}{L^3} \sum_{\ell=1}^{N} Z_\ell \dot{\mathbf{R}}_\ell(t), \tag{3.85}$$

where $\mathbf{R}_\ell$ and Z_ℓ are the position and the atomic number of the ℓth nucleus, respectively. The electronic contribution is the supercell volume average of Eq. (3.56) evaluated over the Thouless' wavefunction:

$$\mathbf{J}_Q^{(\mathrm{el})}(t) = -\mathrm{i}\hbar\dot{\lambda}\frac{e}{L^3}\sum_{n>0}\left(\frac{\langle\Psi_m|\partial_\lambda\Psi_0\rangle}{E_0-E_n}\langle\Psi_0|\hat{\mathbf{v}}|\Psi_n\rangle - \mathrm{cc}\right), \tag{3.86}$$

where cc stands for complex conjugate. It is interesting to notice how the sum over the excited states can be eliminated from Eq. (3.86) introducing the family of Hamiltonians, firstly introduced by Kohn [46], depending on a vector parameter, $\boldsymbol{\kappa}$ [47]:

$$\hat{\mathcal{H}}_{\boldsymbol{\kappa}\lambda} = \frac{1}{2m}\sum_{i=1}^{N_{\mathrm{el}}}|\hat{\mathbf{p}}_i + \hbar\boldsymbol{\kappa}|^2 + \hat{\mathcal{V}}_\lambda. \tag{3.87}$$

The vector parameter $\boldsymbol{\kappa}$ plays the role of a constant vector potential $\mathbf{A} = \hbar c\boldsymbol{\kappa}/e$, i.e. a pure gauge transformation [47]. The many-body velocity operator, $\hat{\mathbf{v}}$, can be thus expressed as

$$\hat{\mathbf{v}} = \frac{1}{\hbar}\partial_{\boldsymbol{\kappa}}\hat{\mathcal{H}}_{\boldsymbol{\kappa}\lambda}\Big|_{\boldsymbol{\kappa}=0}, \tag{3.88}$$

so that Eq. (3.86) reads

$$\mathbf{J}_Q^{(\mathrm{el})}(t) = -\mathrm{i}\dot{\lambda}\frac{e}{L^3}\sum_{n>0}\left(\frac{\langle\Psi_n|\partial_\lambda\Psi_0\rangle}{E_0-E_n}\langle\Psi_0|\partial_{\boldsymbol{\kappa}}\hat{\mathcal{H}}_{\boldsymbol{\kappa}\lambda}|\Psi_n\rangle - \mathrm{cc}\right). \tag{3.89}$$

From static perturbation theory, one can see that

$$|\partial_{\boldsymbol{\kappa}}\Psi_0\rangle = \sum_{n>0}|\Psi_n\rangle\frac{\langle\Psi_n|\partial_{\boldsymbol{\kappa}}\hat{\mathcal{H}}_{\boldsymbol{\kappa}\lambda}|\Psi_0\rangle}{E_0-E_n}, \tag{3.90}$$

and, by virtue of this, the sum over states disappears to leave an expression in terms of a many-body Berry phase in the $(\boldsymbol{\kappa},\lambda)$ variables [42, 47]:

$$\mathbf{J}_Q^{(\mathrm{el})}(t) = \frac{\mathrm{i}e}{L^3}\left(\langle\partial_{\boldsymbol{\kappa}}\Psi_0|\partial_\lambda\Psi_0\rangle - \langle\partial_\lambda\Psi_0|\partial_{\boldsymbol{\kappa}}\Psi_0\rangle\right). \tag{3.91}$$

The total adiabatic electric flux is thus

$$\begin{aligned}\mathbf{J}_Q(t) &= \mathbf{J}_Q^{(\mathrm{nucl})}(t) + \mathbf{J}_Q^{(\mathrm{el})}(t)\\ &= \frac{1}{L^3}\sum_{\ell=1}^{N}Z_\ell\dot{\mathbf{R}}_\ell(t) + \frac{\mathrm{i}e}{L^3}\left(\langle\partial_{\boldsymbol{\kappa}}\Psi_0|\partial_\lambda\Psi_0\rangle - \langle\partial_\lambda\Psi_0|\partial_{\boldsymbol{\kappa}}\Psi_0\rangle\right).\end{aligned} \tag{3.92}$$

3.3.1 *Theory of polarization*

The electric flux in dielectric materials is deeply connected with the macroscopic polarization, since the adiabatic electric flux is the time-derivative of the polarization, i.e.

$$\mathbf{J}_Q = \frac{\mathrm{d}\mathbf{P}}{\mathrm{d}t}. \tag{3.93}$$

As a matter of fact, it is the other way around: a polarization difference is defined as the time-integrated electric flux which, at variance with polarization,

is a measurable quantity. Let us briefly review some concepts in the theory of polarization and see how they fit in with what has been said up to now about the adiabatic electric flux.

The issue with polarization in periodic systems is that PBCs do not allow a trivial definition of the position operator since the latter, with its multiplicative action, maps vectors belonging to the Hilbert space to quantities outside of it. The controversy was solved in 1998 by Resta [48]; in that paper, a formula for (the x component of) the many-body position operator, $\hat{X}$, of the N_{el} electrons in an extended system of linear size L under PBCs was provided:

$$\langle \hat{X} \rangle = \frac{L}{2\pi} \operatorname{Im} \log \langle \Psi_0 | e^{i \frac{2\pi}{L} \hat{X}} | \Psi_0 \rangle , \tag{3.94}$$

where $|\Psi_0\rangle$ is the (possibly many-body) insulating ground state of the electrons. The electronic polarization along direction x is related to $\langle \hat{X} \rangle$ by

$$\mathsf{P}_x^{(\text{el})} = \lim_{L \to \infty} \frac{e}{2\pi} \operatorname{Im} \log \langle \Psi_0 | e^{i \frac{2\pi}{L} \hat{X}} | \Psi_0 \rangle . \tag{3.95}$$

The above statement is proved by realizing that the time-derivative of $\mathsf{P}_x^{(\text{el})}$ equates to the adiabatic electronic flux. To see that, let us compute the time-derivative of the expectation value of the position operator, i.e.

$$\frac{\mathrm{d}}{\mathrm{d}t} \langle \hat{X} \rangle = \frac{L}{2\pi} \operatorname{Im} \left(\frac{\langle \dot{\Psi}_0 | e^{i \frac{2\pi}{L} \hat{X}} | \Psi_0 \rangle}{\langle \Psi_0 | e^{i \frac{2\pi}{L} \hat{X}} | \Psi_0 \rangle} + \frac{\langle \Psi_0 | e^{i \frac{2\pi}{L} \hat{X}} | \dot{\Psi}_0 \rangle}{\langle \Psi_0 | e^{i \frac{2\pi}{L} \hat{X}} | \Psi_0 \rangle} \right) . \tag{3.96}$$

A first order approximation of $e^{i(2\pi/L)\hat{X}} |\Psi_0\rangle$ can be obtained considering the 1D Kohn Hamiltonians (cf Eq. (3.87)):

$$\hat{\mathcal{H}}(\kappa) = \frac{1}{2m} \sum_{j=1}^{N_{\text{el}}} (\hat{p}_i + \hbar\kappa)^2 + \hat{\mathcal{V}}, \tag{3.97}$$

where $\hat{\mathcal{V}}$ is the many-body potential. The ground state of $\hat{\mathcal{H}}(0)$ is $|\Psi_0\rangle$, while the state $e^{i\kappa\hat{X}} |\Psi_0\rangle$ fulfills the equation

$$\hat{\mathcal{H}}(\kappa)\, e^{i\kappa\hat{X}} |\Psi_0\rangle = E_0\, e^{i\kappa\hat{X}} |\Psi_0\rangle . \tag{3.98}$$

An eigenstate of $\hat{\mathcal{H}}(\kappa)$ must satisfy PBCs; therefore, $e^{i\kappa\hat{X}} |\Psi_0\rangle$ is an eigenstate only when κ is an integer multiple of $2\pi/L$ and, in particular, $e^{i(2\pi/L)\hat{X}} |\Psi_0\rangle$ is the ground state of $\hat{\mathcal{H}}(\kappa = 2\pi/L)$. Static perturbation theory at order $1/L$ tells us that

$$e^{i(2\pi/L)\hat{X}} |\Psi_0\rangle \simeq e^{i\gamma_L} \left(|\Psi_0\rangle - \frac{2\pi\hbar}{mL} \sum_{n(\neq 0)} \frac{\langle \Psi_n | \hat{P}_x | \Psi_0 \rangle}{E_0 - E_n} |\Psi_n\rangle \right) , \tag{3.99}$$

where $\hat{P}_x = \sum_{j=1}^{N_{\text{el}}} \hat{p}_j$ is the momentum operator, and γ_L is an arbitrary phase angle[3]. Plugging Eq. (3.99) into Eq. (3.96) yields

$$\frac{e}{L} \frac{\mathrm{d}}{\mathrm{d}t} \langle \hat{X} \rangle \simeq \frac{e\, i\hbar}{mL} \sum_{j(\neq 0)} \frac{\langle \Psi_j | \hat{P}_x | \Psi_0 \rangle}{E_0 - E_j} \langle \dot{\Psi}_0 | \Psi_j \rangle + \text{cc} \tag{3.100}$$

3 This is by no means unimportant, as the expectation value of the position operator is $\langle \hat{X} \rangle \simeq L\gamma_L/(2\pi)$. The fact that γ_L is a phase is why the polarization in extended systems is a lattice rather than a vector.

By comparing the above Equation with Eq. (3.86), and since in this case, the velocity operator is the momentum operator divided by the electronic mass, one can see the consistency with the Thouless' wavefunction [41] and the many-body generalization thereof [49]. In three spatial dimensions, the adiabatic electric flux can be thus elegantly written as

$$\mathbf{J}_Q(t) = \frac{e}{2\pi L^2}\frac{\mathrm{d}}{\mathrm{d}t}\lim_{L\to\infty}\operatorname{Im}\log \mathfrak{z}(t), \tag{3.101}$$

where the quantity $\mathfrak{z}(t)$ is the Resta-Sorella marker, a complex vector that discriminates whether the system is insulating or metallic [50]. Each Cartesian component of $\mathfrak{z}$, denoted by the greek label α, reads

$$\mathfrak{z}_\alpha(t) = \langle\Psi_0(t)|\exp\left\{\mathrm{i}\frac{2\pi}{L}\left(\sum_{\ell=1}^{N} Z_\ell R_{\ell,\alpha}(t) - 2\sum_{j=1}^{N_{\mathrm{el}}}\hat{r}_{j,\alpha}\right)\right\}|\Psi_0(t)\rangle\,. \tag{3.102}$$

The Resta-Sorella marker considers both electronic and nuclear contributions, as one can see from the sums over both nuclei and electrons in the above Equation. The sheet of the Im log function, which features a branch-cut singularity in the complex plane, is chosen so that $\mathbf{J}_Q$ is continuous in time.

A triplet of phase angles,

$$\boldsymbol{\gamma}(t) = \lim_{L\to\infty}\operatorname{Im}\log \mathfrak{z}(t), \tag{3.103}$$

is thus defined, and its electronic component is known as the *single-point Berry phase* [48]. In terms of $\boldsymbol{\gamma}(t)$, the electric flux has the compact form [51]

$$\mathbf{J}_Q(t) = \frac{e}{2\pi L^2}\dot{\boldsymbol{\gamma}}(t). \tag{3.104}$$

The dipole displaced along a trajectory of the system, i.e.,

$$\boldsymbol{\Delta\mu}(t) = L^3\int_0^t \mathbf{J}_Q(t')\,\mathrm{d}t'\,, \tag{3.105}$$

is thus given by

$$\boldsymbol{\Delta\mu}(t) = eL\frac{\boldsymbol{\Delta\gamma}(t)}{2\pi}, \tag{3.106}$$

with $\boldsymbol{\Delta\gamma}(t) = \boldsymbol{\gamma}(t) - \boldsymbol{\gamma}(0)$. Eq. (3.106) says that, as a consequence of the adiabatic evolution of the system, the displaced dipole is proportional to the vector of accumulated phase angles—one component per Cartesian direction. Pictorially, $\Delta\gamma_\alpha(t)$ represents the angle spanned by $\mathfrak{z}_\alpha$ in the complex plane, and $\Delta\gamma_\alpha(t)/(2\pi)$ is the number (in general noninteger) of rotations that $\mathfrak{z}_\alpha$ makes around the origin. Suppose the adiabatic ground state returns to itself after a time τ. In that case, $|\Psi_0(\tau)\rangle = |\Psi_0(0)\rangle$, the system's evolution is cyclic, and the accumulated angle is an integer multiple of 2π; therefore, the transported charge is an integer multiple of the elementary charge. The two scenarios—the case of a generic trajectory, and the one where the trajectory is cyclic—are visualized in Figure 3.1: on the one hand (a), a general dynamics of the system traces open paths in the complex plane; on the other (b), the same initial and final adiabatic ground states imply that also $\mathfrak{z}$ returns to itself. The latter situation defines the number of windings around the origin of the complex plane as a topological invariant, since deforming the path traced by

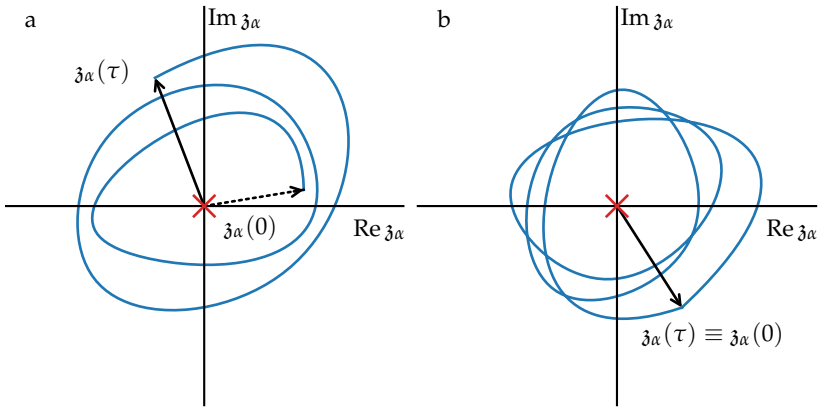

Figure 3.1: Sketch of the path drawn by $\mathfrak{z}_\alpha$ in the complex plane during the dynamics. (a) For a general nuclear trajectory, the path is open. (b) If the initial and final configurations of the nuclei are the same, then also $\mathfrak{z}$ returns to itself: the path in the complex plane is closed.

$\mathfrak{z}$ does not change its *winding number*, provided that the path itself does not *cross* the origin. This condition, i.e., $|\mathfrak{z}_\alpha(t)| \neq 0$, for all α and each t, amounts to saying that the system stays insulating during the entire dynamics [50, 51]. In fact, according to the theory of the insulating state, $\mathfrak{z}$ is related to whether the system is insulating or metallic, its modulus tending to 1 from below in insulators, and to 0 from above in metals, up to the leading order in $1/L$ [52].

3.3.2 *Adiabatic flux in AIMD*

In Ab Initio Molecular Dynamics (AIMD), where the adiabatic limit is enforced by the Born-Oppenheimer approximation, the nuclei are classical particles subject to Newton's equations, and the forces are computed via the Hellmann-Feynman theorem [53, 54] from a time-independent Schrödinger equation. It is customary to compute the adiabatic electric flux exploiting codes that implement polarization theory or Density Functional Perturbation Theory (DFPT) [55]. In this framework, the polarization depends parametrically on time through the nuclear positions; one can thus apply the chain rule to Eq. (3.93) to obtain

$$\mathbf{J}_Q(t) = \frac{e}{L^3} \sum_{\ell=1}^{N} \mathbf{Z}^\star_\ell(t) \cdot \dot{\mathbf{R}}(t). \tag{3.107}$$

The quantity $\mathbf{Z}^\star_\ell$, whose components $eZ^\star_{\ell,\alpha\beta} = L^3 \partial P_\alpha / \partial R_{\ell,\beta}$ represent the effective charge moved in the Cartesian direction α in response to an infinitesimal displacement of the ℓth nucleus in direction β, is called Born Effective Charge (BEC) tensor. It takes into account both the nuclear contribution, trivially given by the motion of the point charge associated with the core, and the change in electronic polarization due to the nuclear displacement.

From a practical standpoint, BECs are computed at a suitable sampling rate along the system's dynamics as a post-processing stage, once the dynamical trajectory is already obtained. From the time series of the BECs and the velocities

of the nuclei, one can compute the adiabatic electric flux according to Eq. (3.107). In the thermodynamic limit, Eqs. (3.107) and (3.104) must be equivalent. Still, only the former is manifestly additive, i.e. it can be written as a sum over contributions due to single nuclei. Additivity can be recovered by noticing that, while $\boldsymbol{\gamma}$ is not additive, its derivative is, as a consequence of linear response: the total flux is the sum of the fluxes due to each nucleus, one at a time [51]. One can thus define quantities

$$\dot{\boldsymbol{\gamma}}_\ell(t) = \frac{2\pi}{L}\mathbf{Z}^\star_\ell(t)\cdot\dot{\mathbf{R}}_\ell(t), \tag{3.108}$$

$$\boldsymbol{\gamma}_\ell(t) = \int_0^t \dot{\boldsymbol{\gamma}}_\ell(t')\,\mathrm{d}t' \tag{3.109}$$

such that $\boldsymbol{\gamma}_\ell(\tau) - \boldsymbol{\gamma}_\ell(0) = \sum_{\ell=1}^N \boldsymbol{\gamma}_\ell(\tau)$, so that the triplet of total accumulated phase angles is decomposed into the sum of the angles accumulated by each nucleus.

3.4 IONIC CONDUCTIVITY

The central quantity in ionic transport is the ionic conductivity, σ, the GK transport coefficient which relates the expectation value of the nonequilibrium electric flux due to a gradient of electric potential in an electronic insulator. The GK formula of σ for an isotropic system in a cubic box of side L is

$$\sigma = \frac{L^3}{3k_\mathrm{B}T}\int_0^\infty \left\langle \mathbf{J}_Q(t)\cdot\mathbf{J}_Q(0)\right\rangle \mathrm{d}t\,, \tag{3.110}$$

where the expectation value in Eq. (3.110) is over an equilibrium ensemble. This expression can be recast to a HE formula (cf Eq. (1.52)):

$$\sigma = \frac{1}{3L^3k_\mathrm{B}T}\lim_{t\to\infty}\frac{\left\langle|\boldsymbol{\Delta\mu}(t)|^2\right\rangle}{2t}, \tag{3.111}$$

in terms of the integrated dipole accumulated along the time-evolution of $\mathbf{J}_Q(t)$. Ionic conductivity can be computed from EMD simulations by sampling the electric flux or the polarization along the system's trajectory and then using the respective equation involving the chosen quantity. The ionic conductivity can also be expressed in terms of phase angles according to Eq. (3.106):

$$\sigma = \frac{e^2}{6\pi L^2k_\mathrm{B}T}\lim_{t\to\infty}\frac{\left\langle|\boldsymbol{\Delta\gamma}(t)|^2\right\rangle}{2t}. \tag{3.112}$$

Among other things, in the next Chapter it will be shown how some topological properties of insulating systems allow to easily compute Eq. (3.112) starting from integer constant charges associated with the atoms in the system, rather than explicitly integrating computing the variance of the accumulated dipole obtained through BECs.

4 TOPOLOGY AND IONIC TRANSPORT

Ever since topology entered the field of condensed matter physics, it has proven to be a powerful tool in the classification of exotic states of matter. Much progress has been made in the past decades in understanding how topological invariants can be computed from the electronic structure of crystalline materials, and it was recently made clear how topological effects are not an exception, but rather something that can be found in most known materials [56]. Static topological effects have been thoroughly investigated [57–62]; at the same time, dynamical effects were studied ever since the seminal works of Thouless and Niu [41, 49], with the introduction of the concept of Thouless' pumps. Despite extensive works in the theory of topological quantum numbers related to the adiabatic evolution of a quantum state (see, e.g., Refs. 63 and 64), the link between topology and the charge transport properties of ionic conductors has been only recently established [31, 51, 65, 66].

The appearance of integer numbers in charge transport has a long history, as it dates back to Faraday's experiments in the 1830s. Verbatim from Ref. 51, Faraday's first law of electrolysis can be rephrased in modern language in this fashion: *when a macroscopic number N of nuclei of a given chemical species passes from one electrode to the other, the transported electrical charge is an integer multiple of N times e*. The important point here is that, in an electrolytic cell containing a nonmetallic compound, only an integer number of elementary charges can be adiabatically transported over a macroscopic distance and, as such, be measured, and not a fractional charge. It is thus experimentally possible to measure an integer charge pertaining to each member of the chemical species at hand. It is important to notice that the measurement is intrinsically dynamical, in that it requires the motion of nuclei across a macroscopic distance, given by the size of the electrolytic cell. The integer charge measured by Faraday is an example of Oxidation State (OS). In chemistry, OSs are integer numbers widely used to describe redox reactions, electrolysis, and many electrochemical processes. In spite of their fundamental nature, they have long eluded a rigorous quantum-mechanical interpretation. In fact, they are usually determined according to an agreed set of rules [67, 68], their simplest—and official—definition being, for an atom, *the charge of this atom after ionic approximation of its heteronuclear bonds* (verbatim from the IUPAC Gold Book [69]). Yet, being measurable quantities, at least in the electrolytic cell setup, they are expected to have a rigorous quantum-mechanical definition which must reflect the fact that ionic conductors carry integer charges over macroscopic distances.

In this Chapter, I shall discuss how OSs can indeed be defined quantum-mechanically thanks to topological arguments (Sec. 4.2), and how this is related to the theory of charge transport in ionic conductors (Sec. 4.3). Before doing so, it is necessary to introduce some jargon and to make some considerations on the topology of the paths generated by the adiabatic dynamics of the nuclei in an electrolyte solution. The content of this Chapter is mostly an adaptation

of Ref. 31 and Ref. 66, works I coauthored together with my Ph.D. advisors Stefano Baroni and Federico Grasselli.

4.1 TOPOLOGY OF THE ATOMIC CONFIGURATION SPACE

4.1.1 *Paths and topology*

The space of all the coordinates of the nuclei—namely, the Atomic Configuration Space (ACS)—is topologically equivalent to a $3N$-dimensional torus, since we adopt PBCs in all the three Cartesian coordinates of each of the N nuclei, independently. We are interested in those paths whose endpoints are a periodic image of one another since it is for these that the adiabatic ground state returns to itself and the theorems on the quantization of charge can be invoked. We focus on *adiabatic paths*, i.e. paths in the ACS that never cross a metallic region, in order to keep the evolution adiabatic. In this light, it is expedient to define the *adiabatic space* as the ACS deprived of the regions where the system is metallic. Different types of charge transport in insulators arise, depending on whether the classification of paths of the adiabatic space coincides with that of the total ACS, and, if they differ, how they do so. We outline the characteristics of these paths with reference to the situations sketched in Fig. 4.1. If each path whose endpoints are replicas of one another can be uniquely specified, up to deformations which do not imply cuts or "exiting the space", by the tuple of $3N$ integers, $\mathbf{n} = (n_{1x}, n_{1y}, \ldots, n_{Nz})$, representing the number of cells spanned by each atom in each Cartesian direction, then Strong Adiabaticity (SA) holds in the adiabatic space [31, 65]. This means that a trivial loop in the ACS (i.e. a path whose endpoints belong to the same cell and coincide, and is thus characterized by $\mathbf{n} = \mathbf{0}$) is also a trivial loop in the adiabatic space, and can be shrunk to a point without crossing any metallic region. The easiest situation is whenever there are no metallic regions for any configuration of the nuclei: this is the case sketched in a two-dimensional ACS in Fig. 4.1a. Notice that, in higher dimensions, the complete insulation of the ACS is not necessary for SA to hold: for instance, removing a metallic point (or even a ball) from a 3-dimensional torus preserves SA of the resulting adiabatic space.

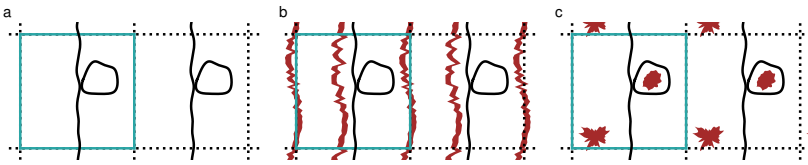

Figure 4.1: Different types of ACSs, according to the metallic regions they feature. The central cell is framed in light blue, while the dotted lines represent the sides of one of its periodic replicas. Metallic regions are depicted in dark red. The black lines are paths in the ACS. (a) An ACS where SA holds everywhere. (b) Metallic walls surround an adiabatic domain, where SA holds locally. (c) Here, SA is broken, in that there exist trivial loops that encircle metallic regions.

In other cases, there might be metallic regions in the ACS that partition the full adiabatic space into disconnected adiabatic *domains* [31], playing the role of "walls" that the system would need to cross if it were to pass from one

adiabatic domain to the other. The classifications of paths on the ACS and on the adiabatic space no longer coincide, since paths with some **n** are not allowed in the entire adiabatic space, as they would imply crossing a metallic region. Nevertheless, if all the adiabatic trivial loops can still be shrunk to a point without closing the gap, the same considerations made above for the case where SA holds everywhere are still valid *within a given adiabatic domain* [31]. This situation is sketched in Fig. 4.1b. Here, SA holds in each adiabatic domain, but not on the whole ACS, due to the presence of metallic walls.

The situation is instead totally different whenever there exist adiabatic trivial loops in the ACS which, despite entirely belonging to the adiabatic space, cannot be shrunk to a point without crossing a metallic region [31, 65]. Here, adiabatic paths that are connected are not necessarily equivalent to one another, which implies that two paths characterized by the same tuple **n** may be topologically different. This is shown in Fig. 4.1c. Here, SA does not hold anymore.

Whether SA holds or not has profound consequences on the definition of OS and on the transport properties of insulating systems. In the following Section, we shall see that only when SA is not dropped the quantum theory of charge transport can be reconciled with Faraday's description, where each atom can be endowed with a well-defined integer charge, and this fact manifests itself in the ionic transport properties of the system [31, 65].

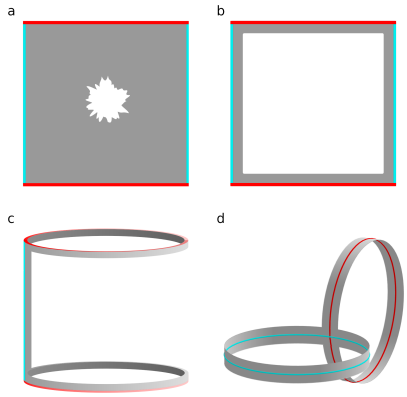

Figure 4.2: A punctured 2-torus retracts to a figure eight. (a) The punctured 2-torus is represented as a square whose opposite sides are identified (as in PBCs) with a hole in it. (b) Since we are interested in the topology of the manifold, the hole can be continuously expanded. (c) The blue sides are glued together. (d) Finally, the red sides are glued together. The resulting manifold, whose fundamental group is no longer Abelian, can be retracted to a "figure eight", ◯-◯. Its fundamental group, $\mathbb{Z} * \mathbb{Z}$ differs from that of the 2-torus, $\mathbb{Z} \times \mathbb{Z}$. Nevertheless, its abelianization, i.e. the first homology class, is $\mathbb{Z} \times \mathbb{Z}$, and the "elementary loops" ◯ and ◯ coincide with those of the torus. In this way, charge transport properties are not altered by a single puncture of the 2-torus.

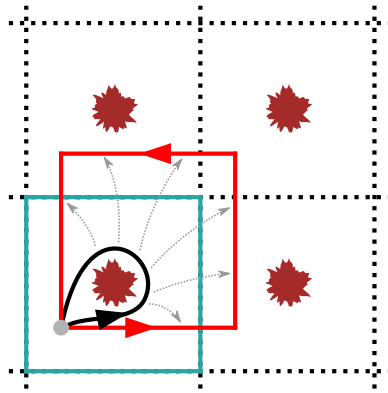

Figure 4.3: Sketch of a 2-dimensional ACS isomorphic to a punctured torus. A single hole is sufficient to change the topological properties of the manifold, as it changes, e.g., its fundamental group (see Fig. 4.2). Nonetheless, the black path can be continuously deformed (the deformation map is represented by the gray, dotted, arrows) to the red one without closing the gap: it is evident that the charge transported along the latter is zero since the charges transported along each side of the square cancel out with those transported along the opposite side, which is just the same path traversed in reverse.

4.1.2 *Homotopy and homology in charge transport*

Two given paths are considered topologically equivalent, or *homotopic*, if they can be deformed into one another neither cutting nor exiting the manifold they belong to [70]. Closed paths starting and ending at the same (base) point—i.e. loops—can be classified accordingly, and the set of the equivalence classes of loops under homotopy, together with the operation of concatenation, is called the *fundamental group* of the manifold, which incorporates information on the presence of important features (like "holes" or "handles") of the manifold [70]. The fundamental group can be commutative (*Abelian*) or not. For instance, the fundamental group of the $3N$-dimensional torus is Abelian, since it is isomorphic to $\mathbb{Z}^{3N}$. Nonetheless, when we "puncture" it (as it happens when we remove metallic regions from the ACS), the fundamental group of the new manifold (that we named *adiabatic space* in Sec. 4.1.1) may change [70], which is exactly what happens when SA is broken [31]. This new fundamental group may be no longer Abelian. In spite of this, the total transported charge is expressed as a line integral that can be split into the *commutative* sum of integrals, each computed over a piece of the original path. Therefore, it is not strictly necessary that two loops are homotopic to transport the same integer charge. It is sufficient that they are *homologous*, i.e. that they share the same, possibly repeated, "elementary loops", with no further restriction on the sequence in which these are taken. More rigorously, to understand if two paths transport the same charge, one must inspect whether they are represented by the same element of the so-called *first homology group*, which is the "abelianization" of the fundamental group [70]. An example of the difference between homotopy and homology is shown in Figs. 4.2 and 4.3; a single metallic region in a 2-dimensional ACS in PBCs is enough to change its

topology from a simple torus to a "figure-eight" (see Fig. 4.2): the fundamental group changes from the Cartesian product $\mathbb{Z} \times \mathbb{Z}$, which is Abelian, to the free product $\mathbb{Z} * \mathbb{Z}$, which is not Abelian[1]. Nonetheless, the first homology group remains the same, and the transported charge along a path that encircles the metallic region is zero, as it can be deformed to a squared path whose opposing faces transport charges which manifestly cancel out with one another, as shown in Fig. 4.3. The black loop and any trivial loop that shrinks to the gray point are homologous, despite they are not homotopic, as they cannot be continuously deformed into one another without crossing the metallic region. Notice that two points need to be removed from a 2-torus to change the first homology group, and make it nontrivial from the transport point of view, as reported below (Sec. 4.4.2.1) for the linear H_3^+ cation discussed in Ref. 31.

4.2 TOPOLOGICAL FOUNDATION OF THE OXIDATION STATES

We are now in a position to characterize how integer numbers can be associated with nuclei in the system according to topology.

4.2.1 *Pendry-Hodges* Gedankenexperiment

Under the condition of SA in the whole ACS, let us now characterize some integer charges that can be associated with the nuclei in the system. We follow a *Gedankenexperiment*, proposed for the first time by Pendry and Hodges [71]. We displace a single nucleus, say the ℓth, from its initial position to the same position in an adjacent replica cell. To perform this task, the other ions are allowed to move out of the way provided their final positions coincide with the initial ones and the electronic gap never closes along the path [51, 65]. Thouless' theorem [41] (and the many-body generalization thereof [49]) ensures that the total charge displaced along this trajectory is an integer multiple of the elementary charge: as it is also expressed by Eq. (3.106) at page 51 and the subsequent discussion in the case of a cyclic path, this integer number is the winding number of $\jmath_\alpha$ around the origin of the complex plane (with α the Cartesian direction around which the nucleus has moved). Let $q_{\ell,\alpha}$ be this number, which we call the *topological charge* of the ℓth atom along direction α. We remark that, for any *static* configuration taken from such artificial evolution, these topological charges cannot be defined. A necessary ingredient for their characterization is the *dynamic* displacement of the selected atom.

An operation of this kind was used by Jiang *et al.* [72] in the case of crystalline solids, where the system is periodic and lattice translations bear physical meaning (see also Sec. 4.4.1). More generally, the values of the topological charges are independent of the macroscopic size of the system closed under PBCs. This validates the procedure also for disordered systems [65]. Moreover, in an electrolytic cell, it is possible to map the physical system to a spatially periodic one, as the electrodes are connected to one another by a wire [51].

1 $\mathbb{Z} \times \mathbb{Z}$ or, equivalently, $\mathbb{Z}^2$, is the group of ordered pairs with the commutative operation of sum. It is Abelian, since $(n, m) + (p, q) \equiv (p + n, q + m) = (p, q) + (n, m)$. Instead, the free product $\mathbb{Z} * \mathbb{Z}$ is for instance represented by the group of two letters (and their inverse), with the noncommutative operation of juxtaposition, where order matters, as in natural language, where being "OK" differs from being "KO"!

4.2.2 *Oxidation states under strong adiabaticity*

In order to establish an equivalence between topological charges and OSs, three features ascribed to the latter must occur in $\{q_{\ell,\alpha}\}$:

i. the topological charges have to be path-independent;

ii. their value must coincide for equivalent atoms;

iii. they must be *isotropic*, i.e. independent of the specific Cartesian direction the atom is moved in.

The first condition is easily proved under SA: consider two different paths having the same endpoints; by the very definition of SA, two such paths can be deformed into one another without ever leaving the insulating state, i.e. without any component of $\boldsymbol{\mathfrak{z}}$ passing through the origin of the complex plane. The second condition can be proved by invoking the additivity of integrals [51, 65]: take any two nuclei, labeled ℓ' and ℓ'', of the same species S, i.e. with the same atomic number, Z; the phases, separately accumulated by each of them in a cyclic path that brings them to their replica in the adjacent position along Cartesian direction α, yield topological charges $q_{\ell',\alpha}$ and $q_{\ell'',\alpha}$. Since SA holds, the initial positions of the two nuclei can be exchanged without crossing a metallic state. Let the nucleus ℓ'

i. exchange position with ℓ'';

ii. be transported to its periodic replica;

iii. exchange positions again with the replica of ℓ'' belonging to the same cell where ℓ' is found after step *ii*.

In this path, the nucleus ℓ' transports a net charge equal to $q_{\ell'',\alpha}$, since the first particle exchange—step *i*—cancels out with the second—step *iii*. At the same time, this path shares the same endpoints with the paths where only ℓ' is moved to its periodic replica, where a charge equal to $q_{\ell',\alpha}$ is transported. Therefore, $q_{\ell',\alpha} = q_{\ell'',\alpha}$ and the topological charge only depends upon the nuclear species, i.e. $q_{\ell',\alpha} = q_{S(\ell'),\alpha}$. The third condition, isotropy, is proved by first noticing that, under SA, the dipole displaced along a supercell vector is parallel to the displacement vector [72]; then, the result simply follows from additivity by equating the dipoles displaced by L along any two Cartesian directions in sequence, say $\mathbf{x} = (1,0,0)$ and $\mathbf{y} = (0,1,0)$, to the dipole displaced along the sum of the two directions, i.e. $(1,1,0)$. We conclude that $q_{\ell,\alpha} = q_\ell$ and $q_{\ell'} = q_{\ell''}$. In this way, we proved that the set of topological charges $\{q_\ell\}$ meet all the requirements for what chemistry would call OSs of the chemical species in the ionic conductor.

A demonstration of the quantization of the charge carried by nuclei in an emblematic liquid electrolyte is shown in Ref. 65 and rediscussed here. A system of molten KCl is modeled through a 64-atom—32 per species—cubic simulation cell with a side $L = 14.07\,\text{Å}$. Nuclei are described as classical particles, while the quantum nature of electrons is included in a mean-field sense through Density Functional Theory (DFT) in the Perdew-Burke-Ernzerhof (PBE) flavor [73].

A configuration is drawn from an AIMD simulation equilibrated at 1200 K and used as a reference. From this configuration, the topological OSs are measured

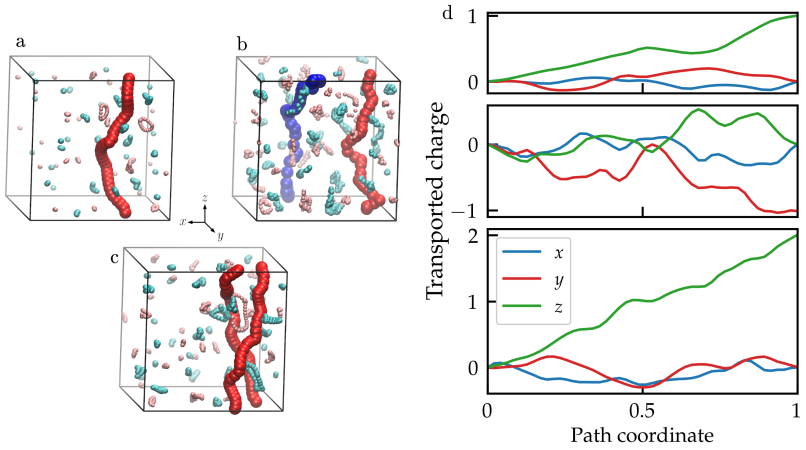

Figure 4.4: Pendry-Hodges *Gedankenexperiment* under SA. In the simulation cell, there is a stoichiometric melt of 32 K and 32 Cl atoms. K and Cl nuclei are the pink and cyan spheres, respectively. The larger spheres are the nuclei in evidence. (a-c) Periodic Minimum Energy Paths (MEPs) of a K nucleus (in red) in the z direction (a); of a cation along $\mathbf{z}$ (in red) and of an anion along $\mathbf{y}$ and $\mathbf{z}$ (in blue) (b); of two cations along $\mathbf{z}$ with an interchange between the two. In panel (d), the charge transported along each direction in the three paths is shown in units of the elementary charge. The path coordinate goes from 0 at the initial configuration to 1 at the final one.

via an implementation of the Pendry-Hodges *Gedankenexperiment*. Different nuclei are randomly chosen and displaced from their initial position to a nearby periodic cell along MEPs, i.e. with the other atoms moving out of the way to minimize the total energy of the system via the nudged elastic bands method [74]. The displaced charge is obtained by integrating the electric flux as given by Eq. (3.107), with the BECs being computed at each step of the trajectory via DFPT [55]. Three versions of this experiment are carried out, as illustrated in Fig. 4.4 by the MEPs in the simulation cell (left panels) and a plot of the respective transported charges (right panels): the displacement of a single K nucleus to one of its periodic images (Fig. 4.4a,d); the displacement of a K nucleus to its replica in direction $\mathbf{z}$, and a Cl nucleus to its replica in the cell in direction $\mathbf{z}+\mathbf{y}$ at the same time (Fig. 4.4b,d); the displacements of two different K nuclei in direction $\mathbf{z}$ at the same time with inversion of their final positions—i.e. the former ends in the periodic replica of the initial position of the latter, and vice versa (Fig. 4.4c,d). The experiments confirm what was said above: as one would expect from chemistry, K nuclei displace a charge equal to $+e$, while Cl nuclei $-e$, in whatever direction they are moved. This means that $q_{\mathrm{K}} = +1$, and $q_{\mathrm{Cl}} = -1$. The charge transported along the directions other than the one where motion happened are exactly zero. Furthermore, charge displacement is additive: when a pair of K and Cl atoms is moved in the same direction, there is no net charge transport. The case where the two nuclei are moved and their positions interchanged is also revealing: while each of the two paths alone is not periodic, their concatenation is, since it is the displacement of a nucleus to its periodic replica two cells apart, rather than one. Each of the

two displacements would carry two elementary charges over a length of two sides of the cell, resulting in a charge of $4e$ for the cyclic path, i.e. $2e$ for half the path, when positions are interchanged.

4.3 TOPOLOGICAL CHARGES AND GAUGE INVARIANCE OF IONIC TRANSPORT

The topological nature of OSs has deep consequences on ionic transport when combined with the gauge invariance of transport coefficients [51, 65]. The quantity of interest is the ionic conductivity, σ, whose expression, given by Eq. (3.112), is reported here for convenience:

$$\sigma = \frac{e^2}{6\pi L^2 k_B T} \lim_{t\to\infty} \frac{\langle |\boldsymbol{\Delta\gamma}(t)|^2 \rangle}{2t}.$$

Combining Eq. (3.109) and (3.112), the latter becomes

$$\sigma = \frac{e^2}{6\pi L^2 k_B T} \lim_{t\to\infty} \frac{\langle |\sum_{\ell=1}^{N} \boldsymbol{\gamma}_\ell(t)|^2 \rangle}{2t} \tag{4.1}$$

According to the gauge invariance of transport coefficients reviewed in Sec. 1.4, any two expressions of the electric dipole differing by a bounded vector yield the same value of ionic conductivity. Let us now prove that, under SA, the displaced dipole defined from the OSs of the atoms in the system, i.e.

$$\begin{aligned} \boldsymbol{\Delta\mu}'(t) &= \sum_{\ell=1}^{N} e\, q_\ell \int_0^t \dot{\mathbf{R}}_\ell(t')\, \mathrm{d}t', \\ &= \frac{eL}{2\pi} \sum_{\ell=1}^{N} \boldsymbol{\gamma}'_\ell(t), \end{aligned} \tag{4.2}$$

where $\boldsymbol{\gamma}'_\ell(t)$ is defined by the second line, yields the same value of σ as the fully quantum-mechanical definition based on Equation (4.1), which employs time-dependent BEC tensors. In formulæ:

$$\lim_{t\to\infty} \frac{\langle |\boldsymbol{\Delta\mu}(t)|^2 \rangle}{2t} = \lim_{t\to\infty} \frac{\langle |\boldsymbol{\Delta\mu}'(t)|^2 \rangle}{2t}, \tag{4.3}$$

which is to say $\sigma = \sigma'$ [65, 66].

The proof goes as follows: let us consider Eq. (4.1); after a long enough time t, which is implicit in the $t \to \infty$ limit, the angles $\boldsymbol{\Delta\gamma}(t)$ accumulated between the initial and final configurations, respectively $\{\mathbf{R}_\ell(0)\}$ and $\{\mathbf{R}_\ell(t)\}$, will be much larger than 2π. By the same token, the nuclei are expected to be in different periodic cells with respect to the one they started in. Given the final configuration, one could always imagine artificially moving each of the nuclei from $\{\mathbf{R}_\ell(t)\}$ to the periodic replica of $\{\mathbf{R}_\ell(0)\}$ in the same cell they are placed at time t. Let us indicate with $\boldsymbol{\delta\gamma}$ the additional phase accumulated during this last portion of trajectory; since it results from displacing all the nuclei within the same cell, it is assured that $\delta\gamma_\alpha$ has an upper bound. The trajectory defined in this way is periodic in PBCs, and therefore the transported charge is an integer multiple of e. From the definition of $\boldsymbol{\gamma}_\ell$ of Eq. (3.109), it follows that each nucleus transports exactly q_ℓ elementary charges. It is precisely the

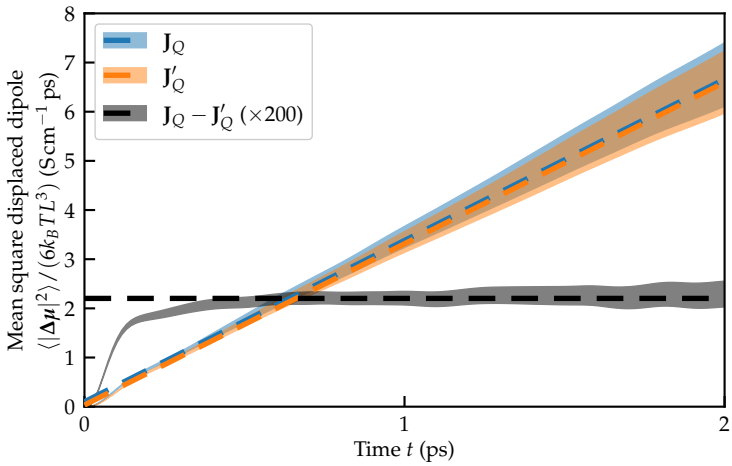

Figure 4.5: Mean Square Displaced Dipole (MSDD) of stoichiometric KCl computed with different definitions of the electric flux. Both the exact electric flux and the topological flux yield the same ionic conductivity, as given by Eq. (4.3).

same as if the phases accumulated by each nucleus had been computed as the quantities $\boldsymbol{\gamma}'_\ell(t)$ appearing in Eq. (4.2), i.e.[2]

$$\boldsymbol{\gamma}'_\ell(t) = \frac{2\pi}{L} q_\ell \mathbf{R}_\ell(t), \tag{4.4}$$

their sum being denoted by $\Delta\boldsymbol{\gamma}'(t)$; i.e. it is equivalent to computing the ionic conductivity using $\Delta\boldsymbol{\mu}'(t)$.

The ionic conductivity computed with $\Delta\boldsymbol{\gamma}'(t) = \Delta\boldsymbol{\gamma}(t) + \delta\boldsymbol{\gamma}$ reads

$$\sigma' = \frac{e}{3L^2 k_B T} \lim_{t\to\infty} \frac{1}{2t} \left[\left\langle \left| \frac{\Delta\boldsymbol{\gamma}(t)}{2\pi} \right|^2 \right\rangle + \left\langle \left| \frac{\delta\boldsymbol{\gamma}(t)}{2\pi} \right|^2 \right\rangle + 2 \left\langle \frac{\Delta\boldsymbol{\gamma}(t) \cdot \delta\boldsymbol{\gamma}(t)}{4\pi^2} \right\rangle \right]. \tag{4.5}$$

For long times, each $\Delta\gamma_\alpha$ is much larger than $\delta\gamma_\alpha$, which is a bounded quantity: we conclude that the second and third terms in Eq. (4.5) do not contribute. This long-time limit may also be probed in general by inspecting whether $|\Delta\boldsymbol{\gamma}| \gg 2\pi$. This proves the theorem of Eq. (4.3). This is also demonstrated numerically for a KCl stoichiometric melt, as shown in Fig. 4.5. The MSDD computed both via Eq. (3.106) and Eq. (4.2) as a function of time have compatible slopes for long enough time, indicating the ionic conductivity computed from them is the same [65, 66].

In this Section, we have illustrated how, under SA, each nucleus carries an integer charge over macroscopic distances which can uniquely be identified with the atomic OS of its species. The OS of a given chemical species is the same for every nucleus of that species; moreover, OSs are additive and independent of atomic positions. The consequence of these facts is that the ionic conductivity

2 The position vector here is actually the integral of the velocity, $\mathbf{R}_\ell(t) = \int_0^t \mathbf{V}_\ell(\tau)\,\mathrm{d}\tau$, in order to avoid the wrapping of atomic coordinates due to PBCs.

of the material can be computed from the dipole displacement given by the sum over nuclei of the atomic OSs times their velocities. Charge transport is purely convective; the only mechanism by which charge can be transported is mass diffusion. This transport regime is referred to as *trivial*.

4.3.1 *Polarization and Wannier Functions*

In the case of independent (e.g., Kohn-Sham) electrons, the insulating singlet ground state of a system of N nuclei and N_{el} electrons can be written as a Slater determinant of $N_{\mathrm{el}}/2$ doubly occupied Bloch orbitals. Equivalently, the same wavefunction can be written on a basis of Wannier Functions (WFs) by means of a unitary transformation, whose positions are referred to as Wannier Centers (WCs), $\{\mathbf{R}_j^{(\mathrm{W})}\}$ [75]. The electronic charge density is thus partitioned into localized contributions. While this partitioning is gauge-dependent, i.e. both WFs and WCs are nonunique, the sum of the WCs in the central cell is gauge-independent, and it happens to be proportional to the total polarization [42]. The total electric current [31, 51],

$$\mathbf{J}_Q(t) = \frac{e}{L^3}\left[\sum_{\ell=1}^{N} Z_\ell \dot{\mathbf{R}}_\ell - 2\sum_{j=1}^{N_{\mathrm{el}}/2} \dot{\mathbf{R}}_j^{(\mathrm{W})}\right], \tag{4.6}$$

assumes a classical-like expression. The Pendry-Hodges *Gedankenexperiment* assumes therefore an intuitively clear meaning: a nucleus, when displaced along a direction of the torus, drags some of the Kohn-Sham WFs, thus transporting an even number of electrons. The resulting OS is the bare charge of the nucleus minus twice the number of transported WFs [31, 51].

4.4 BREAKING OF STRONG ADIABATICITY

In nature, chemically relevant situations occur where different atoms of the same species feature different OSs depending, e.g., on the local chemical environment.

There are circumstances where a meaningful topological definition of OSs is still possible. This is the case exemplified by Fig. 4.1b on page 56: strongly adiabatic domains are completely separated by metallic regions. OSs can be uniquely assigned to nuclei within the same domain, and the properties of OSs discussed above remain valid. For instance, in Ref. 72 (and reviewed in Sec. 4.4.1) the authors found that two OSs for the same atomic species (bismuth) coexist in $BaBiO_3$, where Bi atoms in the octahedral sites feature OSs equal to $+3$ or $+5$, depending on their distance to the O atoms placed at the vertices of the octahedra. Nonetheless, we remark that the exchange of the two Bi atoms *cannot* be possible without crossing a metallic region. The same mechanism is present in ferrous-ferric aqueous solutions, where the charge transfer turning Fe(II) into Fe(III) and vice versa can only be accomplished via a nonadiabatic charge transfer. Another remarkable case where the SA of an insulating system is globally dropped, but the OSs of its nuclei can still be defined, is represented by the insulating subsystem of metal-insulator interfaces [76], where the system is metallic along some Cartesian directions and nonmetallic along others.

A completely different situation occurs when the breakdown of SA is accompanied by the presence of metallic regions that can be encircled by closed

adiabatic paths, as pictured in Fig. 4.1c. In this case, which will be extensively discussed in Secs. 4.4.2.1 and 4.4.2.2, charge transport can no longer be topologically classified in terms of the number of cells spanned by each nucleus along each direction, encoded in $\mathbf{n}$, and the very concept of OS loses much of its topological meaning. In fact, there can be trivial loops in the ACS (i.e. with $\mathbf{n} = 0$) that cannot be shrunk to a point without ever crossing a metallic region. This amounts to saying that $\mathfrak{z}$ (or some Cartesian component thereof) rotates once around the origin of the complex plane, where the system is metallic, even if the configuration does not move to a different periodic replica in the ACS. Thouless' theorem can still be leveraged to conclude that the dipole displaced along such a path is quantized but, at variance with the strongly adiabatic case, it is possibly nonzero, whereas the atomic net displacements vanish because $\mathbf{n} = 0$.

The repercussion of this paradigmatic situation on macroscopic electrical conduction is that charge transport is no more completely correlated to mass transport. This transport regime is somehow intermediate between insulating and metallic behaviors: while the system is always insulating and the charge motion is uniquely dictated by the adiabatic motion of the ions, in this situation a net charge transfer is possible even without the need for a net mass diffusion; we call this regime *nontrivial transport* [31].

4.4.1 *Systems with multiple well-defined oxidation states*

In Ref. 72, Jiang et al. introduced a method to compute the OS of atoms in crystals leveraging arguments from the modern theory of polarization. In particular, they noticed how the change in polarization, $\mathbf{\Delta P}$, along particular paths in the ACS, namely, displacements of an atomic sublattice by a lattice vector, $\mathbf{R}$, can only be given by

$$\mathbf{\Delta P} = \frac{e}{\Omega} \sum_{i=1}^{3} n_i \mathbf{R}_i, \tag{4.7}$$

where Ω is the volume of the unit cell of the crystal, n_i are whole numbers, and $\mathbf{R}_i$ are the lattice vectors defining the unit cell. Atomic OSs are then correctly identified after having made some important considerations regarding paths in the ACS, that were later generalized in Ref. 31. In particular, Jiang et al. noticed that the change in polarization is independent of the details of a path in the ACS as long as the system stays insulating at every point in the path. Actually, one needs to require SA for that to hold, but this was somehow implicitly taken into account in Ref. 72, even though the rigorous formalization of Sec. 4.1 was still to appear. An important consideration on that matter was already present in Ref. 72: namely, that electron transfer cannot happen in a loop under SA because, verbatim, *such electron transfer would mean that at some point on the path there would be delocalized electrons in insulating media. This is not possible without crossing the band gap and causing a metallic state on the loop*. The method to actually compute the OSs is then the following: if the displacement is a particular lattice vector, $\mathbf{R}$, of a unit cell defined by two other vectors, $\mathbf{R}_2$ and $\mathbf{R}_3$, one can build a supercell for the same crystal by lengthening the unit cell m times along the direction of $\mathbf{R}_2$, while keeping the same dimensions along the other directions. This supercell contains the original sublattices plus

their periodic replicas at $k\mathbf{R}'_2/m$, with $k = 2, \dots, m$, and $\mathbf{R}'_2 = m\mathbf{R}_2$ [72]. The supercell volume is accordingly scaled to $\Omega' = m\Omega$. If all the sublattices (the original plus its images) are moved by $\mathbf{R}$, the situation is the same as before, when the crystal was described by its unit cell. On the other hand, if only one of the sublattices is displaced by $\mathbf{R}$, the polarization changes by

$$\Delta\mathbf{P}' = \frac{e}{\Omega'}\left(n'\mathbf{R} + n'_2\mathbf{R}'_2 + n'_3\mathbf{R}_3\right) \tag{4.8}$$

which, by symmetry, must be equal to $\Delta\mathbf{P}/m$, since all the sublattice replicas are equivalent to one another [72]. Thus

$$\Delta\mathbf{P}' = \frac{e}{m\Omega}\left(n'\mathbf{R} + n'_2\mathbf{R}'_2 + n'_3\mathbf{R}_3\right) \tag{4.9}$$

$$= \frac{1}{m}\left[\frac{e}{\Omega}\left(n\mathbf{R} + n_2\mathbf{R}_2 + n_3\mathbf{R}_3\right)\right]. \tag{4.10}$$

The linear independence of the lattice vector implies $n' = n$, $n'_2 = n_2/m$, $n'_3 = n_3$. Moreover, since the integer n_2 must be divisible by m for any choice of the integer m, it follows that $n_2 = 0$. Repeating the same argument in direction $\mathbf{R}_3$ yields $n_3 = 0$. The OS associated to the displaced sublattice is then found as [72]

$$q = \frac{\Omega}{e}\frac{\Delta\mathbf{P}\cdot\mathbf{R}}{|\mathbf{R}|^2}. \tag{4.11}$$

Among other interesting crystalline materials, this methodology was applied to compute the OSs of Bi in $BaBiO_3$ [72]. This perovskite features a collective oxygen octahedral breathing mode that causes the minimal supercell to be a double perovskite with two octahedral sites of different sizes, one large and one small. This leads to a charge disproponation $2Bi^{4+} \rightarrow Bi^{3+} + Bi^{5+}$, the larger Bi^{3+} ion sitting in the large octahedral site, the smaller Bi^{5+} in the small one. The OSs predicted by Eq. (4.11) correctly capture this expected result [72]. This situation can be intuitively understood by looking at Fig. 4.1b on page 56: Bi nuclei can access only periodic replicas of sites equivalent to the one they are located in within the same adiabatic domain. Thus, there cannot be particle exchange between Bi nuclei in different sublattices without closing the electronic gap. In other words, one cannot devise a path in ACS that leads a Bi nucleus originally sitting on a large octahedral site to a small octahedral site without passing through a degenerate state: this can be understood by thinking about the continuous transformation of the coordinates of the oxygen atoms that changes the large octahedron into the small one, and vice versa. The two octahedra will be equal at some point during the continuous transformation, and in that case, the electronic state is clearly degenerate, since the unit cell with two octahedral sites could be replaced by a unit cell with only one of those sites. This implies the gap closure and the consequent breaking of SA.

4.4.2 *Systems where the concept of oxidation state is ill-defined*

Let us now address a different situation, i.e. the one depicted in Fig. 4.1c on page 56. It is the case where metallic regions of the ACS can be encircled by adiabatic paths, thus leading to adiabatic charge pumping and charge transfer without net mass transport while staying electronically insulating. The concept will first be illustrated via two very simple toy models in PBCs, and later for more realistic systems.

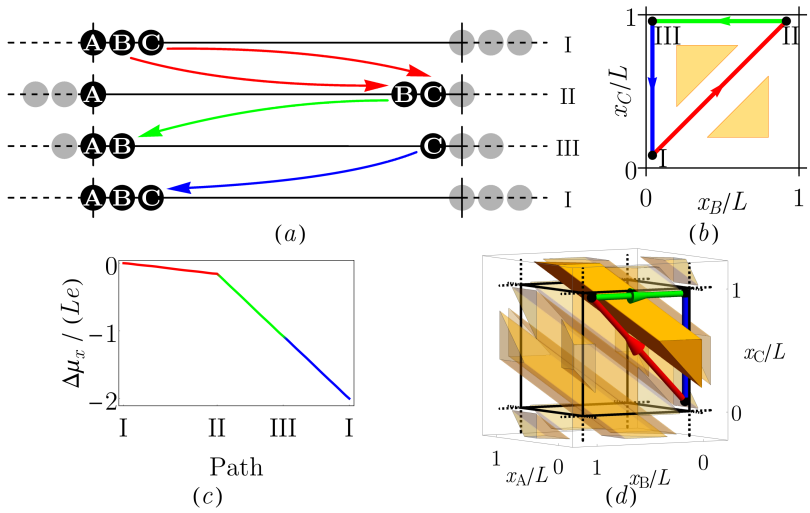

Figure 4.6: Linear H_3^+ in periodic boundary conditions. (*a*) I: Equilibrium configuration: the black circles and the continuous line indicate atoms in the primitive supercell; gray circles and the dashed line indicate their periodic images. II and III are the two intermediate steps of the closed path described in the text. (*b*) The closed path in the 2D projection of the ACS relative to the atoms that participate in the loop; the yellowish areas indicate regions where the ground state is degenerate. (*c*) Dipole displaced along the closed path. Notice that the total displaced dipole is finite and an integer multiple of eL. (*d*) The closed path in the 3D projection of the ACS where also the x coordinate of atom A is shown. The metallic region encircled by the path extends for all values of x_A and the loop cannot be shrunk to a point without crossing it: the loop is thus nontrivial. 3D projections onto subspaces where x_A is substituted with any other atomic coordinate have a similar appearance.

4.4.2.1 *Two toy models*

A very simple system displaying a nontrivial Thouless' pump mechanism is the (linear) tri-hydrogen cation, H_3^+: three protons are aligned and the ground state of the two electrons is a singlet, therefore nondegenerate, resulting in a theoretical equilibrium interatomic distance $\Delta = 0.826$ Å. We treat the molecule using PBCs with period $L = 10.6$ Å $\gg \Delta$ along the three Cartesian directions, thus amounting to enclose the molecule in a cubic supercell of side L. We now consider a closed path in the ACS, consisting of the following three steps (see Fig. 4.6):

i. The B and C protons are first rigidly translated towards the end of the supercell until the distance between C and the periodic image of A (located a $x = L$) is Δ (red arrows, ending at configuration II);

ii. The B proton, now located at $x = L - 2\Delta$, is moved back to its original position (green arrows, ending at configuration III);

iii. Finally, the C proton is moved back from $x = L - \Delta$ to its original position (blue arrows, ending at configuration I).

This path is periodic (i.e. it is isomorphic to a trivial path on the torus), the last configuration being equal to the first. The ionization potential of H_2 (≈ 15.4 eV

according to NIST data [77]) is larger than that of H ($\approx 13.6\,\mathrm{eV}$ [77]); therefore, along the path, the pair of protons that is displaced or left behind stays neutral, and the electronic gap is always larger than that of H_2. The ground state for this system when the protons are farther away than the dihydrogen ion bond distance is of the Heitler-London form [78], with resonating states where unpaired electrons are on top of the protons. This (obviously degenerate) state cannot be captured by a mean-field method such as DFT. This is not important for the sake of the phenomenology of the toy model under consideration, since in the region of the ACS where the Heitler-London ground state is correct the singlet state is also degenerate, as it will be discussed below. The ground state remains an insulating singlet throughout the entire trajectory, as explicitly checked by computing the total energy of the system for both the singlet and the triplet spin states, the former being always smaller than the latter.

If SA holds, the charge transported along the path must vanish trivially; otherwise, a Thouless' pump mechanism may allow a nontrivial charge transport. In order to check if the latter case occurs, we have computed the total dipole displaced along each segment of the path, $\boldsymbol{\Delta\mu}$, according to the modern theory of the polarization in the Wannier representation [42] (cf Sec. 4.3.1),

$$\boldsymbol{\Delta\mu}_{IF} = e\int_I^F \left(\sum_{\ell=1}^{N} Z_\ell \mathbf{dR}_\ell - 2\sum_{j=1}^{N_{\mathrm{el}}/2} \mathbf{dR}_j^{(W)} \right), \tag{4.12}$$

where Z_ℓ is the positive core charge of atom ℓ ($Z_\ell = 1$, in the present case), $\mathbf{R}_j^{(W)}$ is the position of the WC associated to the jth occupied electronic band of the system, N_{el} is the number of electrons ($N_{\mathrm{el}} = 2$, in the present case), and the factor 2 in front of the second sum accounts for the double occupancy of each molecular orbital. Our results, displayed in Fig. 4.6(c), indicate that a net charge, $Q = -2e$ is displaced along the path, thus revealing the existence of nonadiabatic domains in the ACS that the path loops around. Indeed, when the distance between any pair of protons is much larger than the molecular bond length, the ground state consists of two neutral atoms and one proton, and it is degenerate because it does not matter which atoms are neutral and which one is ionized. The regions where this condition occurs are highlighted with yellowish triangles in Fig. 4.6(b), revealing that it is in fact encircled by the closed path. When the full 9-dimensional ACS is considered, the plane depicted in Fig. 4.6(b) is the locus where all the coordinates vanish but x_{B} and x_{C}, and the triangles are the bidimensional sections over this plane of hyperprisms that pierce the entire ACS, so that the loop cannot be shrunk to a point without closing the gap even when embedded in the full 9-dimensional space (i.e. the loop is *nontrivial* in the adiabatic subspace), as illustrated in Fig. 4.6(d).

Notice that, while the total dipole is ill-defined (both because it is intrinsically so when computed in PBCs [79], and because the system is charged), dipole differences are perfectly well-defined also in this case. Our previous considerations on the relative magnitude of the ionization potentials of atomic and molecular hydrogen imply that WCs move (almost) rigidly with the proton *pair* being displaced. This implies that, when displaced individually, protons carry a unit charge, and one would be tempted to attribute an OS $q_{\mathrm{H}} = 1$ to each of them. However, when they move in pairs, they carry a zero charge, a manifest breakdown of charge additivity, due to the breakdown of strong adiabaticity. The overall effect of the different charges transported by H atoms

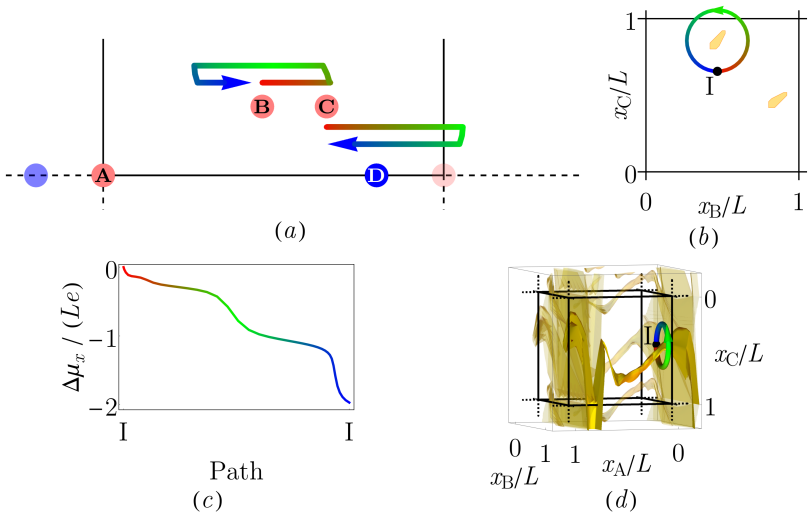

Figure 4.7: A planar configuration of the K_3Cl system undergoing a loop in ACS. (*a*) Initial and final configurations. K and Cl atoms are indicated by pink and blue circles, respectively. The colored curved arrows indicate the 1D trajectories of the two K atoms participating in the loop. The color encodes the fictitious time parametrizing the loop (red → blue). (*b*) The closed path in the 2D projection of the ACS relative to the atoms that participate in the loop; the yellowish areas indicate regions where the ground state is degenerate. (*c*) Dipole displaced along the closed path. (*d*) The closed path in the 3D projection of the ACS where also the x coordinate of atom A is shown. The green dots indicate the positions of the WCs of the electrons in the system.

according to whether they are displaced individually or in pairs is that the total charge transported along the closed path of Fig. 4.6 does not vanish, while the net mass does.

The existence of adiabatic transport anomalies entails the occurrence of two partially conflicting requirements: a high degree of ionicity and the presence of loosely bound localized electron states that can wander through the system without ever closing the gap. Nonstoichiometric molten salts seem therefore ideal candidates to display nontrivial transport [80, 81]. In order to prepare for the study of such systems in Sec. 4.4.2.2, we examine here the simplest molecular system possibly displaying their essential electronic features: the neutral K_3Cl complex. In Fig. 4.7 we show a planar configuration of this system along with a closed path in ACS displaying charge transport without any net mass displacement. As in the previous case, the ground state of the system is a singlet throughout the whole trajectory. The dipole displaced by moving each of the atoms to their periodic images in the neighboring cell along the x direction is, in units of eL, equal to $+1$ for A and C, equal to -1 for B and D. Conversely, moving any of the atoms to its periodic image in a direction perpendicular to the x axis would break the bond of that atom with the rest of the system, resulting in a degenerate ground state. Moreover, since we verified that it is possible to swap atoms B and C without closing the gap, there is no way to uniquely associate an integer charge to each atom, whose OS would thus be topologically ill-defined. Based on our previous arguments, we conclude

therefore that SA is violated here again. In fact, we identified a region in the ACS where the gap closes, as indicated by the shaded area in Fig. 4.7(*b*), and we considered an adiabatic closed path in the ACS which is trivial on the torus, but loops around that region. The x component of the electric dipole displaced along this loop is plotted in Fig. 4.7(*c*). While the total charge displaced along the y and z directions vanishes, we observe an integer charge equal to $-2e$ pumped along the x direction. Here again, we see that an integer charge is adiabatically transported without any net atomic displacements. This Thouless' charge-pump mechanism can be entirely ascribed to the loosely bound Highest-Occupied Molecular Orbital (HOMO). In fact, we checked that the contribution of the lower-lying molecular orbitals to the dipole displaced along the loop vanishes. By the same token, if one computes the charges associated with individual atomic displacements as above, but only considers the contributions to the displaced dipole from lower-lying molecular orbitals, one obtains $+1$ for all the K atoms and -1 for Cl.

4.4.2.2 *Extended systems*

We now move to a more realistic system and consider a model for a $K_x(KCl)_{1-x}$ dilute liquid metal/metal-halide solution. The equilibrium properties of nonstoichiometric molten salts are characterized by the existence of localized electron pairs, often referred to as *bipolarons* [80–82]. The formation of bipolarons is made possible by the balance between the increase in the quantum kinetic and electrostatic electron-electron repulsion energies resulting from the localization of the solvated electron pair and the attractive electron-cation energy gained by accommodating the pair into a cationic hollow, often described as a liquid-state analog of an F center in a crystal; charge transport can then be assimilated to the fast diffusion of the solvated electrons followed by their temporary stabilization in cationic hollows, driven by thermal fluctuations [80–82]. The very existence of such an adiabatic hopping-like mechanism breaks the compelling topological constraints that SA sets on ionic conduction [65] and would not be possible without breaking the latter.

We model the melt with 33 K atoms and 31 Cl atoms, corresponding to a concentration $x \approx 0.06$. This model can be qualitatively described as made of 31 Cl^- anions and 33 K^+ cations, with the addition of two neutralizing solvated electrons whose dynamics is only weakly correlated with the ionic motion [80–82].

We simulate this system within DFT using Car-Parrinello AIMD [83]. Our simulations are performed using a cubic supercell with side $L = 14.07\,\text{Å}$, corresponding to a density $\rho = 1.42\,\text{g/cm}^3$ at a temperature of $T = (1341 \pm 93)\,\text{K}$ (the incertitude on the value of the temperature is a finite-size effect, whereas the statistical incertitude on the average is two orders of magnitude smaller). The dynamics of the system is restricted to the singlet energy surface, as we explicitly verified that the triplet one consistently lies $\approx 0.40\,\text{eV}$ above. This being the case, the system is closed-shell. Nonetheless, the presence of unpaired solvated electrons would not affect our conclusions on nontrivial transport, as long as each spin channel stays gapped and dynamically decoupled from the other, and the system's electronic insulating character and adiabatic evolution are preserved [50, 82]. In Fig. 4.8 we display the time series of the energy gap between the HOMO and the Lowest-Unoccupied Molecular Orbital (LUMO), as

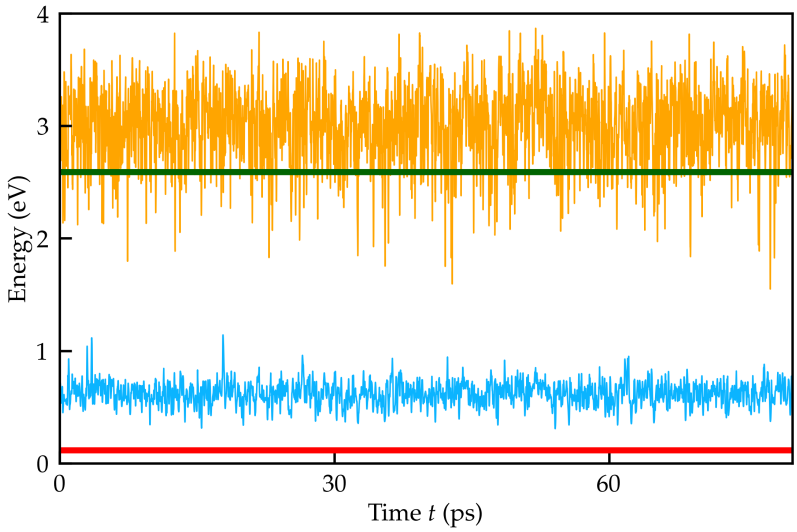

Figure 4.8: Time series of the HOMO/LUMO (blue) and HOMO−1/LUMO (orange) energy gaps. The horizontal red line indicates the thermal energy, $k_B T$. The horizontal green line is the average HOMO/LUMO gap for the stoichiometric $K_{32}Cl_{32}$ system.

well as between the molecular orbital just below the HOMO (HOMO−1) and the LUMO. The HOMO−1 corresponds to the highest molecular orbital localized on Cl^- anions, whereas the HOMO is occupied by the solvated lone pair (see below). The numerical values of these energies are affected by DFT errors that lead to an underestimation of the electronic gaps. Notwithstanding, the system stays electronically insulating along the whole AIMD trajectory, thus confirming the adequacy of an adiabatic treatment of transport in these systems for small enough concentrations. The average HOMO−1/LUMO gap would coincide with the average stoichiometric HOMO/LUMO gap for extremely low concentrations ($x \to 0$). In this limit, the energy level of the lone pair (i.e. the HOMO of the non-stoichiometric system) corresponds to a donor impurity level in the HOMO/LUMO gap of the stoichiometric system, slightly below the bottom of the empty-state band. As the concentration increases, the impurity level broadens to a band, which eventually merges into the empty-state band of the stoichiometric system, thus turning the electrolyte into a metal. If the states near the Fermi energy stay localized by disorder, this transition would be delayed until the Fermi energy crosses the mobility edge. In either case, we believe that our conclusions hold in the electrolyte regime. The value of the concentration appropriate to our model system, $x \approx 0.06$, is below the critical value $x_c \approx 0.1$, at which an insulator-to-metal transition is expected to occur, resulting from experimental [84] and numerical [85, 86] evidence. Similar behavior has been recently evinced using photo-emission spectroscopy for alkali-metal solutions in liquid ammonia [87].

In Fig. 4.9 we display the overlay of several consecutive snapshots from a short segment of our AIMD trajectory. One sees that, by the time the lone pair has covered a distance comparable to the size of the supercell, all the atoms

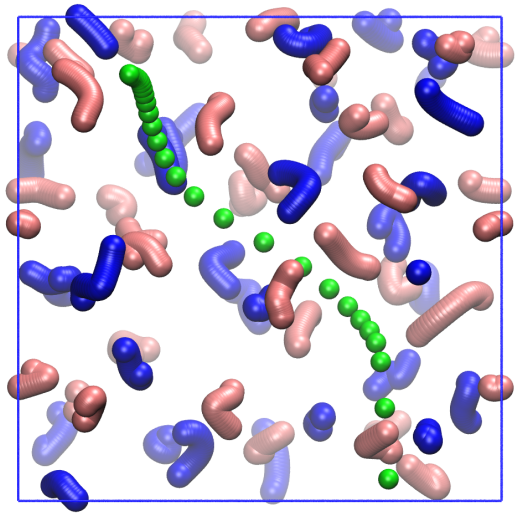

Figure 4.9: Overlay of several consecutive snapshots from a 435 fs-long sample of AIMD trajectory of our $K_{33}Cl_{31}$ model. K^+ ions are depicted in pink, Cl^- ions in blue, while the WC associated with the lone bipolaronic pair is displayed in green.

have traveled only a small fraction of this length. This suggests that charge transport in these systems may be strongly affected by the dynamics of the localized lone pairs, whose very existence we have seen to be closely related to the topological properties of the electronic ground state. Its motion, while being uniquely determined by the atomic adiabatic dynamics, is largely uncorrelated from it. It can thus give rise to a nontrivial transport regime such that electric currents are mainly carried by solvated electrons, not corresponding to any atomic displacements, which is essentially made possible by the breaking of SA. To show this, we computed the dipole displaced along two properly designed loops in the $K_{33}Cl_{31}$ ACS, beginning and ending at the same configuration, where one K atom is moved from its initial position to one of its adjacent periodic images along the x axis, as depicted in Fig. 4.10. The two loops have identical winding numbers: $\boldsymbol{n}_K = (1,0,0)$ for the moving K, and $\boldsymbol{n} = (0,0,0)$ for all the other atoms. Nonetheless, the dipoles displaced along them differ, as reported in panel (c), corresponding to two different topological charges ($q = \pm 1$) for the same K atom. Such a state of affairs is clear evidence that the two loops cannot be deformed into one another without hitting a non-adiabatic region, thus making it impossible to assign a well-defined OS to each atom using the procedure of Refs. 72 and 65, in striking contrast with chemical common sense. Even though in a physical trajectory no such loops in the ACS are expected to occur, nor will a lone pair stay bound to the same ion for much longer than a fraction of the atomic diffusion time, this thought experiment clarifies the links between SA breaking and the establishment of a regime where loops in ACS can be described by nontrivial Thouless' pumps and open trajectories may carry a charge current not corresponding to any ionic currents.

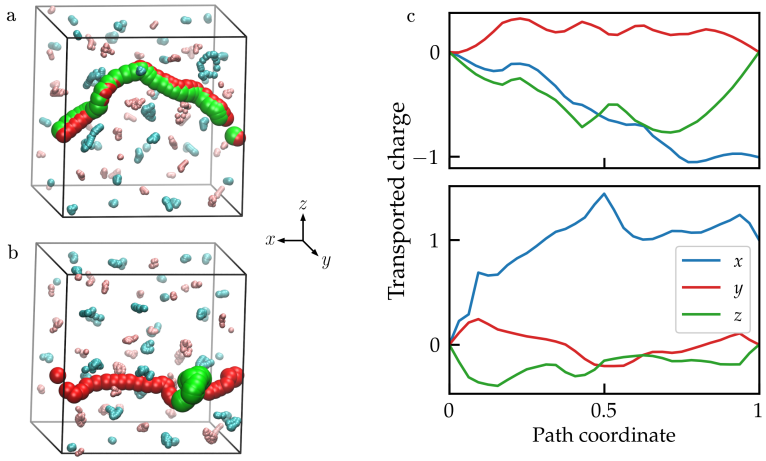

Figure 4.10: Pendry-Hodges *Gedankenexperiment* when SA does not hold. In the simulation cell, there is a nonstoichiometric melt of 33 K nuclei, depicted as pink spheres, and 31 Cl nuclei, in cyan. The green sphere represents the WC associated with the excess lone pair. The larger spheres are the particles in evidence. (a-b) Periodic MEPs of the same K nucleus (in red) in the x direction, starting and ending in the same points in two nearby cells: while for one path the K nucleus drags the WC along its motion (a), in the other it does not (b). In panel (c), the charge transported along each direction for the two paths is shown in units of the elementary charge. The path coordinate goes from 0 at the initial configuration to 1 at the final one.

The transport anomalies displayed in Fig. 4.10 are expected to show conspicuously in the behavior of the ionic BECs, in terms of which the instantaneous charge current can be expressed [65]. The upper panel of Fig. 4.11 displays the time series of the distances from the lone pair of the five atoms originally closest to it. The lower panel displays the corresponding average diagonal elements of the effective-charge tensors. One sees that, when all the atoms are stably far from the lone pair ($t \gtrsim 500\,\mathrm{fs}$), the values of the effective charges are close to what chemical intuition would suggest ($Z^\star_{\mathrm{K},\alpha\alpha} \approx +1$ and $Z^\star_{\mathrm{Cl},\alpha\alpha} \approx -1$). When some of them approach the lone pair, instead, weird things may occur. For one thing, the effective charge of the K atom closest to the lone pair may go negative, meaning that the latter is provisionally dragged by the K ion along its movement. For a second, the effective charge of a Cl atom, while never quite positive, may nearly vanish when it gets close enough to the lone pair; this is likely due to the screening effect of the pair's highly polarizable wavefunction. For a third, effective charges change abruptly when passing from an anomalous to a normal regime: the K effective charge may become relatively large and positive just after having gone negative, and a few Cl charges may correspondingly become relatively large, while staying negative, so as to preserve local charge neutrality. The duration of this transition, a few dozen femtoseconds, is the time it takes for the lone pair to abruptly change its local environment, as witnessed by the steep change of the distances from it of the atoms considered in Fig. 4.11.

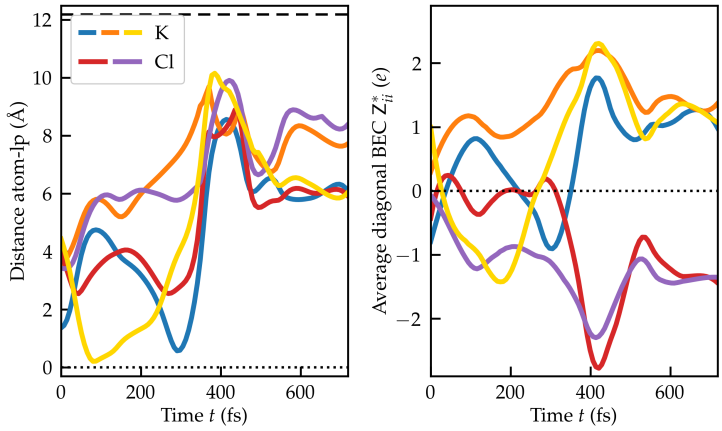

Figure 4.11: Upper panel: time series of the distances from the electron lone pair in $K_{33}Cl_{31}$ of the five nearest atoms. The horizontal lines are guides for the eye: dotted, distance equal to zero; dashed, maximum distance allowed in PBCs, i.e. $\sqrt{3}L/2$. Lower panel: average diagonal elements of the BEC tensor of the five atoms described above; the horizontal dotted line marks the zero value.

In order to evaluate the impact of nontrivial transport on the ionic conductivity of this system, σ is computed using the HE relation (Eq. (3.111)). Alternatively, $\boldsymbol{\Delta\mu}(t)$ has been computed from Eq. (4.12) and from:

$$\boldsymbol{\Delta\mu}'_{IF} = e\int_I^F \left(\sum_\ell q_\ell\, \mathbf{dR}_\ell - 2\mathbf{dR}_{\text{lp}}^{(W)}\right) \tag{4.13}$$

where $\mathbf{w}_{\text{lp}}$ is the position of the lone-pair WC, $q_\ell = +1$ for K atoms, -1 for Cl atoms, and the factor $q_{\text{lp}} = -2$ reflects the occupancy of the loosely bound HOMO. The definition of $\boldsymbol{\Delta\mu}'_{IF}$ differs from that of $\boldsymbol{\Delta\mu}_{IF}$, Eq. (4.12), in that in Eq. (4.13) a fixed OS is associated with all the atoms of the same species in the spirit of Ref. 65—and as it would be in a stoichiometric mixture—while the lone pair occupying the localized and loosely bound HOMO is treated as an independent charge carrier. The results, illustrated in Fig. 4.12, yield the values $16.2 \pm 0.8\,\text{S/cm}$ and $15.9 \pm 0.8\,\text{S/cm}$ for the conductivities computed from definitions Eq. (4.12) and Eq. (4.13), respectively [31]. All the numerical values of the transport coefficients reported here have been evaluated using cepstral analysis (cf Sec. 2.2.2). The two values coincide within statistical errors, giving substance to the topological analysis of nontrivial transport in this system. Maybe fortuitously, these values compare well with the experimental data at such concentration of K atoms [88, 89]. The conductivity is much larger than the value obtained from the ionic contribution in Eq. (4.13) ($3.6 \pm 0.3\,\text{S/cm}$, the green line in Fig. 4.12): this indicates that the conductivity is almost entirely determined by the diffusion of the solvated lone pair, and is in fact much larger than it typically is in stoichiometric molten salts (i.e. $3.2 \pm 0.2\,\text{S/cm}$ [65]). Furthermore, we observe that the total conductivity coincides with the sum of the ionic and lone-pair contributions, implying that the cross-correlation resulting from the product of the first and second terms on the right-hand side of Eq. (4.13) is negligible, as confirmed by the vanishing slope of the red

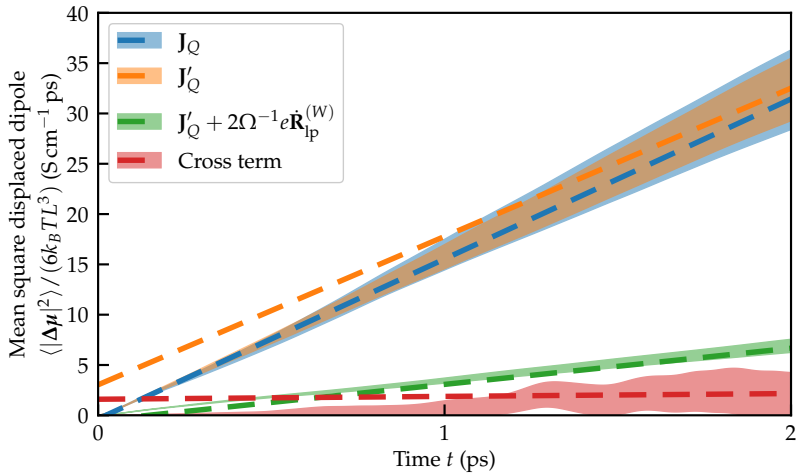

Figure 4.12: MSDDs of nonstoichiometric K-KCl melt computed with different definitions of the electric flux. The topological flux plus the lone pair contribution are equivalent to the exact definition of the electric flux. The topological flux alone yields a value of σ much lower than the correct one. The cross-correlation term is compatible with zero: the ionic and lone-pair contributions are uncorrelated to one another.

curve in Fig. 4.12. The diffusivity D_s of each species s = K, Cl, lp is computed according to the HE formula:

$$D_s = \lim_{t\to\infty} \frac{\left\langle |\Delta\mathbf{R}_s(t)|^2 \right\rangle}{6t}. \tag{4.14}$$

The mobilities, $\mu_s = q_s e D_s / (k_B T)$, are then estimated to be 1.23 ± 0.02, 1.14 ± 0.07, and 102 ± 5 (10^{-3} cm^2 V^{-1} s^{-1}) for K, Cl, and the lone solvated pair, respectively. The lone-pair mobility is two orders of magnitudes larger than the ionic ones, in agreement with experimental evidence [90] and with the observed predominance of the lone-pair contribution to the total conductivity. Since the value of the lone-pair mobility is estimated from a single lone-pair, its value might be only fortuitously similar to what is found in experiments.

4.4.2.3 *The effect of Exact Exchange*

It is well known that standard DFT is affected by spurious self-interaction errors due to the interaction of each electron with the total one-body electron density, including its own density [91]. The double-counting is partially removed by the approximate Exchange and Correlation (XC) functional, but errors are still large, especially for local and semi-local XC functionals [91, 92]. The issue is especially present in one-electron systems [92]. Nonstoichiometric molten salts with excess metal atoms feature solvated electrons, as seen above; the excess electrons are effectively few-electron systems and, as such, are particularly affected by spurious self-interactions. This is somewhat analog to polarons in solids, where excess electrons in semiconductors and insulators couple to the phonons in the lattice and form localized bound states [93–95]. An instructive

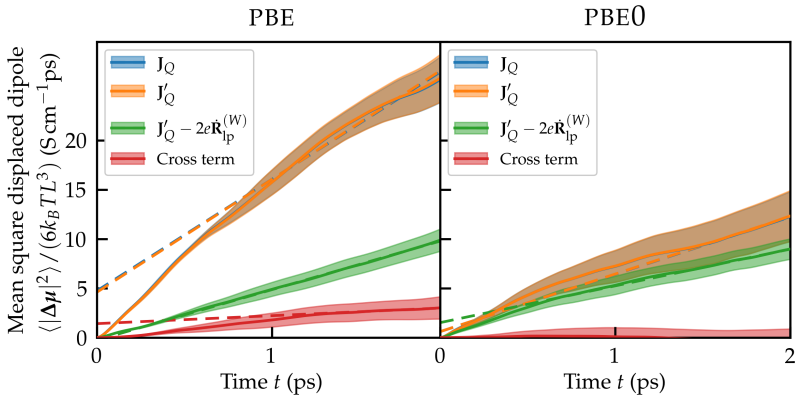

Figure 4.13: Comparison of the ionic conductivity of a nonstoichiometric NaCl melt computed with PBE and PBE0 functional. The MSDDs computed with Eq. (4.12) and Eq. (4.13) are in agreement in both cases, but the values of σ differ between PBE (*left*) and PBE0 (*right*). Since the OSs contribution is the same in both cases, the difference is due to the lone-pair contribution, which is much smaller for the PBE0 functional due to the higher degree of localization of the solvated electron. The cross-correlation of the two fluxes is compatible with zero for both functionals, confirming the lack of correlation between ionic (i.e. mass) and electronic (i.e. lone-pair) transport.

simple model for polarons is the Landau-Pekar (LP) model [96, 97] that, in a nutshell, considers the interaction of an excess electron spanning many crystal unit cells with the lattice in the effective-mass approximation. The total energy of the LP model is [98]

$$E_{\mathrm{LP}} = \frac{\hbar^2}{2m^*} \int |\nabla\psi|^2 \mathrm{d}^3r + \frac{1}{8\pi} \int \mathbf{E}\cdot\mathbf{D}\,\mathrm{d}^3r, \tag{4.15}$$

where $\psi(\mathbf{r})$ is the wavefunction of the excess electron, $\mathbf{E}(\mathbf{r})$ is the macroscopic total electric field, and $\mathbf{D}(\mathbf{r})$ is the electric displacement field. The total energy is thus the sum of the band energy of the excess electron and the electrostatic energy of the dielectric medium. The latter can be written in terms of the electron wavefunction as

$$\frac{1}{8\pi} \int \mathbf{E}\cdot\mathbf{D}\,\mathrm{d}^3r = \frac{e^2}{2}\left(\frac{1}{\epsilon^0} - \frac{1}{\epsilon^\infty}\right) \iint \frac{|\psi(\mathbf{r})|^2 |\psi(\mathbf{r}')|^2}{|\mathbf{r}-\mathbf{r}'|}\,\mathrm{d}^3r\,\mathrm{d}^3r', \tag{4.16}$$

since the electric displacement is related to the free charge-carrier density (in this case, just the excess electron) by $\nabla\cdot\mathbf{D} = 4\pi e|\psi(\mathbf{r})|^2$, and to the macroscopic electric field by $\mathbf{D} = \epsilon^0\mathbf{E}$. The symbols ϵ^0 and ϵ^∞ are the static (electronic and ionic) and high-frequency (electronic only) dielectric constants, respectively. The high-frequency dielectric constant contribution is subtracted in Eq. (4.16) because the electronic screening energy is already explicitly accounted for in the first term of Eq. (4.15) [98]. The total energy of Eq. (4.15) is thus a func-

tional of the electronic wavefunction, $E_{\text{LP}}[\psi]$, whose minimization yields the eigenvalue problem [98]

$$\begin{aligned} -\frac{\hbar^2}{2m^*}\nabla^2\psi(\mathbf{r}) - e^2\left(\frac{1}{\epsilon^0}-\frac{1}{\epsilon^\infty}\right)\int\frac{|\psi(\mathbf{r}')|^2}{|\mathbf{r}-\mathbf{r}'|}\psi(\mathbf{r})\,\mathrm{d}^3r' &= \varepsilon\psi(\mathbf{r}) \\ \hat{\mathcal{H}}_{\text{LP}}\psi(\mathbf{r}) &\equiv \varepsilon\psi(\mathbf{r}), \end{aligned} \tag{4.17}$$

where the last line defines the LP Hamiltonian, $\hat{\mathcal{H}}_{\text{LP}}$, and the normalization condition on $\psi(\mathbf{r})$ is understood. Eq. (4.15) becomes, in terms of the LP eigenvalue, ε,

$$E_{\text{LP}} = \varepsilon + \frac{e^2}{2}\left(\frac{1}{\epsilon^0}-\frac{1}{\epsilon^\infty}\right)\iint\frac{|\psi(\mathbf{r})|^2|\psi(\mathbf{r}')|^2}{|\mathbf{r}-\mathbf{r}'|}\,\mathrm{d}^3r\,\mathrm{d}^3r'\,. \tag{4.18}$$

Polaron localization is readily understood by considering the exponential *ansatz* $\psi(\mathbf{r}) = (\pi r_{\text{p}}^3)^{-1/2}\mathrm{e}^{-|\mathbf{r}|/r_{\text{p}}}$, for the wavefunction, where r_{p} is a measure of the polaron size. The energy becomes [98]

$$E_{\text{LP}}(r_{\text{p}}) = \frac{\hbar^2}{2m^*r_{\text{p}}^2} - \frac{5}{16}\left[\frac{1}{\epsilon^0}-\frac{1}{\epsilon^\infty}\right]\frac{e^2}{r_{\text{p}}}, \tag{4.19}$$

whose minimum is

$$r_{\text{p}}^{\text{min}} = \frac{16}{5}\frac{\hbar^2}{m^*e^2}\left[\frac{1}{\epsilon^0}-\frac{1}{\epsilon^\infty}\right]^{-1}. \tag{4.20}$$

The polaron self-trapping around r_{p} is thus determined by the interplay between the delocalizing effect of the kinetic term and the localizing effect of electrostatic interaction. Now, if one were to include a DFT-like self-interaction term to the LP Hamiltonian, making it something of the form

$$\begin{aligned} \hat{\mathcal{H}}'_{\text{LP}} &= -\frac{\hbar^2}{2m^*}\nabla^2 - e^2\left[\frac{1}{\epsilon^0}-\frac{1}{\epsilon^\infty}\right]\int\frac{|\psi(\mathbf{r}')|^2}{|\mathbf{r}-\mathbf{r}'|}\,\mathrm{d}^3r' + \underbrace{e^2\int\frac{|\psi(\mathbf{r}')|^2}{|\mathbf{r}-\mathbf{r}'|}\,\mathrm{d}^3r'}_{\text{DFT-like self-interaction}} \\ &= -\frac{\hbar^2}{2m^*}\nabla^2 - e^2\underbrace{\left[\frac{1}{\epsilon^0}-\frac{1}{\epsilon^\infty}-1\right]}_{\in[-1,0)}\int\frac{|\psi(\mathbf{r}')|^2}{|\mathbf{r}-\mathbf{r}'|}\,\mathrm{d}^3r'\,, \end{aligned} \tag{4.21}$$

the net effect would be to exclude the possibility of self-trapping since both the kinetic and electrostatic terms are now positive: no polaron could ever be localized [98]. Something similar happens in standard DFT, and that makes it difficult for excess electrons to localize in a dielectric material [98]. Hybrid functionals, where a fraction of the Hartree-Fock exchange functional is added at the expense of a fraction of the XC functional, partially circumvent this issue by reducing the self-interaction error and thus making it simpler for excess electrons to localize. The effect of this change of functional is tested in the case of nonstoichiometric molten NaCl analog to the K-KCl melt described above. Two simulations of $Na_{33}Cl_{31}$ are prepared at the same temperature[3] $T \approx 1250\,\text{K}$ using either the PBE functional of the hybrid PBE0 functional,

3 The actual values of the temperature are $(1260 \pm 130)\,\text{K}$ and $(1280 \pm 160)\,\text{K}$ for PBE and PBE0, respectively.

the latter being the former with 25% of Hartree-Fock exchange [99]. Ionic conductivity calculations are performed according to GK theory, with an explicit account of the topological and electronic lone-pair flux contributions. Since the hybrid functional is expected to localize the excess electron pair more than PBE, the ionic conductivity should be lower in the PBE0 calculation than in the PBE one. In particular, the lone-pair contribution should drop, while the purely ionic contribution should remain approximately the same. Nonetheless, due to the arguments made above about the topology of paths in the ACS, charge transport should still be practically uncorrelated from mass transport, in that the electronic lone pair should contribute to σ independently of the topological flux. Fig. 4.13 shows the comparison between ionic conductivities computed with the two functionals. The PBE0 total conductivity is less than half the PBE value, the reason being the higher degree of localization in the former case. In fact, the OSs contribution, $\mathbf{J}'_Q - 2e\dot{\mathbf{R}}^{(W)}_{\mathrm{lp}}$, is almost the same in both cases, meaning that most of the difference is due to a much lower lone-pair contribution in the case where the hybrid functional is adopted. The cross-correlation term between the OSs flux and the flux due to the lone pair is compatible with zero, once again suggesting the lack of correlation between mass transport and purely electronic transport, even in the case of PBE0 where, locally, the dynamics of the solvated electron pair is more correlated to the ionic motion than in the PBE case.

4.5 CHARGE TRANSFER REACTIONS

Electron Transfer (ET) reactions are a class of chemical reactions that involve an exchange of charge between compounds, i.e., from a reactant state to a product state. The first successful attempts to provide a theory of electrochemical reactions are due to Marcus [100] and Hush [101]. In their seminal works, they were able to address the matter of outer-sphere electron transfer—i.e., where the reacting species remain separated during the whole process—with a particular focus on the role of the solvent reorganization, rather than a detailed account of electronic interactions which, at the time, could not be included in a quantitative treatment due to the complex nature of the calculations involved. We summarize below the main elements of this theory.

A typical Marcus-Hush scenario involves two reacting partners in proximity. There usually is a free energy barrier separating reactants and products. In fact, the initial and final states bear different charges, and reactant and product states are solvated. Therefore, the environment is reorganized for the electron to overcome the barrier and for the ET to happen. The situation can be understood as a two-state system [102]: a reactant and a product state. A simple way to incorporate the effect of the solvent is through a linearly responding heat bath. The Hamiltonian which represents this system is the spin-boson Hamiltonian, i.e.

$$\hat{\mathcal{H}} = -\frac{1}{2}\hbar\Delta\hat{\varsigma}_x - \frac{1}{2}\hbar\epsilon\hat{\varsigma}_z + \frac{1}{2}\mu\mathcal{E}(t)\hat{\varsigma}_z + \hat{\mathcal{H}}_R, \tag{4.22}$$

where $\{\hat{\varsigma}_\alpha\}$ are the Pauli matrices; Δ and ϵ are the hopping rate and on-site bias, respectively; $\mu\mathcal{E}(t)$ describes the collective bath mode coupled to the electronic system and can be thought of as fluctuating dynamical polarization energy due to the local environment [102], and its properties are entirely contained in

its correlation function; $\hat{\mathcal{H}}_R$ is the Gaussian reservoir associated to the solvent. When the bath is purely adiabatic, which is the condition we are interested in, the bath correlation function reduces to a constant, $2k_BT\Lambda$, where Λ can be understood as the reorganization energy of the solvent. The contribution of the bath to the Hamiltonian in Eq. (4.22) plays no role, and what remains reduces to (in matrix form) [103]:

$$\hat{\mathcal{H}} = \frac{\hbar}{2}\begin{pmatrix} \frac{\mu\mathcal{E}}{\hbar} - \epsilon & -\Delta \\ -\Delta & \epsilon - \frac{\mu\mathcal{E}}{\hbar} \end{pmatrix}. \tag{4.23}$$

The eigenstates of $\hat{\mathcal{H}}$—i.e., the electronic adiabatic states—are easily found to have eigenvalues

$$E_\pm(\mathcal{E}) = \pm\frac{\hbar}{2}\sqrt{\Delta^2 + (\epsilon - \mu\mathcal{E}/\hbar)^2}. \tag{4.24}$$

Averaging over the bath fluctuations, one obtains the adiabatic Potential Energy Surface (PES), $F_\pm$, as a function of the mean polarization energy $\mu\mathcal{E}$ [102]:

$$F_\pm(\mathcal{E}) = \frac{\mu^2\mathcal{E}^2}{4\Lambda} \pm \frac{\hbar}{2}\sqrt{\Delta^2 + (\epsilon - \mu\mathcal{E}/\hbar)^2}. \tag{4.25}$$

When there is no on-site bias, i.e., reactant and product are solvated with the same energy, $\epsilon = 0$. The adiabatic surfaces are qualitatively different according to the parameter $p = \Lambda/(\hbar\Delta)$, where the electronic coupling $\hbar\Delta$ can be thought of as the unit of energy. Doing so also for the polarization energy, i.e. defining $\phi = \mu\mathcal{E}/(\hbar\Delta)$, Eq. (4.25) becomes

$$F_\pm(\phi) = \frac{\hbar\Delta}{2}\left(\frac{\phi^2}{2p} \pm \sqrt{1+\phi^2}\right). \tag{4.26}$$

The reactant and product states are located at $\mp\phi_0$, respectively, where $\phi_0 = \sqrt{p^2-1}$. The electronic coupling is so large in the adiabatic limit that p is of order 1 or lower. When $p < 1$, there are no environmental fluctuations; both surfaces feature a single minimum. Therefore, no electron is transferred. For $p \gtrsim 1$, there are two minima in the ground adiabatic surface, separated by a barrier whose height depends on p. The electronic coupling is still large, but sufficient environmental fluctuations allow an electronic transfer. At the opposite limit, $p \gg 1$, there is the nonadiabatic transfer when the fluctuations are so large with respect to the electronic coupling that the gap between F_- and F_+ is tiny, and the electron has a significant probability of jumping to the higher energy surface, invalidating the Born-Oppenheimer approximation.

The two regimes $p \gtrsim 1$ and $p \gg 1$ outlined above where ET can happen can be understood from our perspective as pictured in Fig. 4.14. In the two panels, on the left, there is a sketch of the ACS with the central cell circled in light blue and a periodic replica on its right, like those in Fig. 4.1. On the right are the PESs—the black ones are the Marcus parabolas representing diabatic states, the green one is the adiabatic ground state, and the blue one is the adiabatic excited state. The red horizontal line represents the average energy of the system, the shaded area being the entity of thermal fluctuations, i.e., of the order $2k_BT$.

In panel (a), the ACS features metallic walls that cannot be bypassed. OSs are well-defined only within a given adiabatic domain and, for a given nuclear species, they can be different for different adiabatic domains. Charge can be

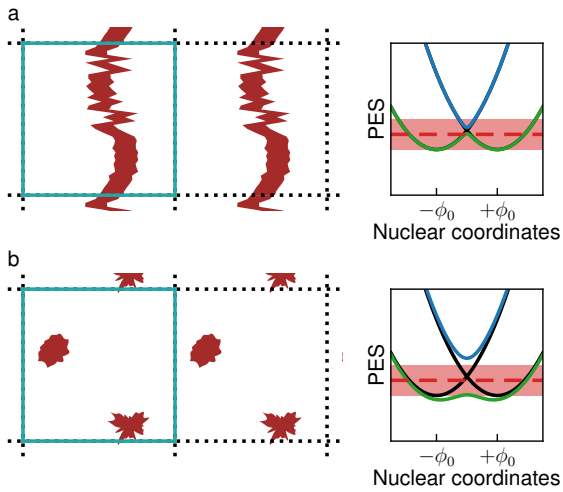

Figure 4.14: Parallel between our topological theory and Marcus-Hush ET theory. (a) ACS with strongly adiabatic domains separated by metallic regions (left) and PESs with $p \gg 1$, signaling nonadiabatic charge transfer (right). (b) ACS where SA is broken (left) and PESs with $p \gtrsim 1$, where adiabatic charge transfer is possible (right).

transferred only by crossing a metallic region, i.e., by breaking adiabaticity. Any electron transfer is nonadiabatic: since the electronic coupling between reactant and product states is too low with respect to the reorganization energy, $p \gg 1$, and the adiabatic energy surfaces practically coincide with the diabatic ones. This phenomenon is observed in physical systems where atoms of the same species feature different OSs, such as the paradigmatic case of the ferrous-ferric exchange in water,

$$\mathrm{Fe}^{2+}(\mathrm{aq}) + \mathrm{Fe}^{3+}(\mathrm{aq}) \rightleftharpoons \mathrm{Fe}^{3+}(\mathrm{aq}) + \mathrm{Fe}^{2+}(\mathrm{aq}). \tag{4.27}$$

For the exchange to happen, the system must pass through a point where the electronic levels are degenerate, and adiabaticity is lost. Panel (b) displays an ACS where SA is broken and there are metallic regions that adiabatic loops can encircle. Therefore, there exist adiabatic paths, sharing the same endpoints, that cannot be deformed into one another without ever crossing a metallic region, as well as trivial loops in the ACS which can pump an integer charge to another cell without any net displacement of the nuclei. As shown in Sec. 4.4, this implies that a topological, unique definition for the atomic OSs is not admitted, and the *adiabatic* motion of an erratic, localized electronic charge can be observed. In the Marcus picture, this is precisely what happens in the intermediate adiabatic regime, $p \gtrsim 1$. Electron transfer can occur due to nuclear fluctuations within the Born-Oppenheimer approximation since the adiabatic surfaces are sufficiently separated. This is observed, e.g., in nonstoichiometric molten salts, where charge is mainly transported by localized electronic charge (polarons or lone pairs) diffusing through the system [31] through an activated Marcus process mediated by the nuclear thermal motion.

Part III

HEAT TRANSPORT IN SOLID-STATE ELECTROLYTES

> In any theoretical treatment of transport problems, it is important to realize at what point the irreversibility has been incorporated. If it has not been incorporated, the treatment is wrong. A description of the situation which preserves the reversibility in time is bound to give the answer zero or infinity for any conductivity. If we do not see clearly where the irreversibility is introduced, we do not clearly understand what we are doing
>
> Rudolph Peierls,
> Transport phenomena, 1974, p. 5

5 THERMAL TRANSPORT IN SOLIDS

Nuclei of atoms in solids are characterized by having well-defined equilibrium positions around which they oscillate. At temperatures below melting, atomic displacements from equilibrium are much smaller than interatomic distances; thus, vibrational properties can be represented on the basis of normal modes in the harmonic approximation, using the phonons quasiparticle picture, while anharmonicity is treated as a perturbation. Anharmonicity is responsible for temperature-dependent frequency shifts and for their broadening, implying finite phonon lifetimes, and ultimately determining the value of the thermal conductivity of a material [104–106]. This picture breaks down in systems that, despite retaining a solid structure, feature partial ionic diffusion. Examples are Solid-State Electrolytes (SSEs), where structural defects that drive the chemical composition of the material away from stoichiometry lead to nonnegligible ionic conduction, and superionic materials, where a phase transition allows a sublattice to melt and behave like a fluid, while others keep their solid-like nature. For these systems, anharmonic lattice dynamics is not valid, and one needs to resort to other methods to compute thermal conductivity, such as EMD.

In this Chapter, I will first review anharmonic lattice dynamics and the Quasi-Harmonic Green-Kubo (QHGK) method to compute the thermal conductivity of solids. Then, I will review the GK theory for thermal transport in the context of EMD, both based on atomistic coarse-grained models and DFT.

5.1 ANHARMONIC LATTICE DYNAMICS

The potential energy of a system of N interacting particles is a function of their positions, $\{\mathbf{R}_\ell\}$, and it can therefore be expanded in a Taylor series in the displacements, $\{\mathbf{u}_\ell\}$, of the coordinates with respect to a given configuration $\{\mathbf{R}^\circ_\ell\}$, i.e. $\mathbf{u}_\ell = \mathbf{R}_\ell - \mathbf{R}^\circ_\ell$. Such expansion reads

$$\begin{aligned}\mathcal{V}(\mathbf{R}_1,\dots,\mathbf{R}_N) = \mathcal{V}(\mathbf{R}^\circ_1,\dots,\mathbf{R}^\circ_N) + \sum_{\ell'} \frac{\partial \mathcal{V}}{\partial \mathbf{u}_{\ell'}} \cdot \mathbf{u}_{\ell'} + \\ + \frac{1}{2} \sum_{\ell',\ell''} \mathbf{u}_{\ell'} \cdot \frac{\partial^2 \mathcal{V}}{\partial \mathbf{u}_{\ell'} \partial \mathbf{u}_{\ell''}} \cdot \mathbf{u}_{\ell''} + \dots,\end{aligned} \tag{5.1}$$

where the expansion coefficients are called Interatomic Force Constants (IFCs). If the reference positions are chosen to be equilibrium positions, i.e., the configuration where the potential energy is minimal, the first-order term in Eq. (5.1) is zero and the second-order term is positive. As long as the system stays solid, and atoms can only oscillate around their equilibrium positions, the displacements are finite and one can approximate $\mathcal{V}$ with some terms of

the expansion in Eq. (5.1). In the harmonic approximation one keeps only the quadratic term in the expansion, characterized by the second-order IFC:

$$\phi''_{\ell\ell'\alpha\alpha'} = \frac{1}{2}\sum_{\ell,\ell',\alpha,\alpha'} \frac{\partial^2 \mathcal{V}}{\partial u_{\ell\alpha}\partial u_{\ell'\alpha'}} u_{\ell\alpha}u_{\ell'\alpha'}, \tag{5.2}$$

which is a positive-definite matrix. The dynamics of the harmonic system can then be described in terms of normal modes, the phonons. The eigenmodes are obtained from the diagonalization of the dynamical matrix, i.e. the second-order IFC rescaled by the atomic masses, $D_{\ell\ell'\alpha\alpha'} = \phi''_{\ell\ell'\alpha\alpha'}/\sqrt{M_\ell M'_\ell}$, whose eigenvalue equation reads [105]

$$\sum_{\ell',\alpha'} D_{\ell\ell'\alpha\alpha'}\eta_{\ell'\alpha'\mu} = \eta_{\ell\alpha\mu}\omega_\mu^2, \tag{5.3}$$

where $\omega_\mu/(2\pi)$ is the frequency of the normal mode η_μ. The normal modes coordinates and momenta can then be defined as

$$\xi_\mu = \sum_{\ell,\alpha}\sqrt{M_\ell}u_{\ell\alpha}\eta_{\ell\alpha\mu}, \qquad \pi_\mu = \sum_{\ell,\alpha}\sqrt{M_\ell}\dot{u}_{\ell\alpha}\eta_{\ell\alpha\mu}. \tag{5.4}$$

The harmonic Hamiltonian of the nuclei (including the trivial kinetic term) becomes, with respect to these coordinates,

$$\mathcal{H}^{(2)} = \frac{1}{2}\sum_\mu \left[\pi_\mu^2 + \omega_\mu^2\xi_\mu^2\right], \tag{5.5}$$

which can be further simplified by introducing the (classical) amplitudes

$$(\alpha_\mu, \alpha_\mu^*) = \sqrt{\frac{\omega_\mu}{2}}\xi_\mu \pm \frac{i}{\sqrt{2\omega_\mu}}\pi_\mu, \tag{5.6}$$

in terms of which the harmonic Hamiltonian is

$$\mathcal{H}^{(2)} = \sum_\mu \omega_\mu \alpha_\mu^*\alpha_\mu. \tag{5.7}$$

The normal modes of a harmonic system are noninteracting and, as such, once they are populated they continue to exist forever. Therefore, in a harmonic system, the value of thermal conductivity is infinite, as there is no thermal dissipation. In order to measure a finite thermal conductivity, anharmonic contributions need to be included. The simplest anharmonic approximation consists of keeping also the third-order term in Eq. (5.1), characterized by the third-order IFC, given by

$$\phi'''_{\ell\ell'\ell''\alpha\alpha'\alpha''} = \frac{1}{6}\sum_{\ell,\ell',\ell'',\alpha,\alpha',\alpha''} \frac{\partial^2 \mathcal{V}}{\partial u_{\ell\alpha}\partial u_{\ell'\alpha'}} u_{\ell''\alpha''}u_{\ell\alpha}u_{\ell'\alpha'}u_{\ell''\alpha''}. \tag{5.8}$$

The Hamiltonian up to third order becomes [107]

$$\begin{aligned}\mathcal{H}^{(3)} &= \sum_\mu \omega_\mu \alpha_\mu^*\alpha_\mu + \\ &+ \sum_{\mu,\nu,\lambda}\Phi_{\mu\nu\lambda}\frac{1}{\sqrt{8\omega_\mu\omega_\nu\omega_\lambda}}(\alpha_\mu + \alpha_\mu^*)(\alpha_\nu + \alpha_\nu^*)(\alpha_\lambda + \alpha_\lambda^*),\end{aligned} \tag{5.9}$$

where $\Phi_{\mu\nu\lambda} = \frac{\partial^3 \mathcal{V}}{\partial \xi_\mu \partial \xi_\nu \partial \xi_\lambda}$ is the third derivative of the potential energy with respect to the normal-mode coordinates. The quantal version of these expressions can be easily obtained by mapping the classical amplitudes to the normal-mode annihilation and creation operators [104]: $\alpha \mapsto \sqrt{\hbar}\hat{a}$ and $\alpha^* \mapsto \sqrt{\hbar}\hat{a}^\dagger$. Since the next sections will be mainly devoted to classical calculations, in the following the notation and the results will refer to classical quantities.

5.2 QUASI-HARMONIC GREEN-KUBO THEORY

In order to access thermal transport properties, one needs an expression for the energy flux. For a solid in the harmonic approximation, the α Cartesian component of the energy flux can be obtained after some rather tedious calculations as [104]

$$J_E^\alpha = \frac{i}{2} \sum_{\mu,\nu} v_{\mu\nu}^\alpha \omega_\mu (\alpha_\nu^* + \alpha_\nu)(\alpha_\mu^* - \alpha_\mu), \tag{5.10}$$

where $v_{\mu\nu}^\alpha$ is the α component of the generalized velocity matrix, i.e.

$$v_{\mu\nu}^\alpha = \frac{1}{2\sqrt{\omega_\mu \omega_\nu}} \sum_{\ell,\beta,\ell',\beta'} (u_{\ell\alpha} - u_{\ell'\alpha}) \mathsf{D}_{\ell\ell'\beta\beta'} \eta_{\mu\ell\beta} \eta_{\nu\ell'\beta'}. \tag{5.11}$$

The (classical) thermal conductivity tensor is given by the GK formula, Eq. (1.50), i.e.

$$\kappa_{\alpha\beta} = \frac{1}{\Omega k_B T} \int_0^\infty \langle J_E^\alpha(t) J_E^\beta(0) \rangle \, dt \,, \tag{5.12}$$

where, in principle, the expectation value is taken over the canonical ensemble of systems defined by the Hamiltonian in Eq. (5.9). When the expression of the energy flux, Eq. (5.10) is plugged into Eq. (5.12), there appear four-point correlation functions in the amplitudes, i.e. terms of the form

$$\langle x_1 x_2 x_3 x_4 \rangle \,, \text{ with } x_{1,2} = \alpha_\mu(t), \alpha_\mu^*(t), \text{ and } x_{3,4} = \alpha_\mu, \alpha_\mu^*. \tag{5.13}$$

Such quantities cannot be computed exactly but in particularly simple cases, so an approximation scheme is required. The QHGK method deals with correlation functions of this form by introducing two distinct approximations [104, 105, 108]:

1. four-point correlation functions are factorized according to Wick (in the quantal case) or Isserlis (in the classical case) theorems into sums of products of two-point correlation functions. Thus

$$\begin{aligned} \hbar^2 \langle \alpha_\mu^*(t) \alpha_\nu(t) \alpha_\lambda^* \alpha_\sigma \rangle \approx n_\mu n_\lambda \delta_{\mu\nu} \delta_{\lambda\sigma} + \\ + \hbar^2 \langle \alpha_\mu^*(t) \alpha_\mu(0) \rangle \langle \alpha_\nu(t) \alpha_\nu^*(0) \rangle \delta_{\mu\sigma} \delta_{\nu\lambda}, \end{aligned} \tag{5.14}$$

   where $n_\mu = k_B T/(\hbar\omega_\mu)$ is the classical occupation of the μth normal mode.[1] In the many-body community, this is referred to as *dressed-bubble approximation*, and it amounts to neglecting vertex corrections to the correlation functions, i.e., phonon decay channels are treated in a mean-field sense, each channel being considered independently as if it were interacting with a heat bath.

1 The $\hbar$ factors are there to provide the correct quantum limit, where $\alpha \mapsto \sqrt{\hbar}\hat{a}$ and $n_\mu \mapsto (e^{\hbar\omega_\mu/(k_B T)} - 1)^{-1}$, the latter being the Bose-Einstein occupation function.

2. The heat bath interacts with the normal modes in a Markovian way, without any memory effect. This results in a two-point correlation function of the form [108]

$$\hbar \langle \alpha_\mu(t)\alpha_\mu^*(t)\rangle \approx n_\mu e^{-i\omega_\mu t-\gamma_\mu|t|}, \tag{5.15}$$

where the *line-width* γ_μ is the decay rate of the μth normal mode.

With these approximations, the thermal conductivity tensor takes the form reminiscent of Boltzmann's kinetic theory [104, 105, 108],

$$\kappa_{\alpha\beta} = \frac{k_B}{\Omega}\sum_{\mu\nu} v_{\mu\nu\alpha}v_{\mu\nu\beta}\tau_{\mu\nu}, \tag{5.16}$$

where

$$v_{\mu\nu\alpha} = \frac{1}{2\sqrt{\omega_\mu\omega_\nu}}\sum_{\ell\ell'\beta\beta'}(R^\circ_{\ell\alpha}-R^\circ_{\ell'\alpha})\mathsf{D}_{\ell\ell'\beta\beta'}\eta_{\mu\ell\beta}\eta_{\nu\ell'\beta'} \tag{5.17}$$

is the generalized velocity tensor, and

$$\tau_{\mu\nu} = \frac{\gamma_\mu+\gamma_\nu}{(\gamma_\mu+\gamma_\nu)^2+(\omega_\mu-\omega_\nu)^2} \tag{5.18}$$

is the generalized normal-mode lifetime. Eq. (5.16) applies to crystalline solids as well as amorphous ones. In the former case, it reduces to the result of the Boltzmann Transport Equation (BTE) for crystals in the Relaxation Time Approximation (RTA), with the bonus of explicitly accounting for inter-band effects [104, 105, 108]; in the latter case, the QHGK theory provides an anharmonic generalization of the Allen-Feldman (AF) theory of harmonic glasses [109, 110]. Interestingly, an equivalent expression can be obtained starting from the so-called Wigner Transport Equation rather than the BTE [106]. Let us briefly review both the BTE and AF approaches.

5.3 BOLTZMANN TRANSPORT EQUATION

In crystals, atomic equilibrium positions are characterized by a discrete lattice coordinate, $\mathbf{a}_\ell$, and an integer label, b_ℓ, enumerating the different coordinates of the basis sites within a unit cell, $\mathbf{d}_{b_\ell}$. The equilibrium position of the ℓth atom thus reads $\mathbf{R}^\circ_\ell = \mathbf{a}_\ell + \mathbf{d}_{b_\ell}$. For the same reason, normal modes can be labeled by a wavevector $\mathbf{q}$ in the reciprocal lattice Brillouin Zone (BZ) and a band index s, so that the normal-mode label is split to $\mu = (\mathbf{q}_\mu, s_\mu)$. The dynamical matrix can thus be expressed as

$$\frac{1}{\sqrt{M_\ell M'_\ell}}\phi''_{\ell\ell'\alpha\alpha'} = \sum_{\mathbf{q}} e^{i\mathbf{q}\cdot(\mathbf{R}^\circ_\ell-\mathbf{R}^\circ_{\ell'})}\mathsf{D}_{bb'\alpha\alpha'}(\mathbf{q}), \tag{5.19}$$

and it fulfills the eigenvalue equation

$$\sum_{b',\alpha'}\mathsf{D}_{bb'\alpha\alpha'}(\mathbf{q})\eta_{\mathbf{q}sb'\alpha'} = \omega^2_{\mathbf{q}s}\eta_{\mathbf{q}sb\alpha}, \tag{5.20}$$

where the eigenvectors are now given by $\eta_{\mathbf{q}_\mu s_\mu b_\ell \alpha} = e^{i\mathbf{q}_\mu \cdot \mathbf{R}^\circ_\ell} \eta_{\mu\ell\alpha}$. In this representation, the velocity matrix, Eq. (5.17), and the generalized lifetimes, Eq. (5.18), become block-diagonal in the wavevector subspace [104]:

$$v_{\mathbf{q}s\mathbf{q}'s'\alpha} = \frac{i\delta_{\mathbf{q}\mathbf{q}}}{\sqrt{\omega_{\mathbf{q}s}\omega_{\mathbf{q}'s'}}} \sum_{\ell\ell'\sigma\sigma'} \eta_{\mathbf{q}sb_\ell\sigma} \frac{\partial D_{b_\ell b'_{\ell'}\sigma\sigma'}(\mathbf{q})}{\partial q_\alpha} \eta_{\mathbf{q}sb'_{\ell'}\sigma'} \equiv v_{\mathbf{q}ss'\alpha}\delta_{\mathbf{q}\mathbf{q}'}, \quad (5.21)$$

$$\tau_{\mathbf{q}s\mathbf{q}'s'} = \frac{\gamma_{\mathbf{q}s} + \gamma_{\mathbf{q}s'}}{(\gamma_{\mathbf{q}s} + \gamma_{\mathbf{q}s'})^2 + (\omega_{\mathbf{q}s} - \omega_{\mathbf{q}s'})^2} \delta_{\mathbf{q}\mathbf{q}'}\tau_{\mathbf{q}ss'}. \quad (5.22)$$

where $\tau_{\mathbf{q}s} = 1/(2\gamma_{\mathbf{q}s})$ is the lifetime of the normal mode labeled by $(\mathbf{q}, s)$. The thermal conductivity tensor acquires the form

$$\kappa_{\alpha\beta} = \frac{k_B}{\Omega} \sum_{\mathbf{q},s,s'} v_{\mathbf{q}ss'\alpha} v_{\mathbf{q}ss'\beta} \tau_{\mathbf{q}ss'}. \quad (5.23)$$

In the case where the phononic bands are well separated, i.e., when, for any wavevector $\mathbf{q}$, it holds that $|\omega_{\mathbf{q}s} - \omega_{\mathbf{q}s'}| \gg \gamma_{\mathbf{q}s} + \gamma_{\mathbf{q}s'}$ for $s \neq s'$, the generalized lifetimes become diagonal in the band index, with $\tau_{\mathbf{q}ss'} = \delta_{ss'}/(2\gamma_{\mathbf{q}s})$, and κ finally reads

$$\kappa_{\alpha\beta} = \frac{k_B}{\Omega} \sum_{\mathbf{q},s} v_{\mathbf{q}s\alpha} v_{\mathbf{q}s\beta} \tau_{\mathbf{q}s}, \quad (5.24)$$

where $v_{\mathbf{q}s\alpha}$ is the group velocity of the sth phonon branch:

$$v_{\mathbf{q}s\alpha} = \frac{1}{2\omega_{\mathbf{q}s}} \sum_{\ell\ell'\sigma\sigma'} \eta_{\mathbf{q}sb_\ell\sigma} \frac{\partial D_{b_\ell b'_{\ell'}\sigma\sigma'}(\mathbf{q})}{\partial q_\alpha} \eta_{\mathbf{q}sb'_{\ell'}\sigma'} = \frac{\partial \omega_{\mathbf{q}s}}{\partial q_\alpha}. \quad (5.25)$$

This expression for the thermal conductivity does not include inter-band scattering events. Eq. (5.24) can be obtained in the BTE approach, where one considers the expression for the nonequilibrium phonon population, $\overline{n}_{\mathbf{q}s\alpha}$, in response to a thermal gradient along the Cartesian direction α, $\nabla_\alpha T = \partial T/\partial r_\alpha$, i.e. [105]

$$\overline{n}_{\mathbf{q}s\alpha} \simeq n_{\mathbf{q}s} + \lambda_{\mathbf{q}s}\nabla_\alpha n_{\mathbf{q}s} = n_{\mathbf{q}s} + \lambda_{\mathbf{q}s} \frac{\partial n_{\mathbf{q}s}}{\partial T} \nabla_\alpha T, \quad (5.26)$$

where $\lambda_{\mathbf{q}s}$ is the phonon mean free path. The energy flux can be written as the sum over phonons of the energy carried by each phonon branch times their group velocity, i.e., using Eq. (5.26),

$$\begin{aligned} J^{\text{kin}}_{E\ \alpha} &= \frac{1}{\Omega} \sum_{\mathbf{q},s} \sum_{\alpha'} \hbar\omega_{\mathbf{q}s} v_{\mathbf{q}s\alpha'} (\overline{n}_{\mathbf{q}s\alpha'} - n_{\mathbf{q}s}) \\ &\simeq -\frac{1}{\Omega} \sum_{\alpha'} \sum_{\mathbf{q},s} \hbar\omega_{\mathbf{q}s} \lambda_{\mathbf{q}s} \frac{\partial n_{\mathbf{q}s}}{\partial T} \nabla_\alpha T. \end{aligned} \quad (5.27)$$

Since the phenomenological Fourier's law (cf Ch. 1) reads $J^{\text{kin}}_{E,\alpha} = -\sum_\beta \kappa_{\alpha\beta}\nabla_\beta T$, one can identify the thermal conductivity with

$$\begin{aligned} \kappa_{\alpha\beta} &= \frac{1}{\Omega} \sum_{\mathbf{q},s} \hbar\omega_{\mathbf{q}s} \frac{\partial n_{\mathbf{q}s}}{\partial T} v_{\mathbf{q}s\alpha} \lambda_{\mathbf{q}s} \\ &= \frac{k_B}{\Omega} \sum_{\mathbf{q},s} v_{\mathbf{q}s\alpha} \lambda_{\mathbf{q}s}. \end{aligned} \quad (5.28)$$

The phonon mean free path can be computed by introducing the BTE,

$$\mathbf{v}_{\mathbf{q}s} \cdot \nabla T \frac{\partial n_{\mathbf{q}s}}{\partial T} = \left.\frac{\partial n_{\mathbf{q}s}}{\partial t}\right|_{\text{scatt.}}, \tag{5.29}$$

that governs the nonequilibrium statistical mechanics of the population numbers. The right-hand side is the *scattering term*, whose linearized form contains all the scattering rates relating 3-phonon scattering events [105]. The inverse of the matrix of scattering rates is in turn used to compute the phonon mean free paths. The problem of computing κ is reduced to the calculation and inversion of the scattering rates matrix. The full BTE solution can be computationally demanding since matrix inversion is an intensive task. A simplifying approximation that usually works well at high enough temperature is the RTA, where only the diagonal part of the scattering-rate matrix is retained: the population of each nonequilibrium mode is assumed to be interacting with a bath of modes at thermal equilibrium. The RTA mean free paths are given by $\lambda_{\mathbf{q}s\alpha} = v_{\mathbf{q}s\alpha}/(2\gamma_{\mathbf{q}s}) = v_{\mathbf{q}s\alpha}\tau_{\mathbf{q}s}$, where $\gamma_{\mathbf{q}s}$ is usually computed from perturbation theory with Fermi's golden rule [43, 105, 108]. Eq. (5.28) becomes therefore the same as Eq. (5.24):

$$\begin{aligned}\kappa_{\alpha\beta} &= \frac{k_B}{\Omega}\sum_{\mathbf{q},s} v_{\mathbf{q}s\alpha}\lambda_{\mathbf{q}s} \\ &= \frac{k_B}{\Omega}\sum_{\mathbf{q},s} v_{\mathbf{q}s\alpha}v_{\mathbf{q}s\beta}\tau_{\mathbf{q}s}\end{aligned} \tag{5.30}$$

This proves that the QHGK method generalizes the RTA-BTE method for crystals including the effect of inter-band scattering.

Noticing that Eq. (5.23) contains also all the terms in Eq. (5.30), in crystals one can easily go one step beyond the QHGK theory by substituting the intra-band part of κ with the full-BTE solution. Recently, the QHGK theory has also been extended to account for all the scattering terms for general solids, without the requirement of lattice periodicity [108].

5.4 ALLEN-FELDMAN MODEL

The AF model describes the heat dissipation due to disorder alone in amorphous systems of harmonically interacting particles [109, 110]. The starting point for the derivation of the AF expression for the thermal conductivity is again the GK formula for $\kappa_{\alpha\beta}$, Eq. (5.12). The only difference with the QHGK derivation is in the expression for the two-point correlation function of the phononic amplitudes, that in the AF model does not contain anharmonic terms:

$$\hbar\,\langle \alpha_\mu(t)\alpha^*_\mu(t)\rangle \approx n_\mu e^{-i\omega_\mu t}. \tag{5.31}$$

The same algebraic steps that lead to Eq. (5.16) in this case yields

$$\kappa_{\alpha\beta} = \frac{\pi k_B}{\Omega}\sum_{\mu\nu} v_{\mu\nu\alpha}v_{\mu\nu\beta}\delta(\omega_\mu - \omega_\nu), \tag{5.32}$$

which is the result of the (classical) AF theory [109, 110]. This expression can be obtained *a posteriori* from the QHGK value, Eq. (5.16), by taking the harmonic limit, $\gamma_\mu \to 0$, and using the nascent delta function

$$\delta(x) = \lim_{\epsilon\to 0}\frac{1}{\pi}\frac{\epsilon^2}{\epsilon^2 + x^2}. \tag{5.33}$$

This proves that the QHGK approach generalizes the AF model to the anharmonic regime.

5.5 SLACK MODEL

Since it will be useful in the next Chapter, I will briefly review here a model for thermal conductivity in crystals popularized in the 1970s [111, 112] called Slack Model (SM). For a crystal with n atoms per unit cell, whose average atomic mass is $\overline{M}$, the (quantum) thermal conductivity in $\mathrm{Wm^{-1}K^{-1}}$ is estimated as

$$\kappa = \frac{2.43 \cdot 10^{-6}}{1 - 0.514/\gamma + 0.228/\gamma^2} \frac{\overline{M}\Theta_D^3 \delta}{\gamma^2 T n^{2/3}}, \tag{5.34}$$

where Θ_D is the Debye temperature in K, $\gamma = \sum_\mu \frac{\Omega}{\omega_\mu} \frac{\partial \omega_\mu}{\partial \Omega}$ is the Grüneisen parameter, δ is the cubic root of the average atomic volume in Å, and $\overline{M}$ is expressed in atomic mass units. The Debye temperature is computed directly from the Debye model, by evaluating the average sound velocity obtained from the angular average of the sound velocities, which are in turn calculated by solving the wave equation for each propagation direction. Eq. (5.34) is valid for face-centered-cubic crystals with one atom per unit cell and approximated in all the other cases. It is known to overestimate the value of thermal conductivity [113], and its popularity in the past decades is mainly due to the unavailability at the time of more accurate computer simulations based, e.g., on the BTE.

5.6 THERMAL CONDUCTIVITY FROM MOLECULAR DYNAMICS SIMULATIONS

In EMD one can compute the thermal conductivity by evaluating the GK formula, as explained in Ch. 1 and Ch. 2. The explicit expression of the energy flux depends on the Hamiltonian of the system. In the context of atomistic simulations, the interatomic potential energy is often described in terms of Force Fields (FFs), i.e. analytical functions of the relative distance among the constituents of the system able to yield the forces acting on the atoms. Empirical FFs are characterized by the functional form of the inter-atomic potential energy and the set of parameters tuned to reproduce physical properties. The parameters can be obtained by fitting the functional form of the FF to experimental data or to accurate quantum chemistry calculations. In recent years, also machine-learning-based FFs have appeared, able to reproduce with high-accuracy *ab initio* results with affordable computational time [114–116]. The Hamiltonian in both these cases takes the general form

$$\mathcal{H}(\{\mathbf{P}\}, \{\mathbf{R}\}) = \sum_{\ell=1}^{N} \frac{P_\ell^2}{2M_\ell} + \mathcal{V}(\{\mathbf{R}\}), \tag{5.35}$$

where $\{\mathbf{R}\}$ and $\{\mathbf{P}\}$ are the positions and momenta of the atoms in the system, respectively. In light of the gauge invariance principle (cf Sec. 1.4), any atomic

decomposition of the energy density, $e(\mathbf{r}, t)$, is good to compute the energy flux. A valid choice is

$$e(\mathbf{r}, t) = \sum_{\ell=1}^{N} \epsilon_\ell(t)\delta(\mathbf{r} - \mathbf{R}_\ell(t)), \tag{5.36}$$

where each atomic energy, ϵ_ℓ, is localized on the respective atom. The atomic energies are phase-space variables and depend on time through the positions and the momenta of the atoms. The energy flux reads

$$\begin{aligned} \mathbf{J}_E(t) &= \frac{1}{\Omega}\int \mathbf{r}\dot{e}(\mathbf{r}, t)\,\mathrm{d}^3 r \\ &= \frac{1}{\Omega}\int \mathbf{r}\sum_{\ell=1}^{N}\left[\frac{\partial e(\mathbf{r}, t)}{\partial \mathbf{R}_\ell}\cdot\dot{\mathbf{R}}_\ell + \frac{\partial e(\mathbf{r}, t)}{\partial \mathbf{P}_\ell}\cdot\mathbf{f}_\ell\right]\mathrm{d}^3 r, \end{aligned} \tag{5.37}$$

where $\mathbf{f}_\ell$ is the force acting on the ℓth atom. The atomic energies are quantities of the form

$$\epsilon_\ell = \frac{P_\ell^2}{2M_\ell} + \mathcal{V}_\ell, \tag{5.38}$$

the first term being the atomic kinetic energy, and the second being the portion of the potential energy assigned to the ℓth atom so that $\mathcal{V} = \sum_\ell \mathcal{V}_\ell$. The gradients appearing in Eq. (5.37) are evaluated as

$$\frac{\partial e(\mathbf{r}, t)}{\partial \mathbf{R}_\ell} = \sum_{\ell'=1}^{N}\left[\frac{\partial \mathcal{V}_{\ell'}}{\partial \mathbf{R}_\ell}\delta(\mathbf{r} - \dot{\mathbf{R}}_{\ell'}) - \delta_{\ell\ell'}\epsilon_{\ell'}\nabla\delta(\mathbf{r} - \mathbf{R}_{\ell'})\right] \tag{5.39}$$

$$\frac{\partial e(\mathbf{r}, t)}{\partial \mathbf{P}_\ell} = \dot{\mathbf{R}}_\ell\delta(\mathbf{r} - \mathbf{R}_\ell), \tag{5.40}$$

so that the energy flux becomes

$$\begin{aligned} \mathbf{J}_E(t) = \frac{1}{\Omega}\int \mathbf{r}\sum_{\ell,\ell'=1}^{N}\Bigg[&\frac{\partial \mathcal{V}_{\ell'}}{\partial \mathbf{R}_\ell}\cdot\dot{\mathbf{R}}_\ell\delta(\mathbf{r} - \mathbf{R}_{\ell'}) - \frac{\partial \mathcal{V}_{\ell'}}{\partial \mathbf{R}_\ell}\cdot\dot{\mathbf{R}}_\ell\delta(\mathbf{r} - \mathbf{R}_\ell) + \\ &- \epsilon_\ell\dot{\mathbf{R}}_\ell\nabla\delta(\mathbf{r} - \mathbf{R}_{\ell'})\Bigg]\mathrm{d}^3 r\,. \end{aligned} \tag{5.41}$$

Integrating by parts the last summand and using the properties of the Dirac delta, one finds:

$$\mathbf{J}_E(t) = \frac{1}{\Omega}\sum_{\ell=1}^{N}\left[\epsilon_\ell\dot{\mathbf{R}}_\ell - \sum_{\ell'=1}^{N}\frac{\partial \mathcal{V}_{\ell'}}{\partial \mathbf{R}_\ell}\cdot\dot{\mathbf{R}}_\ell\left(\mathbf{R}_\ell - \mathbf{R}_{\ell'}\right)\right]. \tag{5.42}$$

This formula is well-defined in PBCs since it only depends on distances between atoms computed according to the minimum-image convention. For this reason, the formula is suitable for EMD simulations of bulk systems. The first term in Eq. (5.42) is often called *kinetic* or *convective energy flux*, while the second is the *virial energy flux*.

5.6.1 *Ab initio heat transport*

The gauge invariance of transport coefficients also allows one to derive the adiabatic energy flux in the framework of DFT [13]. Such flux, dubbed Marcolongo-Umari-Baroni (MUB) energy flux from the name of the authors of Ref. 13, is obtained from the standard definition of the DFT total energy expressed in terms of the Kohn-Sham (KS) eigenvalues, ε_v, eigenfunctions, $\phi_v(\mathbf{r})$, and electronic density, $n(\mathbf{r}) = \sum_v |\phi_v(\mathbf{r})|^2$—the sum being over valence states—i.e.

$$\begin{aligned} E^{\mathrm{DFT}} = &\frac{1}{2}\sum_\ell M_\ell V_\ell^2 + \sum_\ell w_\ell^Z(\{\mathbf{R}\}) + \sum_v \varepsilon_v + \\ &- \frac{e^2}{2}\int \frac{n(\mathbf{r})n(\mathbf{r}')}{|\mathbf{r}-\mathbf{r}'|}\,\mathrm{d}^3r\,\mathrm{d}^3r' + \int (\epsilon^{\mathrm{XC}}[n](\mathbf{r}) - \mu^{\mathrm{XC}}(\mathbf{r}))n(\mathbf{r})\,\mathrm{d}^3r\,, \end{aligned} \tag{5.43}$$

where e is the elementary charge; $\mathbf{R}_\ell$ and $\mathbf{V}_\ell$ are the position and velocity of the ℓth nucleus, respectively; w_ℓ^Z is the ionic electrostatic energy; ϵ^{XC} is the local XC energy density, defined by the relation

$$E^{\mathrm{XC}}[n] = \int \epsilon^{\mathrm{XC}}[n](\mathbf{r})n(\mathbf{r})\,\mathrm{d}^3r\,, \tag{5.44}$$

where E^{XC} is the total XC energy; μ^{XC} is the XC potential

$$\mu^{\mathrm{XC}}(\mathbf{r}) = \frac{\delta E^{\mathrm{XC}}}{\delta n(\mathbf{r})} = \epsilon^{\mathrm{XC}}(\mathbf{r}) + \int \frac{\delta \epsilon^{\mathrm{XC}(\mathbf{r}')}}{\delta n(\mathbf{r})} n(\mathbf{r}')\,\mathrm{d}^3r' \tag{5.45}$$

The DFT energy density, required for the definition of the energy flux, can be defined by the property [13]

$$E^{\mathrm{DFT}} = \int e^{\mathrm{DFT}}(\mathbf{r})\mathrm{d}^3r, \tag{5.46}$$

$$e^{\mathrm{DFT}}(\mathbf{r}) = e^{\mathrm{KS}}(\mathbf{r}) + e^0(\mathbf{r}) + e^{\mathrm{H}}(\mathbf{r}) + e^{\mathrm{XC}}(\mathbf{r}). \tag{5.47}$$

The quantities in the second line above are defined in terms of the instantaneous KS Hamiltonian, $\hat{\mathcal{H}}^{\mathrm{KS}}$, and its eigenvalues and eigenfunctions:

$$e^{\mathrm{KS}}(\mathbf{r}) = \mathrm{Re}\sum_v \phi_v^*(\mathbf{r})\hat{\mathcal{H}}^{\mathrm{KS}}\phi_v(\mathbf{r}), \tag{5.48}$$

$$e^0(\mathbf{r}) = \sum_\ell \delta(\mathbf{r}-\mathbf{R}_\ell)\left[\frac{P_\ell^2}{2M_\ell} + w_\ell^Z\right], \tag{5.49}$$

$$e^{\mathrm{H}}(\mathbf{r}) = -\frac{1}{2}n(\mathbf{r})v^{\mathrm{H}}(\mathbf{r}), \tag{5.50}$$

$$e^{\mathrm{XC}}(\mathbf{r}) = (\epsilon^{\mathrm{XC}}(\mathbf{r}) - \mu^{\mathrm{XC}}(\mathbf{r}))n(\mathbf{r}). \tag{5.51}$$

The MUB energy flux is obtained by integrating the first moment of the time-derivative of the energy density, and the final expression takes the form

$$\mathbf{J}_E^{\mathrm{MUB}} = \mathbf{J}^{\mathrm{KS}} + \mathbf{J}^0 + \mathbf{J}^n + \mathbf{J}^{\mathrm{H}} + \mathbf{J}^{\mathrm{XC}}, \tag{5.52}$$

the terms being

$$\mathbf{J}^{\mathrm{KS}} = \sum_v \Big(\langle\phi_v|\hat{\mathbf{r}}\hat{\mathcal{H}}^{\mathrm{KS}}|\dot{\phi}_v\rangle + \varepsilon_v \langle\dot{\phi}_v|\hat{\mathbf{r}}|\phi_v\rangle \Big)\,, \tag{5.53}$$

$$\mathbf{J}^0 = \sum_{\ell,\mathbf{L}} \sum_{v} \langle (\hat{\mathbf{r}} - \mathbf{R}_\ell - \mathbf{L}) | \dot{\mathbf{R}}_\ell \cdot \nabla_{\ell\mathbf{L}} \hat{v}^0 | \phi_v \rangle \,, \tag{5.54}$$

$$\begin{aligned} \mathbf{J}^n = \sum_{\ell} [\, \dot{\mathbf{R}}_\ell e^0_\ell + \sum_{\ell' \neq \ell} \sum_{\mathbf{L}} (\mathbf{R}_\ell - \mathbf{R}_{\ell'} - \mathbf{L}) (\dot{\mathbf{R}}_{\ell'} \cdot \nabla_{\ell'\mathbf{L}} w^Z_{\ell'}) + \\ - \sum_{\mathbf{L} \neq 0} \mathbf{L} (\dot{\mathbf{R}}_\ell \cdot \nabla_{\ell'\mathbf{L}} w^Z_\ell) \,] \,, \end{aligned} \tag{5.55}$$

$$\mathbf{J}^{\mathrm{H}} = \frac{1}{4\pi e^2} \int \dot{v}^{\mathrm{H}}(\mathbf{r}) \nabla v^{\mathrm{H}}(\mathbf{r}) \mathrm{d}^3 r, \tag{5.56}$$

$$\mathbf{J}^{\mathrm{XC}} = \begin{cases} 0, & \text{LDA}, \\ - \int n(\mathbf{r}) \dot{n}(\mathbf{r}) \boldsymbol{\partial} \epsilon^{\mathrm{GGA}}(\mathbf{r}) \mathrm{d}^3 r, & \text{GGA}. \end{cases} \tag{5.57}$$

The symbol $\mathbf{L}$ indicates a lattice vector; $\nabla_{\ell\mathbf{L}}$ is a shorthand notation for the gradient with respect to the position of the ℓth nucleus in the replica cell characterized by the lattice vector $\mathbf{L}$; LDA and GGA stand for Local Density Approximation and Generalized Gradient Approximation of the XC functional, respectively; in the GGA case, the derivative with respect to the density gradients of the XC local energy per particle is indicated by $\boldsymbol{\partial}\epsilon^{\mathrm{GGA}}$ [13, 117]. All the formulæ reported above are valid within PBCs. This machinery is implemented in Quantum ESPRESSO as the `QEHeat` package [117].

Once the energy flux is available, be it through Eq. (5.42) for atomistic coarse-grained models, or Eq. (5.52) in the case of first-principle simulations, it can be analyzed according to the techniques described in Ch. 2 to obtain an estimate of the thermal conductivity.

6 SOLID-STATE ELECTROLYTES

A PROPER ACCOUNT of heat dissipation is key in the design and actual production of batteries: in fact, an excessively low thermal conductivity may lead to overheating, especially during fast charging cycles, which may itself prompt catastrophic incidents, such as melting or explosion. In light of this, thermal runaway can be rightly considered *the key scientific problem in battery safety research* (verbatim from Ref. 118). In addition, thermal dissipation governs energy saving and scavenging: a compromise must be established between minimizing heat losses while at the same time maximizing electric flow during the charging cycle.

In spite of this, a relatively small number of experimental studies on heat dissipation in fast ionic conductors have been reported in the past years, if compared to the extensive literature on electric transport. There exist experimental measurements performed on superionic materials such as α-$LiIO_3$ and $Li_2B_4O_7$ [119, 120]; sulfates Li_2SO_4 and Ag_2SO_4 [121]; the quasi-1D material $LiCuVO_4$ [122]; lithium aluminum germanium phosphate glass–ceramics compounds of the form $Li_{1+x}Al_xGe_{2-x}(PO_4)_3$ [123]; yttrium-stabilized lithium zirconate phosphates, of the form $Li_{1+x+y}Y_xZr_{2-x}(PO_4)_3$ [124]. Of these, only the last two classes of materials can be directly used as SSEs. From the theoretical standpoint, even fewer works are to be found. Even though some models that account for the contribution of the diffusing ions to thermal transport were introduced in the past decades [125, 126], a thorough study of heat dissipation in SSEs is still missing. The few numerical calculations that can be found in the literature, moreover, are based on lattice-dynamics methods that, by construction, assume that, at all times, atoms are bound to be close to fixed equilibrium positions: in other words, such methods do not include the effect of diffusing ions, which are present in SSEs and are responsible for the nonzero ionic conductivity of such materials. This limitation, stemming from a phonon(/normal-mode)-based approach to heat transport, can be naturally and easily bypassed through the GK theory of linear response which, as seen in Ch. 1 and Ch. 5, holds for solids with anharmonic interactions of any strength, as well as for diffusing systems, such as liquids and superionic solids.

The content of this Chapter is based on Ref. 36, a work I coauthored with my Ph.D. advisors Stefano Baroni and Federico Grasselli about heat transport in the SSE candidate Li_3ClO. Sec. 6.1 contains an adaptation of the published article with slight modifications in the text and in the presentation of the figures, in order for it to fit in with the rest of the thesis.

6.1 TEMPERATURE AND VACANCY-CONCENTRATION DEPENDENCE OF HEAT TRANSPORT IN LI_3CLO

To the best of our knowledge, there exists only one calculation of the thermal conductivity, κ, of Li_3ClO, reporting $\kappa = 22.49\,\mathrm{W\,m^{-1}\,K^{-1}}$ at ambient temperature, i.e., more than one order of magnitude larger than the standard value found in ceramic SSEs [123, 124]. Nonetheless, this seemingly promising result

is obtained via a rather crude approximation to the BTE, namely the SM, known since its development to have a satisfactory agreement with the experiments (i.e., within $\pm 20\%$) only for exceedingly simple materials, such as the rare-gas solids, while it is, in general, poorer for other systems [112]. Furthermore, the SM totally neglects the effects of defects or vacancies and, just like any BTE-based model, it cannot handle the spurious contributions to heat transport induced by the diffusion of Li ions.

We first address the structural and mechanical properties of Li_3ClO, along with their temperature dependence, by means of state-of-the-art *ab initio* calculations based on DFT. Leveraging these results, we then explore the thermal transport of Li_3ClO by calculating its thermal conductivity within

i. the SM;

ii. the BTE;

iii. the GK theory and classical EMD simulations using both classical FFs and machine-learnt interatomic potentials trained on DFT data.

Our results show that the presence of LiCl divacancies in nonstoichiometric systems, though increasing the Li-ion diffusivity, strongly reduces the thermal conductivity—and thus heat dissipation within the electrolyte—with respect to stoichiometric conditions. We find that the dependence of κ on temperature is also reduced, thus making it potentially easier to engineer devices that can safely and efficiently operate in a wide range of temperatures.

The lithium-rich antiperovskite SSE Li_3ClO has emerged in the last decade as a promising candidate for all-solid-state lithium-metal batteries: it is superionic at room temperature with a large ionic conductivity; it is environmentally friendly and made of light and cheap elements; it is not flammable and has demonstrated a good cyclability [127]. Furthermore, its wide electronic band gap leads to a very low electronic conductivity and a large electrochemical stability window [128]. Finally, it is also chemically stable against Li-metal formation, which would negatively affect the battery performance via dendritic short circuits.

Before addressing thermal transport (Sec. 6.1.5), we investigate the structural (Sec. 6.1.1), electronic (Sec. 6.1.2), vibrational (Sec. 6.1.3), and mechanical (Sec. 6.1.4) properties of Li_3ClO, along with their temperature dependence, and we extensively compare our *ab initio* results with the existing literature. These results are not only preliminary to the calculation of transport coefficients, but they also make it possible to draw some general conclusions on the deployment of Li_3ClO for mass production of SSE-based batteries: ductility, stiffness, the magnitude of the mismatch in the lattice constants or in the thermal expansion coefficients between the SSE and the electrodes govern the extent and amplitude of local stresses, particularly at the SSE-electrode junction, and affect the overall performance of Li_3ClO in a real device by either hindering or inducing cracks, mechanical instabilities, or spurious electric fields.

6.1.1 *Structural properties*

The crystal structure of Li_3ClO has the $Pm\bar{3}m$ perovskite space group. The dependence of the lattice parameter on temperature is obtained in the Quasi-Harmonic Approximation (QHA) [129], using the vibrational frequencies com-

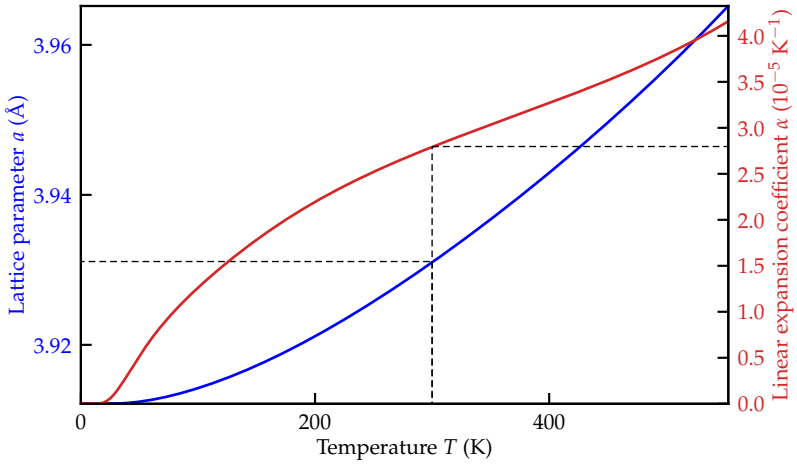

Figure 6.1: QHA structural parameters. Lattice parameter (blue, left y-label) and linear thermal expansion coefficient (red, right y-label) as a function of temperature.

puted as explained in Sec. 6.1.3 and the Murnaghan equation of state [130]. The resulting zero-temperature value, explicitly accounting for zero-point vibrational effects, is 3.91 Å, while the full temperature dependence is reported in Fig. 6.1. The lattice parameter and thermal expansion coefficient computed at Room Temperature (RT), with RT $= 300$ K, are 3.93 Å and $2.77 \cdot 10^{-5}\,\mathrm{K}^{-1}$, respectively, in good agreement with the values previously obtained in other works: Zhang *et al.* [131], Emly *et al.* [132], and Wu *et al.* [133] reported an optimized lattice parameter without the zero-point of 3.85 Å, 3.90 Å, and 3.91 Å, respectively; Braga *et al.* [127] provided both experimental and theoretical data in accordance with one another, namely 3.91 Å [127, 134]. For the linear thermal expansion coefficient, Zhang *et al.* [131] reported a value of $2.11 \times 10^{-5}\,\mathrm{K}^{-1}$ using molecular dynamics simulations in the isothermal-isobaric (NpT) ensemble, while Wu *et al.* [133] reported $\alpha = 3.12 \times 10^{-5}\,\mathrm{K}^{-1}$ within the QHA, in good agreement with our calculation. Braga *et al.* [127] found the larger value $4.65 \times 10^{-5}\,\mathrm{K}^{-1}$ from the slope of the lattice parameter as a function of temperature.

6.1.2 *Electronic band structure*

The electronic band structure of Li_3ClO (Fig. 6.2) exhibits a direct band gap of 6.46 eV at the M in the BZ at the HSE06 level of theory, in good agreement with the values obtained by Wu *et al.* [133] (6.46 eV) and by Emly *et at.* [132], thus making Li_3ClO a wide band-gap insulator and preluding good electrochemical stability.

6.1.3 *Vibrational properties*

The phonon dispersion along high-symmetry lines in the are plotted in Fig. 6.3 together with the corresponding Vibrational Density Of States (VDOS). Notice

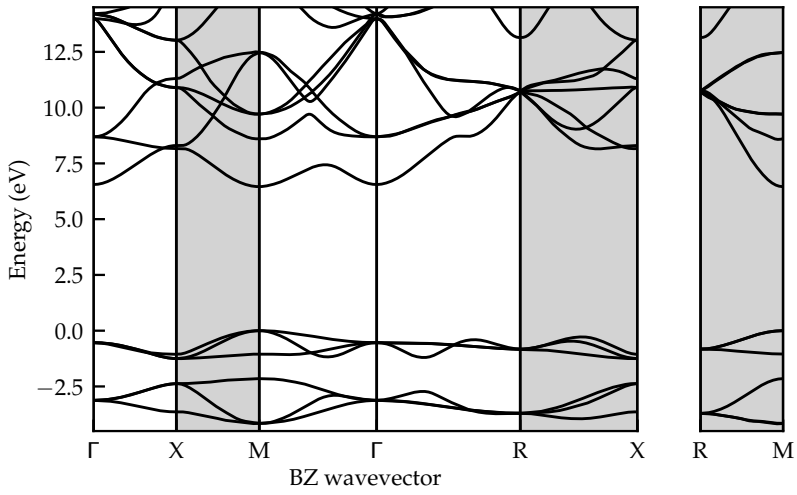

Figure 6.2: Electronic band dispersion of Li_3ClO plotted along high-symmetry lines in the BZ. Grey-shaded areas represent lines that lay on the BZ border.

the presence of a large Longitudinal Optical-Transverse Optical (LO-TO) splitting in the infrared-active mode at the center of the BZ (Γ point), due to the non-analytic behavior of the dynamical matrices induced by the long-range (Coulomb) tails of the inter-atomic interactions. It has been pointed out that a proper account of these tails is essential not only for a correct qualitative description of the vibrational spectrum in the optic region but also for an accurate evaluation of the thermal conductivity, which is more sensitive to the low-frequency portion of the spectrum [135]. The effect of a proper account of the LO-TO splitting on the value of the lattice thermal conductivity of Li_3ClO is examined in Sec. 6.1.6.

The stability at zero temperature of this material has been debated, with different authors claiming the system to be either unstable [136] or stable [133]: methods are employed, the authors find soft modes (imaginary frequencies) at the M and R points in the BZ using a $6 \times 6 \times 6$ supercell. Since the instability is larger when a smaller ($3 \times 3 \times 3$) supercell is used, the occurrence of lattice instabilities may be an artifact due to lack of convergence even when a supercell as large as $6 \times 6 \times 6$ unit cells is used in finite-difference calculations. Using perturbation theory at the zone-center of a supercell,[1] the authors of Ref. 133 do not find any dynamical instabilities. Our calculations, performed within DFPT, confirm the dynamical stability of this system.

6.1.4 *Temperature dependence of the mechanical properties*

Mechanical properties can have a deep influence on the fabrication of any device and, in particular, of alkali-ion solid-state batteries. An important aspect is that there must be good contact between the electrolyte and the electrodes during the activity of a device. A good SSE candidate must be able to sustain large

1 This by construction does not include Nonanalytic Contributions (NAC).

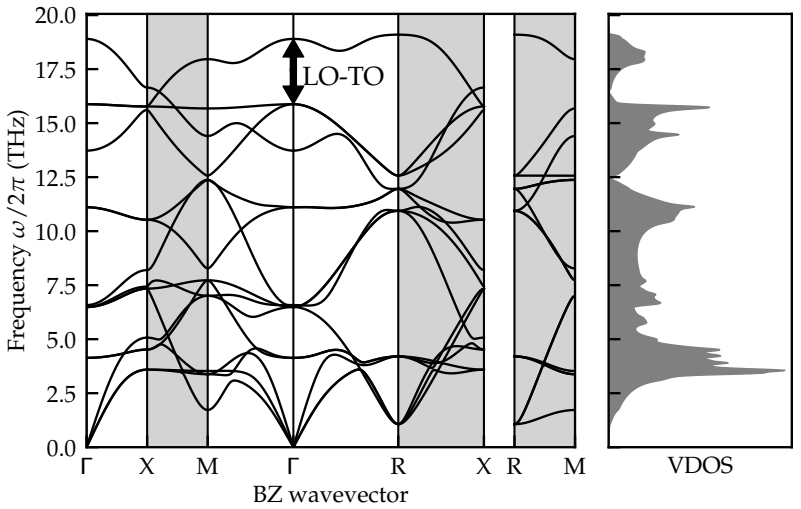

Figure 6.3: Phonon dispersion of Li_3ClO plotted along high-symmetry lines in the BZ and respective density of states. Grey-shaded areas represent lines that lay on the BZ border. The LO-TO splitting at Γ is evident.

strains [137] to prevent the interfaces with cathode and anode to deteriorate in response to the deformation thereof. In this light, excessive stiffness is a feature to be avoided. Another element to consider is the problem of Li deposition at the interface with the cathode, and the subsequent dendrite formation [138], which affects especially liquids. A solid material may partially overcome this obstacle by fine-tuning elastic properties such as the shear modulus and Poisson's ratio [139], even if it has been reported that dendrite growth can still occur for other reasons [140].

The three elastic moduli, namely the bulk modulus B, the Young modulus E, and the shear modulus G, measure how a material responds to volumetric, tensile, and shear stress, respectively; Poisson's ratio, ν, measures the strain response in a direction perpendicular to an applied strain; Pugh's ratio, B/G, is related to how materials are ductile as opposed to brittle. The Chung-Buessem [141] elastic anisotropy index, A_G, and the universal elastic anisotropy [142], A_U, provide a measure to quantify the extent of anisotropy in the elastic response of a crystal and are obtained from the Voigt and Reuss estimates of B and G [142]. The Grüneisen parameter γ is the variation of pressure with thermal energy density at constant volume [143]. All these quantities are computed as a function of temperature within the QHA. The isothermal and adiabatic elastic constants (C_{ij}) as a function of temperature are computed within the QSA.

The temperature dependence of these quantities is shown in Fig. 6.4. Their values at RT and at $T = 0$ are reported in Table 6.1, together with results already available in the literature [131, 137]. While our results at $T = 0$ are comparable with the ones found in other works, at the working temperature the quantities have lower values, in accordance with the fact that the material becomes softer when the temperature is increased. In particular, the temperature dependence

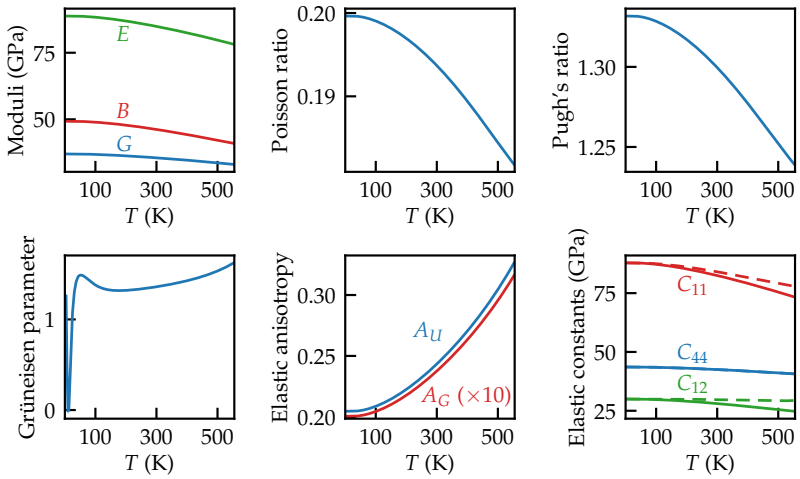

Figure 6.4: Temperature dependence of the macroscopic mechanical properties of Li_3ClO. The elastic constants are computed at the Quasi-Static Approximation (QSA) level; solid lines are isothermal elastic constants, while dashed lines are isoentropic. All the other quantities are computed according to the QHA.

of B and G entails that Pugh's ratio is also decreased, hinting at a greater brittleness [144] of Li_3ClO than previously predicted [133, 137]. Furthermore, the computed value of A_G is higher than what is found in the literature, suggesting that Li_3ClO is slightly more anisotropic than previously thought; this is confirmed by the value of A_U, which allows a broader comparison with other materials.

Table 6.1: Macroscopic mechanical properties of Li_3ClO at RT. For comparison, we report data from other calculations done at zero temperature.

	This work (RT)	This work ($T = 0$)	Ref. 137	Ref. 133
B (GPa)	46.01	48.87	55.70	51.36
E (GPa)	84.86	88.65	99.70	91.93
G (GPa)	35.58	37.01	41.50	38.25
ν	0.19	0.20	0.20	0.20
B/G	1.29	1.32	1.35	1.35
A_G	0.024	0.020	—	0.01
A_U	0.24	0.20	—	—
γ	1.30	1.86	—	—
C_{11} (GPa)	82.32	87.47	102.90	93.68
C_{12} (GPa)	27.85	29.57	32.10	30.20
C_{44} (GPa)	42.55	43.62	46.10	43.33

6.1.5 *Thermal conductivity*

Thermal conduction plays a key role in the quest for promising SSE for battery production. A high value of thermal conductivity is a favorable quality for a SSE candidate to have, since efficient heat dissipation allows the manufacture of safer batteries that do not overheat. A quite high value $\kappa = 22.49\,\mathrm{Wm^{-1}K^{-1}}$ was previously reported [133]. This result was obtained from SM [112], which is based on a rather crude approximation of the BTE [145–147]. At the same level of theory, we obtain $16.55\,\mathrm{W\,m^{-1}\,K^{-1}}$ that is 26% lower and it is likely to be closer to a realistic value. Yet, the coarseness of the approximation makes it impossible to draw conclusions: as already mentioned, the SM is known, since its formulation dating back to the 1960s, to be fairly accurate (to within 20%) only for simple systems such as rare-gas crystals, while it grossly fails for more complex materials. The main issue is to be addressed to the cubic dependence of κ on the Debye temperature Θ_D of the crystal, which itself depends dramatically on the parameters used to estimate it. For instance, if the lattice parameter is reduced by less than 2%, i.e., from the value we compute (3.91 Å) to a value found in the literature [131] (3.85 Å), Θ_D increases by 4% (from 630 K to 653 K) and κ by 12% (from $16.6\,\mathrm{W\,m^{-1}\,K^{-1}}$ to $18.5\,\mathrm{W\,m^{-1}\,K^{-1}}$). This and further approximations in the model—it is for instance insensible to the crystal structure of the material—makes it impossible to produce reliable estimates for κ within the SM. For a more realistic calculation, the BTE must be treated in a detailed fashion relying on the explicit calculation (and inversion) of the phononic scattering-rate matrix to obtain the out-of-equilibrium occupation numbers of the phonons.

As reviewed in Sec. 5.3, the RTA approximates the thermal conductivity of a crystalline solid neglecting both the off-diagonal part of the scattering matrix and inter-band contributions. The accuracy of the RTA for the FF model of Li_3ClO is tested against the QHGK, the full-BTE, and their combination (I-QHGK) [108]; the relative difference between the RTA and the other two methods is shown in the left panel of Fig. 6.5: at low temperature (i.e. $T \lessapprox 200\,\mathrm{K}$) off-diagonal scattering is important, and the RTA underestimates the full-BTE result by up to 20%. At higher temperatures (i.e. $T \gtrapprox 300\,\mathrm{K}$) intra-band effects emerge and induce a relative deviation of the QHGK result with respect to RTA proportional to T. This means that, at RT or above, the RTA alone fails to properly capture the behavior of thermal conductivity. For the sake of comparing *ab initio* results, computed via genuine third-order perturbation theory as implemented in the `D3Q` code [148] distributed with Quantum ESPRESSO, with the FF and the SM ones, the RTA thermal conductivity as a function of temperature is shown in the right panel of Fig. 6.5. Since *ab initio* and FF are in good agreement, this suggests that the chosen classical FF is suitable for investigating the thermal transport properties of Li_3ClO.

As recently pointed out [149, 150], higher-order scattering events can drastically reduce the value of the lattice thermal conductivity; therefore, we test the effect of the inclusion of 4-phonon scattering into the computation of κ. As shown in Fig. 6.6, 4-phonon scattering is found to have a major role in determining the value of the lattice thermal conductivity, being able to reduce κ of at least 15% at RT, the reduction being larger for larger temperatures. Details on the calculation can be found in Sec. 6.1.6.

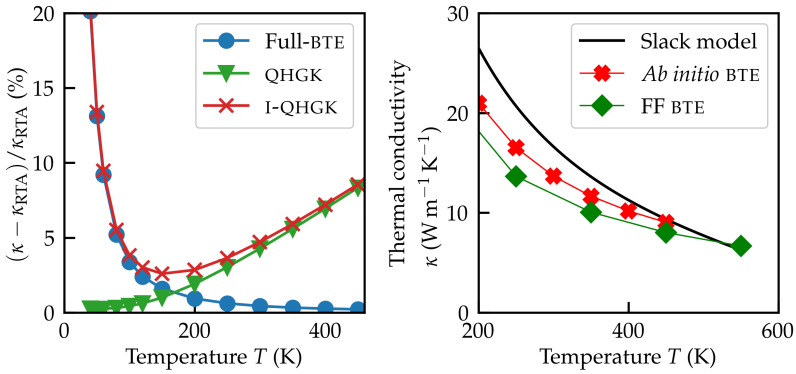

Figure 6.5: (*left*) Relative difference between the RTA and three different approaches: the full solution to the linearized BTE (full-BTE); the QHGK method; the QHGK result with the full-BTE for the intra-band terms (I-QHGK; cf Sec. 5.3 and Ref. 108, from which the data to generate this plot are taken). (*right*) Lattice thermal conductivity of Li_3ClO computed with different methods. RTA calculations include only 3-phonon scattering events.

These facts—the RTA being not enough at high temperature, and higher-order anharmonic effects being nonnegligible—call for a method able to include both higher-order scattering and inter-band effects: EMD simulations together with GK linear response theory (cf Ch. 1) naturally include all the orders of interactions and the full scattering matrix and are therefore a fitting candidate for this role.[2]

The choice of EMD comes with an additional benefit that is of fundamental importance for Li_3ClO: since fast-ion conduction in SSE materials is due to diffusing defects, lattice-dynamical methods are inadequate, as they require the atoms to have fixed equilibrium positions. EMD simulations are not subject to this prerequisite and, therefore, they allow us to access thermal transport in the diffusive regime where fast ion diffusion is mediated by vacancy hopping.

According to the comprehensive studies of Mouta *et al* [151] and Lu *et al* [152], LiCl Schottky pairs—divacancies generated by the removal of neutral groups of atoms that are deposited at the surface of the material—are more likely to appear and give rise to high Li-ion mobility than both other Schottky (Li_2O or Li_3ClO vacancies) and Frenkel (Li vacancies and interstitials) defects. Thus, the nonstoichiometric systems we study are of the form $Li_{3-x}Cl_{1-x}O$, with x the concentration of vacancies that varies between 0 (perfect crystal) and 0.1.

The classical FF described in Sec. 6.1.6 is used to carry out the EMD simulations and sample the energy flux, which in turn is employed to compute κ. To validate this, classical FFs calculations are compared to estimates of κ extracted from a Car-Parrinello AIMD simulation, on which the MUB energy flux is computed according to Ref. 13 as implemented in Ref. 117; and a model obtained via machine-learning techniques. The *ab initio* GK thermal conductivity requires a computationally demanding MUB energy flux (cf Sec. 5.6.1; it requires roughly

2 In EMD phonon occupations obey the equipartition law, while in a lattice-dynamical approach quantum effects can be easily accounted for. This leads to an underestimation of thermal conductivity in EMD with respect to anharmonic lattice dynamics at the same level of the theory. This is unimportant in the temperature of interest here. Further details can be found in Sec. 6.1.6.

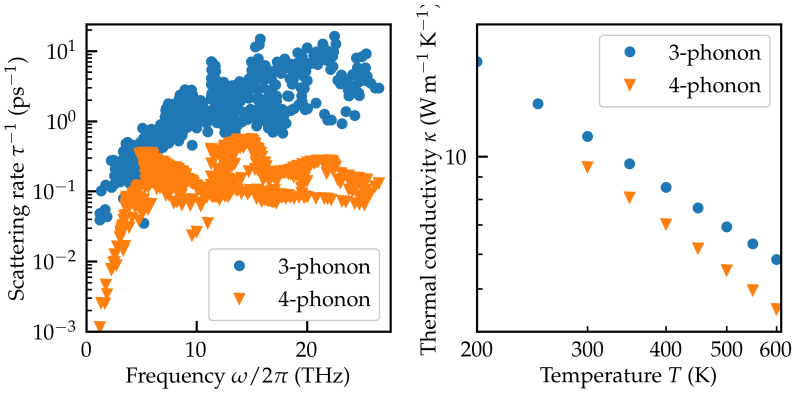

Figure 6.6: Effect of the inclusion of 4-phonon scattering. (*left*) The 4-phonon scattering rates—shown here are at RT—are non-negligible with respect to the three-phonon contribution. (*right*) The lattice thermal conductivity is consequently reduced.

twice the computational time of the AIMD simulation the trajectory is sampled from): therefore, a single calculation at RT is carried out for the sake of checking the accuracy of the FF. We obtain $\kappa_{\mathrm{MUB}} = 6.5 \pm 1.0\,\mathrm{W\,m^{-1}\,K^{-1}}$ at $T = 306\,\mathrm{K}$ on a $4 \times 4 \times 4$ supercell of crystalline Li_3ClO, in close agreement with results from classical FFs (see below).

As for the machine learning model, a Deep Potential-Smooth Edition Neural Network (NN) [114, 153] is trained on a $3 \times 3 \times 3$ supercell of Li_3ClO with a LiCl pair removed. Details on the NN potential, in general, can be found in Appendix. B, while details on the specific model for Li_3ClO and its validation can be found in Sec. 6.1.6. NN-based EMD simulations are carried out for $x = 0$ and $x = 0.1$ across the whole temperature range of interest. Thermal conductivity for the NN model is computed using the methodology developed in Ref. 33. In Fig. 6.7 we show a comparison between the GK thermal conductivity obtained with classical FF and the NN-potentials for these two systems. Results from NN simulations are in close agreement with the *ab initio* ones available at room temperature and, remarkably, with those obtained from classical FFs, over a broad temperature range, thus further validating the accuracy of the latter for the purposes of the present work.

Having thoroughly verified that the classical FFs closely mimic *ab initio*-quality results, we use it to perform a systematic analysis of the thermal transport properties of Li_3ClO in a broad range of temperatures and vacancy concentrations. EMD simulations are carried out on $10 \times 10 \times 10$ supercells. The desired vacancy concentration is obtained by randomly removing the corresponding number of LiCl pairs from the supercell by means of the `Atomsk` code [154]. For each temperature, we employed the temperature-dependent *ab initio* lattice parameter computed in Sec. 6.1.1 in the QHA (independently of vacancy concentration). In the equilibration phase, the canonical ensemble is sampled via the Bussi-Donadio-Parrinello thermostat [155] for 200 ps. At this point, the thermostat is removed and a microcanonical (NVE) production run of 5 ns is carried out to collect the desired data.

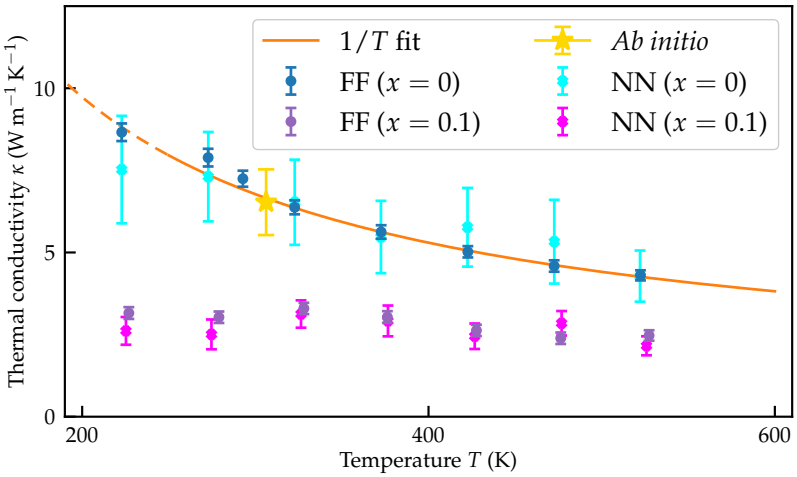

Figure 6.7: GK thermal conductivity of Li_3ClO. Results are obtained from EMD simulations with the classical FFs and with the NN model for the perfect crystalline system ($x = 0$) and the highest concentration ($x = 0.1$) of vacancies we investigate. The $1/T$ fit of the high-temperature behavior of the FFs data at $x = 0$ is shown in orange. The yellow star is the *ab initio* GK result at RT. Error bars represent standard deviations.

The dependence of the thermal conductivity on T and x is shown in Fig. 6.8. The numerical data measured in the EMD simulations are then fitted to a simple function, Eq. (6.2), as described below. The functional form of such dependence should account for the RTA asymptotic $1/T$ behavior (Eucken's law) [156], holding for crystals ($x = 0$) at large temperatures, but should also be able to take into account the breakdown of crystalline order when vacancies are present ($x \neq 0$). The presence of vacancies, while providing access to Li-ion conduction channels, on shorter time scales establishes an effective local disorder, that would result in a contribution to the thermal conductivity describable at different levels of accuracy [104, 106, 110, 157]. The simplest significant approach is to consider the AF model (cf Sec 5.4) of thermal conduction in harmonic glasses, where the thermal conductivity, Eq. (5.32), for high temperature takes the form

$$\kappa_{\mathrm{AF}} \sim \frac{k_{\mathrm{B}}}{\Omega^2} \sum_{\mu} D_{\mu} + \mathcal{O}\left(\frac{1}{T^2}\right), \tag{6.1}$$

i.e., the leading order is constant in temperature. The quantities D_{μ} are temperature-independent modal diffusivities. Notice that EMD with classical nuclei sample, by definition, classical distributions: the occupation of a mode of energy $\hbar\omega$ is thus the first order expansion of Bose-Einstein (BE) distribution, $n_{\mu}(T) \approx k_{\mathrm{B}}T/\hbar\omega_{\mu}$, and the heat capacity per mode reduces to the Dulong-Petit result, $C_{\mu} \approx k_{\mathrm{B}}$. These things considered, we take a fitting function for $\kappa(T, x)$ of the form

$$\kappa_{\mathrm{fit}} = \frac{C_{\mathrm{Euck}}}{T} + C_{\mathrm{AF}}, \tag{6.2}$$

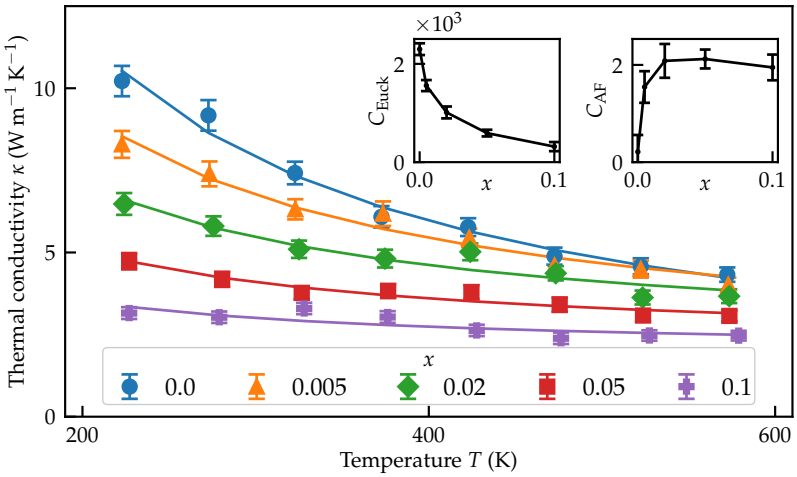

Figure 6.8: GK thermal conductivity as a function of temperature for different values of the concentration of vacancies, x. The solid lines are fits performed according to Eq. (6.2). The insets show the fitting parameters, C_{Euck} and C_{AF}, in units of W m^{-1} and $\text{W m}^{-1}\,\text{K}^{-1}$, respectively, as a function of x. The fitting parameters are also reported in Table 6.2. Error bars represent standard deviations.

where $C_{\text{Euck}}(x)$ and $C_{\text{AF}}(x)$ are vacancy-dependent fitting parameters, incorporating both the Eucken and the AF asymptotics. Their values are reported in Table 6.2 and shown in the inset of Fig. 6.8. C_{AF} has a small value in the $x = 0$ case: this is due to the fact that the perfect crystal has almost completely the Eucken behavior, the only AF-like contribution being due to inter-band effects. As it can be seen from the left panel of Fig. 6.5, the inter-band contribution is linear in T with respect to RTA, which is compatible to adding a (small) constant term to the Eucken law[3]. For higher x, the AF contribution grows sensibly. It is also comforting to notice that $C_{\text{Euck}}(x)$ vanishes as x increases, while $C_{\text{AF}}(x)$ saturates. To have a clear picture of the relative importance of these contributions, we explicitly report, in Fig. 6.9, the decomposition of κ vs T into the Eucken and AF terms at the different vacancy concentrations inspected in the EMD simulations. This picture suggests that, at least in this class of SSE, ionic diffusion may contribute very little to κ, which is instead dominated by the lattice component at low temperatures, and by disorder at high temperatures. This was recently investigated experimentally in Ref. 158 for Ag^+ fast-ion conductors.

Our GK calculations show that the thermal conductivity strongly depends on the presence of defects: in the considered temperature range, even a few-% concentration of defects is able to almost halve the κ with respect to its value for the perfect crystal. This behavior is particularly evident at low temperatures, due to the suppression of the Eucken law when x increases. Nonetheless, when compared to other candidates for battery-oriented SSE, Li_3ClO is characterized

3 In fact, if the relative difference between the QHGK and RTA results is linear, one has $\kappa_{\text{QHGK}} = \kappa_{\text{RTA}}(1 + AT)$, for some constant $A > 0$. Since $\kappa_{\text{RTA}} \simeq B/T$ at high temperature, with $B > 0$, the net behavior is $\kappa_{\text{QHGK}} = B/T + AB$, which is of the same form of Eq. (6.2).

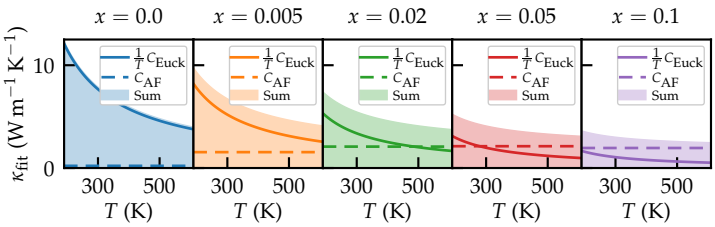

Figure 6.9: Eucken and AF contributions to the fit of Eq. (6.2) on the GK thermal conductivity data.

by a relatively high thermal conductivity and meets the requirements for safe heat dissipation and management.

6.1.6 *Technical and computational details*

This Section contains convergence tests and technical details supporting the results presented in Sec. 6.1

6.1.6.1 *Convergence of the third-order IFC with the supercell*

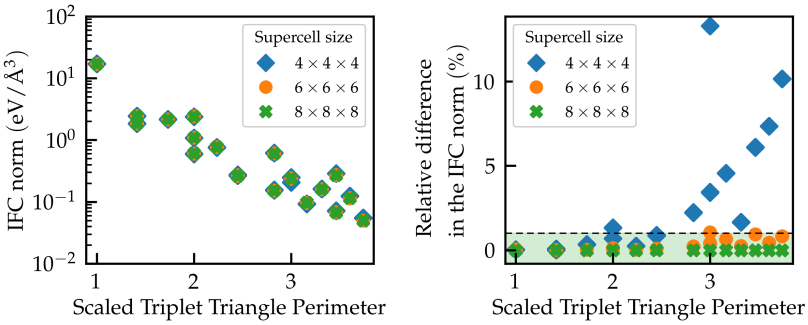

Figure 6.10: Convergence of the third-order IFC with respect to the number of supercell size. (*left*) Triangle plots for different supercell sizes. (*right*) Relative difference in the third-order IFC norms with respect to the reference one with a $8 \times 8 \times 8$ supercell. The green-shaded area indicates values below 1%.

The Interatomic Force Constant (IFC) matrices are computed via finite differences on a supercell. The second order IFC is calculated inexpensively on a $6 \times 6 \times 6$ supercell. The choice of the supercell for the third-order IFC changes substantially the computational cost of the calculations and requires more care. The third-order IFC is computed as a function of the supercell size. This relationship is studied via the so-called "triangle plot". The triangle plot for the third-order IFC computed with 2, 4, 6, and 8 unit cells in each dimension is shown in Fig. 6.10. In the horizontal axis there is the perimeter of the triangle whose vertices are positions of the three atoms involved in each block in the third-order IFC matrix, a block being the $3 \times 3 \times 3$ tensor $\frac{\partial^3 U}{\partial \mathbf{r}_i \partial \mathbf{r}_y \partial \mathbf{r}_k}$. In the vertical

axis, there are the matrix norms of each block. A supercell of size $6 \times 6 \times 6$ is sufficient to have a third-order IFC converged to $\approx 1\%$.

6.1.6.2 *Convergence of the IFC with the number of nearest neighbor shells*

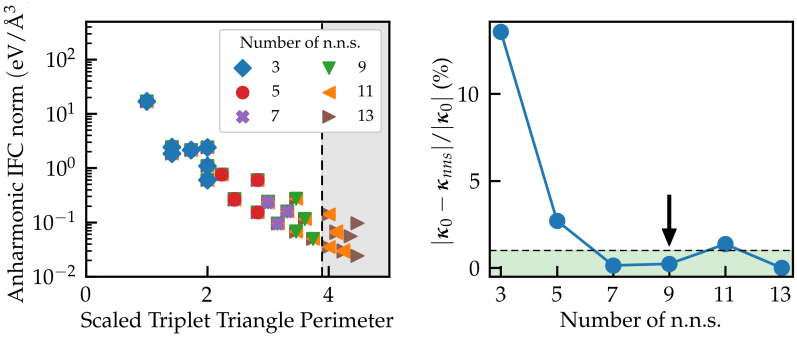

Figure 6.11: Convergence with respect to the number of n.n. shells. (*left*) Triangle plots for different values of the number of n.n. shells; (*right*) relative difference (in Frobenius norm sense) in the lattice thermal conductivity from third-order IFCs computed with different n.n. shells. The green-shaded area indicates values below 1%.

The dependence on the number of included nearest neighbor (n.n.) shells of the third-order IFC is studied both via the triangle plot and by directly computing the thermal conductivity tensor, $\boldsymbol{\kappa}$, on a coarse $12 \times 12 \times 12$ $\mathbf{q}$-points mesh. The triangle plot for the third-order IFC computed with $6 \times 6 \times 6$ supercell is shown in the left panel of Fig. 6.11, while on the right panel there is the relative change in $\boldsymbol{\kappa}$ for a given number of n.n. shells, denoted by $\boldsymbol{\kappa}_{nns}$, with respect to $\boldsymbol{\kappa}_0$, i.e. the thermal conductivity tensor obtained with the highest number of n.n. shells available. Frobenius matrix norms are employed to take into account the off-diagonal elements. A number of n.n. shells equal to 9 is sufficient to converge the thermal conductivity tensor well below 1%.

6.1.6.3 *Convergence of the thermal conductivity with the number of q-points*

The convergence of κ with the number of $N_{\mathbf{q}}$ of $\mathbf{q}$-points is tested by computing the thermal conductivity tensor for different reciprocal space meshes for different temperatures. The results are then analyzed in terms of the relative change in $\boldsymbol{\kappa}$ for a given $N_{\mathbf{q}}$, denoted by $\boldsymbol{\kappa}_{N_{\mathbf{q}}}$, with respect to $\boldsymbol{\kappa}_0$, i.e. the thermal conductivity tensor obtained with the highest $N_{\mathbf{q}}$ available. Convergence is deemed satisfactory when the change is consistently lower than 1%. From Fig. 6.12, one can see that a mesh of $20 \times 20 \times 20$ $\mathbf{q}$-points is sufficient to provide converged results.

6.1.6.4 4-*phonon contributions*

4-phonon calculations are carried out via the `Fourphonon` code [159], an extension to `ShengBTE`. Since 4-phonon calculations are quite expensive, scattering rates and thermal conductivity for three- and 4-phonon processes are performed on a coarse mesh of $10 \times 10 \times 10$ $\mathbf{q}$-points with IFCs coming from a

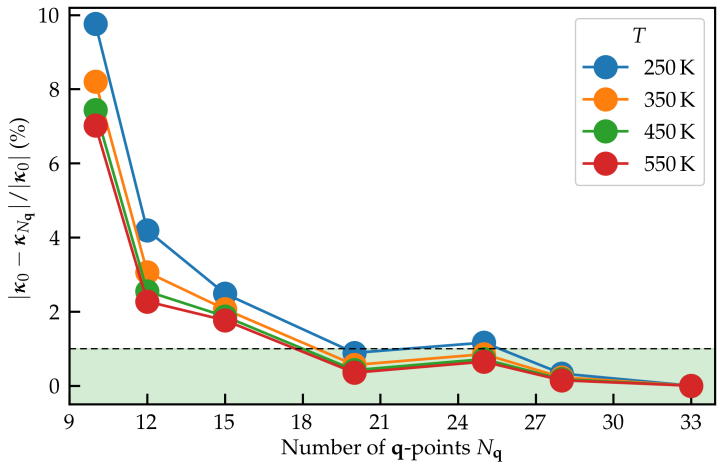

Figure 6.12: Convergence with respect to the number of $\mathbf{q}$-points.

$4 \times 4 \times 4$ supercell, and with fourth-order IFCs that includes contributions from the first n.n. shell only. The scale parameter for Gaussian broadening is reduced to 0.1 from the default value of 1.0.

6.1.6.5 *Effect of the inclusion of NAC on thermal conductivity*

The effect of the inclusion (or lack thereof) of NAC to the dynamical matrix is addressed in the left panel of Fig. 6.13. The exclusion of NAC produces a variation of up to 5% to the value of κ in the temperature range of interest.

6.1.6.6 *Equipartition vs. BE statistics*

In the quantum regime, phonons obey the BE statistics, while in the classical regime they obey the equipartition law. Since the difference between the two occupations is always negative at finite T, at the same level of the theory, the thermal conductivity computed with equipartition will be lower than the one computed with BE distribution. The importance of this difference Li_3ClO is checked by modifying `ShengBTE` to allow occupations according to the equipartition law. The results are shown in the right panel of Fig. 6.13. As expected, being the classical occupation the high-temperature expansion of the BE distribution, the difference is lower at higher temperatures. This contribution alone, around 5% in most of the temperature range, is not enough to explain the difference between the BTE-based and EMD-based values of κ.

6.1.6.7 *Vacancy-dependent GK thermal conductivity*

GK thermal conductivity from FF based EMD simulations are fitted for each value of the vacancy concentration x. The fitting function is Eq. (6.2). The values of the fitting parameters C_{Euck} and C_{AF}, obtained via standard linear regression of $\log(\kappa)$ versus $\log(1/T)$, are shown in Table 6.2.

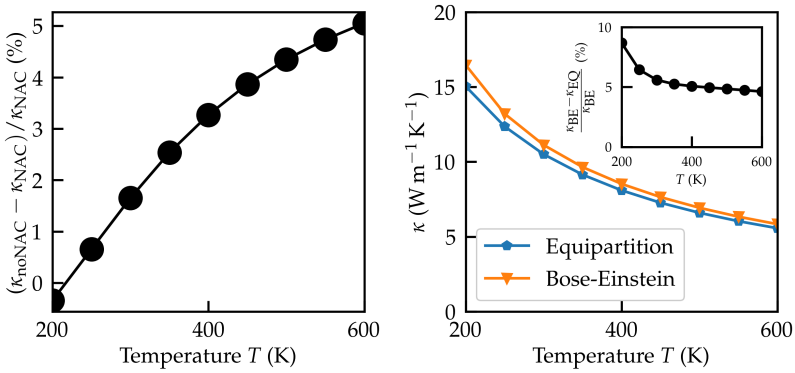

Figure 6.13: (*left*) Relative difference in thermal conductivity including versus excluding NAC. (*right*) Comparison between lattice thermal conductivity computed with BE occupations and with the equipartition law. In the inset, their relative difference is plotted as a function of temperature.

Table 6.2: Values of the fitting parameters C_{Euck} (in W m^{-1}) and C_{AF} (in W m^{-1} K^{-1}) in Eq. (6.2).

	$x = 0$	$x = 0.005$	$x = 0.02$	$x = 0.05$	$x = 0.1$
C_{Euck}	2300 ± 120	1560 ± 110	1010 ± 120	590 ± 70	320 ± 90
C_{AF}	0.2 ± 0.3	1.5 ± 0.3	2.1 ± 0.3	2.1 ± 0.2	1.9 ± 0.3

6.1.6.8 *Validation of the NN model*

A Deep Potential-Smooth Edition NN model [114, 153] (cf App. B) is trained on a set of AIMD simulations at different temperatures, enriched with additional configurations chosen by the `dpgen` software [115]. The system used for the training of the NN is a $3 \times 3 \times 3$ supercell of Li_3ClO with a LiCl pair removed. The root mean squared errors of the trained model are 0.11 ± 0.01 meV/atom and 15 ± 3 meV/Å for the energy and the forces, respectively. The uncertainty on the root-mean-square errors is their standard deviation over four different models differing by the choice of the initial random seed.

The locality test [160] is performed to assess the influence of long-range interactions on the NN model, not explicitly considered here. For a given atom, the atoms within a chosen radius (in PBCs) from it are kept fixed. A random perturbation is applied to the positions of all the other atoms placed outside the sphere. The forces acting on the atom at the center of the sphere are collected for several different random perturbations, computed both with the NN model and *ab initio*. The average deviation between the NN and *ab initio* forces, defined as $\sigma_f = \sqrt{\langle |\mathbf{f}_{AI} - \mathbf{f}_{NN}|^2 \rangle}$, quantifies the dependence of the atom's properties on its neighbors; hence the name of locality test. This procedure is carried out for different values of the cutoff and for each atomic species in the system. The results obtained with a $4 \times 4 \times 4$ supercell are shown in Fig. 6.14. Force deviations are at most compatible with the errors on the training set and exhibit a mildly decreasing dependence on the cutoff of the sphere. The error is computed as the standard error on the average of 10 equivalent configurations.

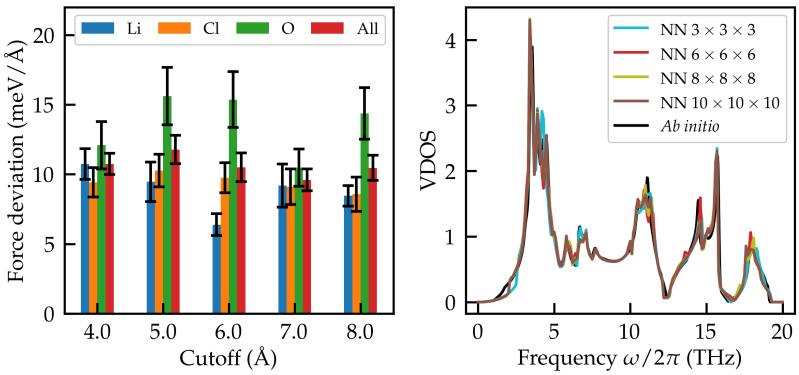

Figure 6.14: (*left*) Average force deviations for the locality test. The error bars represent the standard deviation of the force deviation sample. (*right*) Phonon density of states for different supercell sizes compared with the *ab initio* result.

This is consistent with the assumption that the local environment is dominant in determining the properties of an atom and validates the model we employ. Phonon density of states is computed and compared to the *ab initio* results for different supercells. The results are satisfactory and are shown in Fig. 6.14.

CONCLUSIONS

In this thesis, I have discussed some topics relative to charge and heat transport in ionic conductors. The role of topology in reconciling Faraday's first law of electrolysis—i.e., that charges associated with ions in motion are whole numbers—to a quantum-mechanical description of electronically insulating fluids has been addressed. It has been shown how, according to the topology of paths in the space of all the coordinates of a system of atoms under periodic boundary conditions, called the atomic configuration space, one can discriminate among different kinds of ionic conductors. When strong adiabaticity holds, ionic transport is trivial: atoms of the same species have the same oxidation state, which is the integer charge adiabatically displaced by an atom along a macroscopic distance. Ionic conductivity has the same formal expression as the one of a classical fluid of point charges. If strong adiabaticity only holds on subdomains of the atomic configuration space, the subdomains being separated by regions where adiabaticity breaks, atoms of the same species can display different oxidation states, depending on the particular subdomain. This case is exemplified by ionic solids where like atoms are found in different chemical environments, and passing from one environment to the other requires passing from a degenerate configuration. Finally, strong adiabaticity is completely violated when the atomic configuration space features regions where the electronic gap is closed that can be encircled by adiabatic paths. By Thouless' theorem, this implies the possibility of pumping integer charges without a net mass displacement. Ionic transport is in the nontrivial regime, and charge transport is uncorrelated from mass transport.

Another fundamental transport property of ionic conductors, heat conductivity, has been investigated in the case of the solid-state electrolyte Li_3ClO. The thermal conductivity of Li_3ClO has been computed through anharmonic lattice dynamics and equilibrium molecular dynamics simulations performed with semi-empirical and machine-learned force fields. It has been shown how the presence of vacancies, the mediators of ionic diffusion in solid-state electrolytes, sensibly affects the value of thermal conductivity. The net effect of the existence of diffusing vacancies is to introduce a glass-like contribution to the thermal conductivity, which increases with the vacancy concentration: the higher the concentration of vacancies, the larger the effect, up to a point where the glass-like contribution saturates to some value. At the same time, the crystal-like contribution to thermal conductivity decreases with the concentration of vacancies as the system becomes less and less ordered.

Part IV

APPENDIX

There are only two perfectly
useless things in this world.
One is an appendix, and the other
is Poincaré.

Georges Clemenceau
referring to his political rival
Raymond Poincaré, as quoted in
*Paris 1919: Six months that changed
the world*, by Margaret MacMillan.

A

DETAILS ON CEPSTRAL ANALYSIS

In this Appendix I will present detailed calculations needed to arrive at the exact expressions for the expectation value and variance of the cepstral estimator.

Let us consider the cepstral expansion of $S(\omega)$:

$$C_n = \frac{1}{N}\sum_{k=0}^{N-1} \log(S(\omega_k))\, e^{2\pi i k n/N}, \tag{A.1}$$

with C_n the cepstral coefficients. The zero-frequency value of $\log(S(\omega))$ is obtained inverting the discrete Fourier transform in Eq. (A.1) as

$$\log(S(0)) = C_0 + 2\sum_{n=1}^{\frac{N}{2}-1} C_n + C_{\frac{N}{2}}. \tag{A.2}$$

Since we only have an estimate of the true PSD, we can only access an estimate of the cepstral coefficients, given by

$$\begin{aligned} \mathcal{C}_n &= \frac{1}{N}\sum_{k=0}^{N-1} \log(\mathcal{S}_k)\, e^{2\pi i k n/N}, \\ &= \frac{1}{N}\sum_{k=0}^{N-1} \log(S(f_k))\, e^{2\pi i k n/N} + \frac{1}{N}\sum_{k=0}^{N-1} \log(\xi_k)\, e^{2\pi i k n/N} \\ &\equiv C_n + \mu_n \end{aligned} \tag{A.3}$$

Since the periodogram is even in k, there are only $N/2$ independent terms in the sums in Eq. (A.3), and the latter can be written as

$$\begin{aligned} \mathcal{C}_n = \frac{1}{N}\Bigg[&\log(S(0)) + \log(\xi_0) + 2\sum_{k=1}^{\frac{N}{2}-1} \log(S(f_k))\, \cos(2\pi k n/N) + \\ &+2\sum_{k=1}^{\frac{N}{2}-1} \log(\xi_k)\, \cos(2\pi k n/N) + (-1)^n \log(S(\omega_{N/2})) + \\ &+(-1)^n \log(\xi_{N/2})\Bigg], \end{aligned} \tag{A.4}$$

the stochastic part being

$$\mu_n = \frac{1}{N}\left[\log(\xi_0) + 2\sum_{k=1}^{\frac{N}{2}-1} \log(\xi_k)\, \cos(2\pi k n/N) + (-1)^n \log(\xi_{N/2})\right] \tag{A.5}$$

The probability distribution of $\mathcal{C}_n$ does not have a closed expression, but its moments are readily computed from the Cumulant Generating Function (CGF) of μ_n:

$$\mathcal{K}_{\mu_n}(s) = \log\left\langle e^{s\mu_n}\right\rangle, \tag{A.6}$$

where s is an auxiliary variable. By plugging Eq. (A.5) into Eq. (A.6) one obtains

$$\mathcal{K}_{\mu_n}(s) = \log\left\langle \exp\left[\frac{s}{N}\left(\log(\xi_0) + \right.\right.\right. \\ \left.\left.\left. +2\sum_{k=1}^{\frac{N}{2}-1}\log(\xi_k)\,\cos(2\pi kn/N) + (-1)^n\log(\xi_{N/2})\right)\right]\right\rangle \tag{A.7}$$

Since, for different k, the random variables ξ_k are independent from one another, one gets

$$\begin{aligned}\mathcal{K}_{\mu_n}(s) &= \log\langle\exp\left(s\log(\xi_0)/N\right)\rangle + \\ &+\sum_{k=1}^{\frac{N}{2}-1}\log\langle\exp\left[2s\log(\xi_k)\,\cos(2\pi kn/N)/N\right]\rangle + \\ &\quad+\log\langle\exp\left((-1)^n s\log(\xi_{N/2})/N\right)\rangle \\ &= \log\left\langle\xi_0^{s/N}\right\rangle + \sum_{k=1}^{\frac{N}{2}-1}\log\left\langle\xi_k^{2s\cos(2\pi kn/N)/N}\right\rangle + \log\left\langle\xi_{N/2}^{(-1)^n s/N}\right\rangle\end{aligned} \tag{A.8}$$

If we define

$$\tau_k(s) = \begin{cases} s/N, & \text{if } k = 0 \\ 2s\cos(2\pi kn/N)/N, & \text{if } k \notin \{0, N/2\}, \\ (-1)^n s/N, & \text{if } k = N/2 \end{cases} \tag{A.9}$$

Eq. (A.8) becomes

$$\mathcal{K}_{\mu_n}(s) = \log\left\langle\xi_0^{\tau_0(s)}\right\rangle + \sum_{k=1}^{\frac{N}{2}-1}\log\left\langle\xi_k^{\tau_k(s)}\right\rangle + \log\left\langle\xi_{N/2}^{\tau_{N/2}(s)}\right\rangle \tag{A.10}$$

$$= \sum_{k=0}^{N/2}\log\left\langle\xi_k^{\tau_k(s)}\right\rangle \tag{A.11}$$

whose value is [161]

$$\mathcal{K}_{\mu_n}(s) = \sum_{k=0}^{N/2}\log\left[\left(\frac{2}{\nu}\right)^{\tau_k(s)}\frac{\Gamma(\frac{\nu}{2}+\tau_k(s))}{\Gamma(\frac{\nu}{2})}\right]. \tag{A.12}$$

The mean and variance of μ_n are computed as

$$\langle\mu_n\rangle = \left.\frac{\partial\mathcal{K}_{\mu_n}}{\partial s}\right|_{s=0}, \tag{A.13}$$

$$\operatorname{Var}\mu_n = \left.\frac{\partial^2\mathcal{K}_{\mu_n}}{\partial s^2}\right|_{s=0}. \tag{A.14}$$

which yield the result

$$\langle\mu_n\rangle = \delta_{n0}\lambda_\nu = \delta_{n0}\left(\psi(\nu/2) - \log(\nu/2)\right) \tag{A.15}$$

$$\operatorname{Var}\mu_n = \frac{\psi'(\frac{\nu}{2})}{N}, \tag{A.16}$$

where $\psi(x)$ is the digamma function, i.e. the logarithmic derivative of the Euler Gamma function [27].

Analogous calculations lead to the statistical properties of $\mathcal{L}_0^\star$, i.e.

$$\begin{aligned}\mathcal{L}_0^\star &= \mathcal{C}_0 - \lambda_\nu + 2\sum_{n=1}^{P^\star-1}\mathcal{C}_n \\ &= C_0 + 2\sum_{n=1}^{P^\star-1} C_n + \mu_0 - \lambda_\nu + 2\sum_{n=1}^{P^\star-1}\mu_n \\ &= C_0 + 2\sum_{n=1}^{P^\star-1} C_n + \mathcal{M}_0^\star,\end{aligned} \tag{A.17}$$

where $\mathcal{M}_0^\star$ is the stochastic part of $\mathcal{L}_0^\star$. Its CGF is

$$\begin{aligned}\mathcal{K}_{\mathcal{M}_0^\star}(s) &= \log\left\langle \mathrm{e}^{s\mathcal{M}_0^\star}\right\rangle \\ &= \log\left\langle \mathrm{e}^{s(\mu_0-\lambda_\nu)+2s\sum_{n=1}^{P^\star-1}\mu_n}\right\rangle \\ &= -s\lambda_\nu + \log\left\langle \mathrm{e}^{s\mu_0+2s\sum_{n=1}^{P^\star-1}\mu_n}\right\rangle\end{aligned} \tag{A.18}$$

By plugging in the expressions of μ_0 and μ_n one obtains

$$\begin{aligned}\mathcal{K}_{\mathcal{M}_0^\star}(s) = -s\lambda_\nu + \log\Bigg\langle \exp\Bigg\{ &\frac{s}{N}\left[\log\xi_0 + 2\sum_{k=1}^{\frac{N}{2}-1}\log\xi_k + \log\xi_{\frac{N}{2}}\right] + \\ &\frac{2s}{N}\sum_{n=1}^{P^\star-1}\left[\log\xi_0 + 2\sum_{k=1}^{\frac{N}{2}-1}\log\xi_k\cos\tfrac{2\pi kn}{N} + (-1)^n\log\xi_{\frac{N}{2}}\right]\Bigg\}\Bigg\rangle,\end{aligned} \tag{A.19}$$

which can be written as

$$\begin{aligned}\mathcal{K}_{\mathcal{M}_0^\star}(s) = -s\lambda_\nu + \log\Bigg\langle \exp\Bigg\{ &\log\xi_0\frac{2P^\star-1}{N}s + \\ &+\sum_{k=1}^{\frac{N}{2}-1}\log\xi_k\left(1+2\sum_{n=1}^{P^\star-1}\cos\left(\tfrac{2\pi kn}{N}\right)\right)\frac{2s}{N} - \log\xi_{N/2}\frac{(-1)^{P^\star}}{N}s\Bigg\}\Bigg\rangle.\end{aligned} \tag{A.20}$$

This time it is expedient to define

$$\tau_k(s) = \begin{cases}\frac{2P^\star-1}{N}s, & \text{if } k=0 \\ \left(1+2\sum_{n=1}^{P^\star-1}\cos(2\pi kn/N)\right)\frac{2s}{N}, & \text{if } k\notin\{0,N/2\}, \\ \frac{(-1)^{P^\star-1}}{N}s, & \text{if } k=N/2,\end{cases} \tag{A.21}$$

in terms of which Eq. (A.20) takes the same form as Eq. (A.10), so that the former reads

$$\mathcal{K}_{\mathcal{M}_0^\star}(s) = -s\lambda_\nu + \sum_{k=0}^{N/2}\log\left[\left(\frac{2}{\nu}\right)^{\tau_k(s)}\frac{\Gamma(\frac{\nu}{2}+\tau_k(s))}{\Gamma(\frac{\nu}{2})}\right]. \tag{A.22}$$

The average value of $m_0^\star$ is computed as

$$\begin{aligned}
\langle m_0^\star \rangle &= \left.\frac{\partial \mathcal{K}_{m_0^\star}}{\partial s}\right|_{s=0} \\
&= -\lambda_\nu + \lambda_\nu \left[\frac{2P^\star - 1}{N} + \right. \\
&\quad \left. + \frac{2}{N} \sum_{k=1}^{\frac{N}{2}-1} \left(1 + 2 \sum_{n=1}^{P^\star - 1} \cos(2\pi k n / N)\right) + \frac{(-1)^{P^\star - 1}}{N}\right] \\
&= \frac{\lambda_\nu}{N} \left[2P^\star - 3 + 4 \sum_{k=1}^{\frac{N}{2}-1} \sum_{n=1}^{P^\star - 1} \cos(2\pi k n / N) + (-1)^{P^\star - 1}\right] \\
&= \frac{\lambda_\nu}{N} \left[2P^\star - 3 + 3 + (-1)^{P^\star} - 2P^\star + (-1)^{P^\star - 1}\right] \\
&= 0.
\end{aligned} \tag{A.23}$$

Its variance is

$$\begin{aligned}
\operatorname{Var} m_0^\star &= \left.\frac{\partial^2 \mathcal{K}_{m_0^\star}}{\partial s^2}\right|_{s=0} \\
&= \psi'(\nu/2) \left[\left(\frac{2P^\star - 1}{N}\right)^2 + \right. \\
&\quad \left. + \sum_{k=1}^{\frac{N}{2}-1} \frac{4}{N^2} \left(1 + 2 \sum_{n=1}^{P^\star - 1} \cos(2\pi k n / N)\right)^2 + \frac{1}{N^2}\right] \\
&= \psi'(\nu/2) \left[\frac{4(P^\star)^2 - 4P^\star + 2}{N^2} + \right. \\
&\quad \left. + \sum_{k=1}^{\frac{N}{2}-1} \frac{4}{N^2} \left(1 + 2 \sum_{n=1}^{P^\star - 1} \cos(2\pi k n / N)\right)^2\right]
\end{aligned} \tag{A.24}$$

The sum over k is evaluated as follows:

$$\begin{aligned}
\mathfrak{S} &= \sum_{k=1}^{\frac{N}{2}-1} \frac{4}{N^2} \left(1 + 2 \sum_{n=1}^{P^\star - 1} \cos(2\pi k n / N)\right)^2 \\
&= \frac{4}{N^2} \sum_{k=1}^{\frac{N}{2}-1} \left(1 + 4 \sum_{n=1}^{P^\star - 1} \cos(2\pi k n / N) + \right. \\
&\quad \left. 4 \sum_{n,m=1}^{P^\star - 1} \cos(2\pi k n / N) \cos(2\pi k m / N)\right) \\
&= \frac{4}{N^2} \left\{\frac{N}{2} - 1 + 4 \sum_{n=1}^{P^\star - 1} \sum_{k=1}^{\frac{N}{2}-1} \cos(2\pi k n / N) + \right. \\
&\quad \left. 2 \sum_{n,m=1}^{P^\star - 1} \sum_{k=1}^{\frac{N}{2}-1} \left[\cos\left(\tfrac{2\pi k (n-m)}{N}\right) + \cos\left(\tfrac{2\pi k (n+m)}{N}\right)\right]\right\}.
\end{aligned} \tag{A.25}$$

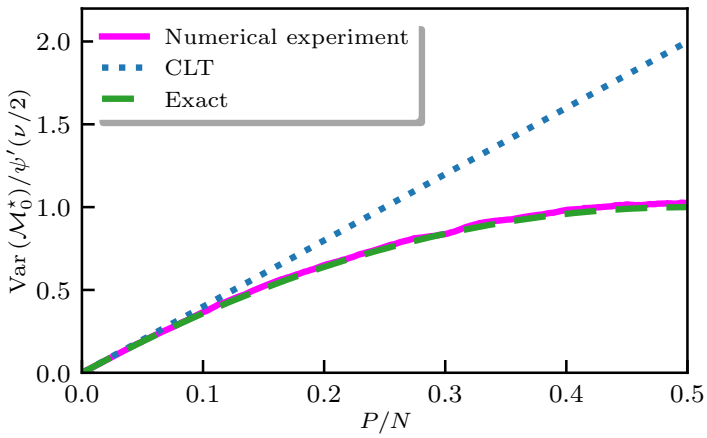

Figure A.1: Variance of $m_0^\star$ as a function of the number of retained cepstral coefficients, P, divided by N. The central limit theorem formula is valid only for small values of P/N.

The first sum over k and n in the last line of Eq. (A.25) evaluates to

$$\begin{aligned}\mathfrak{S}_1 &= \sum_{n=1}^{P^\star-1}\sum_{k=1}^{\frac{N}{2}-1}\cos(2\pi kn/N)\\ &= \frac{1}{2}\sum_{n=1}^{P^\star-1}\left[\cot(\pi n/N)\sin(\pi n)-\cos(\pi n)-1\right]\\ &= \frac{1}{4}\left[3+(-1)^{P^\star}-2P^\star\right].\end{aligned} \tag{A.26}$$

The sum over k, n and m in Eq. (A.25) evaluates to

$$\begin{aligned}\mathfrak{S}_2 &= \sum_{n,m=1}^{P^\star-1}\sum_{k=1}^{\frac{N}{2}-1}\left[\cos\left(\tfrac{2\pi k(n-m)}{N}\right)+\cos\left(\tfrac{2\pi k(n+m)}{N}\right)\right]\\ &= \frac{1}{2}\sum_{n,m=1}^{P^\star-1}\Big[-2-\cos(\pi(n-m))+\cot\left(\tfrac{\pi(n-m)}{N}\right)\sin(\pi(n-m))+\\ &\qquad -\cos(\pi(n+m))+\cot\left(\tfrac{\pi(n+m)}{N}\right)\sin(\pi(n+m))\Big]\\ &= \frac{1}{2}\left[-3-(-1)^{P^\star}+4P^\star-2(P^\star)^2\right]+\\ &\quad+\frac{1}{2}\sum_{n,m=1}^{P^\star-1}\left[\cot\tfrac{\pi(n-m)}{N}\sin[\pi(n-m)]+\cot\tfrac{\pi(n+m)}{N}\sin[\pi(n+m)]\right]\\ &= \frac{1}{2}\left[-3-(-1)^{P^\star}+4P^\star-2(P^\star)^2+NP^\star-N\right]\end{aligned} \tag{A.27}$$

Thus, $\mathfrak{S}$ reads

$$\begin{aligned}\mathfrak{S} &= \frac{4}{N^2}\left[\frac{N}{2} - 1 + 4\mathfrak{S}_1 + 2\mathfrak{S}_2\right] \\ &= \frac{4P^\star - 2}{N} + \frac{8P^\star - 8(P^\star)^2 - 4}{N^2}\end{aligned} \tag{A.28}$$

Finally, Eq. (A.24) becomes

$$\begin{aligned}\operatorname{Var} m_0^\star &= \psi'(\nu/2)\left[\frac{4(P^\star)^2 - 4P^\star + 2}{N^2} + \frac{4P^\star - 2}{N} + \frac{8P^\star - 8(P^\star)^2 - 4}{N^2}\right] \\ &= \psi'(\nu/2)\left[\frac{4P^\star - 2}{N} + \frac{4P^\star - 4(P^\star)^2 - 2}{N^2}\right]\end{aligned} \tag{A.29}$$

This result differs from the one obtained in Ref. 26 using a generalized central limit theorem [162], which is correct up to $\mathcal{O}(1/N)$. The comparison of the two formulas and the numerical result is shown in Fig. A.1. In practical cases, the approximated version is sufficient, since the value of $P^\star$ is virtually never larger than $\approx 10\%$ of the length of the time series.

B NEURAL-NETWORK POTENTIALS

In the last decade, a combination of standard electronic-structure methods, based on DFT, and new machine-learning techniques have allowed the construction of inter-atomic potentials possessing quantum mechanical accuracy at a cost that is only marginally higher than that of classical force fields [116, 160, 163–165]. In particular, NN potentials based on the Deep Potential (DP) framework [153] use a local decomposition of the total potential energy of a system of interacting atoms and divide it into atomic contributions, thus making the method aptly to the computation of the energy flux.

B.1 DEEP NEURAL NETWORKS

The task of a NN is to approximate some function $F^\star$ [166]. The name "network" recalls its construction as a composite and possibly complicated nonlinear function. A simple one can consider a NN with three *layers*, represented by the three functions $F^{(1)}$, $F^{(2)}$, and $F^{(3)}$, connected under composition:

$$F(\mathbf{x}) = F^{(3)}(F^{(2)}(F^{(1)}(\mathbf{x}))). \tag{B.1}$$

The number of layers is the *depth* of the network. The final layer is called the *output layer*. During NN training, the function $F(\mathbf{x})$ is driven to match $F^\star(\mathbf{x})$: the training data is made of (possibly noisy) examples of the target function $F^\star$ evaluated at different training points. Each point $\mathbf{x}$ is accompanied by a label $y \approx F^\star(\mathbf{x})$ that specifies the value the NN model should reproduce, i.e. what the output layer should yield [166]. The behavior of the other—*hidden*—layers is not specified by the training data. Each hidden layer is usually specified by an array of values, whose dimensionality defines the *width* of the model. Each element of the array is called a neuron, since the whole concept of NNs is loosely inspired by how brains work; in most NNs, their functional form is a linear transformation defined by learned parameters followed by a fixed nonlinear function, called *activation function*:

$$F_j^{(1)} = \sigma\left(b_j^{(1)} + W_{i,j}^{(1)} I_i\right), \tag{B.2}$$

where b_j are called biases, W_{ij} are the weights of the neurons, and σ is the activation function. A general NN with L hidden layers takes the form:

$$\mathbf{y}(\mathbf{I};\mathbf{W}) = \mathbf{F}^{(L)}\left(\mathbf{F}^{(L-1)}\left(\cdots \mathbf{F}^{(1)}\left(\mathbf{I}\right)\right)\right) \tag{B.3}$$

$$\begin{aligned} &= \sigma\left(\mathbf{b}^{(L)} + \mathbf{W}^{(L)} \cdot \sigma\left(\mathbf{b}^{(L-1)} + \right.\right. \\ &\quad \left.\left. + \mathbf{W}^{(L-1)} \cdot \sigma\left(\cdots \sigma(\mathbf{b}^{(1)} + \mathbf{W}^{(1)} \cdot \mathbf{I})\right)\right)\right), \end{aligned} \tag{B.4}$$

where the symbol $\mathbf{W}$ includes both the weights $\mathbf{W}^{(l)}$ and the biases $\mathbf{b}^{(l)}$.

The model is usually optimized through the minimization of a loss function, L, in the space of parameters, $\mathbf{W}$, using minimization algorithms such as the

stochastic gradient descent [166] or Adam [167]. In many applications, L takes the following form [166]:

$$L(\mathbf{W}) = \frac{1}{B}\sum_{b=1}^{B} |\mathbf{y}(\mathbf{I}_b;\mathbf{W}) - \mathbf{F}^\star(\mathbf{I}_b)|^2, \tag{B.5}$$

where $\mathbf{F}^\star$ is the target function and b is summed over a batch of B training data set.

B.2 CONSTRUCTION OF NEURAL-NETWORK POTENTIALS

B.2.1 *Descriptor*

A NN potential requires a descriptor able to encode atomic environments. Consider a system of N atoms, whose configurations are represented by the set of atomic positions, $\{\mathbf{R}_1, \mathbf{R}_2, \ldots, \mathbf{R}_N\} \in \mathbb{R}^{3N}$. The N_ℓ neighbors of the ℓth atom are those atoms whose positions are within a chosen cutoff radius, R_{cut}, from $\mathbf{R}_\ell$. The *local environment matrices* $\tilde{K}_\ell \in \mathbb{R}^{N_n \times 4}$ are defined in order to encode the local environment:

$$\tilde{K}_\ell = \begin{pmatrix} \frac{\sigma(R_{1\ell})}{R_{1\ell}} & \frac{\sigma(R_{1\ell})x_{1\ell}}{R_{1\ell}^2} & \frac{\sigma(R_{1\ell})y_{1\ell}}{R_{1\ell}^2} & \frac{\sigma(R_{1\ell})z_{1\ell}}{R_{1\ell}^2} \\ \frac{\sigma(R_{2\ell})}{R_{2\ell}} & \frac{\sigma(R_{2\ell})x_{2\ell}}{R_{2\ell}^2} & \frac{\sigma(R_{2\ell})y_{2\ell}}{R_{2\ell}^2} & \frac{\sigma(R_{2\ell})z_{2\ell}}{R_{2\ell}^2} \\ \vdots & \vdots & \vdots & \vdots \end{pmatrix}, \tag{B.6}$$

where $\sigma(R_{q\ell})$ is a smoothing function:

$$\sigma(R_{q\ell}) = \begin{cases} 1, & R_{q\ell} < R_{\text{smth}} \\ -6\Theta^5 + 15\Theta^4 - 10\Theta^3 + 1, & R_{\text{smth}} < R_{q\ell} < R_{\text{cut}} \\ 0, & R_c < R_{q\ell} \end{cases} \tag{B.7}$$

$\Theta = \frac{R_{q\ell} - R_{\text{smth}}}{R_{\text{cut}} - R_{\text{smth}}}$, and R_{smth} is the smoothing cutoff radius that switches the interaction smoothly to zero. The model encodes local environments within the cutoff radius, under the assumption that all the important interactions die off within such length scales. The descriptor should preserve the natural symmetries of the physical system: rotation, translational invariance, and permutational invariance (e.g., a "relabeling" of atoms of the same species). To achieve so, the local-environment matrices are made symmetry-preserving by a suitably defined transformation that yields quantities $\tilde{D}_\ell$ [165].

B.2.2 *Target quantities*

The symmetry-preserving descriptors, $\tilde{D}_\ell$, are fed to the NN model, which returns local atomic energies $\epsilon_{s(\ell)}(\tilde{D}_\ell)$ depending on the species $s(\ell)$ of the ℓth atom, and on its local environment [114]. The (extensive) total potential energy of the system is the sum of atomic contributions:

$$E = \sum_\ell \epsilon_{s(\ell)}(\tilde{D}_\ell). \tag{B.8}$$

The NN model is trained to return the local energy corresponding to any symmetry-preserving local environment. The training is achieved minimizing a loss function, L, with respect to the parameters of the model, i.e., the coefficients of the neurons in the layers:

$$L = p_E \Delta E^2 + \frac{p_F}{3N} \sum_\ell \Delta f_\ell^2, \tag{B.9}$$

where ΔE^2 and Δf_ℓ^2 are the mean squared deviations of the total potential energy and of the force acting of the ℓth atom, respectively, between the reference calculation and the predictions of the NN model. The weights given to the energy and force portions of the loss function, p_E and p_F, can be tuned to optimize the efficiency of the training process, and account for the difference in physical dimensions between energy and force. Forces are computed from the local energies as

$$\begin{aligned} \mathbf{f}_\ell &= -\frac{\partial E}{\partial \mathbf{R}_\ell} = -\frac{\partial}{\partial \mathbf{R}_\ell} \sum_{\ell'} \epsilon_{s(\ell')}(\tilde{D})_{\ell'}) \\ &= -\sum_{\ell'} \frac{\partial \epsilon_{s(\ell')}}{\partial \tilde{D}_{\ell'}} \frac{\partial \tilde{D})_{\ell'}}{\partial \mathbf{R}_\ell}, \end{aligned} \tag{B.10}$$

and the virial as

$$\Xi_{\alpha\beta} = \sum_\ell R_{\ell\alpha} f_{\ell\beta} = -\sum_{\ell \neq \ell'} R_{\ell\ell'\alpha} \frac{\partial \epsilon_{s(\ell)}}{\partial R_{\ell\ell'\beta}}, \tag{B.11}$$

where $R_{\ell\ell'\beta} = R_{\ell\beta} - R_{\ell'\beta}$.

ACKNOWLEDGMENTS

A Ph.D. thesis is hardly a one-man job. During my four years at SISSA, I had the privilege of working with many wonderful people, and I would like to express my heartfelt appreciation for their contributions to this work. I thank Stefano Baroni, whose teachings and mentorship instilled in me the importance of work ethics and excellence. I am deeply grateful for Federico Grasselli's invaluable guidance, which was fundamental in accomplishing my research, and friendship, which I sincerely appreciate.

Days would have been definitely duller without my colleagues. I thank Davide Tisi for his wholeheartedness and kindness; Riccardo Bertossa, for without him, compiling codes would have been more of a nightmare than it already has; Cesare Malosso, with whom I shared many conversations on neural networks and pizza making; Alfredo Fiorentino, whose innate physical intuition and analytical skills will lead him far away in his scientific career; Enrico Drigo, for bringing back memories of childish songs of arguable political correctness; Giacomo Tenti, for conceiving dilemmas that force one to face one's deepest fears.

Not by work only doth man live. Sometimes one simply needs to enjoy a starry night under a willow tree. I thank Alberto Monte, Giacomo Labbri, and Davide De Biasio.

I owe a debt of gratitude to my mother and father, who have always supported me in everything I do.

Finally, and most importantly, I thank Maria for always being by my side and her unwavering encouragement during the most challenging moments.

[1] Hugo Touchette. "When is a quantity additive, and when is it extensive?" In: *Physica A: Statistical Mechanics and its Applications* 305.1-2 (Mar. 2002), pp. 84–88. ISSN: 0378-4371. DOI: 10.1016/s0378-4371(01)00644-6. URL: https://doi.org/10.1016/s0378-4371(01)00644-6.

[2] Leo P Kadanoff and Paul C Martin. "Hydrodynamic equations and correlation functions." In: *Annals of Physics* 24 (Oct. 1963), pp. 419–469. ISSN: 0003-4916. DOI: 10.1016/0003-4916(63)90078-2. URL: https://doi.org/10.1016/0003-4916(63)90078-2.

[3] Dieter Forster. *Hydrodynamic Fluctuations, Broken Symmetry, and Correlation Functions*. CRC Press, Mar. 2018. ISBN: 9780429493683. DOI: 10.1201/9780429493683. URL: https://doi.org/10.1201/9780429493683.

[4] Stefano Baroni, Riccardo Bertossa, Loris Ercole, Federico Grasselli, and Aris Marcolongo. "Heat transport in insulators from ab initio Green-Kubo theory." In: *Handbook of materials modeling: Applications: Current and emerging materials* (2020), pp. 809–844.

[5] Lars Onsager. "Reciprocal Relations in Irreversible Processes. I." In: *Physical Review* 37.4 (Feb. 1931), pp. 405–426. ISSN: 0031-899X. DOI: 10.1103/physrev.37.405. URL: https://doi.org/10.1103/physrev.37.405.

[6] Lars Onsager. "Reciprocal Relations in Irreversible Processes. II." In: *Physical Review* 38.12 (Dec. 1931), pp. 2265–2279. ISSN: 0031-899X. DOI: 10.1103/physrev.38.2265. URL: https://doi.org/10.1103/physrev.38.2265.

[7] Gerd Röpke. *Nonequilibrium Statistical Physics*. Wiley, Mar. 2013. ISBN: 9783527410927, 9783527671397. DOI: 10.1002/9783527671397. URL: https://doi.org/10.1002/9783527671397.

[8] Melville S Green. "Markoff random processes and the statistical mechanics of time-dependent phenomena." In: *The Journal of Chemical Physics* 20.8 (1952), pp. 1281–1295.

[9] Melville S. Green. "Markoff Random Processes and the Statistical Mechanics of Time-Dependent Phenomena." In: *The Journal of Chemical Physics* 20.8 (Aug. 1952), pp. 1281–1295. ISSN: 0021-9606, 1089-7690. DOI: 10.1063/1.1700722. URL: https://doi.org/10.1063/1.1700722.

[10] Ryogo Kubo. "Statistical-Mechanical Theory of Irreversible Processes. I. General Theory and Simple Applications to Magnetic and Conduction Problems." In: *Journal of the Physical Society of Japan* 12.6 (June 1957), pp. 570–586. ISSN: 0031-9015, 1347-4073. DOI: 10.1143/jpsj.12.570. URL: https://doi.org/10.1143/jpsj.12.570.

[11] Ryogo Kubo, Mario Yokota, and Sadao Nakajima. "Statistical-Mechanical Theory of Irreversible Processes. II. Response to Thermal Disturbance." In: *Journal of the Physical Society of Japan* 12.11 (Nov. 1957), pp. 1203–1211. ISSN: 0031-9015, 1347-4073. DOI: 10.1143/jpsj.12.1203. URL: https://doi.org/10.1143/jpsj.12.1203.

[12] Stephen Stackhouse, Lars Stixrude, and Bijaya B. Karki. "Thermal Conductivity of Periclase (MgO) from First Principles." In: *Physical Review Letters* 104.20 (May 2010), p. 208501. ISSN: 0031-9007, 1079-7114. DOI: 10.1103/physrevlett.104.208501. URL: https://doi.org/10.1103/physrevlett.104.208501.

[13] Aris Marcolongo, Paolo Umari, and Stefano Baroni. "Microscopic theory and quantum simulation of atomic heat transport." In: *Nature Physics* 12.1 (Oct. 2015), pp. 80–84. ISSN: 1745-2473, 1745-2481. DOI: 10.1038/nphys3509. URL: https://doi.org/10.1038/nphys3509.

[14] Loris Ercole, Aris Marcolongo, Paolo Umari, and Stefano Baroni. "Gauge Invariance of Thermal Transport Coefficients." In: *Journal of Low Temperature Physics* 185.1-2 (Apr. 2016), pp. 79–86. ISSN: 0022-2291, 1573-7357. DOI: 10.1007/s10909-016-1617-6. URL: https://doi.org/10.1007/s10909-016-1617-6.

[15] Riccardo Bertossa, Federico Grasselli, Loris Ercole, and Stefano Baroni. "Theory and Numerical Simulation of Heat Transport in Multicomponent Systems." In: *Physical Review Letters* 122.25 (25 June 2019), p. 255901. ISSN: 0031-9007, 1079-7114. DOI: 10.1103/physrevlett.122.255901. URL: https://doi.org/10.1103/physrevlett.122.255901.

[16] Federico Grasselli and Stefano Baroni. "Invariance principles in the theory and computation of transport coefficients." In: *The European Physical Journal B* 94.8 (Aug. 2021), p. 160. ISSN: 1434-6028, 1434-6036. DOI: 10.1140/epjb/s10051-021-00152-5. URL: https://doi.org/10.1140/epjb/s10051-021-00152-5.

[17] A. Einstein. "Über die von der molekularkinetischen Theorie der Wärme geforderte Bewegung von in ruhenden Flüssigkeiten suspendierten Teilchen." In: *Annalen der Physik* 322.8 (1905), pp. 549–560. ISSN: 0003-3804, 1521-3889. DOI: 10.1002/andp.19053220806. URL: https://doi.org/10.1002/andp.19053220806.

[18] Eugene Helfand. "Transport Coefficients from Dissipation in a Canonical Ensemble." In: *Physical Review* 119.1 (July 1960), pp. 1–9. ISSN: 0031-899X. DOI: 10.1103/physrev.119.1. URL: https://doi.org/10.1103/physrev.119.1.

[19] N. Galamba, C. A. Nieto de Castro, and James F. Ely. "Equilibrium and nonequilibrium molecular dynamics simulations of the thermal conductivity of molten alkali halides." In: *The Journal of Chemical Physics* 126.20 (May 2007), p. 204511. ISSN: 0021-9606, 1089-7690. DOI: 10.1063/1.2734965. URL: https://doi.org/10.1063/1.2734965.

[20] Aris Marcolongo, Loris Ercole, and Stefano Baroni. "Gauge Fixing for Heat-Transport Simulations." In: *Journal of Chemical Theory and Computation* 16.5 (Apr. 2020), pp. 3352–3362. ISSN: 1549-9618, 1549-9626. DOI: 10.1021/acs.jctc.9b01174. URL: https://doi.org/10.1021/acs.jctc.9b01174.

[21] Michel Plancherel and Mittag Leffler. "Contribution À L'Étude de la reprÉsentation D'une fonction arbitraire par des intÉgrales dÉfinies." In: *Rendiconti del Circolo Matematico di Palermo* 30.1 (Dec. 1910), pp. 289–335. ISSN: 0009-725X, 1973-4409. DOI: 10.1007/bf03014877. URL: https://doi.org/10.1007/bf03014877.

[22] Loris Ercole. "Ab Initio Simulation of Heat Transport in Silica Glass." PhD Thesis. Scuola Internazionale Superiore di Studi Avanzati—SISSA, Trieste, Italy, 2018.

[23] Norbert Wiener. "Generalized harmonic analysis." In: *Acta Mathematica* 55.0 (1930), pp. 117–258. ISSN: 0001-5962. DOI: 10.1007/bf02546511. URL: https://doi.org/10.1007/bf02546511.

[24] A. Khintchine. "Korrelationstheorie der stationären stochastischen Prozesse." In: *Mathematische Annalen* 109.1 (Dec. 1934), pp. 604–615. ISSN: 0025-5831, 1432-1807. DOI: 10.1007/bf01449156. URL: https://doi.org/10.1007/bf01449156.

[25] Bruce P Bogert. "The quefrency alanysis of time series for echoes; Cepstrum, pseudo-autocovariance, cross-cepstrum and saphe cracking." In: *Time series analysis* (1963), pp. 209–243.

[26] Loris Ercole, Aris Marcolongo, and Stefano Baroni. "Accurate thermal conductivities from optimally short molecular dynamics simulations." In: *Scientific Reports* 7.1 (Nov. 2017), pp. 1–11. ISSN: 2045-2322. DOI: 10.1038/s41598-017-15843-2. URL: https://doi.org/10.1038/s41598-017-15843-2.

[27] Milton Abramowitz and Irene A Stegun. *Handbook of mathematical functions with formulas, graphs, and mathematical tables*. Vol. 55. US Government printing office, 1964.

[28] N. R. Goodman. "The Distribution of the Determinant of a Complex Wishart Distributed Matrix." In: *The Annals of Mathematical Statistics* 34.1 (Mar. 1963), pp. 178–180. ISSN: 0003-4851. DOI: 10.1214/aoms/1177704251. URL: https://doi.org/10.1214/aoms/1177704251.

[29] Martin Bilodeau and David Brenner. *Theory of Multivariate Statistics*. Springer New York, 1999. ISBN: 9780387987392, 9780387226163. DOI: 10.1007/b97615. URL: https://doi.org/10.1007/b97615.

[30] H. Akaike. "A new look at the statistical model identification." In: *IEEE Transactions on Automatic Control* 19.6 (Dec. 1974), pp. 716–723. ISSN: 0018-9286. DOI: 10.1109/tac.1974.1100705. URL: https://doi.org/10.1109/tac.1974.1100705.

[31] Paolo Pegolo, Federico Grasselli, and Stefano Baroni. "Oxidation States, Thouless' Pumps, and Nontrivial Ionic Transport in Nonstoichiometric Electrolytes." In: *Physical Review X* 10 (4 Nov. 2020), p. 041031. DOI: 10.1103/PhysRevX.10.041031. URL: https://link.aps.org/doi/10.1103/PhysRevX.10.041031.

[32] Federico Grasselli, Lars Stixrude, and Stefano Baroni. "Heat and charge transport in H2O at ice-giant conditions from ab initio molecular dynamics simulations." In: *Nature Communications* 11.1 (July 2020), pp. 1–7. ISSN: 2041-1723. DOI: 10.1038/s41467-020-17275-5. URL: https://doi.org/10.1038/s41467-020-17275-5.

[33] Davide Tisi, Linfeng Zhang, Riccardo Bertossa, Han Wang, Roberto Car, and Stefano Baroni. "Heat transport in liquid water from first-principles and deep neural network simulations." In: *Physical Review B* 104.22 (22 Dec. 2021), p. 224202. ISSN: 2469-9950, 2469-9969. DOI: 10.1103/physrevb.104.224202. URL: https://doi.org/10.1103/physrevb.104.224202.

[34] Nicholas W. Lundgren, Giuseppe Barbalinardo, and Davide Donadio. "Mode localization and suppressed heat transport in amorphous alloys." In: *Physical Review B* 103.2 (Jan. 2021), p. 024204. ISSN: 2469-9950, 2469-9969. DOI: 10.1103/physrevb.103.024204. URL: https://doi.org/10.1103/physrevb.103.024204.

[35] Viktor Rozsa and Giulia Galli. "Solvation of simple ions in water at extreme conditions." In: *The Journal of Chemical Physics* 154.14 (Mar. 2021), p. 144501. ISSN: 0021-9606, 1089-7690. DOI: 10.1063/5.0046193. URL: https://doi.org/10.1063/5.0046193.

[36] Paolo Pegolo, Stefano Baroni, and Federico Grasselli. "Temperature- and vacancy-concentration-dependence of heat transport in Li3ClO from multi-method numerical simulations." In: *npj Computational Materials* 8.1 (Jan. 2022), p. 24. ISSN: 2057-3960. DOI: 10.1038/s41524-021-00693-4. URL: https://doi.org/10.1038/s41524-021-00693-4.

[37] Cesare Malosso, Linfeng Zhang, Roberto Car, Stefano Baroni, and Davide Tisi. "Viscosity in water from first-principles and deep-neural-network simulations." In: *npj Computational Materials* 8.1 (July 2022). ISSN: 2057-3960. DOI: 10.1038/s41524-022-00830-7. URL: https://doi.org/10.1038/s41524-022-00830-7.

[38] Abraham. Savitzky and M. J. E. Golay. "Smoothing and Differentiation of Data by Simplified Least Squares Procedures." In: *Analytical Chemistry* 36.8 (July 1964), pp. 1627–1639. ISSN: 0003-2700, 1520-6882. DOI: 10.1021/ac60214a047. URL: https://doi.org/10.1021/ac60214a047.

[39] Mark D. Schluchter. *Mean Square Error*. (In preparation). Sept. 2014. DOI: 10.1002/9781118445112.stat05906. URL: https://doi.org/10.1002/9781118445112.stat05906.

[40] Andrea Cepellotti, Giorgia Fugallo, Lorenzo Paulatto, Michele Lazzeri, Francesco Mauri, and Nicola Marzari. "Phonon hydrodynamics in two-dimensional materials." In: *Nature Communications* 6.1 (Mar. 2015), pp. 1–7. ISSN: 2041-1723. DOI: 10.1038/ncomms7400. URL: https://doi.org/10.1038/ncomms7400.

[41] D. J. Thouless. "Quantization of particle transport." In: *Physical Review B* 27.10 (10 May 1983), pp. 6083–6087. ISSN: 0163-1829. DOI: 10.1103/physrevb.27.6083. URL: https://doi.org/10.1103/physrevb.27.6083.

[42] David Vanderbilt. *Berry Phases in Electronic Structure Theory. Electric Polarization, Orbital Magnetization and Topological Insulators*. Cambridge University Press, Oct. 2018. ISBN: 9781316662205, 9781107157651. DOI: 10.1017/9781316662205. URL: https://doi.org/10.1017/9781316662205.

[43] J. J. Sakurai and Jim Napolitano. *Modern Quantum Mechanics*. Cambridge University Press, Sept. 2017. ISBN: 9781108499996. DOI: 10.1017/9781108499996. URL: https://doi.org/10.1017/9781108499996.

[44] Ali Mostafazadeh. "Generalized adiabatic product expansion: A nonperturbative method of solving the time-dependent Schrödinger equation." In: *Journal of Mathematical Physics* 40.7 (July 1999), pp. 3311–3326. ISSN: 0022-2488, 1089-7658. DOI: 10.1063/1.532889. URL: https://doi.org/10.1063/1.532889.

[45] Timothy B. Boykin. "An alternative view of the continuity equation in quantum mechanics." In: *American Journal of Physics* 68.7 (July 2000), pp. 665–667. ISSN: 0002-9505, 1943-2909. DOI: 10.1119/1.19506. eprint: https://doi.org/10.1119/1.19506. URL: https://doi.org/10.1119/1.19506.

[46] Walter Kohn. "Theory of the Insulating State." In: *Physical Review* 133.1A (Jan. 1964), A171–A181. ISSN: 0031-899X. DOI: 10.1103/physrev.133.a171. URL: https://doi.org/10.1103/physrev.133.a171.

[47] Raffaele Resta. "Adiabatic electronic flux in molecules and in condensed matter." In: *The Journal of Chemical Physics* 156.20 (May 2022), p. 204118. ISSN: 0021-9606, 1089-7690. DOI: 10.1063/5.0087883. eprint: https://doi.org/10.1063/5.0087883. URL: https://doi.org/10.1063/5.0087883.

[48] Raffaele Resta. "Quantum-Mechanical Position Operator in Extended Systems." In: *Physical Review Letters* 80.9 (Mar. 1998), pp. 1800–1803. ISSN: 0031-9007, 1079-7114. DOI: 10.1103/physrevlett.80.1800. URL: https://doi.org/10.1103/physrevlett.80.1800.

[49] Q Niu and D J Thouless. "Quantised adiabatic charge transport in the presence of substrate disorder and many-body interaction." In: *Journal of Physics A: Mathematical and General* 17.12 (Aug. 1984), pp. 2453–2462. ISSN: 0305-4470, 1361-6447. DOI: 10.1088/0305-4470/17/12/016. URL: https://doi.org/10.1088/0305-4470/17/12/016.

[50] Raffaele Resta and Sandro Sorella. "Electron Localization in the Insulating State." In: *Physical Review Letters* 82.2 (Jan. 1999), pp. 370–373. ISSN: 0031-9007, 1079-7114. DOI: 10.1103/physrevlett.82.370. URL: https://doi.org/10.1103/physrevlett.82.370.

[51] Raffaele Resta. "Faraday law, oxidation numbers, and ionic conductivity: The role of topology." In: *The Journal of Chemical Physics* 155.24 (Dec. 2021), p. 244503. ISSN: 0021-9606, 1089-7690. DOI: 10.1063/5.0077718. URL: https://doi.org/10.1063/5.0077718.

[52] Raffaele Resta. "Theory of the insulating state." In: *La Rivista del Nuovo Cimento* 41.9 (2018), pp. 463–512.

[53] Hans Hellmann et al. "Einführung in die Quantenchemie. Von H. Hellmann. 350 S.,43 Abb., 35 Tab. Franz Deuticke, Leipzig u. Wien 1937. Pr. geh. RM. 20,-. geb. RM. 22,-." In: *Angewandte Chemie* 54.11-12 (Mar. 1941), pp. 156–156. ISSN: 0044-8249, 1521-3757. DOI: 10.1002/ange.19410541109. URL: https://doi.org/10.1002/ange.19410541109.

[54] R. P. Feynman. "Forces in Molecules." In: *Physical Review* 56.4 (Aug. 1939), pp. 340–343. ISSN: 0031-899X. DOI: 10.1103/physrev.56.340. URL: https://doi.org/10.1103/physrev.56.340.

[55] Stefano Baroni, Stefano de Gironcoli, Andrea Dal Corso, and Paolo Giannozzi. "Phonons and related crystal properties from density-functional perturbation theory." In: *Reviews of Modern Physics* 73.2 (July 2001), pp. 515–562. ISSN: 0034-6861, 1539-0756. DOI: 10.1103/revmodphys.73.515. URL: https://doi.org/10.1103/revmodphys.73.515.

[56] Maia G. Vergniory, Benjamin J. Wieder, Luis Elcoro, Stuart S. P. Parkin, Claudia Felser, B. Andrei Bernevig, and Nicolas Regnault. "All topological bands of all nonmagnetic stoichiometric materials." In: *Science (New York, N.Y.)* 376.6595 (May 2022), eabg9094. ISSN: 0036-8075, 1095-9203. DOI: 10.1126/science.abg9094. URL: https://doi.org/10.1126/science.abg9094.

[57] D. J. Thouless, M. Kohmoto, M. P. Nightingale, and M. den Nijs. "Quantized Hall Conductance in a Two-Dimensional Periodic Potential." In: *Physical Review Letters* 49.6 (Aug. 1982), pp. 405–408. ISSN: 0031-9007. DOI: 10.1103/physrevlett.49.405. URL: https://doi.org/10.1103/physrevlett.49.405.

[58] Michael Victor Berry. "Quantal phase factors accompanying adiabatic changes." In: *Proceedings of the Royal Society of London. A. Mathematical and Physical Sciences* 392.1802 (Mar. 1984), pp. 45–57. ISSN: 0080-4630. DOI: 10.1098/rspa.1984.0023. URL: https://doi.org/10.1098/rspa.1984.0023.

[59] F. D. M. Haldane. "Model for a Quantum Hall Effect without Landau Levels: Condensed-matter Realization of the "Parity Anomaly"." In: *Physical Review Letters* 61.18 (Oct. 1988), pp. 2015–2018. ISSN: 0031-9007. DOI: 10.1103/physrevlett.61.2015. URL: https://doi.org/10.1103/physrevlett.61.2015.

[60] Yasuhiro Hatsugai. "Chern number and edge states in the integer quantum Hall effect." In: *Physical Review Letters* 71.22 (Nov. 1993), pp. 3697–3700. ISSN: 0031-9007. DOI: 10.1103/physrevlett.71.3697. URL: https://doi.org/10.1103/physrevlett.71.3697.

[61] Charles L Kane and Eugene J Mele. "Z 2 topological order and the quantum spin Hall effect." In: *Physical review letters* 95.14 (2005), p. 146802.

[62] M. Z. Hasan and C. L. Kane. "Colloquium: Topological insulators." In: *Reviews of Modern Physics* 82.4 (Nov. 2010), pp. 3045–3067. ISSN: 0034-6861, 1539-0756. DOI: 10.1103/revmodphys.82.3045. URL: https://doi.org/10.1103/revmodphys.82.3045.

[63] Lorenzo Privitera and Giuseppe E. Santoro. "Quantum annealing and nonequilibrium dynamics of Floquet Chern insulators." In: *Physical Review B* 93.24 (June 2016), p. 241406. ISSN: 2469-9950, 2469-9969. DOI: 10.1103/physrevb.93.241406. URL: https://doi.org/10.1103/physrevb.93.241406.

[64] Matteo M. Wauters, Angelo Russomanno, Roberta Citro, Giuseppe E. Santoro, and Lorenzo Privitera. "Localization, Topology, and Quantized Transport in Disordered Floquet Systems." In: *Physical Review Letters* 123.26 (Dec. 2019), p. 266601. ISSN: 0031-9007, 1079-7114. DOI: 10.1103/physrevlett.123.266601. URL: https://doi.org/10.1103/physrevlett.123.266601.

[65] Federico Grasselli and Stefano Baroni. "Topological quantization and gauge invariance of charge transport in liquid insulators." In: *Nature Physics* 15.9 (July 2019), pp. 967–972. ISSN: 1745-2473, 1745-2481. DOI: 10.1038/s41567-019-0562-0. URL: https://doi.org/10.1038/s41567-019-0562-0.

[66] Paolo Pegolo, Stefano Baroni, and Federico Grasselli. "Topology, Oxidation States, and Charge Transport in Ionic Conductors." In: *Annalen der Physik* 534.10 (Aug. 2022), p. 2200123. ISSN: 0003-3804, 1521-3889. DOI: 10.1002/andp.202200123. eprint: https://onlinelibrary.wiley.com/doi/pdf/10.1002/andp.202200123. URL: https://doi.org/10.1002/andp.202200123.

[67] Aron Walsh, Alexey A. Sokol, John Buckeridge, David O. Scanlon, and C. Richard A. Catlow. "Oxidation states and ionicity." In: *Nature Materials* 17.11 (Oct. 2018), pp. 958–964. ISSN: 1476-1122, 1476-4660. DOI: 10.1038/s41563-018-0165-7. URL: https://doi.org/10.1038/s41563-018-0165-7.

[68] Hannes Raebiger, Stephan Lany, Raffaele Resta, and Alex Zunger. "Oxidation numbers as Social Security Numbers: Are they predictive or postdictive?" In: *Nature Precedings* (Dec. 2009), pp. 1–1. ISSN: 1756-0357. DOI: 10.1038/npre.2009.4012.1. URL: https://doi.org/10.1038/npre.2009.4012.1.

[69] Alan D McNaught, Andrew Wilkinson, et al. *Compendium of chemical terminology*. Vol. 1669. Blackwell Science Oxford, 1997.

[70] Allen Hatcher. *Algebraic Topology*. Cambridge University Press, 2001.

[71] J B Pendry and C H Hodges. "The quantisation of charge transport in ionic systems." In: *Journal of Physics C: Solid State Physics* 17.7 (Mar. 1984), pp. 1269–1279. ISSN: 0022-3719. DOI: 10.1088/0022-3719/17/7/019. URL: https://doi.org/10.1088/0022-3719/17/7/019.

[72] Lai Jiang, Sergey V. Levchenko, and Andrew M. Rappe. "Rigorous Definition of Oxidation States of Ions in Solids." In: *Physical Review Letters* 108.16 (16 Apr. 2012), p. 166403. ISSN: 0031-9007, 1079-7114. DOI: 10.1103/physrevlett.108.166403. URL: https://doi.org/10.1103/physrevlett.108.166403.

[73] John P. Perdew, Kieron Burke, and Matthias Ernzerhof. "Generalized Gradient Approximation Made Simple." In: *Physical Review Letters* 77.18 (18 Oct. 1996), pp. 3865–3868. ISSN: 0031-9007, 1079-7114. DOI: 10.1103/physrevlett.77.3865. URL: https://doi.org/10.1103/physrevlett.77.3865.

[74] Graeme Henkelman, Blas P. Uberuaga, and Hannes Jónsson. "A climbing image nudged elastic band method for finding saddle points and minimum energy paths." In: *The Journal of Chemical Physics* 113.22 (Dec. 2000), pp. 9901–9904. ISSN: 0021-9606, 1089-7690. DOI: 10.1063/1.1329672. URL: https://doi.org/10.1063/1.1329672.

[75] Nicola Marzari and David Vanderbilt. "Maximally localized generalized Wannier functions for composite energy bands." In: *Physical Review B* 56.20 (Nov. 1997), pp. 12847–12865. ISSN: 0163-1829, 1095-3795. DOI: 10.1103/physrevb.56.12847. URL: https://doi.org/10.1103/physrevb.56.12847.

[76] Massimiliano Stengel and Nicola A. Spaldin. "Ab initio theory of metal-insulator interfaces in a finite electric field." In: *Physical Review B* 75.20 (20 May 2007), p. 205121. ISSN: 1098-0121, 1550-235X. DOI: 10.1103/physrevb.75.205121. URL: https://doi.org/10.1103/physrevb.75.205121.

[77] Charles Hagwood. *Mathematician; National Institute of Standards and Technology (NIST)*. NIST Atomic Spectra Database. 2014. DOI: 10.5948/9781614441168.055. URL: https://doi.org/10.5948/9781614441168.055.

[78] W. Heitler and F. London. "Wechselwirkung neutraler Atome und homöopolare Bindung nach der Quantenmechanik." In: *Zeitschrift für Physik* 44.6-7 (June 1927), pp. 455–472. ISSN: 1434-6001, 1434-601X. DOI: 10.1007/bf01397394. URL: https://doi.org/10.1007/bf01397394.

[79] Richard M. Martin. "Comment on calculations of electric polarization in crystals." In: *Physical Review B* 9.4 (4 Feb. 1974), pp. 1998–1999. ISSN: 0556-2805. DOI: 10.1103/physrevb.9.1998. URL: https://doi.org/10.1103/physrevb.9.1998.

[80] A. Selloni, R. Car, M. Parrinello, and P. Carnevali. "Electron pairing in dilute liquid metal-metal halide solutions." In: *The Journal of Physical Chemistry* 91.19 (Sept. 1987), pp. 4947–4949. ISSN: 0022-3654, 1541-5740. DOI: 10.1021/j100303a013. URL: https://doi.org/10.1021/j100303a013.

[81] E. S. Fois, A. Selloni, M. Parrinello, and R. Car. "Bipolarons in metal-metal halide solutions." In: *The Journal of Physical Chemistry* 92.11 (June 1988), pp. 3268–3273. ISSN: 0022-3654, 1541-5740. DOI: 10.1021/j100322a039. URL: https://doi.org/10.1021/j100322a039.

[82] A. Selloni, P. Carnevali, R. Car, and M. Parrinello. "Localization, hopping, and diffusion of electrons in molten salts." In: *Physical Review Letters* 59.7 (Aug. 1987), pp. 823–826. ISSN: 0031-9007. DOI: 10.1103/physrevlett.59.823. URL: https://doi.org/10.1103/physrevlett.59.823.

[83] R. Car and M. Parrinello. "Unified Approach for Molecular Dynamics and Density-Functional Theory." In: *Physical Review Letters* 55.22 (Nov. 1985), pp. 2471–2474. ISSN: 0031-9007. DOI: 10.1103/physrevlett.55.2471. URL: https://doi.org/10.1103/physrevlett.55.2471.

[84] W. W. Warren. "Metal-Metal Salt Solutions." In: *Molten Salt Chemistry*. Springer Netherlands, 1987, pp. 237–257. ISBN: 9789401082174, 9789400938632. DOI: 10.1007/978-94-009-3863-2_11. URL: https://doi.org/10.1007/978-94-009-3863-2_11.

[85] E. Fois, A. Selloni, and M. Parrinello. "Approach to metallic behavior in metal–molten-salt solutions." In: *Physical Review B* 39.7 (Mar. 1989), pp. 4812–4815. ISSN: 0163-1829. DOI: 10.1103/physrevb.39.4812. URL: https://doi.org/10.1103/physrevb.39.4812.

[86] Pier Luigi Silvestrelli, Ali Alavi, Michele Parrinello, and Daan Frenkel. "Nonmetal-metal transition in metal–molten-salt solutions." In: *Physical Review B* 53.19 (19 May 1996), pp. 12750–12760. ISSN: 0163-1829, 1095-3795. DOI: 10.1103/physrevb.53.12750. URL: https://doi.org/10.1103/physrevb.53.12750.

[87] Tillmann Buttersack et al. "Photoelectron spectra of alkali metal–ammonia microjets: From blue electrolyte to bronze metal." In: *Science* 368.6495 (June 2020), pp. 1086–1091. ISSN: 0036-8075, 1095-9203. DOI: 10.1126/science.aaz7607. URL: https://doi.org/10.1126/science.aaz7607.

[88] D. Nattland, H. Heyer, and W. Freyland. "Metal-Nonmetal Transition in Liquid Alkali Metal-Alkalihalide Melts: Electrical Conductivity and Optical Reflectivity Study." In: *Zeitschrift für Physikalische Chemie* 149.1 (Jan. 1986), pp. 1–15. ISSN: 2196-7156, 0942-9352. DOI: 10.1524/zpch.1986.149.1.001. URL: https://doi.org/10.1524/zpch.1986.149.1.001.

[89] H. R. Bronstein and M. A. Bredig. "The Electrical Conductivity of Solutions of Alkali Metals in their Molten Halides." In: *Journal of the American Chemical Society* 80.9 (May 1958), pp. 2077–2081. ISSN: 0002-7863, 1520-5126. DOI: 10.1021/ja01542a014. URL: https://doi.org/10.1021/ja01542a014.

[90] William W. Warren, B. F. Campbell, and G. F. Brennert. "Picosecond recombination dynamics of electrons in ionic liquids." In: *Physical Review Letters* 58.9 (Mar. 1987), pp. 941–944. ISSN: 0031-9007. DOI: 10.1103/physrevlett.58.941. URL: https://doi.org/10.1103/physrevlett.58.941.

[91] Yingkai Zhang and Weitao Yang. "A challenge for density functionals: Self-interaction error increases for systems with a noninteger number of electrons." In: *The Journal of Chemical Physics* 109.7 (Aug. 1998), pp. 2604–2608. ISSN: 0021-9606, 1089-7690. DOI: 10.1063/1.476859. URL: https://doi.org/10.1063/1.476859.

[92] Junwei Lucas Bao, Laura Gagliardi, and Donald G. Truhlar. "Self-Interaction Error in Density Functional Theory: An Appraisal." In: *The Journal of Physical Chemistry Letters* 9.9 (Apr. 2018), pp. 2353–2358. ISSN: 1948-7185, 1948-7185. DOI: 10.1021/acs.jpclett.8b00242. URL: https://doi.org/10.1021/acs.jpclett.8b00242.

[93] G. Lindemann, R. Lassnig, W. Seidenbusch, and E. Gornik. "Cyclotron resonance study of polarons in GaAs." In: *Physical Review B* 28.8 (Oct. 1983), pp. 4693–4703. ISSN: 0163-1829. DOI: 10.1103/physrevb.28.4693. URL: https://doi.org/10.1103/physrevb.28.4693.

[94] R.D Popp and R.B Murray. "Diffusion of the Vk-polaron in alkali halides: Experiments in NaI and RbI." In: *Journal of Physics and Chemistry of Solids* 33.3 (Jan. 1972), pp. 601–610. ISSN: 0022-3697. DOI: 10.1016/0022-3697(72)90069-8. URL: https://doi.org/10.1016/0022-3697(72)90069-8.

[95] P. M. Chaikin, A. F. Garito, and A. J. Heeger. "Excitonic Polarons in Molecular Crystals." In: *Physical Review B* 5.12 (June 1972), pp. 4966–4969. ISSN: 0556-2805. DOI: 10.1103/physrevb.5.4966. URL: https://doi.org/10.1103/physrevb.5.4966.

[96] Lev Davidovich Landau. "Electron motion in crystal lattices." In: *Phys. Z. Sowjet.* 3 (1933), p. 664.

[97] Solomon Pekar. "Local quantum states of electrons in an ideal ion crystal." In: *Zhurnal Eksperimentalnoi I Teoreticheskoi Fiziki* 16.4 (1946), pp. 341–348.

[98] Weng Hong Sio, Carla Verdi, Samuel Poncé, and Feliciano Giustino. "Ab initio theory of polarons: Formalism and applications." In: *Physical Review B* 99.23 (2019), p. 235139.

[99] Carlo Adamo and Vincenzo Barone. "Toward reliable density functional methods without adjustable parameters: The PBE0 model." In: *The Journal of Chemical Physics* 110.13 (Apr. 1999), pp. 6158–6170. ISSN: 0021-9606, 1089-7690. DOI: 10.1063/1.478522. URL: https://doi.org/10.1063/1.478522.

[100] R. A. Marcus. "On the Theory of Oxidation-Reduction Reactions Involving Electron Transfer. I." In: *The Journal of Chemical Physics* 24.5 (May 1956), pp. 966–978. ISSN: 0021-9606, 1089-7690. DOI: 10.1063/1.1742723. URL: https://doi.org/10.1063/1.1742723.

[101] N. S. Hush. "Adiabatic Rate Processes at Electrodes. I. Energy-Charge Relationships." In: *The Journal of Chemical Physics* 28.5 (May 1958), pp. 962–972. ISSN: 0021-9606, 1089-7690. DOI: 10.1063/1.1744305. URL: https://doi.org/10.1063/1.1744305.

[102] Ulrich Weiss. *Quantum Dissipative Systems*. WORLD SCIENTIFIC, Nov. 2011. ISBN: 9789814374910, 9789814374927. DOI: 10.1142/8334. URL: https://doi.org/10.1142/8334.

[103] Benny Carmeli and David Chandler. "Effective adiabatic approximation for a two level system coupled to a bath." In: *The Journal of Chemical Physics* 82.7 (Apr. 1985), pp. 3400–3404. ISSN: 0021-9606, 1089-7690. DOI: 10.1063/1.448942. URL: https://doi.org/10.1063/1.448942.

[104] Leyla Isaeva, Giuseppe Barbalinardo, Davide Donadio, and Stefano Baroni. "Modeling heat transport in crystals and glasses from a unified lattice-dynamical approach." In: *Nature Communications* 10.1 (Aug. 2019), p. 3853. ISSN: 2041-1723. DOI: 10.1038/s41467-019-11572-4. URL: https://doi.org/10.1038/s41467-019-11572-4.

[105] Giuseppe Barbalinardo, Zekun Chen, Nicholas W. Lundgren, and Davide Donadio. "Efficient anharmonic lattice dynamics calculations of thermal transport in crystalline and disordered solids." In: *Journal of Applied Physics* 128.13 (Oct. 2020), p. 135104. ISSN: 0021-8979, 1089-7550. DOI: 10.1063/5.0020443. URL: https://doi.org/10.1063/5.0020443.

[106] Michele Simoncelli, Nicola Marzari, and Francesco Mauri. "Unified theory of thermal transport in crystals and glasses." In: *Nature Physics* 15.8 (May 2019), pp. 809–813. ISSN: 1745-2473, 1745-2481. DOI: 10.1038/s41567-019-0520-x. URL: https://doi.org/10.1038/s41567-019-0520-x.

[107] Alfredo Fiorentino. "Theory and Numerical Simulation of Heat Transport in Disordered Systems." Master's Thesis. Università degli Studi di Trieste, 2020.

[108] Alfredo Fiorentino and Stefano Baroni. "From Green-Kubo to the full Boltzmann kinetic approach to heat transport in crystals and glasses." In: *arXiv preprint arXiv:2206.01279* (2022).

[109] Philip B. Allen and Joseph L. Feldman. "Thermal Conductivity of Glasses: Theory and Application to Amorphous Si." In: *Physical Review Letters* 62.6 (Feb. 1989), pp. 645–648. ISSN: 0031-9007. DOI: 10.1103/physrevlett.62.645. URL: https://doi.org/10.1103/physrevlett.62.645.

[110] Philip B. Allen and Joseph L. Feldman. "Thermal conductivity of disordered harmonic solids." In: *Physical Review B* 48.17 (Nov. 1993), pp. 12581–12588. ISSN: 0163-1829, 1095-3795. DOI: 10.1103/physrevb.48.12581. URL: https://doi.org/10.1103/physrevb.48.12581.

[111] G.A. Slack. "Nonmetallic crystals with high thermal conductivity." In: *Journal of Physics and Chemistry of Solids* 34.2 (Jan. 1973), pp. 321–335. ISSN: 0022-3697. DOI: 10.1016/0022-3697(73)90092-9. URL: https://doi.org/10.1016/0022-3697(73)90092-9.

[112] Glen A Slack. "The thermal conductivity of nonmetallic crystals." In: *Solid State Physics: Advances in Research and Applications, Vol. 54* 34 (1979), pp. 1–71.

[113] Tiantian Jia, Gang Chen, and Yongsheng Zhang. "Lattice thermal conductivity evaluated using elastic properties." In: *Physical Review B* 95.15 (Apr. 2017), p. 155206. ISSN: 2469-9950, 2469-9969. DOI: 10.1103/physrevb.95.155206. URL: https://doi.org/10.1103/physrevb.95.155206.

[114] Linfeng Zhang, Jiequn Han, Han Wang, Wissam Saidi, Roberto Car, and Weinan E. "End-to-end Symmetry Preserving Inter-atomic Potential Energy Model for Finite and Extended Systems." In: *Advances in Neural Information Processing Systems*. Ed. by S. Bengio, H. Wallach, H. Larochelle, K. Grauman, N. Cesa-Bianchi, and R. Garnett. Vol. 31. Curran Associates, Inc., 2018. URL: https://proceedings.neurips.cc/paper/2018/file/e2ad76f2326fbc6b56a45a56c59fafdb-Paper.pdf.

[115] Yuzhi Zhang, Haidi Wang, Weijie Chen, Jinzhe Zeng, Linfeng Zhang, Han Wang, and Weinan E. "DP}-{GEN: A concurrent learning platform for the generation of reliable deep learning based potential energy models." In: *Computer Physics Communications* 253 (Aug. 2020), p. 107206. ISSN: 0010-4655. DOI: 10.1016/j.cpc.2020.107206. URL: https://doi.org/10.1016/j.cpc.2020.107206.

[116] Zheyong Fan, Zezhu Zeng, Cunzhi Zhang, Yanzhou Wang, Keke Song, Haikuan Dong, Yue Chen, and Tapio Ala-Nissila. "Neuroevolution machine learning potentials: Combining high accuracy and low cost in atomistic simulations and application to heat transport." In: *Physical Review B* 104.10 (10 Sept. 2021), p. 104309. ISSN: 2469-9950, 2469-9969. DOI: 10.1103/physrevb.104.104309. URL: https://doi.org/10.1103/physrevb.104.104309.

[117] Aris Marcolongo, Riccardo Bertossa, Davide Tisi, and Stefano Baroni. "QEHeat: An open-source energy flux calculator for the computation of heat-transport coefficients from first principles." In: *Computer Physics Communications* 269 (Dec. 2021), p. 108090. ISSN: 0010-4655. DOI: 10.1016/j.cpc.2021.108090. URL: https://doi.org/10.1016/j.cpc.2021.108090.

[118] Xuning Feng, Minggao Ouyang, Xiang Liu, Languang Lu, Yong Xia, and Xiangming He. "Thermal runaway mechanism of lithium ion battery for electric vehicles: A review." In: *Energy Storage Materials* 10 (Jan. 2018), pp. 246–267. ISSN: 2405-8297. DOI: 10.1016/j.ensm.2017.05.013. URL: https://doi.org/10.1016/j.ensm.2017.05.013.

[119] N.R. Abdulchalikova and A.E. Aliev. "Thermal properties of Li conducting superionic matirials." In: *Synthetic Metals* 71.1-3 (Apr. 1995), pp. 1929–1932. ISSN: 0379-6779. DOI: 10.1016/0379-6779(94)03112-j. URL: https://doi.org/10.1016/0379-6779(94)03112-j.

[120] A. É. Aliev, V. F. Krivorotov, and P. K. Khabibullaev. "Specific heat and thermal conductivity of superionic conductors in the superionic phase." In: *Physics of the Solid State* 39.9 (Sept. 1997), pp. 1378–1382. ISSN: 1063-7834, 1090-6460. DOI: 10.1134/1.1130083. URL: https://doi.org/10.1134/1.1130083.

[121] Afaf A.Abd El-Rahman, Mohamed M. El-Desoky, and Abd El-Wahab A. El-Sharkawy. "Electrical and thermal properties of polycrystalline Li2SO4 and Ag2SO4." In: *Journal of Physics and Chemistry of Solids* 60.1 (Jan. 1999), pp. 119–127. ISSN: 0022-3697. DOI: 10.1016/s0022-3697(98)00254-6. URL: https://doi.org/10.1016/s0022-3697(98)00254-6.

[122] L. S. Parfen'eva, A. I. Shelykh, I. A. Smirnov, A. V. Prokof'ev, W. Assmus, H. Misiorek, J. Mucha, A. Jezowski, and I. G. Vasil'eva. "Heat transport over nonmagnetic lithium chains in LiCuVO4, a new one-dimensional superionic conductor." In: *Physics of the Solid State* 45.11 (Nov. 2003), pp. 2093–2098. ISSN: 1063-7834, 1090-6460. DOI: 10.1134/1.1626742. URL: https://doi.org/10.1134/1.1626742.

[123] Yuantao Cui, Morsi M. Mahmoud, Magnus Rohde, Carlos Ziebert, and Hans Juergen Seifert. "Thermal and ionic conductivity studies of lithium aluminum germanium phosphate solid-state electrolyte." In: *Solid State Ionics* 289 (June 2016), pp. 125–132. ISSN: 0167-2738. DOI: 10.1016/j.ssi.2016.03.007. URL: https://doi.org/10.1016/j.ssi.2016.03.007.

[124] Sajad Yazdani, Raana Kashfi-Sadabad, Mayra Daniela Morales-Acosta, Raul David Montaño, Tuoc Ngoc Vu, Huan Doan Tran, Menghan Zhou, Yufei Liu, Jian He, and Michael Thompson Pettes. "Thermal transport in phase-stabilized lithium zirconate phosphates." In: *Applied Physics Letters* 117.1 (July 2020), p. 011903. ISSN: 0003-6951, 1077-3118. DOI: 10.1063/5.0013716. URL: https://doi.org/10.1063/5.0013716.

[125] M.J. Rice and W.L. Roth. "Ionic transport in super ionic conductors: A theoretical model." In: *Journal of Solid State Chemistry* 4.2 (Mar. 1972), pp. 294–310. ISSN: 0022-4596. DOI: 10.1016/0022-4596(72)90121-1. URL: https://doi.org/10.1016/0022-4596(72)90121-1.

[126] K Yonashiro. "Thermal conductivity in superionic conductors." In: *Solid State Ionics* 27.3 (July 1988), pp. 157–167. ISSN: 0167-2738. DOI: 10.1016/0167-2738(88)90005-7. URL: https://doi.org/10.1016/0167-2738(88)90005-7.

[127] M. H. Braga, J. A. Ferreira, V. Stockhausen, J. E. Oliveira, and A. El-Azab. "Novel Li3ClO based glasses with superionic properties for lithium batteries." In: *Journal of Materials Chemistry A: Materials for Energy and Sustainability* 2.15 (2014), pp. 5470–5480. ISSN: 2050-7488, 2050-7496. DOI: 10.1039/c3ta15087a. URL: https://doi.org/10.1039/c3ta15087a.

[128] Xujie Lü, Gang Wu, John W. Howard, Aiping Chen, Yusheng Zhao, Luke L. Daemen, and Quanxi Jia. "Li-rich anti-perovskite Li3OCl films with enhanced ionic conductivity." In: *Chemical Communications* 50.78 (2014), pp. 11520–11522. ISSN: 1359-7345, 1364-548X. DOI: 10.1039/c4cc05372a. URL: https://doi.org/10.1039/c4cc05372a.

[129] S. Baroni, P. Giannozzi, and E. Isaev. "Density-Functional Perturbation Theory for Quasi-Harmonic Calculations." In: *Reviews in Mineralogy and Geochemistry* 71.1 (Jan. 2010), pp. 39–57. ISSN: 1529-6466. DOI: 10.2138/rmg.2010.71.3. URL: https://doi.org/10.2138/rmg.2010.71.3.

[130] F. D. Murnaghan. "The Compressibility of Media under Extreme Pressures." In: *Proceedings of the National Academy of Sciences* 30.9 (Sept. 1944), pp. 244–247. ISSN: 0027-8424, 1091-6490. DOI: 10.1073/pnas.30.9.244. eprint: https://www.pnas.org/content/30/9/244.full.pdf. URL: https://doi.org/10.1073/pnas.30.9.244.

[131] Yi Zhang, Yusheng Zhao, and Changfeng Chen. "Ab initio study of the stabilities of and mechanism of superionic transport in lithium-rich antiperovskites." In: *Physical Review B* 87.13 (Apr. 2013), pp. 1–8. ISSN: 1098-0121, 1550-235X. DOI: 10.1103/physrevb.87.134303. URL: https://doi.org/10.1103/physrevb.87.134303.

[132] Alexandra Emly, Emmanouil Kioupakis, and Anton Van der Ven. "Phase Stability and Transport Mechanisms in Antiperovskite Li3OCl and Li3OBr Superionic Conductors." In: *Chemistry of Materials* 25.23 (Nov. 2013), pp. 4663–4670. ISSN: 0897-4756, 1520-5002. DOI: 10.1021/cm4016222. URL: https://doi.org/10.1021/cm4016222.

[133] Musheng Wu, Bo Xu, Xueling Lei, Kelvin Huang, and Chuying Ouyang. "Bulk properties and transport mechanisms of a solid state antiperovskite Li-ion conductor Li3OCl: Insights from first principles calculations." In: *Journal of Materials Chemistry A* 6.3 (2018), pp. 1150–1160. ISSN: 2050-7488, 2050-7496. DOI: 10.1039/c7ta08780b. URL: https://doi.org/10.1039/c7ta08780b.

[134] Yusheng Zhao and Luke L. Daemen. "Superionic Conductivity in Lithium-Rich Anti-Perovskites." In: *Journal of the American Chemical Society* 134.36 (Aug. 2012), pp. 15042–15047. ISSN: 0002-7863, 1520-5126. DOI: 10.1021/ja305709z. URL: https://doi.org/10.1021/ja305709z.

[135] Aamir Shafique and Young-Han Shin. "The effect of non-analytical corrections on the phononic thermal transport in InX (X = S, Se, Te) monolayers." In: *Scientific Reports* 10.1 (Jan. 2020), pp. 1–10. ISSN: 2045-2322. DOI: 10.1038/s41598-020-57644-0. URL: https://doi.org/10.1038/s41598-020-57644-0.

[136] Min-Hua Chen, Alexandra Emly, and Anton Van der Ven. "Anharmonicity and phase stability of antiperovskite Li3OCl." In: *Physical Review B* 91.21 (21 June 2015), p. 214306. ISSN: 1098-0121, 1550-235X. DOI: 10.1103/physrevb.91.214306. URL: https://doi.org/10.1103/physrevb.91.214306.

[137] Zhi Deng, Zhenbin Wang, Iek-Heng Chu, Jian Luo, and Shyue Ping Ong. "Elastic Properties of Alkali Superionic Conductor Electrolytes from First Principles Calculations." In: *Journal of The Electrochemical Society* 163.2 (Nov. 2015), A67–A74. ISSN: 0013-4651, 1945-7111. DOI: 10.1149/2.0061602jes. URL: https://doi.org/10.1149/2.0061602jes.

[138] Wu Xu, Jiulin Wang, Fei Ding, Xilin Chen, Eduard Nasybulin, Yaohui Zhang, and Ji-Guang Zhang. "Lithium metal anodes for rechargeable batteries." In: *Energy Environ. Sci.* 7.2 (2 2014), pp. 513–537. ISSN: 1754-5692, 1754-5706. DOI: 10.1039/c3ee40795k. URL: https://doi.org/10.1039/c3ee40795k.

[139] Charles Monroe and John Newman. "The Impact of Elastic Deformation on Deposition Kinetics at Lithium/Polymer Interfaces." In: *Journal of The Electrochemical Society* 152.2 (2005), A396. ISSN: 0013-4651. DOI: 10.1149/1.1850854. URL: https://doi.org/10.1149/1.1850854.

[140] Mickaël Dollé, Lucas Sannier, Bernard Beaudoin, Michel Trentin, and Jean-Marie Tarascon. "Live Scanning Electron Microscope Observations of Dendritic Growth in Lithium/Polymer Cells." In: *Electrochemical and Solid-State Letters* 5.12 (2002), A286. ISSN: 1099-0062. DOI: 10.1149/1.1519970. URL: https://doi.org/10.1149/1.1519970.

[141] D. H. Chung and W. R. Buessem. "The Elastic Anisotropy of Crystals." In: *Journal of Applied Physics* 38.5 (Apr. 1967), pp. 2010–2012. ISSN: 0021-8979, 1089-7550. DOI: 10.1063/1.1709819. URL: https://doi.org/10.1063/1.1709819.

[142] Shivakumar I. Ranganathan and Martin Ostoja-Starzewski. "Universal Elastic Anisotropy Index." In: *Physical Review Letters* 101.5 (Aug. 2008), p. 055504. ISSN: 0031-9007, 1079-7114. DOI: 10.1103/physrevlett.101.055504. URL: https://doi.org/10.1103/physrevlett.101.055504.

[143] Frank D. Stacey and Jane H. Hodgkinson. "Thermodynamics with the Grüneisen parameter: Fundamentals and applications to high pressure physics and geophysics." In: *Physics of the Earth and Planetary Interiors* 286 (Jan. 2019), pp. 42–68. ISSN: 0031-9201. DOI: 10.1016/j.pepi.2018.10.006. URL: https://doi.org/10.1016/j.pepi.2018.10.006.

[144] S.F. Pugh. "Relations between the elastic moduli and the plastic properties of polycrystalline pure metals." In: *The London, Edinburgh, and Dublin Philosophical Magazine and Journal of Science* 45.367 (Aug. 1954), pp. 823–843. ISSN: 1941-5982, 1941-5990. DOI: 10.1080/14786440808520496. URL: https://doi.org/10.1080/14786440808520496.

[145] R. Peierls. "Zur kinetischen Theorie der Wärmeleitung in Kristallen." In: *Annalen der Physik* 395.8 (1929), pp. 1055–1101. ISSN: 0003-3804, 1521-3889. DOI: 10.1002/andp.19293950803. URL: https://doi.org/10.1002/andp.19293950803.

[146] J.M. Ziman. *Electrons and Phonons*. Amen House, London E.C.4: Oxford University Press, Feb. 2001. ISBN: 9780198507796. DOI: 10.1093/acprof:oso/9780198507796.001.0001. URL: https://doi.org/10.1093/acprof:oso/9780198507796.001.0001.

[147] Alan J. H. McGaughey, Ankit Jain, and Hyun-Young Kim. "Phonon properties and thermal conductivity from first principles, lattice dynamics, and the Boltzmann transport equation." In: *Journal of Applied Physics* 125.1 (Jan. 2019), p. 011101. ISSN: 0021-8979, 1089-7550. DOI: 10.1063/1.5064602. URL: https://doi.org/10.1063/1.5064602.

[148] Lorenzo Paulatto, Francesco Mauri, and Michele Lazzeri. "Anharmonic properties from a generalized third-order ab initio approach: Theory and applications to graphite and graphene." In: *Physical Review B* 87.21 (June 2013), p. 214303. ISSN: 1098-0121, 1550-235X. DOI: 10.1103/physrevb.87.214303. URL: https://doi.org/10.1103/physrevb.87.214303.

[149] Tianli Feng and Xiulin Ruan. "Quantum mechanical prediction of four-phonon scattering rates and reduced thermal conductivity of solids." In: *Physical Review B* 93.4 (Jan. 2016), p. 045202. ISSN: 2469-9950, 2469-9969. DOI: 10.1103/physrevb.93.045202. URL: https://doi.org/10.1103/physrevb.93.045202.

[150] Tianli Feng, Lucas Lindsay, and Xiulin Ruan. "Four-phonon scattering significantly reduces intrinsic thermal conductivity of solids." In: *Physical Review B* 96.16 (Oct. 2017), p. 161201. ISSN: 2469-9950, 2469-9969. DOI: 10.1103/physrevb.96.161201. URL: https://doi.org/10.1103/physrevb.96.161201.

[151] Rodolpho Mouta, Maria Águida B. Melo, Eduardo M. Diniz, and Carlos William A. Paschoal. "Concentration of Charge Carriers, Migration, and Stability in Li3OCl Solid Electrolytes." In: *Chemistry of Materials* 26.24 (Dec. 2014), pp. 7137–7144. ISSN: 0897-4756, 1520-5002. DOI: 10.1021/cm503717e. URL: https://doi.org/10.1021/cm503717e.

[152] Ziheng Lu, Chi Chen, Zarah Medina Baiyee, Xin Chen, Chunming Niu, and Francesco Ciucci. "Defect chemistry and lithium transport in Li3OCl anti-perovskite superionic conductors." In: *Physical Chemistry Chemical Physics* 17.48 (2015), pp. 32547–32555. ISSN: 1463-9076, 1463-9084. DOI: 10.1039/c5cp05722a. URL: https://doi.org/10.1039/c5cp05722a.

[153] Jiequn Han, Linfeng Zhang, Roberto Car, and Weinan E. "Deep Potential: A General Representation of a Many-Body Potential Energy Surface." In: *Communications in Computational Physics* 23.3 (2018), pp. 629–639. ISSN: 1815-2406. DOI: 10.4208/cicp.oa-2017-0213. URL: https://doi.org/10.4208/cicp.oa-2017-0213.

[154] Pierre Hirel. "Atomsk: A tool for manipulating and converting atomic data files." In: *Computer Physics Communications* 197 (Dec. 2015), pp. 212–219. ISSN: 0010-4655. DOI: 10.1016/j.cpc.2015.07.012. URL: https://doi.org/10.1016/j.cpc.2015.07.012.

[155] Giovanni Bussi, Davide Donadio, and Michele Parrinello. "Canonical sampling through velocity rescaling." In: *The Journal of Chemical Physics* 126.1 (Jan. 2007), p. 014101. ISSN: 0021-9606, 1089-7690. DOI: 10.1063/1.2408420. URL: https://doi.org/10.1063/1.2408420.

[156] A. Eucken. "Über die Temperaturabhängigkeit der Wärmeleitfähigkeit fester Nichtmetalle." In: *Annalen der Physik* 339.2 (1911), pp. 185–221. ISSN: 0003-3804, 1521-3889. DOI: 10.1002/andp.19113390202. URL: https://doi.org/10.1002/andp.19113390202.

[157] A. Einstein. "Elementare Betrachtungen über die thermische Molekularbewegung in festen Körpern." In: *Annalen der Physik* 340.9 (1911), pp. 679–694. ISSN: 0003-3804, 1521-3889. DOI: 10.1002/andp.19113400903. URL: https://doi.org/10.1002/andp.19113400903.

[158] Tim Bernges et al. "Considering the Role of Ion Transport in Diffuson-Dominated Thermal Conductivity." In: *Advanced Energy Materials* 12.22 (Apr. 2022), p. 2200717. ISSN: 1614-6832, 1614-6840. DOI: 10.1002/aenm.202200717. URL: https://doi.org/10.1002/aenm.202200717.

[159] Zherui Han, Xiaolong Yang, Wu Li, Tianli Feng, and Xiulin Ruan. "FourPhonon: An extension module to ShengBTE for computing four-phonon scattering rates and thermal conductivity." In: *Computer Physics Communications* 270 (Jan. 2022), p. 108179. ISSN: 0010-4655. DOI: 10.1016/j.cpc.2021.108179. URL: https://doi.org/10.1016/j.cpc.2021.108179.

[160] Albert P. Bartók, Mike C. Payne, Risi Kondor, and Gábor Csányi. "Gaussian Approximation Potentials: The Accuracy of Quantum Mechanics, without the Electrons." In: *Physical Review Letters* 104.13 (Apr. 2010), p. 136403. ISSN: 0031-9007, 1079-7114. DOI: 10.1103/physrevlett.104.136403. URL: https://doi.org/10.1103/physrevlett.104.136403.

[161] Steven E Pav. "Moments of the log non-central chi-square distribution." In: *arXiv preprint arXiv:1503.06266* (2015).

[162] Magda Peligrad and Wei Biao Wu. "Central limit theorem for Fourier transforms of stationary processes." In: *The Annals of Probability* 38.5 (Sept. 2010), pp. 2009–2022. ISSN: 0091-1798. DOI: 10.1214/10-aop530. URL: https://doi.org/10.1214/10-aop530.

[163] Jörg Behler and Michele Parrinello. "Generalized Neural-Network Representation of High-Dimensional Potential-Energy Surfaces." In: *Physical Review Letters* 98.14 (Apr. 2007), p. 146401. ISSN: 0031-9007, 1079-7114. DOI: 10.1103/physrevlett.98.146401. URL: https://doi.org/10.1103/physrevlett.98.146401.

[164] J. S. Smith, O. Isayev, and A. E. Roitberg. "{ANI}-1: An extensible neural network potential with DFT accuracy at force field computational cost." In: *Chemical Science* 8.4 (2017), pp. 3192–3203. ISSN: 2041-6520, 2041-6539. DOI: 10.1039/c6sc05720a. URL: https://doi.org/10.1039/c6sc05720a.

[165] Linfeng Zhang, Jiequn Han, Han Wang, Roberto Car, and Weinan E. "Deep Potential Molecular Dynamics: A Scalable Model with the Accuracy of Quantum Mechanics." In: *Physical Review Letters* 120.14 (Apr. 2018), p. 143001. ISSN: 0031-9007, 1079-7114. DOI: 10.1103/physrevlett.120.143001. URL: https://doi.org/10.1103/physrevlett.120.143001.

[166] Ian Goodfellow, Yoshua Bengio, and Aaron Courville. *Deep Learning*. MIT Press, 2016. URL: http://www.deeplearningbook.org.

[167] Diederik P Kingma and Jimmy Ba. "Adam: A method for stochastic optimization." In: *arXiv preprint arXiv:1412.6980* (2014).

COLOPHON

This document was typeset in LaTeX using the typographical look-and-feel `classicthesis` developed by André Miede and Ivo Pletikosić. Most of the graphics in this thesis are generated using the python package `matplotlib` and Wolfram Mathematica. The bibliography is typeset using `biblatex`.